# Liquid Crystalline Phase Behavior and Fiber Spinning of Double-Stranded DNA Stabilized Single-Walled Carbon Nanotube Dispersions

by

Geyou Ao

A dissertation submitted to the Graduate Faculty of
Auburn University
in partial fulfillment of the
requirements for the Degree of
Doctor of Philosophy

Auburn, Alabama
May 7, 2012

Keywords: single-walled carbon nanotubes, double-stranded DNA, nematic and cholesteric liquid crystal, phase behavior, macroscopic assembly

Approved by

Virginia A. Davis, Chair, Mary and John H. Sanders Associate Professor of Chemical Engineering
Mark E. Byrne, Daniel F. & Josephine Breeden Associate Professor of Chemical Engineering
Yoon Y. Lee, Uthlaut Family Professor of Chemical Engineering
Aleksandr Simonian, Professor of Materials Engineering

# Abstract

This dissertation describes the first discovery and characterization of lyotropic cholesteric single-walled carbon nanotube (SWNT) liquid crystals phase where the SWNT acts as a mesogens and is not simply inserted into an existing lyotropic dispersion. The liquid crystal phase was formed by concentrating mixtures of SWNT and aqueous double-stranded deoxyribonucleic acid (dsDNA). The characteristic cholesteric liquid crystal fingerprint texture with multi-colored regions was obtained due to the presence of the cholesterogenic forming biopolymer dsDNA. Depending on the dispersion methodology, the polydomain nematic phase previously reported for other lyotropic carbon nanotube dispersions could also be obtained. The phase behavior and dispersion microstructure were affected by the relative concentrations of dsDNA and SWNT and whether small bundles were removed prior to concentrating the dispersions.

The phase behavior and rheology of aqueous dsDNA/SWNT dispersions were determined by a combination of rheology and optical microscopy. The results indicated that SWNT in dsDNA/SWNT dispersions behave as rigid rods. With increasing concentration the dispersions transitioned from a dilute phase with free rotational and translational rod motion, to a semidilute phase where rod rotation was inhibited, to a biphasic regime consisting of isotropic and liquid crystalline phases, and finally to a single liquid crystalline phase. The results of this research will enable new fundamental investigations comparing nematic and cholesteric liquid crystalline phase behavior and shear response. The simpler, aqueous cellulose nanocrystal (CNC)

system was also investigated to provide greater insights into the more complex dsDNA/SWNT system. The CNC system also formed a cholesteric liquid crystal, but the effects of concentration on rheological properties were markedly different from both the dsDNA/SWNT system and classical lyotropic liquid crystalline polymers.

The assembly of biopolymer stabilized SWNT dispersions into films and fibers was also investigated. In the case of cholesteric dsDNA/SWNT dispersions, casting films onto a substrate without any applied shear enabled retention of the helical microstructure. This finding may enable the production of films that possess not only SWNT strength and conductivity, but also with optical signatures. Shearing cholesteric dispersions during processing resulted in densely packed aligned films that have potential use as polarized films. Preliminary investigations of wet solution spinning of dsDNA/SWNT dispersions showed the significant impact the coagulant had on fiber microstructure. Investigation of lysozyme, (1-tetradecyl) trimethyl-ammonium bromide, SWNT dispersions (LSZ/TTAB/SWNT) fiber spinning resulted in promising microstructural characteristics and mechanical properties. As a result, fiber spinning optimization is being pursued by other researchers.

The results of this research highlight the rich rheology and phase behavior of nanocylinder dispersions. These insights have provided a foundation for producing aligned bulk materials consisting of nanocylinder building blocks. In particular, the previously never achieved lyotropic cholesteric microstructure from SWNT dispersions and the potential enhanced biocompatibility of dsDNA/SWNT suggest that the range of applications that can be processed from liquid crystalline nanotube dispersions may be even broader than previously thought.

# Acknowledgments

Pursuing my PhD degree in Auburn University has been one of the most rewarding and unforgettable journey of my life. However, I would not be able to accomplish this research without the contributions of numerous people.

I am grateful to my advisor and dissertation committee: Virginia A. Davis for the vision and guidance which make this research possible and for her support and encouragement; Mark E. Byrne and Yoon Y. Lee for their classroom instruction and interest in my research; Aleksandr Simonian for generously agreeing to let me use lab instruments related to this research.

I thank other researchers at Auburn University, especially: Vinod K. Radhakrishnan for training me on instruments at the beginning of this research; Matthew J. Kayatin for helping to solve experimental problems and useful discussions during the entire period of this project; Daniel W. Horn for fiber spinning experiments and his insights in developing the fiber spinning process; Esteban E. Ureña-Benavides for useful discussions on rheology of liquid crystal SWNT dispersions; and Michelle Aono for characterizing the double-stranded nature of DNA used in this research. I also thank Philippe Poulin's Group at CNRS-CRPP France for helping me understand fiber spinning techniques of SWNT dispersions.

Last but not least, I thank my family and friends, especially my parents and my best friend Boelos Khereid for their constant support and encouragement. They make me believe that life is wonderful and full of happiness.

# Table of Contents

## List of Figures

# List of Tables

# Chapter 1

## Introduction

Large area assemblies of single-walled carbon nanotubes (SWNT) have numerous potential applications including strong antimicrobial coatings,[1-3] artificial muscles,[4] chemical sensors[5,6] electrical wires,[7,8] hydrogen storage[9] and high strength fibers.[10-14] However, translating the remarkable mechanical, thermal, and electrical properties of individual SWNT into macroscopic objects is hindered by the strong van der Waals attraction between SWNT and the random entanglements resulting from many synthesis schemes. Lyotropic liquid crystalline SWNT dispersions are recognized as a key potential precursor for the fluid phase processing of carbon nanotubes into aligned materials with outstanding properties.[10] Several research groups have achieved lyotropic carbon nanotube liquid crystalline phases; however, they have all been polydomain nematics.[15-20] With the exception of SWNT in cholorosulfonic acid,[20] the nematic phase has always had numerous defects compared to traditional rod-like polymer liquid crystals. While shear and other forces applied during processing can be used to anneal defects between domains, it has been shown that dispersions with larger domain size and fewer defects result in fewer defects in the assembled solid material.[20] The lack of a smooth liquid crystal microstructure in most systems has been deemed a key impediment to producing macroscale materials with outstanding properties.[21] Furthermore, while nematic liquid crystalline phases are useful for producing aligned films and fibers, the inability to produce cholesteric SWNT dispersions has limited the range of potential applications. An inherent property of the cholesteric microstructure is the selective reflection of visible light; there is growing interest in using films produced from cholesteric phases in security papers and passive optical devices such as circular polarizers, notch filters, and reflective displays.[22,23] The majority of cholesteric film research to date has focused on cellulose nanowhiskers; until now it has not been possible to achieve this microstructure with SWNT.

In parallel to the ongoing advancements in bottom-up assembly of liquid crystalline nanocylinder (*e.g.* nanotubes, nanowires, nanowhiskers) dispersions,[24] there has been growing interest in dispersing carbon nanotubes in solutions of biological molecules such as DNA and enzymes. These materials are some of the best known dispersants for carbon nanotubes due to their amphiphobic nature and potential for π–π interactions;[1,25,26] they also offer the advantages of green chemistry, potential biocompatibility and multi-functionality. Pioneering work by Philippe Poulin's group at Centre de Recherché Paul Pascal - Centre National de la Recherché Scientifique (CRPP-CNRS) in Bordeaux, France demonstrated that evaporation of low concentration dispersions of SWNT in single-stranded DNA (ssDNA)[16] and biological hyaluronic acid (HLA)[17] resulted in liquid crystalline phase formation. In addition, Hobbie et al have shown that SWNT dispersed in bile salts can be assembled into fibrils as a result of the mesogenic nature of the solvent and geometrical confinement.[27] It is noteworthy that, in addition to enabling carbon nanotube dispersion, many biological molecules are themselves mesogenic. For example, tobacco mosaic virus (TMV) was the material used in Onsager's original work on liquid crystalline phase formation.[28] More recently, the rod-like bacteriophage *f*d virus has been studied as a model system; this research includes fascinating work examining the phase behavior of dispersions containing both rods and spheres.[29,30] In addition, the long and stiff helical structure of DNA molecules enables formation of multiple liquid crystalline phases;[31,32] the critical concentration for cholesteric formation depends on factors such as the number of DNA base pairs and the ionic strength.[31-34] Cholesteric liquid crystalline phases of DNA are even evidenced to form *in vivo*.[35-37]

Characterizing the phase behavior of lyotropic liquid crystalline dispersions of SWNT using rheology is in its infancy; most of the systems studied to date having been binary systems of carbon nanotubes in Newtonian solvents. The rheology of characterizing the liquid crystal SWNT dispersions is promising for understanding the flow microstructure and subsequent properties of macroscopic assemblies of nanomaterials. The well studied rheology of liquid crystalline polymers (LCPs) can be used as a guide for better understanding the complex and new field of rheology study on liquid crystal nanocylinders. With that being said, there is still a dilemma. Although the rheology of model LCPs such as hydroxypropylcellulose (HPC),[38-40] poly ($\gamma$ benzyl-L-glutamate) (PBLG)[41,42] or poly ($\gamma$ benzyl glutamate) (PBG)[43,44] solutions have been widely studied, there are still struggling efforts to understand this field due to the lack of their universal rheological properties. In the case of SWNT, the flow behavior of the resulting liquid crystals became even more complicated due to the additional inherent 20 - 40 $k_BT/nm$,[45,46] van der Waals attraction between SWNT. In addition, the complex interplay between intermolecular interactions, molecular conformation, shear flow, and molecular orientation state all affect the rheological properties of LCPs solutions.[40,43] The characteristic rheological properties of nematic LCPs that differ from ordinary polymers and low molecular weight liquid crystals (LMWLCs) have led to the development of new molecular theories such as those of Doi, Marrucci and Larson.[47-49] However, the direct modeling of nematics with highly textured structures is so complicated that those theories adopted a simple geometry for calculation such as monodisperse rigid rods under an anisotropic excluded volume potential. However, potential polydispersity and flexibility, textural defects, and various molecular interactions existing in the real LCPs systems lead to discrepancies between experimental results and theories.

This work compares the rheology and phase behavior of dsDNA/SWNT dispersions produced by two different methods. The phase behavior and dispersion microstructure were affected by the dsDNA:SWNT ratio and the state of small bundles of SWNT existing in the dispersions. If there was not sufficient dsDNA to stabilize the dispersion, large aggregates formed at relatively low concentration. With sufficient dsDNA, evaporation of bulk dispersions, comprised of both bundled and individual SWNT, resulted in nematic phase formation. Evaporation of dsDNA/SWNT supernatants resulted in cholesteric phase formation. To the author's knowledge, this is the first lyotropic cholesteric SWNT liquid crystal formed without integrating the SWNT into an existing liquid crystal matrix. Understanding the difference in phase behavior of nematic and cholesteric dsDNA/SWNT dispersions with concentration, textural effects and shear flow is important for improving the properties of their macroscopic assemblies. The origin of the cholesteric structure can be directly attributed to the majority of the dsDNA retaining its helical structure during dispersion preparation. This structure can be retained or eliminated during processing into aligned films. The potential enhanced biocompatibility of dsDNA/SWNT and the previously never achieved cholesteric microstructure suggest that the range of applications that can be processed from liquid crystalline nanotube dispersions may be even broader than previously thought.

In addition, macroscopic assembly of fibers by solution spinning from different SWNT dispersions was investigated. For fiber spinning from bulk (non-centrifuged) dsDNA/SWNT dispersions, both wet spinning into 1-butanaol coagulant bath and dry spinning at ambient conditions were conducted. In addition, solution spinning from SWNT dispersion stabilized by the enzyme lysozyme (LSZ) and cationic surfactant (1-tetradecyl) trimethyl-ammonium bromide (TTAB) was performed. Co-flow stream of polyvinyl alcohol (PVA) polymer coagulation bath was used to aide alignment. The goal of using lysozyme as a dispersant was to produce mechanically robust fibers with better electrical and thermal properties as well as possessing antibacterial properties due to the lytic activity of lysozyme against gram positive bacteria. These fibers are potentially useful for first responders and military clothing. In general, fibers produced from LSZ/TTAB/SWNT dispersions coagulated in PVA solution, showed better overall mechanical and electrical properties when compared to fibers obtained from dsDNA/SWNT dispersions either by wet or dry spinning.

This dissertation summarizes research on the phase behavior and rheology of lyotropic dsDNA/SWNT and cellulose nanocrystals (CNC) aqueous dispersions and macroscopic assembly of film and fibers of SWNT in both dsDNA and lysozyme. Chapter 2 provides background information on materials used including SWNT and dsDNA, molecular interaction between dsDNA/SWNT, liquid crystals, phase behavior and rheology of rods dispersed in liquids, film coatings and fiber spinning. Chapter 3 provides information on instrumentation and experimental techniques. The results and discussions are divided into three chapters; Chapter 4 provides information on phase behavior and rheology of aqueous dsDNA/SWNT dispersions, Chapter 5 describes film coatings from cholesteric dsDNA/SWNT liquid crystals, and fiber spinning of dsDNA/SWNT and LSZ/TTAB/SWNT dispersions, and Chapter 6 provides information on phase behavior and rheology of lyotropic sulfonated CNC suspensions. Finally, Chapter 7 summarizes the conclusions of this research and provides possible directions for future work in the field of SWNT liquid crystals.

## Chapter 2

## Background

The discovery of Buckminsterfullerene in 1985 by Sir Harry Kroto, Richard Smalley and Bob Curl, and coworkers at Rice University, which led to their being awarded the Nobel Prize in chemistry in 1996, has been the direct stimulus for the systematic study of carbon filaments of very small diameters in nano-scale size including carbon nanotubes (CNTs).[50] The observation of multi-walled carbon nanotubes (MWNTs) by Iijima in 1991 and the subsequent identification of SWNT along with Bethune et al. two years later in 1993 launched the current explosion of interest in CNTs.[51-53] Furthermore, Smalley and coworkers at Rice University successfully obtaining synthetic, high quality, bundles of aligned SWNT by laser vaporization of a graphite target in 1996 was a major breakthrough in the field which enabled providing large amount of high quality raw materials for scientific research.[54] The subsequent studies on achieving synthetic nanotubes with higher yield and narrow diameter and chirality distributions have been actively conducted by different methods such as electric arc,[55] chemical vapor deposition (CVD),[56] and high-pressure carbon monoxide (HiPco).[57] Synthesized nanotubes have finite lengths, and also contain impurities such as metal catalyst particles, amorphous carbons, and fullerenes. These impurities often impede their uniform assembly into macroscopic objects. Thus, purification after synthesis is often required, but this can lead to more defects in the nanotubes and the formation of highly packed bundles. Therefore, improved yields and properties of synthetic CNTs are a key need for their further application in new generation of materials.

However, the major obstacle for the current studies is turned out to be difficulty in obtaining dispersions of CNTs as individuals or small bundles into solvents or polymers. Ironically, this obstacle is due to the $sp^2$ hybridized molecular perfection of the material which makes it less compatible with other materials; this is especially true for SWNT. Thus, in the past few years, chemical functionalization of CNTs, by both covalent interaction and non-covalent interaction, has become a main focus of this field. The goal is to improve the solubility of nanotubes and as a result translate their unique properties, to the largest extent into macroscopic applications. In particular, chemical modification of CNTs with biological molecules has started to attract significant attention ever since the early work done by Malcolm Green, Edman Tsang and coworkers in the mid-1990s on interacting biomolecules including enzymes and DNA oligomers with CNTs.[58,59] This chapter provides general background information relevant to this dissertation including carbon nanotubes and their stabilization with biomolecules (especially DNA), phase behavior and rheology of isotropic rod dispersions and their liquid crytal phases, and macroscopic assembly into films and fibers.

## 2.1. Carbon Nanotubes

Carbon nanotubes (CNTs) are allotropes of carbon with the structure of seamless cylinders derived from rolling up graphene sheets of honeycomb lattice representing a single atomic layer of crystalline graphite. As synthesized CNTs have hemispherical fullerene like caps,[60] but these are typically removed during purification due to the lower strain in the C-C bond. The bonding in CNTs is primarily $sp^2$ hybridized carbon atoms covalently bonded to each other, although there may be some $sp^3$-bonded atoms at defect sites and in the regions of high curvature.[61] CNTs can be classified as single-walled carbon nanotubes (SWNT), double-walled carbon nanotubes (DWNT) or multi-walled carbon nanotubes (MWNT) according to their structure. Typically SWNT are single-shell cylinders with typical diameters of ~1 nm and lengths that typically range from 0.1 to 10 μm, while DWNT and MWNT are nested arrangement of SWNT in two or several coaxial cylinders. The typical diameter of MWNTs is ~30 nm and they usually have longer lengths than SWNT with a range of 0.5 to 50 μm. The commercial availability of DWNT is not as abundant as SWNT and MWNT. The typical diameter of DWNT is ~4 nm with lengths smaller than 20 μm. The simplest way of specifying the structure of an individual tube is in terms of its 1D unit cell, defined by the vectors $\mathbf{C}_h$ and **T,** where **T** is the translational vector of 1D unit cell and normal to $\mathbf{C}_h$ (Figure 2.1). The length of the chiral vector $\mathbf{C}_h = n\mathbf{a}_1 + m\mathbf{a}_2$ is used to define the circumference of any carbon nanotube, where $\mathbf{a}_1$ and $\mathbf{a}_2$ are the unit cell base vectors of the graphene sheet.[62]

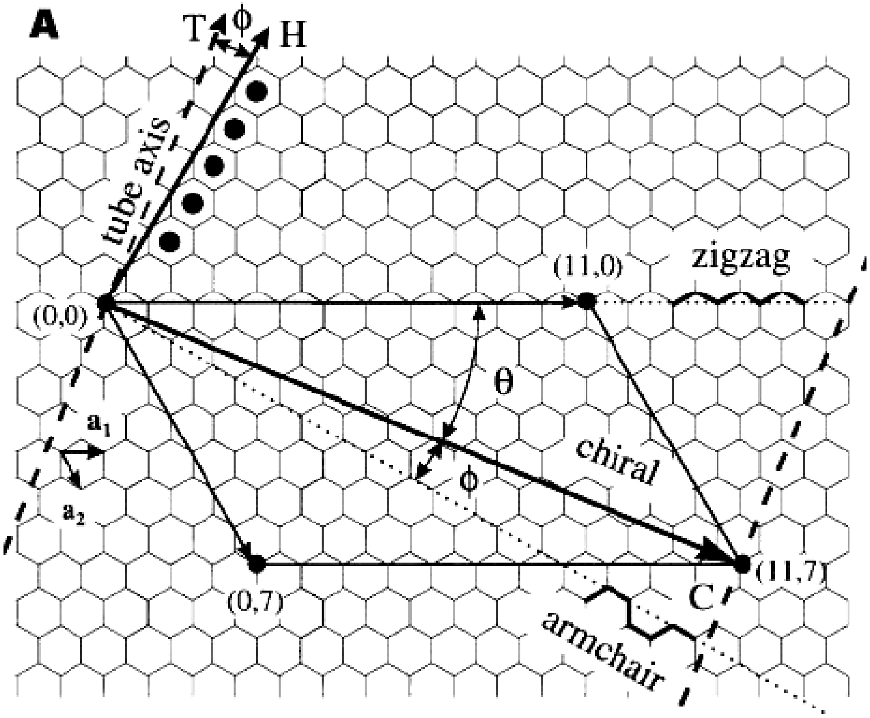

Figure 2.1. Construction of carbon nanotube from single graphene sheet.[63]

Each pair of integers ($n$, $m$) with $0 \leq |m| \leq n$ represents a possible nanotube structure. It can be seen from Figure 2.1 that, $m = 0$ denotes zigzag nanotubes, and the $n = m$ denotes armchair nanotubes. All other vectors ($n$, $m$) correspond to chiral nanotubes. The chiral angle $\phi$ between the tube axis T and H, which indicates the direction of the closest hexagon rows to the tube axis, can also be used to describe three distinct types of nanotube structures. The zigzag and armchair nanotubes have chiral angles of $30^o$ and $0^o$, respectively, while chiral nanotubes corresponds to chiral angles of $0^o < \phi < 30^o$. Figure 2.2 provides a description of the structure of SWNT with different chiralities.

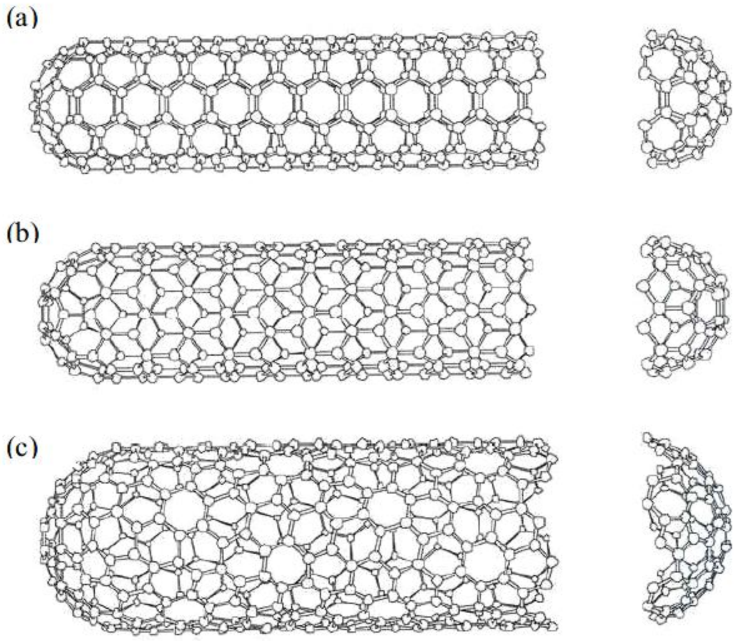

Figure 2.2. Schematic theoretical model for a SWNT with the tube axis normal to: (a) the $\theta = 30^o$ direction with *(n,m)* = (5,5) (an "armchair" tube), (b) the $\theta = 0^o$ direction with *(n,m)* = (9,0) (a "zigzag" tube), and (c) a general direction $0^o < \theta < 30^o$ with *(n,m)* = (10,5) (a "chiral" tube). Reproduced from Dresselhaus et al.[64]

The angle at which a graphene sheet is rolled up determines not only the chirality, but also determines whether the nanotubes behave as a metal or semiconductor. Armchair nanotubes ($n = m$) are ballistic conductors, while other chiralities are considered to be metallic if ($m - n$) is a multiple of 3, which corresponds to a very small bandgap.[65] Other nanotubes are semiconducting when ($m - n$) is not a multiple of 3. The nanotube diameter $d_t$ is given by

$$d_t = \frac{|C_h|}{\pi} = \frac{\sqrt{3} \cdot a_{c-c} \cdot \sqrt{n^2 + m^2 + nm}}{\pi} \tag{2.1}$$

Where $|\mathbf{C}_\mathrm{h}|$ is the circumference length, and $a_{c\text{-}c}$ = 1.42 Å is the carbon-carbon (C-C) bond length. Furthermore, the molecular weight of SWNT with a given length $L_t$, and diameter $d_t$, can be calculated from the definition of the 1D unit cell. The length of **T** is given as:

$$|\mathbf{T}| = \sqrt{3}\mathrm{L}/\mathrm{d_R} \tag{2.2}$$

where L is the circumference of nanotube, $\mathrm{L} = |\mathbf{C}_\mathrm{h}|$, and $d_R$ is the highest common divisor of (2n+m, 2m+n). In addition, the number of carbon atoms per 1D unit cell is:

$$\mathrm{n_c} = 4(\mathrm{n}^2 + \mathrm{m}^2 + \mathrm{nm})/\mathrm{d_R} \tag{2.3}$$

For an individual tube of length $L_t$, the total number of carbon atoms N and further the molecular weight MW of the tube can be derived from the following equations:

$$\mathrm{N} = \mathrm{L_t n_c}/|\mathbf{T}| \tag{2.4}$$

$$\mathrm{MW} = \frac{48\,\pi\,\mathrm{L_t}\,\mathrm{d_t}}{3\,\sqrt{3}\,\mathrm{a}_{\mathrm{c-c}}^2} \tag{2.5}$$

As a result, the molecular weight of a typical SWNT with 1nm in diameter and 1 μm in length is $1.40 \times 10^6$ g/mol.

As mentioned above, one of the surprising characteristics of CNTs is their electronic conductivity which can be either metallic, like copper, or semiconducting, like silicon. The ballistic conductance of armchair nanotubes can be as high as 1 μΩ·cm at 25 °C.[65] It is well established that, the experimental thermal conductivity κ of SWNT is more than 3000 W/ m Ꝁ which is equal or higher than that of diamond with κ value of 3320 W/ m Ꝁ.[66-68] In addition, the thermal conductivity of as high as 6600 W/ m Ꝁ at room temperature was obtained for a (10,10)

SWNT by molecular dynamics simulation.[69] Since the carbon-carbon bond in the graphene wall of nanotubes is one of the strongest in nature, CNTs are considered to be the stiffest and strongest materials ever occurring in nature or being synthetically produced. The tensile modulus of SWNT can be over 600 GPa, while tensile strength can be over 37 GPa, approximately 60 times the strength of steel, while six times lighter than steel.[65,70,71] These remarkable properties of nanotubes together with their low density ~1.4 g/cm$^3$ provide these relatively new types of nanomaterials a huge potential in a wide range of applications.

## 2.2. Deoxyribonucleic Acid

The genetic molecule deoxyribonucleic acid (DNA), nature's most important building block, was first described by James Watson and Francis Crick in 1953 and formed double helical structure. Their double helical model was based on X-ray diffraction data of DNA fibers which were provided by two different groups, one was Maurice Wilkins and colleagues and the other was Rosalind Franklin and Raymond Gosling. A representation of the model of Watson-Crick double helix is shown in Figure 2.3a. Understanding the double helical structure of DNA has been the great achievement in realizing the importance and significance of DNA as the genetic material. The repeating units of DNA are called nucleotides which are composed of nitrogen containing aromatic bases, which are purine or pyrimidine rings, five-carbon ribose sugars, and a backbone of phosphate groups. The molecular weight of double-stranded DNA (dsDNA) can be approximated as MW (dsDNA) = (number of nucleotides $\times$ 607.4) + 157.9. Thus, the molecular weight of a dsDNA molecule with 750 base pairs is about $9.11\times10^5$ g/mol which is the approximate dsDNA length used in this work after sample preparation. The initial length of the native dsDNA used is more than 10,000 base pairs. The phosphate group of a nucleotide is formed from a central phosphorous atom covalently bonded to 4 oxygen atoms. The electronegative oxygen atoms of phosphate groups are responsible for stabilizing DNA through ionic interactions with cations in the cell. The sugar-phosphate backbones helically rotate around the outer surface of DNA moving in opposite directions and form two different sized grooves of major and minor grooves. The major groove is approximately 50% wider than the minor. DNA helical structure is mainly stabilized by the base stacking of A-T (Adenine-Thymine) and G-C (Guanine-Cytosine) base pairs that promotes hydrophobic interactions between the non-polar portions of the bases (Figure 2.3c). The hydrogen bonding between complementary bases is another force contributor for holding the DNA double helix together with two hydrogen bonds between A-T base pairs and three hydrogen bonds between G-C base pairs (Figure 2.3b). Typically, the hydrogen bonds in DNA are 2-3 kcal/mol which is weaker than most hydrogen bonds (3-7 kcal/mol) due to geometric constraints within the double helix.[72]

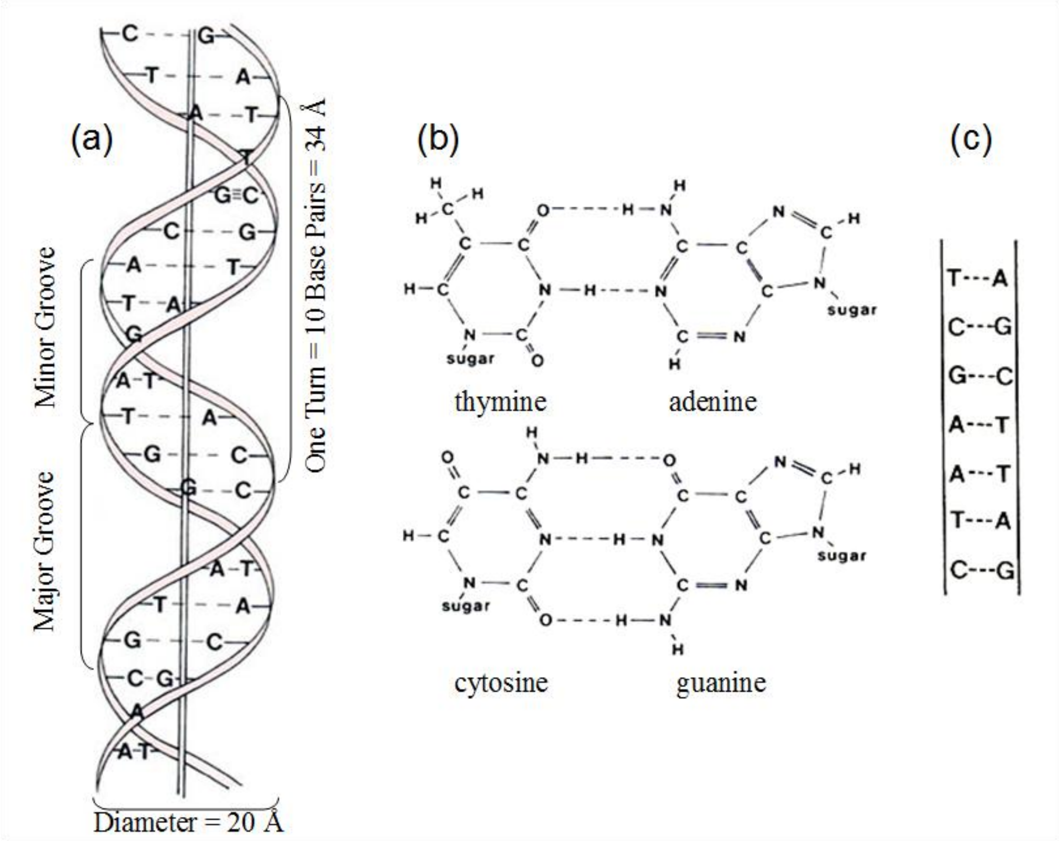

Figure 2.3. Watson-Crick DNA double helix and base pairs.[73]

DNA molecules can adopt different conformations depending on the environmental factors such as salt concentration and presence of alcohol. The main types of conformations are B-DNA, A-DNA, and Z-DNA. B-DNA is believed to the native conformation occurring in vivo. It has right-handed double helical structure of 10 base pairs per turn with well defined major and minor grooves and is found at low salt concentration. In fact, the DNA double helix structure discovered by Watson and Crick is known as the B form. The typical diameter of DNA helix is 20 Å with small deviations according to the conformational changes. A-DNA is quite rare and is found in solutions with higher salt concentrations or with alcohol added. A-DNA has righ-handed helix very similar to B-DNA, but it has 11 base pairs per turn and a diameter of 26

Å. As for Z-DNA, it has left-handed helix and occurs for DNA molecules with alternating poly (dG-dC) sequences in solutions with high salt concentrations or alcohol existence. Z-DNA has more compact cylinder-like structure and has 12 base pairs per turn with a diameter of 18 Å. The double-helical structure of DNA is remarkably stable with a relatively high melting temperature $T_m$. It is reported that the $T_m$ of the DNA from salmon testes used in this research is 87.5°C in 0.15M sodium choloride plus 0.015M sodium citrate solution.[74] Melting or denaturation of DNA occurs when the external forces overcome the stabilizing forces of hydrogen bonding and base-stacking. Denaturation is usually accomplished by increasing the solution temperature or alkali treatment due to ionization of the base.[74] Acid treatment is not an option because strong acid will degrade the DNA. However, under mild conditions like slow cooling, the two single strands of denatured DNA can find their complementary stands and base pairs with them to from hydrogen bonded double helix. In this work, DNA has been considered as a biopolymer, a specially sequenced copolymer that has been selected by evolution to have a particular property. One difference between random copolymers and DNA is that the former one can produce an ensemble of all possible arrangements of the repeating units.[75]

### 2.3. Lysozyme

In this research, lysozyme (LSZ) was also used as a dispersing agent for SWNT in producing robust and electrically conductive fibers by solution spinning. These fibers are potentially useful for first responders and military clothing. Lysozyme (LSZ) is a relatively small, globular enzyme catalyzing chemical reactions and can be found in many biological systems such as egg white, human tears, saliva and other secretions. It provides efficient antibacterial activity against gram positive bacteria by breaking down components of the cell wall peptidoglycan of bacteria. Lysozyme is comprised of a single polypeptide chain of 129 amino acid residues with the approximate size of 30 Å in diameter and a molecular weight of approximately 14,000 g/mol (Figure 2.4).[76,77] The polyampholytic nature of lysozyme, which contains multiple hydrophilic domains and more than 35 % of hydrophobic residues,[78] makes it a competitive dispersant for hydrophilic or hydrophobic molecules. In its native state, LSZ contains 42% α-helices and 6% β-sheets of protein secondary structure which are folded within its polypeptide chain.[78] Furthermore, the existence of four disulfide bridges formed between the thiol groups of cysteine residues provides crosslinks which prevent complete loss of tertiary globular structure.[79] Due to the disulfide bridges, LSZ is relatively stable having the isoelectric point of 11 and a relatively high denaturation temperature of 76$^{o}$C.[80] When dispersing SWNT in LSZ solution, partial denaturation of LSZ occurs during sonication and leads to the exposure of the native internal hydrophobic domains to the surface which can further interact with the side-walls of SWNT through hydrophobic interactions. The outside hydrophilic groups of LSZ help stabilizing the LSZ/SWNT hybrids in aqueous dispersion through electrostatic forces.[78]

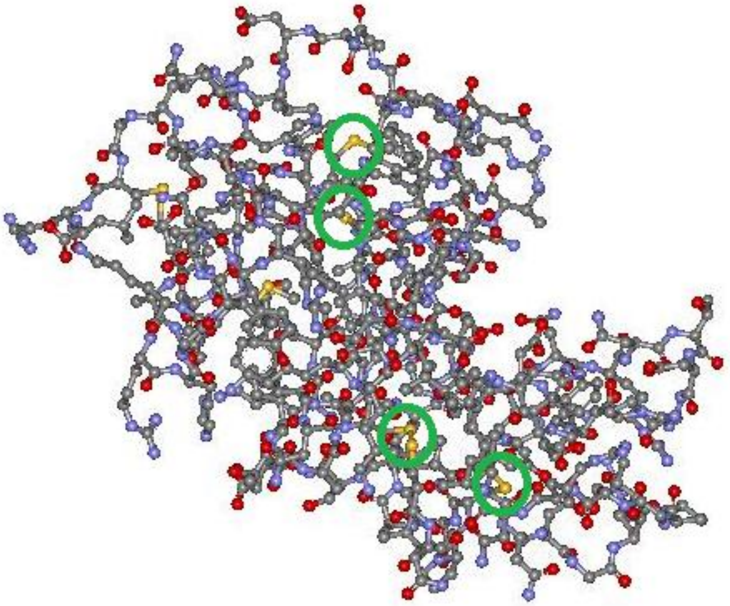

Figure 2.4. Ball-and-stick representation of lysozyme structure highlighting the disulfide bridges at the core. All protein atoms are shown as balls, and bonds between atoms are shown as a stick. Carbon, nitrogen, oxygen and sulfur atoms are colored grey, blue, red and yellow, respectively. Adapted from Szymanska et al.[81]

### 2.4. Cellulose Nanocrystals

The aim of studying the phase behavior of cellulose nanocrystals (CNC) aqueous suspensions in this work is to answer the following question; "how does the simpler cholesterogenic aqueous cellulose nanorod systems compared to the complex ternary system (DNA, SWNT, water)? " Cholesteric phase forming system, CNC in water, may give some insights on the rheology of cholesteric system since it avoids the complication of the DNA phase which is not truly rigid rods. Also, the comparatively simple binary system of CNC suspensions (CNC and water) is expected to provide better understanding in rheological behavior of cholesteric liquid crystals. However, the phase behavior and rheology of cholesteric liquid crystal forming dsDNA/SWNT dispersions are the main focus of this work and will be discussed in detail in the following sections.

Cellulose nanocrystals are considered to be the most abundant naturally occurring nanorods which can be produced from plants (e.g. cotton, ramie, cellulose), trees, bacteria and animals (tunicate) via the condensation polymerization of glucose. They have great potential to be used as fillers in renewable polymer matrices to create mechanically strong and optically smart nanocomposites and are also attractive material, because of their environmentally friendly nature. CNC are commonly isolated from their raw materials by acid hydrolysis process. Most typically, sulfuric acid is used resulting in the sulfonated CNC structure shown in Figure 2.5.

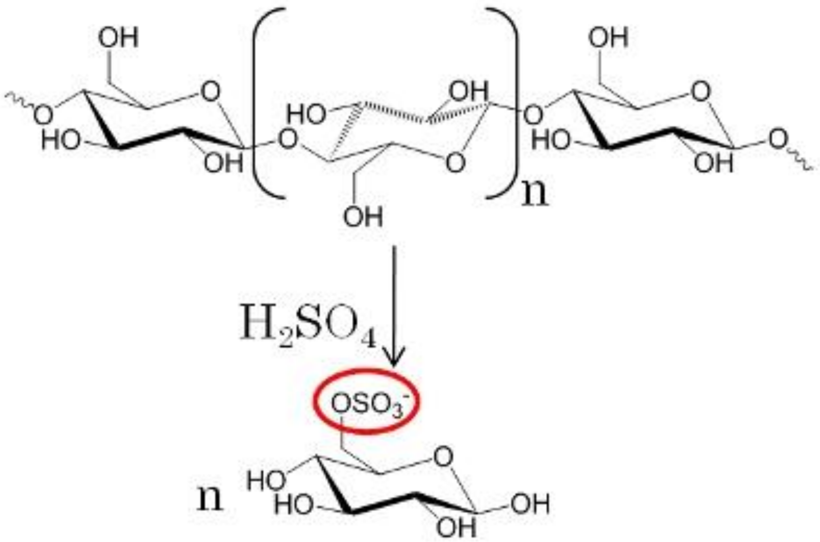

Figure 2.5. Chemical structure of sulfonated cellulose after acid hydrolysis.

The properties of cellulose suspensions depend on both the material origin and the hydrolysis conditions.[82,83] The lateral dimensions of cellulose nanocyrstals range from 3-30 nm[84] have various aspect ratios *L/d* (*L* being the length and *d* the diameter) from almost a particle *L/d* =1 to about 100 can be obtained by acid hydrolysis of different sources based cellulose.[85] It has been observed that aqueous suspensions of sulfonated CNC can go through dilute, biphasic, and single phase liquid crystal regime with increasing concentration of dispersed rods in lyotropic systems. Revol et al.[86] identified the type of liquid crystalline phase formed from sulfonatd aqueous CNC suspensions as chiral nematic (cholesteric). This particular ordered structure gives rise to many of the optical and mechanical properties of their resulting films. The crystal modulus of cellulose was first experimentally determined by Sakurada et al.[87] using X-ray diffraction and gave a value of 138 GPa for cellulose-I. This value lies within the range of theoretical estimates of 100-160 GPa using molecular dynamics/mechanics methods.[82,88] The tensile strength of cellulose crystals should be in the order of 10 GPa.[85] Thus, CNC is considered as a possible alternative material of carbon nanotubes in terms of their relatively high mechanical properties and aspect ratios. However, much more research is needed on this new popular material. The optical properties of CNC films obtained from its liquid crystalline phase can be controlled by tuning its cholesteric pitch. In general, stronger interparticle interactions result in smaller pitch. With increasing suspension concentration across the biphasic regime, the pitch decreases from ~80 to 10 μm.[83] In addition, Pan et al.[23] showed that the cholesteric pitch of cellulose films even fit the equation describing the correlation of concentration and pitch, established for chiral nematic polymer solutions. The effect of concentration on pitch is given in the following equation,[23,89]

$$\ln(1/P) = k\ln(c) + A \tag{2.6}$$

where $P$ is pitch, $c$ is concentration, $A$ is a constant dependant on the solvent, temperature, and the molecular weight of the solute polymer and $k$ is solvent-dependant with typical value less than 2. Moreover, adjusting the ionic strength of suspensions by adding electrolytes could control the pitch and further control the wavelength of reflected light through subsequent films.[83,85,90] Typically, with increasing concentration of electrolytes such as HCL, NaCl, and KCl, the cholesteric pitch both in the cellulose suspensions[83] and films[23] decreases due to reduction in pre-existing Coulombic repulsion between acid hydrolyzed CNC rods.[22] The cholesteric pitch can also be affected by some other factors such as presence of magnetic field and its exposure time, and temperature.[23] As a result, these properties provide promising potential application in security papers and passive optical devices such as circular polarizers, notch filters, and reflective displays.[22,23] Furthermore, the cheap and abundant nature of CNC makes it a promising material for a wide range of future applications such as liquid crystal displays, and even can be used as a template of generating other nanoparticles to obtain products with improved properties.

The ready dispersion of CNC in various solvents, even water, provides the possibility of obtaining liquid crystals and further applications into films with improved optical and mechanical properties. The presence of charge such as introduction of $-SO_3H$ groups on their surface during the hydrolysis step promotes dispersibility in aqueous solvents due to electric repulsion. Hydrogen bonds created by dispersing CNC into aqueous solvents is another factor promoting the dispersibility as well as providing the basis of its mechanical strength.[85,91] However, the effect of pH due to the surface charge, on the phase behavior of CNC aqueous suspensions needs to be considered carefully too.

## 2.5. Biopolymer Stabilization of Carbon Nanotubes

Interest in the biological functionalization of nanotubes has exploded in the last decade ever since the pioneering work of Malcolm Green, Edman Tsang, and coworkers[58,59] who immobilized enzymes and DNA oligomers on the nanotube surfaces in the mid 1990s. In addition, biologically modified MWNT have been used as nanoprobes for high resolution imaging such as tips for AFM.[92] Biomolecules, such as proteins and nucleic acids, can be bound to CNTs either by covalent or by non-covalent functionalization. The exciting part of this new emerging technology is that, it can combine nature's toolbox with the unique properties of nanostructures,[93] introducing molecular recognition and bio-directed self-assembly capabilities together with potential biocompatible characteristics to nanomaterials. It has been reported that SWNT can be readily coated with the protein, streptavidin, and be solubilized in it by sonication.[94,95] Integration of enzymes to nanotubes was also studied broadly to render the nanosystems antimicrobial enzymatic activity as well as strong mechanical properties which are provide by the CNTs.[1] While much of the biological functionalization of CNTs have been aimed at biosensor development, a large number of studies have been also aimed at finding possible therapeutic applications, such as targeted drug delivery, cancer treatment, artificial muscles and "feeling" artificial skin.[4,96-99] Among all the biomolecules used to modify nanotubes, DNA and other nucleic acids are of great potential interest. At the basic level, nucleic acids could provide good solubilization of nanotubes enabling higher quality materials with more uniform properties. Nucleic acid functionalized CNTs might have great potential in biosensor applications due to their remarkable recognition abilities such as the perfect, well studied complementary base pairing mechanism of DNA and binding of proteins with specific mechanisms. Furthermore, DNA-guided macroscopic assembly of CNTs system is possible due to the DNA's ability to form various liquid crystalline phases at different conditions. Also, the prospect of nanotubes serving as strong carriers to deliver therapeutic DNA into cells is perhaps one of the most exciting future applications of biologically functionalized CNTs.[100,101]

Although integration of biopolymers onto CNTs would improve the stability and biocompatibility of the system, the potential toxicity studies of nanotubes, which is still at an early research stage, have aroused concerns about potential safety issues. Several studies reported that direct injection of SWNT into the lungs of mice would cause inflammation of the lung tissue, or even lead to death.[102,103] However, the authors pointed out that mechanical blockage of the large airways by aggregates of nanotubes might be the reason for causing death, rather than the toxicity of nanotubes.[104] In order to provide a correct assessment of nanotubes' toxicity, inhalation toxicity studies rather than direct injection, and better initial material characterization of the nanotubes are needed, because synthetic nanotubes always have catalytic and amorphous carbon impurities. The safety and risk management of engineered carbon-based nanomaterials (CNM) has become increasingly demanding. The number of toxicology studies on carbon nanotubes is growing significantly in each year. Preliminary investigations conducted by several U.S. government research centers showed that engineered CNM including fullerenes and multi-walled carbon nanotubes can become airborne during handling and mixing in solution by sonication in a laboratory process.[105] This indicated that laboratory workers may be at increased risk of exposure to engineered nanomaterials. The UK Health and Safety Executive (HSE) published an safety information sheet on the Risk Management of Carbon Nanotubes in 2009. It provides suggestions on precautionary approaches to the risk management of all CNTs including understanding the health and safety information of the materials before use, using protective equipment during handling, and appropriate disposal of waste carbon nanotube materials. A regularly updated resource for the latest information is the website of Rice University-based International Council on Nanotechnology (ICON). It includes links to the Centers for Disease Control and Prevention's (CDC) Public Health Grand Rounds Event "Preventing Adverse Health Effects from Nanotechnology," a safe handling guide, and excerpts from the latest toxicology and environmental impact studies.

## 2.6. Interaction of DNA with Single-Walled Carbon Nanotubes

The intriguing results of being able to obtain good dispersions of CNTs in aqueous solutions of both natural DNA[106,107] and short, custom-synthezied oligonucleotides[108,109] necessitate the discussion of how the DNA molecules interact with CNTs on a molecular level. However, the molecular-level information on the thermodynamics and structure of DNA/SWNT hybrids is still not fully resolved.[110] In fact, different types of molecular interactions between DNA and CNTs have been proposed based on experiments or molecular simulations, with most of them using SWNT. It is generally agreed that the main driving force of DNA/SWNT interaction is the π-π stacking between the plane of aromatic nucleotide bases and the nanotube side walls which are oriented parallel to each other.[97,107-109,111,112] When SWNT are stabilized by single-stranded DNA (ssDNA) in an aqueous environment, the strong adsorption of DNA onto SNWTs will lead to the wrapping mechanism of ssDNA around SWNT.[109,112] The ionized phosphate backbone of the DNA renders hydrophilicity to the ssDNA/SWNT hybrids and prevents coated SWNT from aggregating by electrostatic repulsion. However, if there are complementary ssDNA molecules exist in the dispersion, SWNT precipitation could occur due to the formation of hydrogen bonds in the corresponding double-stranded DNA (dsDNA) product.[111] Similarly, competing molecules with extended aromatic rings may also cause SWNT precipitation through the formation of attractive π-π stacking with SWNT walls by displacing the initial ssDNA coating from the SWNT.[111] Depending on the application, this SWNT precipitation will be useful for either purification of sorted nanotubes,[113,114] or releasing the gene for drug delivery.[99,115] Besides stabilizing SWNT in aqueous environment, ssDNA with specific sequences can selectively recognize different chiralities of SWNT structure which provides the possibility of purifying synthetic mixtures of SWNT to yield single-chirality species with the same electronic type.[109] In addition to π-stacking, the physical interactions between DNA molecules and SWNT also involve van der Waals attractive forces, hydrophobic interaction forces, and electrostatic attraction between the DNA backbone and the charged SWNT.[116,117] Molecular dynamics simulations of short ssDNA segment with eight adenine bases even shows the spontaneous insertion of ssDNA into SWNT with appropriate diameter. The encapsulation of oligonucleotide into SWNT is due to the combined action of van der Waals attraction and hydrophobic interaction of exposed ssDNA bases to the interior of the SWNT wall.[116] The tube-size is also one of the influencing factors of the insertion process of the oligonucleotide where the critical diameter of the SWNT is suggested to be 1.08 nm. The encapsulation of ssDNA into SWNT from solution is further observed by experimentally using a modified electrophoresis method.[118]

Compared to the interaction of ssDNA with SWNT, there are fewer studies on the molecular interaction between dsDNA and SWNT. However, conflicting results make it hard to model real systems which involve many experimental variables. One type of interaction mechanism proposed for dsDNA/SWNT system is that, an array of SWNT with appropriate diameter can actually fit into the major grooves of the long helical dsDNA molecule by calculating the electronic structure of dsDNA/SWNT system in vacuum.[119] Another molecular simulation study used short dsDNA segment of 12 base pairs and SWNT with similar lengths as of dsDNA. It shows that the dsDNA molecule absorbed onto the SWNT wall by either hydrophobic or electrostatic interaction depending on whether the SWNT wall was charged or not.[117] More specifically, for a B-DNA structure and uncharged SWNT system, only one end of the dsDNA segment binds to the SWNT surface through the hydrophobic driving force caused by the hydrophobic nature of the exposed dsDNA end base pair planes and the SWNT wall surface. However, in the case of A-DNA, both ends of the dsDNA molecule are able to adsorb onto the SWNT wall without inducing high bending energy. As for the positively charged SWNT, both forms of dsDNA (A-DNA and B-DNA) molecules interact with SWNT in the same way; the negatively charged dsDNA backbone binds to the nanotube wall due to the strong Coulombic interactions. In addition, the charged SWNT may promote the transition of DNA from the A to B form upon interaction with the DNA backbone. Different interaction mechanisms of long natural dsDNA (~10000 base pairs before sample preparation) with random sequences and SWNT has also been investigated. The initial dsDNA/SWNT dispersions involved both small bundles and individual SWNT.[107] It was suggested that spontaneous unzipping of dsDNA on the SWNT surface would occur followed by an ordered helical wrapping of the SWNT surface during a long time period of around 35 days. This slow wrapping mechanism is considered to be affected by several factors like the length of the DNA sequence and the diameter of nanotubes. The authors believe that natural DNA bound on the SWNT surface turns into ssDNA and wraps around a nanotube via base-nanotube stacking interactions.[113]

## 2.7. Phase Behavior of Biopolymer-Stabilized Carbon Nanotube Dispersions

Liquid crystalline (LC) phase behavior of CNTs dispersed in biological solutions has been studied in recent years. Liquid crystallinity is an alternative way to help align nanotubes by transferring the ordered, self-organizing characteristic of the LC media into the system. Fundamentally, a molecule is said to be mesogenic if it is able to form LC phases,[120] and a liquid crystal is a mesophase that has the fluidity of a liquid and the order of a crystal. There are two types of liquid crystals: lyotropes and thermotropes. The phase transitions of lyotropic liquid crystals are driven primarily by changes in concentrations. While for the other system, thermotropic liquid crystals, the LC transitions occur with temperature changes only. A large amount of biological materials, such as proteins, carbohydrates, lipids and nucleic acids, have been found to form various LC phases *in vivo* as well as *in vitro* under well-defined conditions.[121] The general idea is that well dispersed CNTs in small bundles or even in individuals can be obtained by using good dispersing agents of biopolymers at relatively low concentrations. Further, single LC phases of CNTs dispersions in biopolymers could be successfully obtained by increasing concentrations of both nanotubes and biomolecules by solvent evaporation[16] or spontaneous phase separation.[17,122] According to Onsager (1949), Flory (1956), and Doi–Edwards (1986) theories, before forming single phase liquid crystals, the phase behavior of fluid dispersed rods goes through different regimes with increasing concentration: dilute, semidilute, isotropic concentrated, and biphasic. In general, the Brownian motion of rotation and translation of rods is inhibited as the concentration increases. Rotation is inhibited in the semidilute regime and both rotation and translation are inhibited in the isotropic concentrated regime.[47] At a critical concentration of $\phi_I$ the system enters the biphasic regime: phases of randomly dispersed rods and oriented rods coexist. The fraction of the liquid crystalline phase increases with concentration until the system turns into single LC phase at the critical concentration of $\phi_{LC}$. The graphical description of these phase transitions are illustrated in Figure 2.6. The critical concentrations at which the ordered phase first appears and at which the fully LC single phase are achieved depend on both the solvent quality and aspect ratio distribution of rods. The solvent quality is a measure of the energetic interactions between rods and solvent.[123]

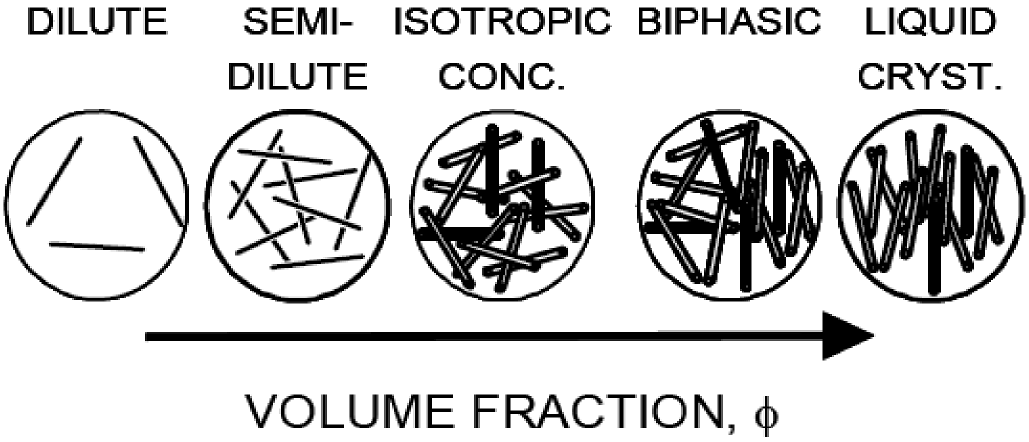

Figure 2.6. Concentration regimes for rod-like molecules. Adapted from Davis et al 2004,[19] and Doi and Edwards 1986.[47]

The formation of liquid crystals can be evidenced by several methods including imaging technology to directly observe the aligned morphology and examining the bulk properties by rheological study. Davis et al[20] reported the only complete experimental phase diagram of SWNT in superacids. In general, there are few phase diagrams for nanocylinder liquid crystals. The center panel of Figure 2.7 shows the first phase diagram of SWNT dispersion in superacids, presenting the effects of both solvent quality and concentration.[20] The solvent quality is measured by SWNT protonation. Traversing the phase diagram from left to right (low concentration to high concentration of rods, constant solvent quality) results in a transition from an isotropic (I) phase to a biphasic system in which the isotropic phase is in equilibrium with a liquid crystalline (LC) phase, and then to a single LC phase.

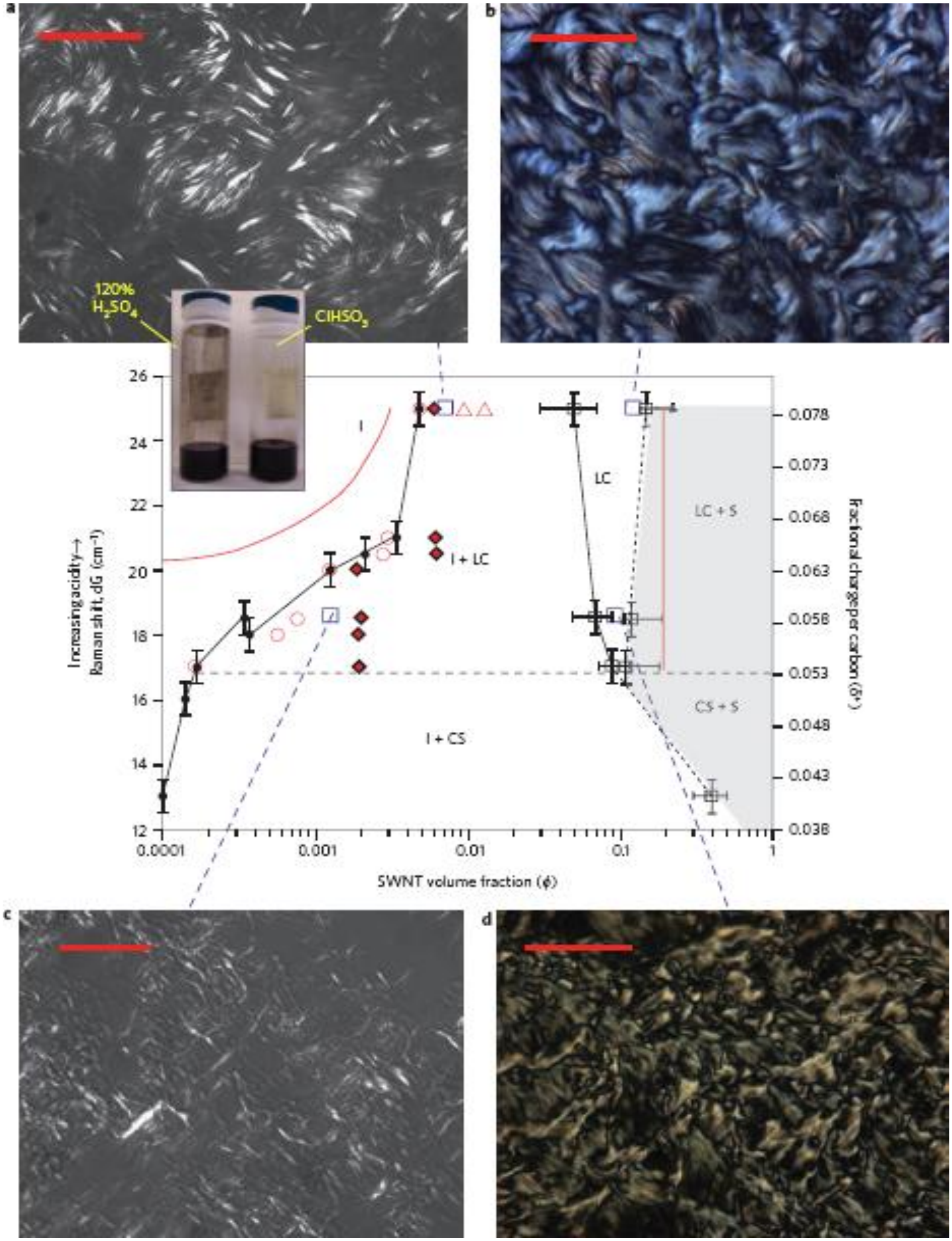
a
b
c
d
120% $H_2SO_4$
ClHSO$_3$
I
LC
I + LC
LC + S
I + CS
CS + S
Increasing acidity →
Raman shift, dG (cm$^{-1}$)
fractional charge per carbon (δ+)
SWNT volume fraction (ϕ)
26
24
22
20
18
16
14
12
0.0001
0.001
0.01
0.1
1
0.078
0.073
0.068
0.063
0.058
0.053
0.048
0.043
0.038

Figure 2.7. Phase diagram of single-walled carbon nanotubes (SWNT) in superacids and cross-polarized light micrographs showing the effect of solvent quality and SWNT concentration on microstructure. Phases include isotropic (I), liquid-crystalline (LC), crystal solvate (CS) and solid (S). Solvent quality is quantified by fractional charge per carbon, measured by the shift dG of the Raman G peak of SWNT (514 nm laser). Black symbols denote experimental results and red symbols refer to model predictions.[20] Circles designate the isotropic concentration $\phi_i$ from experiment (filled circles) and model (open circles). Black and red diamonds indicate the initial system concentration before phase separation. Open red triangles indicate $\phi_i$ and $\phi_n$ in a system of monodisperse hard-rods (Onsager). Red lines are the model predictions of the isotropic and liquid-crystalline stability limits, that is, cloud curves. Black dotted lines connect the experimental data points to denote experimental phase boundaries such as the LC/LC+S vertical boundary, the LC+S/CS+S horizontal boundary, and the I+LC/I+CS diagonal boundary. An LC+CS regime may also exist within the shaded region, as suggested by Papkov[124]. **a–d**, Light microscopy shows morphology just inside the biphasic region at 1.21 vol % in $ClSO_3H$ **(a)**, 0.132 vol % in 120% $H_2SO_4$ **(c)**, and in the liquid-crystalline phase at 12.1 vol % in $ClSO_3H$ **(b)** and 10.6 vol % in 120% $H_2SO_4$ **(d)**. Liquid-crystalline domains are larger, defect density is lower, and domain orientation changes more gradually in $ClSO_3H$ **(b)** than in 120% $H_2SO_4$ **(d)**. Scale bars: 50 μm **(a)** and 20 μm **(b–d)**.

### 2.7.1. Onsager versus Flory Lattice Theory

Onsager (1949) and Flory (1956) theories are considered to be historically important for expressing the phase transitions of molecules from an isotropic to a nematic liquid crystalline state. Both theories are built upon the basic idea of excluded volume interactions between hard rod-like molecules in a given volume. Rod-like molecules cannot interpenetrate and the excluded volume of adjacent rods would exclude the center of mass of any other rod from this particular region as shown in Figure 2.8. The excluded volume of two spherocylinders with particular orientations can be calculated from the following equation:

$$V_{excl} = -2L^2 d|\sin(\gamma)| - 2\pi d^2 L - {}^4\!/_3\,\pi d^3 \tag{2.7}$$

where L is the length, d is the diameter, and the $\gamma$ is the relative angle between two spherocylinders. For rods with high aspect ratios, the above equation is approximated as $V_{excl} \approx -2L^2 d|\sin(\gamma)|$. Therefore, the excluded volume of two rods is proportional to the angle between their molecular long axes with a minimum value for parallel rods and the largest value for perpendicularly orientated rods. As a result, the formation of liquid crystalline phase with reduced free volume is caused by the domination of increasing translational entropy over lowering orientational entropy due to parallel alignments of rods.[48,120]

For nematic liquid crystals, the parameter describing the degree of molecular orientation is given by the following equation. The orientational order parameter *S* equals to:

$$S = {}^3\!/_2\,\langle \cos^2\theta \rangle - {}^1\!/_2 \tag{2.8}$$

where θ is the angle between a rod and the nematic local director n, and the brackets “⟨ ⟩”, denote an average over all rods. For a completely isotropic orientation of molecules $S = 0$, while for a perfect parallel orientation of rod-like molecules *S= 1*. The orientational order parameter for liquid crystals will be always smaller than the value of unity.

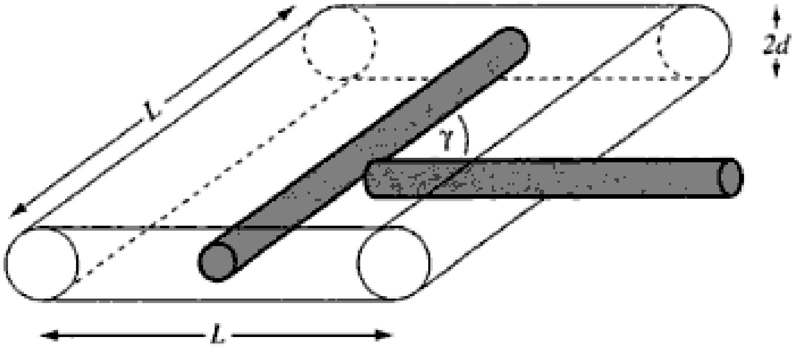

Figure 2.8. A diagrammatic representation of the excluded volume of two rod-like molecules, of length L and diameter d. γ is the angle between the molecular long axes. Adapted from Donald et al. 2006.[120]

**Onsager Theory.** Onsager was the first to propose a theory in 1949 using tobacco mosaic virus (TMV) to describe the rod orientation distribution during the phase transition from isotropic to nematic liquid crystalline phase. Onsager's approach has considered an ideal solution of monodisperse, long, hard rods interacting only by excluded volume forces in an athermal solvent and truncated the interaction free energy of rigid rods at the second viral coefficient. As a result, the phase boundaries of biphasic chimney obtained from Onsager theory are:

$$\phi_I = 3.34\left({}^{d}/_{L}\right) \tag{2.9}$$

$$\phi_N = 4.49\left({}^{d}/_{L}\right) \tag{2.10}$$

The order parameter at nematic phase boundary is S = 0.848. Onsager theory is most accurate for an ideal solution of rods with aspect ratio higher than 100,[125] and at dilute concentrations where only pairwise excluded volume interactions are significant.[48] However, in real systems, the biphasic region widens due to many factors including the polydispersity, the flexibility of rod-like molecules, and the existence of other types of attractive forces such as depletion interaction, sedimentation forces, and the balance of short-range electrostatic repulsion and long-range van der Waals attraction which is especially important for nanorods.[120,126] Later adaptations to Onsager theory including attractive interactions[127] and polydispersity[126] enable it to be used for a broader range of real systems. Although Onsager theory has been less popular for rod-like polymers, it is gaining increasing application for nanocylinder systems, in addition to rigid rod-like viruses such as TMV, M13, and bacteriophage *fd* viruses.

**Flory Theory.** In 1956, Flory's lattice-based theory was proposed for predicting the nematic phase transition. Flory theory is better known because it works well for rod-like polymer liquid crystals. Flory theory can be applied for densely packed systems and predict the formation of nematic phase in a solvent-free melt when the aspect ratio L/d is greater than 6.4.[128] According to the Flory theory, rod-like molecules are divided into many fixed lattice cells and the partition function and free energy are obtained by calculating the packing effects of segmented rods. The critical concentration of rod-like particles in an athermal solvent are:

$$\phi_\mathrm{I} = \frac{8}{\mathrm{L}/\mathrm{d}}\left(1 - \frac{2}{\mathrm{L}/\mathrm{d}}\right) \tag{2.11}$$

$$\phi_\mathrm{N} = \frac{12}{\mathrm{L}/\mathrm{d}} \tag{2.12}$$

Extension of the Flory lattice framework incorporated the effects of the Flory-Huggins interaction parameter $\chi$ and molecular flexibility which gave it having great popularity in modeling polymeric liquid crystals. The parameter $\chi$ is an inverse function of temperature with negative values of $\chi$ corresponding to a good solvent in which the reduction of free energy would occur due to the enthalpy decrease. However, the rod-solvent interactions introduced in Flory theory are only applicable at short ranges and indicate the compatibility between rod and solvent.[126] The biphasic regions broadens with increase in positive values of $\chi$ (for less favorable solvents) and for increasing polydispersity or flexibility.[129-131] When $\chi$ is positive, there is a tendency toward chemically driven segregation due to the insufficient entropy of mixing ($T\Delta S_{mix}$).

### 2.7.2. Friedelian Classes of Liquid Crystals

Friedel classified liquid crystals (LCs) into nematic, cholesteric, and smectic in 1922. Nematic LC phases are typically characterized by an orientational ordering of molecules which do not have positional order and the alignment of rod-like molecules is relative to the vector, known as the director **n**, as illustrated in Figure 2.9a. The ‘threaded’ texture observed under transmitted light microscope without polarizers and Schlieren texture with polarized light microscopy are characteristic optical properties of nematic phases. As for the cholesteric phase, locally the molecules are arranged in a nematic phase, but they follow a helical path about an axis perpendicular the director due to the chiral character of the constituting molecules as shown in Figure 2.9b. Fingerprint textures consisting of near-parallel sets of swirling lines are considered as the typical optical texture of cholesteric phase by polarized light microscopy study. Chirality could be a prominent factor on determining the liquid-crystalline phase behavior and the material properties.[132] However, the relationship between macroscopic cholesteric structure and the microscopic chiral properties of constituting molecules has not been well understood. Both long range orientational and positional order in smectic phase result in a layered structure (Figure 2.9c) and has a characteristic optical texture called focal-conic fan texture.

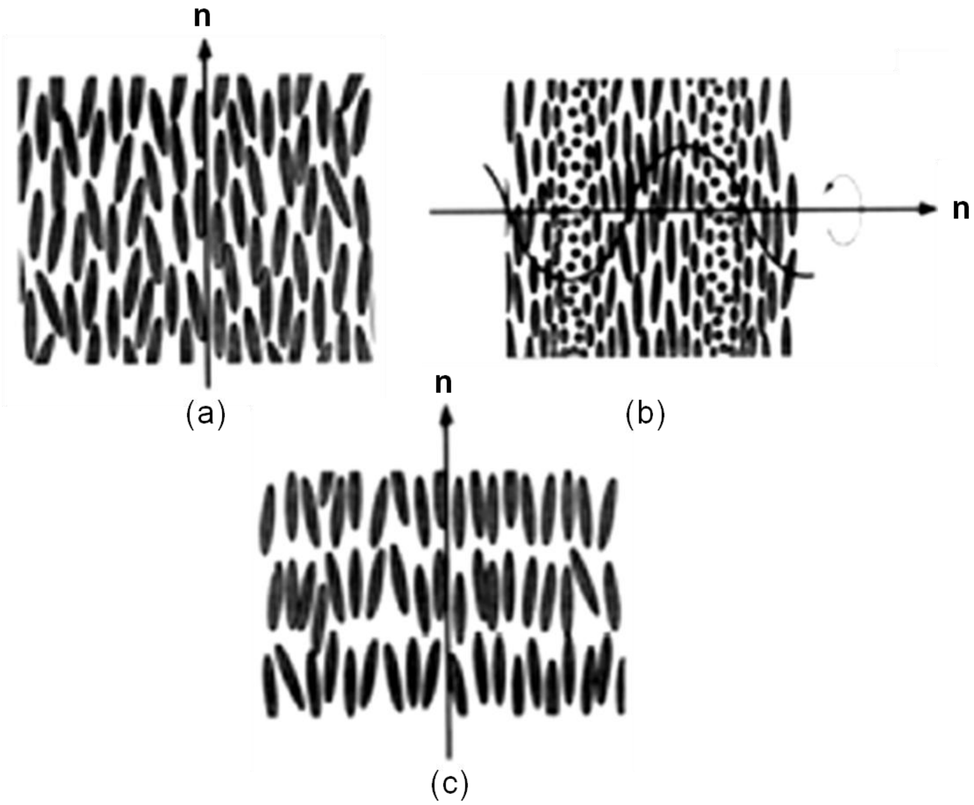

Figure 2.9. Representations of molecular organizations in the three Friedelian classes of liquid crystals: (a) nematic; (b) cholesteric; and (c) smectic.[120]

### 2.7.3. Liquid Crystallinity of Biopolymer-Stabilized Nanotube Dispersions

Although the first carbon nanotube liquid crystal phases were not discovered less than ten years ago,[15,16,19] there have already been several studies of biopolymer – SWNT liquid crystals. Moulton et al.[17] reported nematic LC phase formation for SWNT dispersed in biological hyaluronic acid (HLA) solutions. HLA is one of the chief components of the extracellular matrix and contributes significantly to cell proliferation and migration. The dispersion of SWNT was obtained by sonication assistance and at a certain concentration range of both SWNT and HLA, and evolution of nematic LC phase occurred spontaneously over time in tightly sealed vials with phase separation occurring throughout the dispersions. The highest concentration of SWNT forming nematic LC was 0.5 wt %, and the HLA concentration was chosen as 0.5 wt % or 1.0 wt %. The nematic phase was confirmed by strong birefringence under polarized light microscopy. When rotating the samples between cross polars, and the different domains turned bright and dark based on the relative alignment between their director and the polarization vector of the light.

Highly concentrated suspensions of SWNT in gellan gum (a water-soluble polysaccharide which is used primarily as a gelling agent) were used to form LC phases by another research group.[133] Gellan gum has been shown to a good dispersing agent for stabilizing SWNT in aqueous solution by non-covalent polymer wrapping. The authors could not detect a LC phase for the highly concentrated raw SWNT suspensions, which they assumed was due to the coexistence of large amount of spherical carbonaceous impurities. However, after a purification procedure, they observed large-scale bireflection from both the highly concentrated purified SWNT suspensions and their dried solid composite membranes using polarized light microscopy. Large domains of aligned structures in the dried membranes was further observed using scanning electron microscopy (SEM). The actual concentration of above mentioned highly concentrated purified SWNT suspension was 46 mg/ml of SWNT, which is about 3.2 vol % considering the density of SWNT is 1.45 g/cm$^3$ and the mass ratio was in the range of 10 ~ 20 mg gellan gum to 50 mg SWNT. In addition, Hobbie et al. have shown that SWNT dispersed in bile salts can be assembled into fibrils as a result of the mesogenic nature of the solvent and geometrical confinement.[134] Bile salts, which are produced in the liver, play a critical role in digestion by solubilizing the fat through the formation of mixed-lipid micelles.[135]

### 2.7.4. Liquid Crystallinity of DNA-Stabilized SWNT Dispersions

Nucleic acids dispersants, such as single-stranded DNA (ssDNA), have proven to be an excellent dispersing agents for SWNT through $\pi$-stacking with the nanotube's graphene side walls in aqueous solution with the aid of high power ultrasonication at low temperatures.[97,108,113] One important advantage of biopolymer stabilization of CNTs with sonication assistance is that it better preserves the intrinsic properties of nanotubes compared to other ways of covalent or oxidative functionalization[15,136] which cause damage to the $sp^2$ hybridized structure of nanotubes. However, some reduction in SWNT length and defect creation can still occur. Although another way of dispersing nanotubes, superacids protonation,[19] would not cause damage to the nanotubes, handling in superacids is quite a difficult process and not as environmentally friendly as using aqueous solvents. Another potential advantage of using biological dispersants especially DNA is their unique properties of forming lyotropic liquid crystalline phase under certain conditions. Like some other biopolymers, such as rod-like bacteriophage $fd$,[137] the long and stiff helical structure of dsDNA molecules enables the formation of cholesteric phase in solution above a certain critical concentration which depends on the number of DNA base pairs, ionic strength and the experimental conditions used.[31-34] This twisted LC cholesteric organization of DNA is are even evidenced to form *in vivo*.[35,37,138] It was reported that natural DNA with relatively short molecular length of approximately 500 Å could also form precholesteric phase at lower concentration prior to forming cholesteric phase. At even higher concentrations, natural DNA can form into multiple high-density phases.[139-141] The first microscopic theory of the cholesteric phase was proposed by Straley in 1976 and predicted that the formation of a cholesteric phase was entirely due to the entropy driven excluded volume interactions which resembled the Onsager theory (1949) describing a nematic solution of rod-like molecules. One of observable features of DNA cholesterics is the cholesteric pitch in the typical fingerprint textures which may be directly dependant on the molecular length of DNA fragments as well as on the interaxial spacing of molecules and the solvent conditions like osmotic pressure and ionic strength.[140,141]

Badaire et al.[16] reported the first water-based nematic phase of non-covalently functionalized CNTs with nanotube concentrations up to above 4 wt % (~ 2.5 vol % for SWNT density of 1.3 g/cm$^3$) by dispersing them in nearly equal concentration of denatured DNA. In their work, nematic phases of higher concentrations of SWNT stabilized by denatured DNA were obtained by solvent evaporation due to the unique phase diagram of DNA-nanotube suspensions which has linearly separated domains of dispersed and aggregated nanotubes. Unlike low-molecular-weight surfactants used to disperse nanotubes, denatured DNA does not cause depletion induced aggregation between nanotube bundles, making it an ideal candidate for acquiring highly concentrated systems.[16,21] More ordered LC phases than the nematic phase had not yet been reported. However, given the premise that natural DNA can form cholesteric, and even higher density phases, above certain critical concentrations under well defined conditions, more ordered LC phase formation could be achieved at higher concentrations of CNTs by incorporating natural DNA with nanotubes in an appropriate way.

## 2.8. Rheology of Liquid Crystalline Polymers

Rheology can probe the microstructure of dispersions and may even be able to qualitatively and perhaps quantitatively predict changes of microstructure due to various processing conditions including shear, temperature, and solvent removal in the assembly of macroscopic objects (e.g. films and fibers). Comparison of dsDNA/SWNT liquid crystal rheology to the rheological signatures of lyotropic nematic liquid crystalline polymers (LCPs) can provide better understanding of the phase behavior of nematic and cholesteric dsDNA/SWNT dispersions created in this research. Understanding the difference in phase behavior of nematic and cholesteric dsDNA/SWNT dispersions with concentration, textural effects, and shear flow is required to improve the properties of their macroscopic assemblies. The complex rheology of LCPs is very different from the ordinary polymers and low molecular weight liquid crystals (LMWLCs), and the subject of LCPs phase behavior is still somewhat controversial. Moreover, the insufficient rheological data of LCPs are mainly on lyotropic nematic LC phases and the flow properties of cholesterics have been studied little. Although, the rheology of model LCPs such as hydroxypropylcellulose (HPC),[38-40] poly (γ benzyl-L-glutamate) (PBLG)[41,42] or poly (γ benzyl glutamate) (PBG)[43,44] solutions have been widely studied, there are still struggling efforts to understand this field due to the lack of universality in rheological properties of LCPs. Especially, when applied to nanoscale rods like SWNT, the flow behavior of the resulting liquid crystals became even more complicated due to the additional strong van der Waals attractions between SWNT and their polydispersity. The complex interplay between intermolecular interactions, molecular conformation, shear flow, and molecular orientation state are considered to be the factors responsible for the unique rheological properties of LCP solutions.[40,43] In general, the known evidence of lyotropic nematic LCPs include following and will be discussed in more details in Section 2.8.2:

- Maximum in viscosity versus concentration curve
- Three region viscosity versus shear rate curve
- First normal stress difference changes sign with increasing shear rate
- Long oscillatory transients after start up flow of steady shear
- Cox-Merz rule not obeyed

### 2.8.1. Rheology of Dilute and Semidilute Brownian Rods Dispersions

The Brownian motion of rods is caused by the thermal fluctuation of the solvent molecules. As mentioned above, spontaneous alignment may occur for anisotropic mesogens like rods and platelets with increasing concentration, or with external shear force and electric field. However, at low concentrations, rods are distributed with random orientations especially in dilute or semidilute dispersions. Understanding the rheological behavior of isotropic system is therefore important and can provide the first step towards the development of rheological models for rods materials including cylindrical nanomaterials.[142,143] If rods (length $L$ and diameter $d$) can be considered to have dilute behavior in suspensions, they need to satisfy the following conditions; the rods are able to rotate freely both translational and rotational without being impeded by the neighboring rods, and the volume swept by a single rod rotation about its mass of center is large around $L^3$. When the number concentration of rods $\nu$ reaches a value proportional to $L^{-3}$, rod-rod interaction is expected; this is the semidilute regime where the rotational motion of Brownian rods will be hindered. In Doi-Edwards theory (1986), dilute behavior is defined when the number concentration of Brownian rods is $\nu < \frac{1}{L^3}$ and the semidilute behavior occurs in the range of $\frac{1}{L^3} << \nu << \frac{1}{dL^2}$. Since the average distance between neighboring rods is very large compared to the rod diameter in the dilute and semidilute regimes, rods can be treated as thin line particles in these dispersions states.[144] With increasing concentration, the onset of the concentrated isotropic regime occurs around $\nu \approx 1/dL^2$ where the dimension of rod diameter becomes comparable to the distances between neighboring rods. In the isotropic concentrated regime, excluded-volume interactions take effect and isotropic packing of rods starts to be difficult. Rod motion is confined to straw-like volumes. At even higher concentrations, the rods are spontaneously oriented into anisotropic state, and Brownian motion of rods no longer exists.[145] However, Mori et al.[146] found that, experimentally, the transition from dilute to semidilute behavior occurs more than 30 times the theoretical estimation giving $\nu_o L^3 \approx 30$. Since number concentration of rods is related to the volume fraction $\phi$ of rods as $\phi = \pi d^2 L \nu / 4$, the critical concentration of semidilute behavior occurs when $\phi_o \approx 30\pi d^2 / 4L^2 = 24(d/L)^2$. This corresponds to 0.24 vol % of the dispersed phase for rods with aspect ratio of 100.[48]

Characterization of size and length to diameter ratio (aspect ratio) distribution of nanocylinders dispersed in fluids, is significantly important in better understanding the phase behavior of the dispersions in this study. Based on Onsager (1949) and Flory (1956) theories of rods in fluids, the aspect ratio of rods together with their polydispersity, and rigidity, and the solvent quality are considered to be the major factors affecting the formation of lyotropic liquid crystals. Particularly, the biphasic region should be broadened by polydispersity and decreasing solvent quality. Fortunately, the average aspect ratio of dilute dispersions of Brownian nanorods can be rheologically determined using the Kirkwood-Auer-Batchelor (KAB) Equation. The zero-shear viscosity of a (monodisperse) solution or dispersion of Brownian rigid rods can be used to calculate the average aspect ratio. The zero shear viscosity, $\eta_o$, of a dilute suspension of rods is[147]

$$\eta_o \equiv \lim_{\dot{\gamma}\to 0} \eta\left(\dot{\gamma}\right) = \eta_s + \frac{4}{5}\kappa_B T \tau \nu \qquad (2.13)$$

where $\eta_s$ is the solvent viscosity, $\kappa_B$ is Boltzmann's constant, $T$ is temperature, $\nu$ is the number of rods per unit volume, and $\tau \equiv \xi/\left(3\kappa_B T\right)$ is the rotational relaxation time of the rods, and $\xi$ is the perpendicular drag coefficient of the rods. The number concentration of rods is $\nu \equiv \phi/\left(\pi R^2 L\right)$ where R is the rod radius. The perpendicular drag coefficient $\xi$ on a slender cylinder [148] is $\xi = \frac{\pi \eta_S L^3}{6}\varepsilon f(\varepsilon)$ where,

$$\varepsilon = \frac{1}{\ln(L/R)} \quad \text{and} \quad f(\varepsilon) = \frac{1+0.64\varepsilon}{1-1.5\varepsilon} + 1.659\varepsilon^2$$

This yields the KAB relationship indicating that the intrinsic viscosity $[\eta]$ of dilute dispersions of (monodisperse) Brownian rods is:

$$[\eta] \equiv \lim_{\phi\to 0} \frac{\eta_o - \eta_s}{\eta_s\,\phi} = \frac{2\left(L/R\right)^2}{45\left[\ln\left(L/R\right)\right]}\left[\left(\frac{1+\dfrac{0.64}{\ln\left(L/R\right)}}{1-\dfrac{1.5}{\ln\left(L/R\right)}}\right) + \frac{1.659}{\left(\ln\left(L/R\right)\right)^2}\right] \qquad (2.14)$$

Therefore, L/R (and aspect ratio L/d where d is the rod diameter) can be directly obtained from the low shear rate plateau of a master curve generated from dilute dsDNA/SWNT dispersions of different concentrations (multiple concentrations reduce error). In the polydisperse case, the viscosity contributions of each subpopulation of length are additive and the viscosity average length is related to the ratio of the third and first moments of the distribution of length:

$$\frac{L_{visc}}{d} = \frac{1}{d}\sqrt{\frac{\left\langle L^3 \right\rangle}{\left\langle L \right\rangle}} \tag{2.15}$$

where, $\left\langle L^n \right\rangle = \frac{\sum_{i=1}^{N} L_i^n}{N}$, $\left\langle L \right\rangle$ and $\left\langle L^3 \right\rangle$ are the first and third moments of the length distribution, $N$ is the total number of rods, and $n$ is the moment of interest.[149]

Applicability of this theory to new systems requires Brownian rigid rod behavior of dilute dispersions or the collapse of viscosity versus shear rate curves from samples of different concentrations onto a single master curve. In the latter case, the Newtonian plateau should transition toward the shear thinning region at a Weissenberg number $W_i$ of approximately 0.2 ($W_i = \tau_{rot}\dot{\gamma}$) and the slope in the shear thinning region should be -0.5 and commence at $W_i = 1$ as shown in Figure 2.10. Fortunately, rotational rheology of SWNT up to 4 micron in length in superacids ($\eta_s \sim 30$ mPa • s)[19] and single particle tracking of SWNT in surfactants ($\eta_s \sim 1$ mPa • s)[150] revealed the Brownian rods behavior of the dilute SWNT. In addition, it was reported that even germanium nanowires with long lengths (up to 8 µm) and high aspect ratios, can undergo Brownian motion in a dilute suspension.[143]

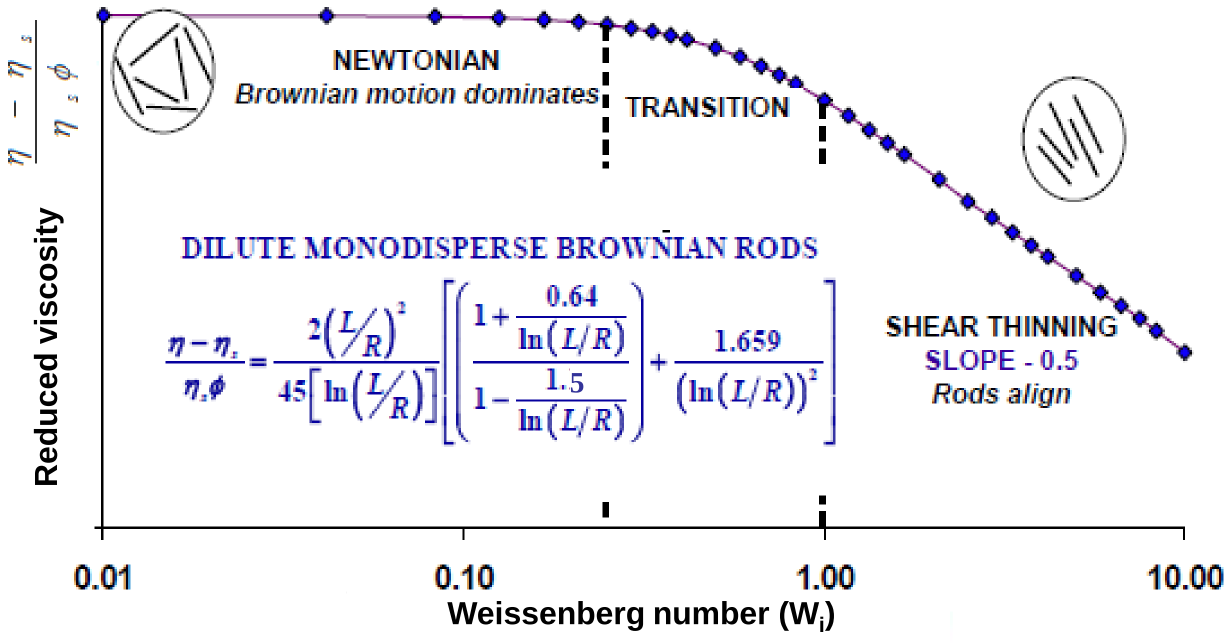

Figure 2.10. Universal shear thinning curve of monodisperse dilute Brownian rods.[151]

In the semidilute regime, Doi–Edwards theory predicted the zero-shear viscosity of semidilute solutions of rods using the tube model where the movement of a test rod is confined by the surrounding rods:

$$\eta_o = (\kappa_B T L^6 / 10\beta D_{ro})\nu^3 \tag{2.16}$$

where $D_{ro} = \frac{1}{6\tau}$ is the dilute-solution rotary diffusivity of the particle, and $\beta$ is a dimensionless constant. Rearranging the equation 2.16 gives the relationship $\eta_o \propto \phi^3$. Thus, when zero-shear viscosities are plotted against concentration on a logarithmic scale for semidilute solutions of rods, the slope of the curve is 3. An example of experimental data in qualitative agreement with the semidilute theory is given in the Figure 2.11 below. However, the window of semidilute behavior with slop of 3 appears to be very narrow in the range of 2.5 - 5 wt % which is almost nonexistent. The narrowness of semidilute window can be attributed to small molecular length, polydispersity, and molecular flexibility.[144] As a comparison, the Kirkwood-Auer-Batchelor equation predicts that, the slope in the dilute regime is related only to the rod aspect ratio and is smaller than 1 when the $\eta_o$ is plotted against concentration. Specifically, the larger the rod aspect ratio is, the higher the slope which approaches closer to 1.

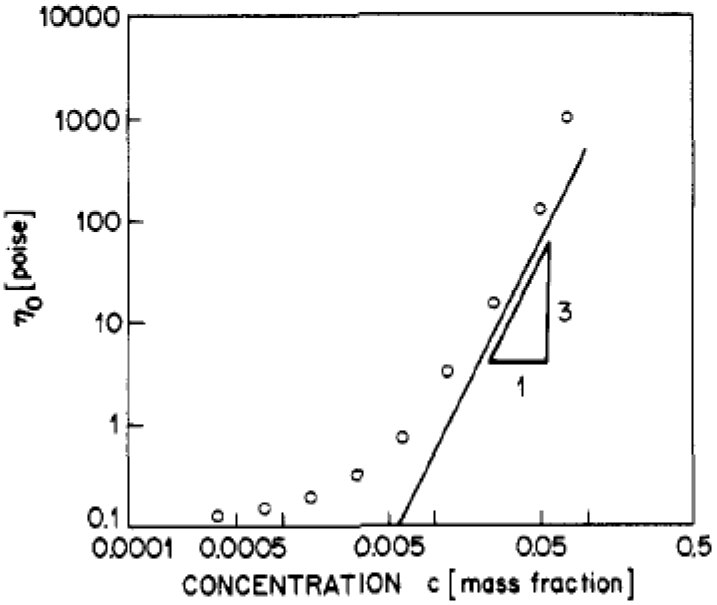

Figure 2.11. Zero-shear viscosity versus concentration for PBLG.[144]

In this study, the ternary system of dsDNA/SWNT dispersion is relatively complicated. Due to the excess amount of viscous dsDNA used to stabilize SWNT either in non-centrifuged (dsDNA:SWNT=7.5:1 by weight) or supernatant (dsDNA:SWNT=5.1:1 by weight) dispersions, the resulting rheology of dilute SWNT (<0.03 wt % or 500 ppm of SWNT) in dsDNA solution might reflect the phase behavior of dsDNA rather than the SWNT. Based on the UV-vis analysis performed in this study, the dispersibility of SWNT in dsDNA solutions is also affected by the volume of samples prepared. The volume of starting 0.75 wt % dsDNA-0.1 wt % SWNT dispersions used to get concentrated liquid crystal is typically 150 mL. In order to ensure the consistency in experimental data, same volume of 150 mL samples with identical weight ratios of dsDNA to SWNT were used. More specifically, the steady shear viscosities of both non-centrifuged and supernatant dispersions of dsDNA/SWNT with various concentrations in dilute regime were tested in the shear rate range from 0.01 to 100 1/s given the condition that they are in accessible instrument torque transducer range. If the viscosity versus shear rate curves from samples of different concentrations collapse onto a single master curve as described above, the difference in average aspect ratio in the dilute regime between the bulk (non-centrifuged) dispersion and the supernatant of dsDNA/SWNT dispersion can be detected by rheology. Since this approach has only been used for dispersions of rods in Newtonian fluids, it is not known if the presence of the dsDNA will prevent applicability of this method.

### 2.8.2. Rheological Signatures of Nematic Liquid Crystalline Polymers

Although LCPs have very different rheological properties when compared to ordinary polymers, their isotropic phases have similar rheological behavior to ordinary polymers.[152] To determine the complexity of the microstructure in a flowing LCP, one need only look at the steady state viscosity behavior.[41] Rheological signatures of LCPs in lyotropic nematic phase are described in the sections below.

**Maximum in Viscosity versus Concentration Curve.** A well-known rheological characteristic of lyotropic nematic LCPs is the nonmonotonic relationship between viscosity and concentration at a constant temperature. In lyotropic LCPs, the low shear viscosity goes through maximum in the biphasic regime and the magnitude of this maximum decreases with increasing shear rate.[48] The viscosity increases as a function of increasing concentration as long as the system is predominantly isotropic. However, the increasing proportion of the anisotropic phase with concentration results in a decrease in viscosity as a lower shear stress is required for orientation. The sharp decrease in viscosity in the biphasic regime may be due to the relative ease of molecules sliding past each other in the partially ordered phase than isotropic concentrated state. This is supported by the fact that the alignment in liquid crystal is due to the gain in translational entropy compensating for the loss of orientational entropy. With further increase in concentration, viscosity decreases with concentrations within the liquid crystal phase. The viscosity decreasing sharply on the transition to liquid crystal phase is a complex characteristic which implies a reverse trend to the common knowledge obtained from ordinary polymers that viscosity increases monotonically with increasing polymer concentrations. Once the order can no longer be increased, the viscosity once again keeps increasing with concentration.

**Three Region Viscosity versus Shear Rate Curve.** The rheological behavior of lyotropic nematics also has a typical shape of viscosity as a function of shear rate. It often has three viscosity regions of shear thinning, almost constant viscosity, and additional shear thinning with increasing shear rate. The three distinct regions occurred in viscosity versus shear rate curve in some of nematic LCPs are shown in Figure 2.12. Region I shear thinning is the most distinguishing feature for lyotropic nematic LCPs and have been observed in several types of model systems at high concentrations such as HPC and PBLG.[41,153] Even for SWNT dispersed in superacids solutions, possible three region behavior was reported with a very narrow region II plateau between the two shear thinning regions.[19] Regions analogous to a low shear rate “Newtonian plateau” in Region II and shear thinning at high shear rate in Region III are common for isotropic solutions of flexible or rigid polymers. The polydomain structure of nematic phase is considered to be preserved at the first shear thinning region and part of the second region with a constant viscosity both appearing at low shear rate.

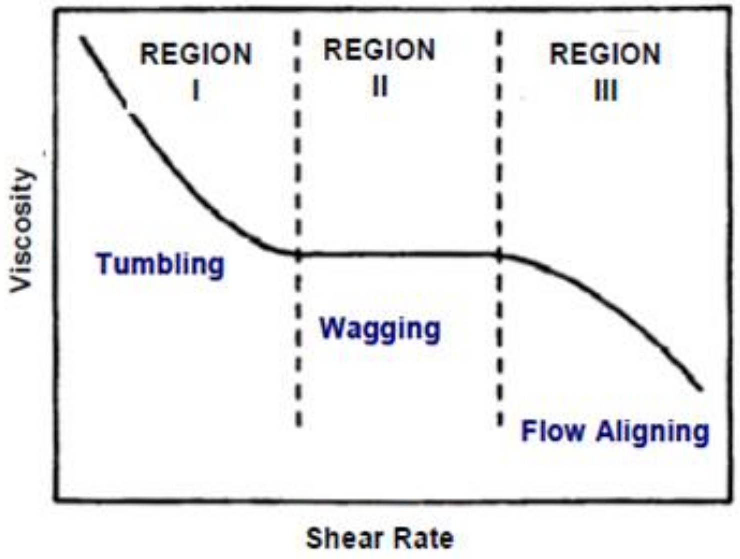

Figure 2.12. Viscosity versus shear rate curve showing a three region behavior. For some LCPs, the low-shear-rate Region 1 is not found.[150,152]

Region I has generally been observed only in high viscosity, “tumbling” nematics where the shear viscosity in Region II exceeds ~10 Pa・s. Typically, region I shear thinning is believed to be related to director tumbling in liquid crystalline phase upon shear flow. However, Region I is not seen in all lyotropic nematic polymeric liquid crystals and depends on many factors such as specific materials used, flexibility of rods, defect texture, or the range of shear rates covered.[153] It is also suggested that Region I of LCPs can be associated with cholestericity. At the low shear rate of Region I some LCPs like HPC show diffraction characteristics of the cholesteric phase and the cholestericity is further broken down by the higher shear flow in Region II.[48]

In this work, the high viscosities resulting from the long rod length and high aspect ratio of SWNT (L ~ 500 nm, D ~ 1 nm) coupled with liquid crystalline phase formation when stabilized by dsDNA, could be expected to enable measurement of Region I behavior in dsDNA/SWNT dispersion. However, due to the following reasons, it is not apparent whether a three region behavior can be expected in the LC phase of dsDNA/SWNT dispersions.

a) In the bulk, both thermotropic and lyotropic materials contain so many orientational defect that homogeneity typically persist over domains no larger than about one micron.[154] Region I behavior is also associated with small characteristic texture length scales on the order of one micron. The defect texture in the dsDNA/SWNT nematic and cholesteric liquid crystals and the presence of excess or free dsDNA may have an effect on the polydomain liquid crystal texture leading to a complex ternary system (SWNT, dsDNA, and water).

b) 40% PBLG (MW=238,000) solution which showed Region I shear thinning also suffered from complex hysteresis consisting of two distinct viscosity braches for steady shear viscosity measurement with different preshearing.[41] This behavior may be due to the texture elasticity and the change in defect texture upon shear flow indicating that Region I behavior is extremely sensitive to the sample preshear history. Thus, an exploration of preshear protocols for “wiping off” the flow history is required to testing for Region I in dsDNA/SWNT liquid crystal.

c) Not all LCPs exhibited Region I shear thinning. Due to the fact that all rheometers have detection limits on shear stress, it is relatively difficult to test Region I experimentally. Further, with the low shear rate involved in shear thinning of Region I, several other problems are have to be considered such as sample evaporation and extremely long time needed for testing which again highly demanding a reasonable preshear protocol.

**First Normal Stress Difference Changes Sign.** The unique rheological properties of nematic LCPs have led to the development of new molecular theories such as Doi, Marrucci and Larson.[47-49] However, the direct modeling of nematics with highly textured structures are so complicated that those theories adopted a simple geometry for calculation. For example, the Doi model assumes only monodisperse rigid rods and an anisotropic excluded volume potential when predicting the two sign changes in the first normal force difference $N_1$ for lyotropic LCPs. Due to the polydispersity and flexibility of rods, textural defects, and various molecular interactions existing in the real LCPs systems, the experimental results would have discrepancies with theory. Figure 2.13 shows the $N_1$ changing signs with increasing shear rate for lyotropic nematic LCPs. The negative $N_1$ was first reported by Kiss and Porter in 1978.[155] Since then, few LCP solutions showed two sign changes in $N_1$ where at lower shear rates $N_1$ was positive and increased with shear rate due to the tumbling of average molecular orientation (i.e., the "director"), and at intermediate shear rate $N_1$ suddenly dropped and changes to negative due to the director wagging which would cause low molecular order. At even higher shear rates, the $N_1$ became positive again due to the flow alignment of rods.[48,152] This change in $N_1$ also corresponded to the universal three region steady-shear viscosity behavior in flow curve. The origin of negative $N_1$ is still controversial in spite of considerable research.[48,156] It is widely believed that the occurrence of a negative relative minimum in $N_1$ is associated with a flow transition between director tumbling and flow-aligning behavior.[156,157] Correspondingly, the sign change observed in some LCPs occurred near the onset of shear thinning Region III in the viscosity versus shear rate curve.

On the other hand, for conventional polymeric liquids, or for nontumbling liquid crystals, $N_1$ increased monotonically with increasing shear rate (only positive $N_1$).[158] Along with relative minimum in the $N_1$ flow curve, even if the minimum was positive, the oscillatory response in transient flow were considered to be indirect evidences of director tumbling.[39,159] Theories also indicate that tumbling is affected by polymer flexibility which would increase as the temperature increases.[38,160,161]

The rheology of nanocylinder liquid crystals would be an extension of well understood flow behavior of model LCPs such as HPC and PBG at moderate concentrations. For cholesteric liquid crystals of dsDNA/SWNT dispersions, it might be possible that the typical curve of two sign changes of $N_1$ would occur outside the experimental shear-rate range, or cholesterics may have different character in negative $N_1$ behavior as compared to nematic LCPs. These possibilities are discussed in Chapter 4.

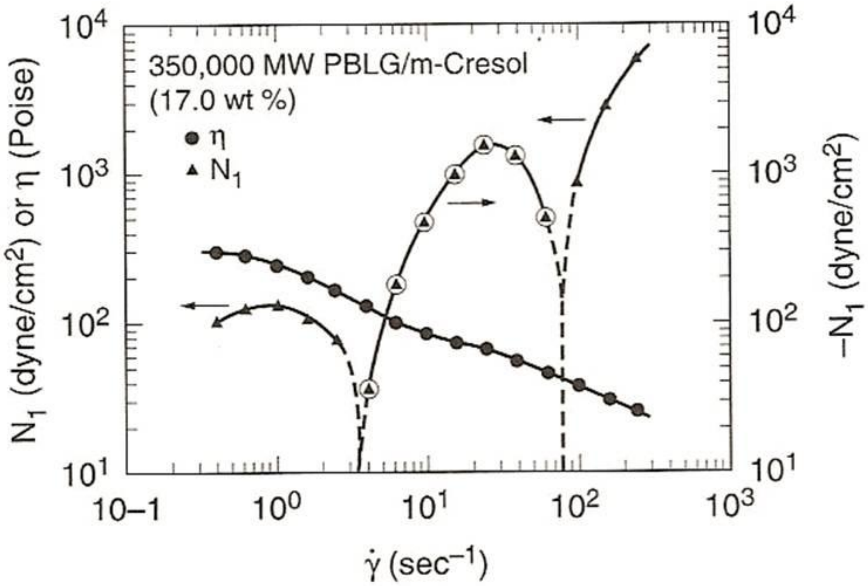

Figure 2.13. Shear viscosity and first normal stress difference versus shear rate for 17 % PBLG (MW=350,000) in *m*-cresol. The circled triangles are negative $N_1$ values.[48,155]

**Long Oscillatory Transients.** Another striking behavior of LCPs in a shear flow is long oscillatory transients achieved before reaching steady state. Typically for liquid crystals, the transient response is complex and much longer in duration than 100 shear units. While for isotropic suspensions and ordinary polymer solutions, the oscillatory transients last a few shear units at most.[49] Moreover, in Region II of the viscosity versus concentration curve, the oscillation period is fairly regular and roughly inversely proportional to shear rate. As a result, when the transient stress response obtained at different shear rates in Region II are plotted against shear units the maximum and the minimum of the curves will overlap.[162] However, to the author's knowledge, it has never before been possible to achieve definitive Region II transient stress plots for nanocylinder liquid crystals including SWNT. Varying the shear rate range coupled with evaluating the distortion texture due to transient flow by shear cell will be a feasible approach to investigate the rheological properties of dsDNA/SWNT liquid crystals occurring in Region II

**Cox-Merz Rule Not Obeyed.** The Cox-Merz rule states that, the modulus of complex viscosity $\eta^*(\omega)$, a linear viscoelastic material property, equals to steady shear viscosity $\eta(\dot{\gamma})$ at equal values of angular frequency $\omega$ ($s^{-1}$) and shear rate $\dot{\gamma}$ ($s^{-1}$). However, unlike ordinary polymers, lyotropic nematic LCPs have a common characteristic of not obeying the empirical Cox-Merz rule. Basically, polymeric fluids having a complex deformation-dependant microstructure would fail to obey the Cox-Merz rule.[163,164] Although many studies have been contributed to the well-established Cox-Merz rule relating the linear viscoelastic material properties to the nonlinear flow curve ever since its introduction in 1958,[165] the first molecular theory successfully predicting this rule for monodisperse polymer was proposed by Marrucci late in 1996.[166,167] Molecular theory predicting the Cox-Merz rule was later extended to a polydisperse polymers by Mead et al.[168,169] using the same molecular mechanism proposed in Marrucci's work for fast flows which is convective constraint release (CCR). The CCR is the nonlinear relaxation mechanism and the longest relaxation time in fast flows scales with $\dot{\gamma}^{-1}$ independent of molecular weight. According to above molecular theories, the Cox-Merz relationship is an unphysical coincidence indicating no physical similarities in the dynamics of polymers or molecular relaxation mechanisms between linear and nonlinear flows. The Cox-Merz rule is due to the CCR process and the similar mathematical relationship between steady shear and complex dynamic viscosities at identical high dimensionless shear rates or frequencies which has the same relaxation mechanisms transition from linear to nonlinear flow regions.[169]

### 2.8.3. Shear Effects on Liquid Crystal Rheology

In this section, the change in polydomain texture of nematic LCPs upon shear will be discussed since it is widely believed that the rheological phenomena are associated with texture evolution during shear. The texture of a bulk sample of an LCP is defined as the spatial variation in the director, which is the direction of average molecular orientation.[170] The polydomain texture in LCPs is relatively stable under shear when compared to small molecule organic liquid crystals due to the high aspect ratio of rods and long relaxation time in LCPs. Furthermore, Marrucci[171] defines the texture length scale $a$, which can be thought as the diameter of a domain, a volume over which uniformity persist in the orientation,[170] as below

$$a \propto \left( \frac{K}{\eta \dot{\gamma}} \right)^{1/2} \tag{2.17}$$

where K is a typical Frank elastic constant, $\eta\dot{\gamma}$ is viscous energy density. This relation indicates that the refinement of texture would occur as the flow rate increases. In fact, the defects of polydomain liquid crystals can be annealed with the application of external force. Shear flow alignment could be a feasible approach to achieving higher degree of rod alignment since it is used widely in films or fiber processing. However, effectively controlling the shear rate is an important task considering the characteristic three region viscosity curve as a function of shear rate which is discussed before. Except for the shear rate range of Region III where flow alignment occurs, shear can also result in other behaviors such as low shear aggregation, yielding, jamming, vorticity alignment, and shear banding. Shear banding is one of the regularly observed textures in LCPs which is considered to be caused by the distortions of nematic director field under shear. Usually, shear banding refers to dispersion segregating into birefringent bands of high and low concentration as a result of shear.[48] Interestingly, the same sequence of texture evolution with shear was reported for both a low-molecular-weight polyester melt[38] in the nematic range and PBLG solution.[172] For start-up of shearing at lower stain, shear bands perpendicular to shear flow quickly form. With increasing strain, stripes parallel to flow begin to appear and the perpendicular bands started to disappear until only the parallel stripes remain. The difference between "stripes" and "bands" is that, the former are parallel to the flow direction while the latter are perpendicular to it. At even higher strain, the stripes would break down into a fine-scale "speckled" texture. However, bands orthogonal to the previous shear direction appear again after the cessation of shear. Although the phenomena of this particular sequence are not completely understood, it is highly considered to be related to the tumbling nature of LCPs.

Furthermore, bands have been observed for almost all LCPs, their origins still have been an ongoing source of research.[173] The shear banding is a quasi-periodic texture with the annealing or healing time, $t_a$, for the spontaneous disappearance of a disclination texture from a nematic of viscosity η and thickness h as

$$t_a \approx \frac{\eta h^2}{K} \tag{2.18}$$

where K is the characteristic Frank constant.[48] Due to the high viscosity in LCPs with comparison to small molecule nematics, the textures are much more persistent in LCPs. The effective "director diffusivity", $K/\eta$, of small molecule nematics is on the order of $10^{-6}$ $cm^2/s$, while for polymeric nematics $K/\eta \sim 10^{-8}$ to $10^{-10}$ $cm^2/s$. Since LCPs have much long relaxation time, preshear protocol is needed to obtain reliable dynamic measurements by "wiping off" the previous flow history.

In this work, the effect of small shear rate applied for a few seconds on the cholesteric pitch of dsDNA/SWNT liquid crystal was investigated by polarized light microscopy coupled with shear cell. The phase behavior of dsDNA/SWNT liquid crystals upon shear was also conducted by rheology including dynamic and steady shear test.

### 2.8.4. Temperature Effects on Liquid Crystal Rheology

The motivation for investigating the temperature effects on the rheology in this work is seeing if there is a difference in nematic and cholesteric system of dsDNA/SWNT. Time-temperature superposition (TTS) is a valuable tool for describing the viscoelastic behavior of lyotropic polymers where the phase transition is only affected by concentration rather than temperature. It can show the phase behavior at a "reference temperature" by obtaining data at several temperatures to generate a master curve covering many decades of time or frequency whereas only a range of three or four decades can be obtained at a single temperature.[174] Shift factors for the magnitudes of measured stresses (vertical shift factor, $b_T$) and for time or frequency (horizontal shift factor, $a_T$) can be used to create the master curve. Usually, the shift along the vertical axis is often small or negligible. While the temperature dependence of shift factor $a_T$ can be expressed as the empirical WLF (Williams-Landel-Ferry) equation;[175,176]

$$\log \frac{\eta T_r \rho_r}{\eta_r T \rho} = \frac{-C_1\,(T - T_r)}{C_2 + T - T_r} = \log a_T \tag{2.19}$$

where $C_1$ and $C_2$ are two material specific coefficients, and $T_r$ is the reference temperature. The change in temperature times density (vertical shift factor) $b_T = T_r \rho_r / T\rho$ is small and can be ignored in most cases. The WLF equation reveals that shifting of viscosity, which is composed of both stress and time, requires the application of both shift factors such as $\frac{b_T}{a_T}\eta\,(T)$ versus $\dot{\gamma} a_T$. The WLF relation is usually appropriate for temperature changes in the range of $T_g$ to $T_g+100\ K$ for melts of glassy polymers where $T_g$ is the glass transition temperature.

The TTS principle only applies to thermorheologically simple materials where the material structures do not fundamentally change in the temperature range considered. Thus, this technique would fail for polymers with complex relaxation mechanism and with phase transition or chemical change occurring within the temperature range measured. However, with some exceptions, TTS principle was also reported to hold for some polymer blends with individual components having different relaxation mechanisms.[177] Moreover, time-temperature superposition is not always applicable for rod-like polymers. The solvent quality of rod-like polymers can be tuned by simply changing temperature which further resulted in the change of phase boundaries. On the other hand, the phase behavior of SWNT in superacids[19] and even low aspect ratio CdSe-cylcohexane[178] has been found to be temperature insensitive. However, little rheology has been done for the latter case. For SWNT in superacids, although the phase transition is independent of temperature, LC phase behavior was obtained with improved solvent quality by using superacids with different protonating abilities.

### 2.8.5. Persistence Length Effects on Rheology

Recent reports on SWNT in superacids[19] showed all five rheological signatures of LCPs listed above and come to the conclusion that SWNT can form liquid crystals when appropriately dispersed. Possible three region behavior was observed for SWNT in 102% $H_2SO_4$. Also, both the shear viscosity and the first normal stress difference oscillated for over 800 shear units for 7.6 vol % SWNT in superacids. However, the new system of dsDNA/SWNT dispersions appears to be very different and has the added complexity of DNA which is not really a rigid rod. A molecule is effectively a rigid rod, if the rod contour length $L$ is much shorter than the persistence length, $\lambda_P$ ($L$ << $\lambda_P$). Some molecules, such as helical DNA, collagen, or PBLG, are called "semiflexible" with $L \approx \lambda_P$. They are stiffer than ordinary flexible polymers like polystyrene but are not rigid rods.[179] Persistence length is the length scale over which a filament shows significant curvature induced by thermal fluctuations. This is because the dynamics of 1D rods in a viscous medium are essentially dominated by the balance of Brownian forces, which tend to bend them, and elastic forces, which oppose this curvature.[180] The simplest model for molecules with uniform distribution of flexibility is the inextensible elastic beam with bending rigidity $\kappa = EI$, where $E$ is the elastic modulus and $I$ is the area moment of inertia about the filament axis. A hollow cylinder of inner radius $r_i$ and outer radius $r_o$, has a moment of inertia of $I = \pi(r_o{}^4 - r_i{}^4)$.[181] As a result, the persistence length can be expressed as the ratio of bending rigidity to thermal energy, $\lambda_P = \kappa / k_B T$, where $k_B$ is the Boltzmann constant, and $T$ is the absolute temperature. The persistence length of DNA measured by light scattering is around 0.053 μm, which is about the length of 150 base pairs.[182] However, under low-salt conditions, the effective persistence length of DNA is expected to be longer due to the electrostatic repulsion of charges along the molecules.[48] The prediction of the bending rigidity of SWNT according to the theory based on a continuum model for a hollow cylinder of radius $R$ is $\kappa = \pi C R^3$, where the "in-plane stiffness" $C$ is estimated as ≈ 345 J/m$^2$.[183,184] This results in $\lambda_P$=134 μm for SWNT with typical diameter of 1 nm. This model indicates a diameter dependent bending rigidity and persistence length of nanotubes. Considering that the length of the majority of commercial SWNT is $L \sim 500$ nm, which gives $\lambda_P/L$ on the order of 100 and they are effectively rigid rods ($\lambda_P >> L$). The individual shape fluctuations of SWNT can be measured by fluorescence microscopy. The experimental values of $\lambda_P$ obtained from fluorescence microscopy range from 26 to 138 μm for SWNT of diameter from 0.77 to 1.15 nm and length larger than 3μm.[180] The persistence length of each SWNT can also be determined rheologically from the dynamic data. The theoretical relationship between persistence length and bending relaxation times is;[181,185,186]

$$\lambda_P \approx \frac{\gamma}{\tau_n \kappa_B T \left( \frac{\left(n + \frac{1}{2}\right)\pi}{L} \right)^4} \tag{2.20}$$

where $\gamma \approx 4\pi\eta / \ln(L/d)$ is the friction coefficient, and $\tau_n \approx \gamma / \kappa q^4$ is the relaxation time of mode $n$, with $q \approx (n + 1/2)\pi / L$. The model and experimental measurements show $\lambda_P \approx 26 \sim 138$ μm for SWNT indicating that SWNT is rigid rod up to L ~ 3 μm.

## 2.9. Macroscopic Assembly of Biopolymer-Stabilized Carbon Nanotube Dispersions

The remarkable properties of nanomaterials can often be only realized if they are processed into useful macroscopic formats. Generally, aligned CNTs could promise enhanced mechanical, optical, electrical, thermal, magnetic properties for the resulting macroscopically assembled objects. The recent achievements in obtaining nematic LC phase from the dispersion of SWNT in superacids[19], in biological hyaluronic acid and denatured DNA solutions[16,17] and aqueous dispersion of acid treated MWNTs[15] not only opened up the rich interest in LC study with nanomaterials but also provided a novel approach to process CNTs nanomaterials with large-scale of alignment of nanotubes. However, obtaining a better dispersion of CNTs at the really first stage still remains to be a challenge due the inherent van der Waals attraction between the tubes, which is on the order of 20 - 40 $k_B T/nm$.[45,46] Alignment on a larger scale over macroscopic areas is also an obstacle which is important for potential applications of CNTs. Several methods have been developed to obtain a good dispersion of nanotubes in solvent including ultrasonication, surface modification of nanotubes,[187] surfactant addition[21,188] and further using external forces of electrical, magnetic and shear flow to obtain large-scale ordered structure of CNTs. Typically, macroscopic assemblies of CNTs materials have been achieved in the formats of films, coatings and fibers by different methods, while fluid phase possessing is considered to be a promising route.

### 2.9.1. Films/Coatings

Several methods of fluid phase processing of CNTs into films and coatings were reported recently, including drop drying,[189,190] spin coating,[191] shear alignment,[192] and layer-by-layer assembly.[1] Alan H. Windle's group demonstrated films of CNTs obtained by drop drying of the biphasic or LC aqueous dispersions of both MWNT and SWNT with oxidative acid treatment.[189,190] It was confirmed that the typical textures of the LC dispersion was retained in the resulting thin films including birefringence and ordered structure on drying by evaporation. However, predominant alignment of the nanotubes parallel to the edge of the dried sample was also found. This segregation effect of significantly greater quantity of nanotubes on the periphery than in the center was explained to be due to the "ring effect" in dried coffee stains.[193] The driving force for this effect is considered to be minimizing energy in the field by orientation of the nanotubes.

Integrating biomolecules with CNTs for direct alignment during macroscopic assembly is becoming more attractive due to increased recognition of the benefits of incorporating nature's toolbox with nanomaterials. Making use of the desirable features of biological systems, such as the abilities of precise self-assembly and molecular recognition, is a feasible route to achieve broadly aligned nanomaterials with highly improved properties and biocompatible capability. A possible approach to obtain a uniform macroscopically aligned film from lyotropic nematic suspension of SWNT stabilized by denatured DNA was reported by mechanical shearing.[192] It was important to note that alignment in their study is achieved when only started with a nematic LC material not isotropic suspension, which further proved that alignment is also due to the intrinsic properties of the liquid crystal and not only to the flow. However, the alignment of nanotubes in the films was weaker than the above discussed systems by stabilizing the MWNT and SWNT with oxidative acid treatment. This result was attributed to the following reasons like polydispersity and waviness of nanotubes materials, residual catalysts impurities and poor dispersion of tubes. One should keep in mind that stabilizing pristine nanotubes with denatured DNA could promise retaining the unique properties of nanotubes without damage. It is also possible that, due to the viscous properties of DNA, the presence of it in the final film product especially when DNA coated on the film surface, hindered direct and clear observation of nanotubes alignment in the system, while it is more straightforward to observe the alignment in acid treated tubes dispersed only in water.

Besides macroscopic assembly of films from LC phase of CNTs dispersions, large scale biomimetic SWNT coatings from DNA and lysozyme (LSZ) stabilized isotropic dispersions were fabricated by layer-by-layer by assembly with electrostatic interaction between layers.[1] The resulting coatings of 68 layers with 205 nm thickness, showed relatively strong mechanical properties of high hardness of 1 GPa and Young's modulus of 22 GPa, while retaining significant antibacterial activity of LSZ. Uniform orientation of SWNT within each layer was achieved by applying directed air stream between each deposition step.

### 2.9.2. Fiber Spinning

Fiber spinning is also one of the viable routes of fluid processing to produce scalable and industrial quantities of CNTs fibers. Fiber spinning methods include melt spinning and solution spinning. Melt spinning is not an option due to the nature of CNTs; they decompose prior to melting around 750 $^{o}$C in air and 2000 $^{o}$C in an inert atmosphere. Furthermore, the melting and decomposition temperature of biopolymers are relatively low. For example, DNA denatures in boiling solvents and undergoes a significant decomposition at 175 $^{o}$C and followed by a more dramatic change starting at 205 $^{o}$C under nitrogen. The maximum decomposition rate occurs at 220 $^{o}$C, and above 205 $^{o}$C DNA pyrolysis occurs.[194] Thus, solution spinning is the most feasible approach. However, the combination of various steps involved in solution spinning such as solvent removal, shaping, and the handling of the resulting fiber makes solution spinning a very complex process.[195] Generally, there are two types of solution spinning: dry-spinning and wet-spinning. Both methods involve pressure-driven extrusion of macromolecular dispersions through small orifices into a coagulation region. In the absence of drawing, the cross section of the fiber is on the order of orifice diameter. However, the exact dimensions depend on the particular solidifying conditions of the extruding fiber. During dry-spinning, the dispersion, typically called a dope, is extruded into a heated chamber, and the coagulation of the fiber occurs by solvent evaporation. For wet-spinning, the dispersion is extruded into a coagulation bath. Fiber formation is achieved by the solvent leaving the fiber by diffusing into the bath. The ultimate fiber properties of these methods are affected by many factors, including properties of initial dispersion, extrusion speeds, and post treatments such as drawing. For wet-spinning, additional parameters include the diffusion mechanism of solvent, the temperature and flow behavior of the bath, and potential chemical reactions between the solvent and the bath.

Vigolo and Poulin et al.[14] demonstrated the first SWNT fiber spinning process by introducing flow-induced alignment. Isotropic surfactant stabilized SWNT dispersions were injected into the co-flowing steam of a polymer solution with certain contents of polyvinyl alcohol (PVA). PVA provides a strong bridging attraction between the nanotube bundles. The resulting fibers did not show a good alignment, and the mechanical and electrical properties of the fibers were not very promising with Young’s modulus in the range of 10-20 GPa, which is far weaker than the modulus of individual nanotubes,[196] and a high resistivity of about 0.1 Ω·cm.

However, this spinning process provided a simple and feasible approach to scaled-up production. It is noteworthy to mention the systematic fiber spinning processes developed at Rice University which successfully produced well-aligned continuous macroscopic fibers composed solely of SWNT which are originally dispersed in superacids. Several spinning techniques including wet-jet wet spinning, dry-jet wet spinning, and coagulant co-flow extrusion provided a feasible approach to industrial scale-up process of fiber spinning with large-scale alignment of nanotubes.[10,20,197] The neat SWNT fibers produced via solution spinning of the original dispersion of high ordered superacids/SWNT with 8 wt% SWNT, showed much improved properties than those of SWNT fibers involving polymers (PVA) mentioned previously. The Young's modulus of neat SWNT fibers was 120 ± 10 GPa and the tensile strength obtained was 116 ± 10 MPa. In addition, electrical resistivity of 0.2 mΩ·cm and thermal conductivity of 21 W/K·m were obtained for neat SWNT fibers.[10]

Poulin's group also demonstrated fiber spinning from denatured DNA-stabilized dispersions, and achieved stronger mechanical properties compared to their previously characterized fibers from nanotubes dispersed in conventional surfactants, such as sodium dodecyl sulfate (SDS).[198] SDS is an anionic surfactant, and stabilize the nanotubes through electrostatic repulsion which overcome the van der Waals interactions. Due to the presence of non-conducting DNA chains forming uniform coating by wrapping around the CNTs, the electrical properties of fibers were lowered. Although DNA molecules have a negatively charged phosphate backbone, the intrinsic conductive property of DNA is still an unsolved problem with its conductivity being influenced by many factors, such as DNA sequence, molecular length, interaction between molecules, microstructure and the environment of DNA, to name a few.[199] However, with thermal annealing to remove impurities in DNA fibers, the conductivity was considerably increased while compromising the mechanical properties due to partial removal of DNA and the coagulant, which was PVA in this case. As an alternative, annealing the CNTs before fiber production led to smaller improvements in conductivity without damaging the mechanical properties. In general, doubling of Young's modulus and tensile strength was obtained with respect to the reference SDS fibers. Although stretching, or drawing, is considered to be one possible approach to achieve better alignment of nanotubes in the tube, both the electrical and mechanical properties of DNA fibers in this study did not show any improvement in these properties upon stretching. These behaviors were not well understood yet, but they indicate the specific influence of DNA.

# Chapter 3

# Experimental Details

## 3.1. Materials

The representative properties of different sources of single-walled carbon nanotubes (SWNT) used in this research are shown in Table 3.1. Two batches of SWNT were used for characterizing the phase behavior, films, and preliminary investigations on fiber spinning. High-Pressure carbon monoxide process (HiPco) SWNT (Batch 183.6) from Rice University (Houston, TX) were purified by a thermal oxidation-acid extraction cycle.[200] A TA instruments (New Castle, DE) Q500 thermo gravimetric analyzer (TGA) and Zeiss EM 10C 10CR high-resolution transmission electron microscope (TEM) confirmed a purity of 98-99 %. Unidym SWNT, also produced by the HiPco process, were supplied by Unidym, Inc. (Menlo Park, CA). The batch Lot# P0900 used had 92 % purity which was confirmed by TGA. In the later part of fiber spinning, Rice HiPco SWNT of batch 187.2 were used. According to TGA, the purity of purified SWNT used in PVA coagulated LSZ/SWNT fibers was 99 %, while the raw SWNT without purification had a purity of 64.8 %. The purity of SWNT in fiber spinning from dsDNA/SWNT bulk dispersions by both dry and wet spinning methods was 99 %. The physical dimension of SWNT, length and diameter, were measured by atomic force microscopy (AFM).

Table 3.1. Representative properties of SWNT used in this research.

| Source | Batch | Purity (%) | Average Aspect Ratio $\langle L \rangle / \langle D \rangle$ | Raman D:G ratio 514 & 785 nm laser |
|---|---|---|---|---|
| Rice | 183.6 | 98-99 | ~ 550 | ~0.06 (514 nm)<br>~0.04 (785 nm) |
| Unidym | P0900 | 92 | ~ 600 | ~ |
| Rice | 187.2 | 64.8<br>99 | ~ 826 | 0.1 (514 nm)<br>0.1 (785 nm) |

Salmon testes double-stranded DNA (dsDNA) with 5.4 % sodium salt was purchased from Sigma-Aldrich, Inc. (Saint Louis, Missouri). The % G-C content for dsDNA from salmon testes was reported to be 41.2 % and the $T_m$ (melting temperature) was reported to be 87.5 °C in 0.15 M sodium chloride plus 0.015 M sodium citrate.[74] The UV-Vis absorbance profile (Ultrospec 2100Pro UV-Vis spectrophotometer) proved a pure preparation of DNA with the absorbance ratio at 260 and 280 nm wavelength $A_{260}/A_{280}$ = 1.86. The $A_{260}/A_{280}$ ratio of 1.8 - 2.0 is generally an indication of a pure DNA where the $A_{280}$ corresponds to the maximum UV light absorbance of protein.[72] Dialyzed, lyophilized LSZ from chicken egg white was purchased from Sigma-Aldrich, Inc. (Saint Louis, Missouri). Cationic surfactant (1-tetradecyl) trimethyl-ammonium bromide, 98% (TTAB) was obtained from Alfa Aesar. Sulfonated cellulose nanocrystal (CNC) suspensions were prepared at Clemson University. The representative properties of CNC were the following; average length of 107 ± 55 nm, average width of 20.5 ± 6.1 nm, and average hight of 8.9 ± 2.8 nm with a rectangular cross section.

### 3.2. Preparation of SWNT Aqueous Dispersions

All dispersions of SWNT in dsDNA were achieved by sonication assistance (Sonics VC 750, Newtown, CT) using a standard probe of 13 mm diameter with a replaceable tip (made of titanium alloy Ti-6AL-4V, # 630-0406) in de-ionized water (DI water). The probe tip of the sonicator causes a cavitation field in the liquid through rapid vibration and the subsequent collapse of violently formed microscopic bubbles releasing significant energy which affects the objects in the surrounding cavitation filed. The mechanical vibration is provided by transforming the electrical signal produced by ultrasonic generator through a convertor/transducer and is transmitted into bath or down horn. The strong shear force produced from the cavitation process can exfoliate the SWNT bundles during sonication, and may also cause damage or cutting of the tubes due to the fluid friction at the surface of nanotubes.[201,202] The radial elongation flow resulting from the collapsing of a cavitation bubble can produce theoretically predicted strain rates $d\epsilon/dt$ of up to $10^9$ $s^{-1}$ causing a large relative velocity between nanotubes and liquid. Furthermore, the resulting friction force is scaled approximately as $\mu\ d\epsilon/dt\ L$ where $\mu$ is fluid viscosity and $L$ is the length of the nanotubes. Nanotubes will break when this applied shear stress exceeds the tensile strength of tubes which is about 37 GPa.[201,203] It has been also reported that the dispersibility of SWNT in different organic solvents during a cavitation process is affected by the sonication time, and output power, as well as solvent qualities such as viscosity, vapor pressure, surface tension, and density.[202]

Two types of initial dsDNA/SWNT dispersions were prepared for further evaporation to get higher concentrations of SWNT. When using dsDNA as the dispersing agent for SWNT, both cholesteric and nematic phase formation is possible, but which phase forms depends on the preparation method. In a typical experiment, dsDNA was dissolved in water at 35 $^{o}$C for about

45 min by stirring with a magnetic bar. SWNT powders were mixed with aqueous the solution of dsDNA, and the mixtures were sonicated for 30 min at power level of 50 W in an ice bath to obtain a fine black dispersion. Both the low temperature used in making dsDNA solution and the ice bath applied during sonication provided a favorable condition for keeping the DNA as double stranded. The ice batch is also an effective way to prevent solvent evaporation caused by the high energy released during sonication process. The phase behavior of dispersions of 1.0 wt % dsDNA/0.1 wt % SWNT (10.0:1.0, Rice SWNT 183.6), 0.75 wt % dsDNA/0.1 wt % SWNT (7.5:1.0, Unidym SWNT) and 0.5 wt % dsDNA/0.1 wt % SWNT (5.0:1.0, Rice SWNT 183.6) were investigated using cross-polarized microscopy and rheology. Though 0.1 wt % dsDNA/ 0.1 wt % SWNT (1.0:1.0, Rice SWNT 183.6) were also prepared, obvious agglomeration was observed during slow evaporation of this dispersion. This was due to the fact that insufficient dsDNA was present to stabilize the SWNT, which resulted in aggregate formation with increasing concentration. Hence, former three sets of dispersions were used for further analysis. Based on a SWNT density of 1.45 g/cm$^3$, dsDNA density of 1.7 g/cm$^3$, and a water density of 1.0 g/cm$^3$, these ratios corresponded to 0.59 vol % dsDNA/0.07 vol % SWNT (8.5:1.0), 0.44 vol % dsDNA/0.07 vol % SWNT (6.4:1.0), and 0.29 vol % dsDNA/0.07 vol % SWNT (4.3:1.0). The conversion of weight percent to volume percent is given in the Equation 2 in Appendix 1. In addition to studying the phase behavior of the bulk dispersions, dispersions of 0.44 vol % dsDNA/0.07 vol % SWNT were centrifuged at 17,000 g for 3 hours to remove bundles and the resulting supernatants of individual SWNT[1] were evaporated. This resulted in a cholesteric phase of dsDNA/SWNT dispersion. Interestingly, repeated thermogravimetric analyses and mass balances on various concentrations of centrifuged dsDNA/SWNT samples showed that the dsDNA:SWNT volume ratio decreased from 6.4:1.0 to 4.4:1.0 (weight ratio of 5.1:1.0) in the

supernatant. Each of above dispersions were collected separately and used for slow evaporation at room temperature by rotating on an orbital shaker. Samples were collected at different time intervals and the concentrations of nanotubes were monitored by TGA for gel-like suspension obtained from Unidym SWNT dispersion and UV-Vis spectrophotometer for dilute dispersions of all kinds.

For dsDNA/SWNT fibers, both 4.4:1.0 by volume dsDNA:SWNT supernatant dispersions with ~2.0 vol % SWNT and 6.4:1.0 by volume dsDNA:SWNT bulk dispersion with ~3.4 vol % SWNT were used which were prepared by the same method given above. As for lysozyme/SWNT fiber spinning, dispersions of 0.4 wt % LSZ/0.4 wt % TTAB/0.4 wt % SWNT (non-purified Rice SWNT 187.2 with purity of ~ 64.8 % SWNT) and 0.4wt % LSZ/0.4 wt % TTAB/0.6 wt % SWNT (purified Rice SWNT 187.2 with purity of 99 %) were used. They were prepared by sonication using 3 mm diameter probe at the power level of 25 W with 0.5 s pulse on and 0.2 s pulse off setting. The time span used for sonicating LSZ/TTAB/SWNT (non-purified SWNT) is 1 hr 15 min, while for LSZ/TTAB/SWNT (purified SWNT) is 1 hr 45 min. In addition, LSZ/TTAB/SWNT dispersions were centrifuged at 1,000 g for half an hour prior to use to precipitate the big bundles of SWNT which are not well dispersed.

### 3.3. Characterization of Double-Stranded DNA

In order to determine the length and double-stranded characteristic of DNA used, three sets of DNA only solutions in DI water with initial concentration of 0.75 wt % were prepared accordingly. Those were DNA aqueous solution before sonication, after sonication, and after sonication and centrifugation, respectively, using the same experimental protocol as preparing the DNA/SWNT dispersions. DNA fragments were determined to be 750 bp and smaller in size after sonication by running DNA samples on 1 % agarose gel in 0.5x TAE buffer with Bionexus Hi-Lo DNA marker. Ethidium bromide was stained for visualization. DNA fragments were analyzed to be double stranded even after sonication/centrifugation by both UV-vis absorbance spectrophotometer and fluorometric quantification. DNA samples with starting concentrations of 7.5 μg/μL were diluted in TE to create different concentrations of solutions. After plating 100 μL of DNA samples in duplicate on a 96 well plate, 100 μL of picogreen working solution (25μL picogreen stock in 5 ml TE) was added to each well. The fluorescence of DNA assayed with picogreen reagent (Invitrogen, Cat#P11495) was measured by SPECTRAFluor Plus fluorescence spectroscopy (TECAN, Instrument serial number 94385) in relative fluorescent units (RFU). RFU was normalized by subtracting off TE only (blank) RFU from all measurements before graphing.

### 3.4. Macroscopic Assembly of Films and Fibers

Wet-jet solution spinning was used for fiber spinning from the cholesteric phase dsDNA/SWNT dispersions (~1.98 vol % of SWNT). The extrusion process was controlled by Harvard Apparatus (Holliston, MA) PHD 4400 Hpsi high force/high pressure programmable syringe pump which has average linear force of >200 lbs. A high pressure 8 mL stainless steel (#316 SS) syringe (0.11 $in^3$ cross sectional area) with a 1/16″ Swagelok$^{TM}$ fitting was secured to the syringe pump. Pressure in excess of 1500 psi can be achieved when this syringe is used in PHD 4400 Hpsi. Upchurch Scientific (Oak Harbor, WA) 1/16″ outer diameter of 2″ long pre-cut stainless steel tubing with small orifice diameters (125 μm, 180μm) were adapted to the syringe. The end of tubing was submerged ~ 1 cm below the liquid surface of coagulant bath which was positioned below the tubing. Different coagulants were used for preliminary fiber spinning including various alcohols and acetone coagulants, but fibers were only obtained in some of them such as ethanol (95 %), 2-propanol (99.8 +%), and tert-butanol. The fiber spinning process is depicted in Figure 3.1.

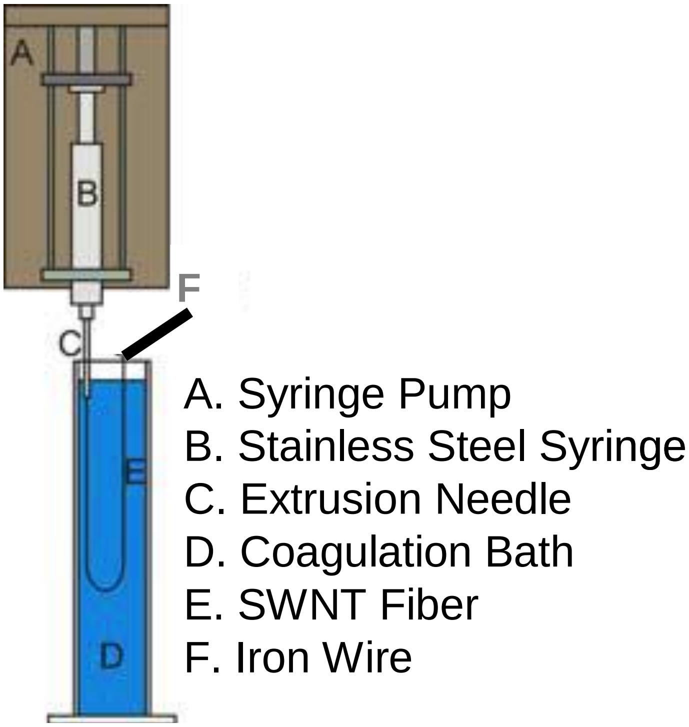

Figure 3.1. An illustration of a typical syringe extrusion process showing the fiber extrusion and collection method.

As for polyvinyl alcohol (PVA) coagulated LSZ/TTAB/SWNT fibers, the same fiber spinning setup reported in Vigolo et al.[14] was used in this research (Figure 3.2). The LSZ/TTAB/SWNT dispersions were tangentially injected into the circular trajectory of the 5 wt% PVA (MW=195,000) coagulation bath rotated at 100 rpm speed. The tip of the syringe needle (0.5 mm diameter) was submerged into the polymer solution with 1-2 cm deep and located at a distance of ~2 cm from the rotation axis of the polymer solution. The alignment of the nanotubes took place at the tip in the direction of fluid velocity due to the shear contribution of polymer flow. The PVA coated SWNT ribbon is later transferred and rinsed in DI water bath. Finally, the dry fibers were obtained by hang drying the ribbons in the room temperature.

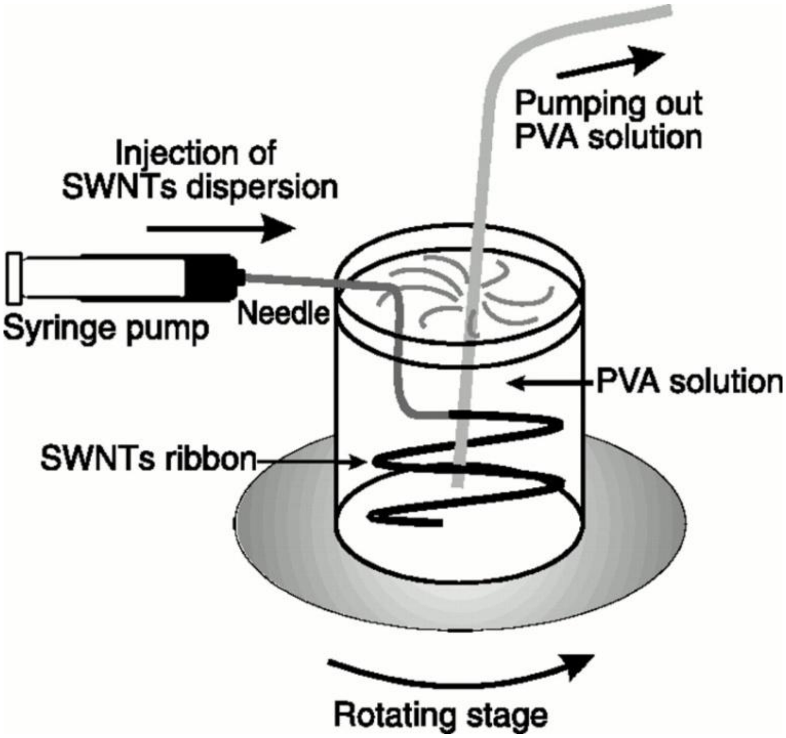

Figure 3.2. Schematic drawing of the experimental set-up used to make nanotubes ribbons. Adapted from Vigolo et al.[14]

Carbon nanotube films were also prepared from the cholesteric phase of dsDNA/SWNT dispersions (~1.98 vol % of SWNT) by simply drying droplets of samples in ambient condition or vacuum oven. Films were pretreated with linear shear or no shear, on 1 cm wide copper tape. Nice translucent films were obtained by peeling them off the copper tape substrates after drying (Chapter 5).

### 3.5. Mechanical and Electrical Testing of Fibers

Both Zwick/Roell 72.5 and Instron 5565 Calibration Lab machines were used to determine the mechanical properties of the fibers produced in this research. Fiber samples were glued into a paper testing frame with a gauge length of 26 mm as shown in Figure 3.3. The load cell used for this testing was 100 cN with a cross-head separation speed of 0.54 mm/min (2 % of initial fiber length). The load and gauge length were balanced and zeroed before each run. The raw test data collected for each sample were load force, extension, and time. The cross sectional area of fiber at break was measured by directly imaging the cross section under optical microscopy and calculating the irregular area using image analysis by drawing the contour line of the fiber cross section. The contour line of a fiber cross section is not a perfect circle, so the method of calculating the area by assuming an ordered shape of circle would cause a larger error in the mechanical properties results. The cross sectional area of fiber at each individual time was given by the following relationship $S_t = L_f \times S_f / L_t$ based on the assumption of constant fiber volume and uniform deformation; $L_i \times S_i = L_f \times S_f = L_t \times S_t$ where $L$ is the length, $S$ is the cross sectional area, $i$ is the initial value, $f$ is the final value, and $t$ is the value at a particular time.

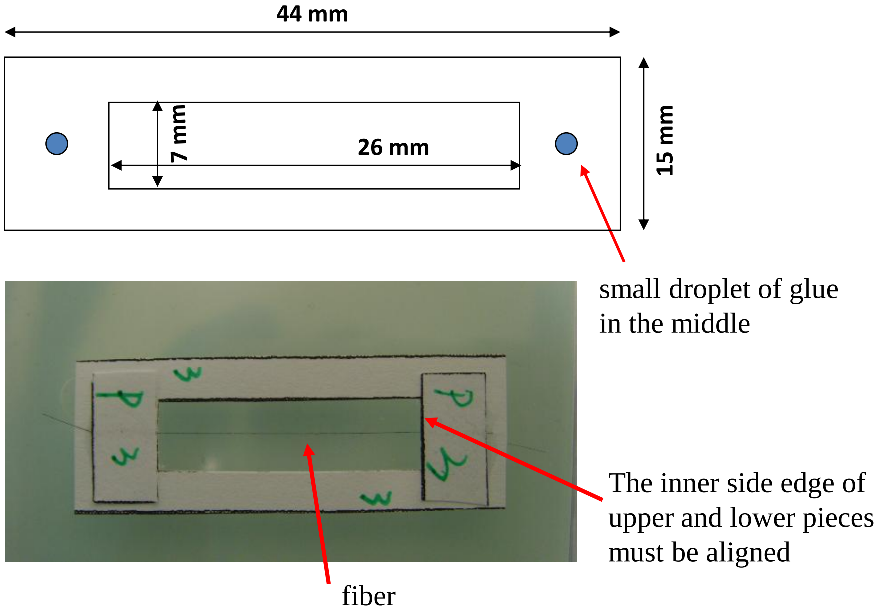

Figure 3.3. The test frame for mechanical testing of SWNT fibers. The fiber sample was secured onto the paper frame by droplets of super glue (Loctite® 431Adehesif Instantane, #234D67 or Gorilla wood glue, Cincinnati, OH).

The electrical resistance of the processed fibers was measured by the 2-wire Ohms method using an HP 34401A Multimeter (Santa Clara, CA). The fibers were placed on slides and Pelco® colloidal silver paste from Ted Pella, Inc. (United States) was used to create the lead contacts which were separated about ~ 1mm apart. The fiber cross sectional area was obtained from optical microscopy.

## 3.6. Microscopy

**Optical Microscopy.** Optical anisotropy is one of the fundamental properties of liquid crystals, as well as crystals. The propagation of a ray of light through the medium depends on its orientation.[120] Isotropic and anisotropic materials can be distinguished by polarized light microscopy as the specimen is rotated relative to the crossed polarizers. The intensity of the polarization of isotropic materials remains permanently zero, when the circular stage is rotated through 360 degrees in crossed polarizers. This is called extinction, due to the samples remaining as dark. For anisotropic materials, typical birefringence would be observed by rotating the sample between crossed polarizers with the intensity of polarization vary cyclically, from zero up to a maximum after 45 degrees and back down to zero after a 90 degree rotation. A specimen will be in extinction, when the permitted vibration directions of light passing through are parallel with those of two polarizing filters of either the polarizer of analyzer.

In this experiment, optical microscopy was performed on a Nikon (Melville, NY) Eclipse 80i optical microscope with transmitted light using precleaned glass slides and coverslips for liquid crystal samples. Polarizing microscopy was also used for examining the birefringence character of translucent films obtained from cholesteric phase of dsDNA/SWNT dispersions with transmitted light. Both reflected and transmitted light can be used for polarized microscopy, and reflected light is mostly used for the study of opaque materials, for example, metals, silicon wafers, mineral oxides and sulphides. A Linkam (Tadworth, UK) optical rheology system – CSS450 assembled with the Nikon microscope was also used for investigating the shear and temperature effects on the sample microstructure. The Linkam shear cell can perform steady shear, step rate, and oscillatory tests with shear rate and angular frequency changing in the range of 0.001 to 10 rads/sec.

**Scanning Electron Microscopy.** The surface morphology of macroscopically assembled films and fibers from cholesteric dsDNA/SWNT dispersions was monitored by JEOL 7000F FE-scanning electron microscope (SEM) (Tokyo, Japan) with energy dispersive X-ray spectroscopy (EDS) after sputter coating the films and fibers with gold.

### 3.7. Spectroscopy

**UV-visible Spectroscopy.** An Ultrospec 2100Pro UV-vis spectrophotometer was used to obtain UV-vis calibration curves for dsDNA/SWNT dispersions (Unidym SWNT) with dsDNA:SWNT ratio of 7.5:1. Samples were placed in a Starna quartz cell and pure water was taken as a background. The typical wavelength range was from 200-900 nm. The absorbance peak at 745 nm wavelength was chosen to obtain the extinction coefficient $\varepsilon$ of Unidym SWNT dispersion by checking dsDNA/SWNT with different concentrations. But for dsDNA/SWNT dispersions obtained from Rice SWNT, the $\varepsilon$ was determined by absorbance at 763 nm wavelength. According to the Beer-Lambert Law $A = \varepsilon \ell c$, the absorbance $A$ has linear relationship with the concentration $c$ (mg/L or ppm). The concentration of the substance can be deduced by measuring the absorbance with known path length $\ell$ (cm) and the molar absorptivity (extinction coefficient, L mg$^{-1}$ cm$^{-1}$).

**Raman Spectroscopy.** The spatial distribution of fibers spun from cholesteric dsDNA/SWNT dispersions was evaluated by Raman scattering studies which were carried out with Renishaw (Hoffman Estates, IL) inVia Raman microscope with a Leica 50x/0.75 NA “N-plan” objective and Prior (Rockland, MA) scanning stage. A Spectra-Physics (Irvine, CA) 263 air-cooled ion laser was used for 514 nm wavelength irradiation and a SDL (San Jose, Ca) 8530 high power laser was used for 785 nm irradiation. All measurements were taken under ambient conditions.

### 3.8. Thermogravimetric Analysis

The concentration of nanotubes in dsDNA/SWNT dispersions (Unidym SWNT) was measured by TA instruments (New Castle, DE) Q500 thermo gravimetric analyzer (TGA) for concentrated gel-like suspensions. The same TGA standard profile under nitrogen environment was used for all samples by purging the chamber with sample gas at a constant flow rate of 60 $cm^3$/min with a constant nitrogen balance protection at a flow rate of 40 $cm^3$/min. Samples underwent a 10 $^oC$ /min ramp to 120 $^oC$ and were isothermal for 15 min, then ramped again with the same speed of 10 $^oC$ /min up to 800 $^oC$ and then kept isothermal for 45 min.

### 3.9. Rheology

Rheological data was acquired in an Anton Paar (GmbH) Physica MCR 301 rheometer, which is equipped with TruGap and Toolmaster to detect and control the measuring gap in the geometry. Generally, for dsDNA/SWNT dispersions, a double gap geometry (i.d. = 24.644 mm, o.d. = 26.675 mm) was used for lower concentrations below 0.35 wt %. For the higher concentrations above 0.60 wt %, a parallel plate fixture (25 mm diameter) was used. For lyotropic cellulose nanocrystals (CNC) suspensions, Mooney-Ewart (o.d.= 22.192 mm) or double gap geometries were used for the low viscosity samples; 25 mm parallel plates and cone and plate ($2^o$ nominal angle) geometries were used for the high viscosity samples. The temperature of the samples was controlled by Peltier temperature control device and Peltier upper oven[204] counter-cooled at 20 $^oC$ of circulating water bath. Samples were loaded when the fixtures were at 10 $^oC$ if not indicated otherwise. Care was taken during each measurement to ensure that the torques, deformations and speeds recorded were well within the capabilities of the instrument as quoted by the manufacturer. Some of the fundamental rheological parameters can be defined by a Two-Plate-Model as shown in Figure 3.4. The shear force $F$ is applied to the upper plate with the shear area $A$ and lead to the resulting movement with velocity $v$ and a deflection of $s$. The lower plate is stationary ($v = 0$). The distance between the plates is $h$. For simple shear, motion is along one coordinate direction ($x_1$) with velocity varying in a second coordinate ($x_2$) orthogonal to the shear geometry resulting in a laminar flow in the form of layers.[205] The shear stress, shear rate and shear viscosity at steady state are calculated as:

$$\tau = F / A \tag{3.1}$$

$$\dot{\gamma} = \frac{\partial v_1}{\partial x_2} \tag{3.2}$$

$$\eta\,(\dot{\gamma}) = \frac{\tau\,(\dot{\gamma})}{\dot{\gamma}} \tag{3.3}$$

where,

$\tau =$ Shear stress (Pa)

$\dot{\gamma} =$ Shear rate (1/s)

$\eta =$ Steady shear viscosity (Pa s)

and the magnitude of the shear rate equals to $\dot{\gamma} = \frac{v}{h}$.

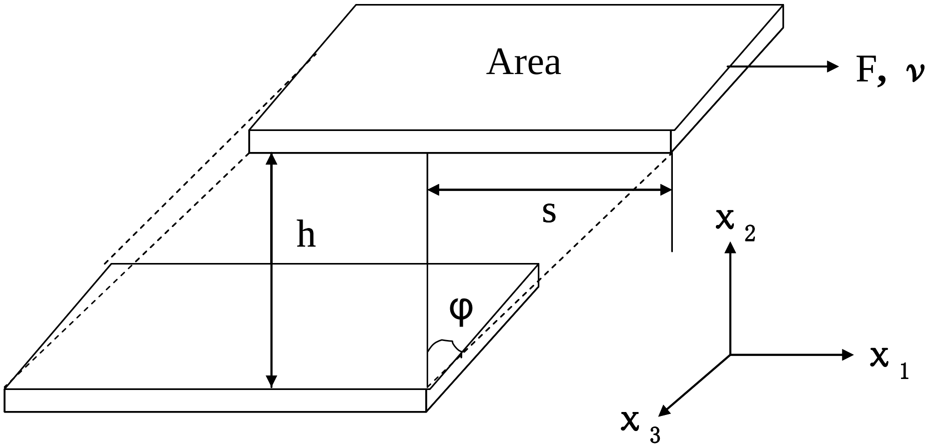

Figure 3.4. The Two-Plate-Model for simple shear test with relative coordinate system.

For oscillatory tests, the upper plate is moved back and force by the shear force ±F and the deformation is $\pm\gamma = \pm s/h = \pm\tan\varphi$ where $\gamma$ is shear strain (%) and $\varphi$ is deflection angle. Other important parameters obtained from oscillatory test are storage modulus G’ and loss modulus G”. The G’ value is a portion of the shear energy applied on a sample stored as the deformation energy representing the elastic behavior of a sample. While the G” value is a portion of energy lost to the sample as shear heat representing the viscous behavior of a sample. The notations of G’ and G” are given below:

$$G' = (\frac{\tau}{\gamma})\cos(\delta) \tag{3.4}$$

$$G'' = (\frac{\tau}{\gamma})\sin(\delta) \tag{3.5}$$

where, $\delta$ is the phase angle.

Moreover, the overall resistance to deformation of a material during the shear process is measured by complex modulus $G^*$ and the overall resistance to flow under oscillatory shear is measured by complex viscosity $\eta^*$. The magnitudes of above parameters are defined by following equations:

$$\left|G^*\right| = \left|\frac{\tau(t)}{\gamma(t)}\right| = \sqrt{(G')^2 + (G'')^2} \tag{3.6}$$

$$\left|\eta^*\right| = \left|\frac{\tau(t)}{\dot{\gamma}(t)}\right| = \left[\left(\frac{G'}{\omega}\right)^2 + \left(\frac{G''}{\omega}\right)^2\right]^{1/2} \tag{3.7}$$

where, $\omega$ is angular frequency (1/s).

When shearing a viscoelastic material between two parallel surfaces not only viscous shear stress $T_{12}$ is applied on the fluid, but also normal stress differences $N_1$ and $N_2$ are present. The tensor $T_{\mathrm{ii}}$ is defined as the sum of pressure and the extra stress as shown by Equation 3.8.

$$T_{ii} = -P + \tau_{ii} \tag{3.8}$$

since most liquids are considered incompressible, the pressure term is eliminated in the following expressions for the first and second normal stress differences $N_1$ and $N_2$;

$$N_1 = T_{11} - T_{22} = \tau_{11} - \tau_{22} \tag{3.9}$$

$$N_2 = T_{22} - T_{33} = \tau_{22} - \tau_{33} \tag{3.10}$$

typically, at a negative $N_1$, the liquid tends to force the plates together and at the positive $N_1$ the liquid pushes up on the plates. Also, $N_1$ is always positive in sign for isotropic materials and $N_2$ is usually found to be negative and smaller than $N_1$ in magnitude. Moreover, $N_2$ tends to bulge the fluid at the edge of the plates.[206,207]

## Chapter 4

## Rheology and Phase Behavior of Aqueous dsDNA/SWNT dispersions

This chapter describes the primary focus of this research and summarizes the results of extensive investigation into the phase behavior and rheology of aqueous dsDNA/SWNT dispersions in a broad SWNT concentration range from isotropic to biphasic to fully liquid crystalline phases. In addition, basic characterizations of materials used are also included such as UV-vis absorbance of SWNT in aqueous dispersions and double-stranded nature of DNA.

### 4.1. Determining SWNT Concentration

The equation for the conversion of SWNT concentration measured in units of milligram per liter or weight percent to volume percent is provided in Appendix-A. The concentration of SWNT (in mg/L) in dilute dispersions was determined by UV-vis spectrophotometer. In this experiment, for dilute dsDNA/SWNT (Unidym SWNT and Rice SWNT 187.2) dispersions without centrifugation, UV-vis absorbance at 745 nm wavelength with extinction coefficient ( $\varepsilon$ ) of 0.0257 L/(mg·cm) was determined. But for the dsDNA/SWNT dispersion obtained from Rice SWNT 183.6, $\varepsilon$ 0.0247L/(mg·cm) at 763 nm wavelength was used due to the occurrence of Van Hove singularity peak at this particular wavelength (Figure 4.1). However, $\varepsilon$ of the supernatant differed dramatically from that of the bulk (non-centrifuged) dispersions due to the elimination of SWNT bundles.

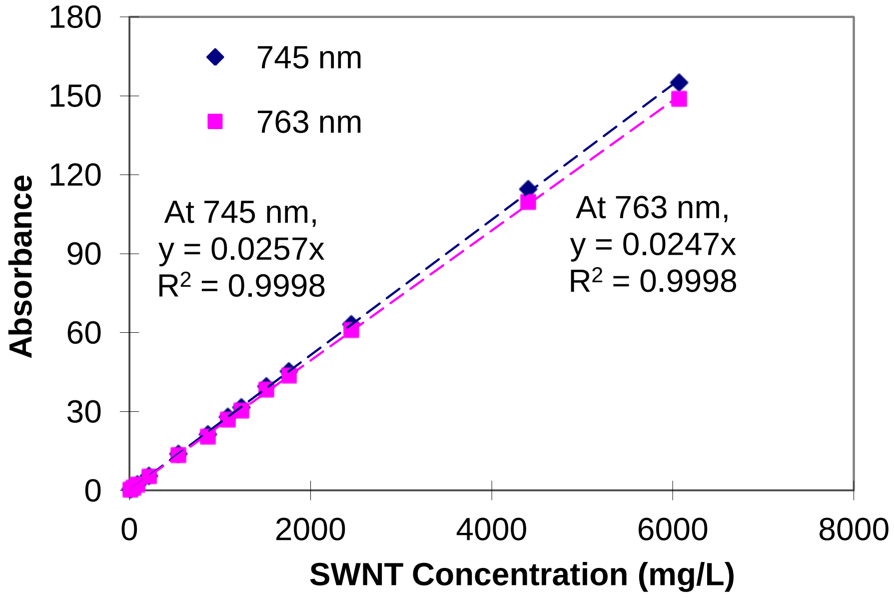

Figure 4.1. UV-vis calibration curves for dsDNA/SWNT dispersions with dsDNA:SWNT weight ratio of 7.5:1 without centrifugation using Unidym SWNT.

The extinction coefficient was also found to be dependent on the volume of sample sonicated. Figure 4.2 illustrates the calibration curves obtained from supernatant of dsDNA/SWNT dispersions prepared from different initial volumes. These results highlight the importance of verifying extinction coefficients, particularly if the results are to be extrapolated to samples that were concentrated by orders of magnitude. The concentration of SWNT in supernatant was determined by a mass balance assuming dsDNA:SWNT ratio in the sediment after centrifugation is the same as in initial dispersion which is 7.5:1. Figure 4.3 shows the full UV-vis spectra of supernatant dispersions with increasing SWNT concentrations. The van Hove singularity peaks obtained between 500 to 800 nm of wavelength indicate that SWNT were dispersed predominantly as individuals.[1]

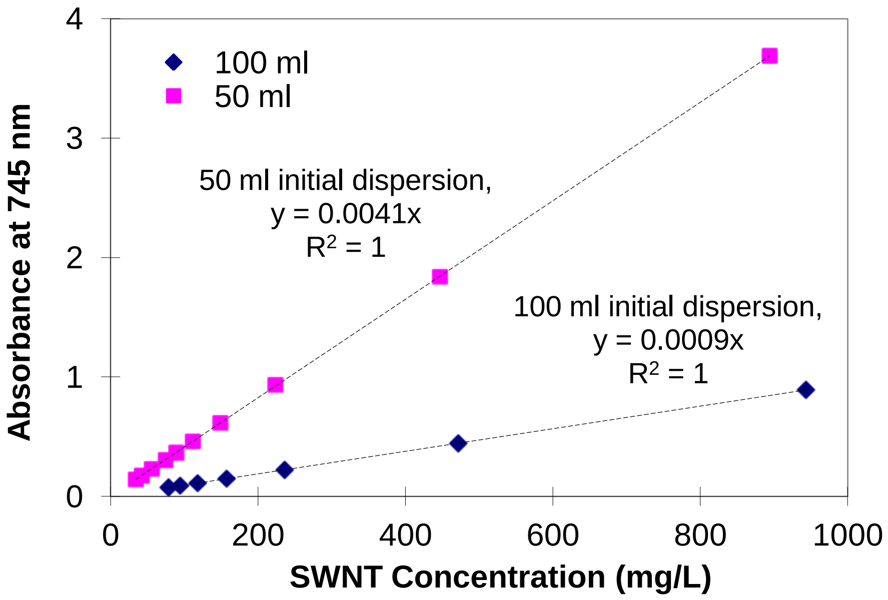

Figure 4.2. UV-vis calibration curves for supernatant dsDNA/SWNT dispersions with different initial volumes preparation using Unidym SWNT. The concentration of SWNT in supernatant was calculated by mass balance assuming the dsDNA:SWNT ratio in sediment is 7.5:1.

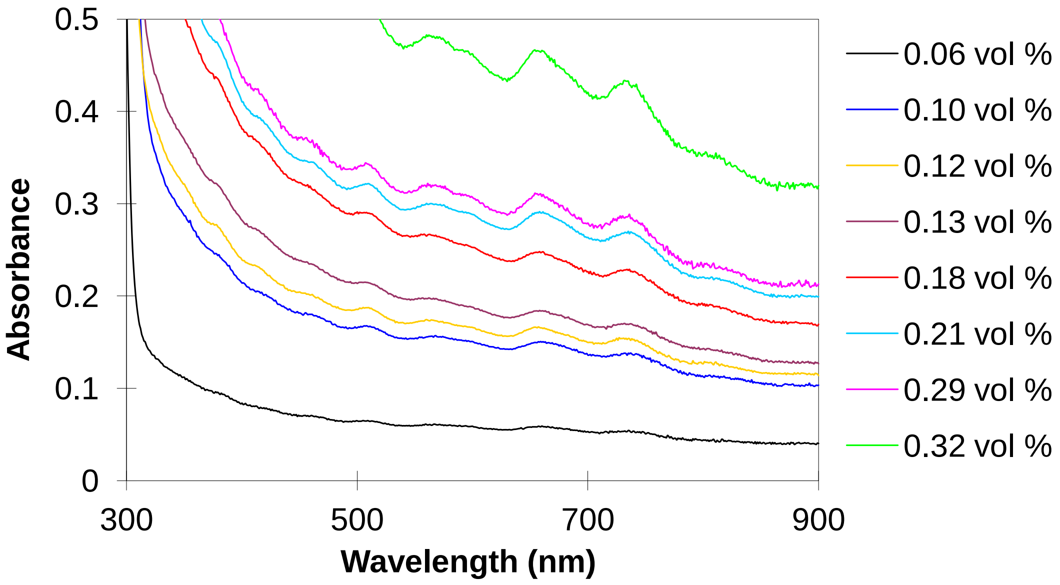

Figure 4.3. UV-vis spectra for supernatant of dsDNA/SWNT dispersions with dsDNA:SWNT weight ratio of 5.1:1.0 at different SWNT concentrations using Unidym SWNT.

The concentration of SWNT (in wt %) in evaporated samples of dsDNA/SWNT dispersions with relatively high concentration was determined by TGA analysis. In order to quantify the SWNT concentration with low error, the TGA of dsDNA raw material without dissolving in water was also measured (Figure 4.4). The weigh loss of dsDNA at 124.3 $^{o}$C was ~22.6 % and at 206.0 $^{o}$C was ~24.3 %, respectively, under the standard profile described in section 3.8. Previous researchers[194] showed that the relative weight losses of their dsDNA sample under nitrogen from salmon sperm at 124.2 $^{o}$C was -8.0 % and at 206.8 $^{o}$C it was -10.6 %. It was shown that dsDNA undergoes a significant decomposition at 175 $^{o}$C and followed by a more dramatic change starting at 205 $^{o}$C. The maximum decomposition rate occurs at 220 $^{o}$C and above 205 $^{o}$C the DNA pyrolysis occurs.[194] In this research, the initial weight loss at 124.3 $^{o}$C was -22.6 % which is much higher than -10.6 %; this might be due to the dsDNA sample having more water absorption. Also, the sample was held isothermal at 120 $^{o}$C for 15 min at which point all the water would be vaporized. However, from 124-206 $^{o}$C the weight loss percentages have small differences both are around ~2 %. All the comparison data are summarized in Table 4.1.

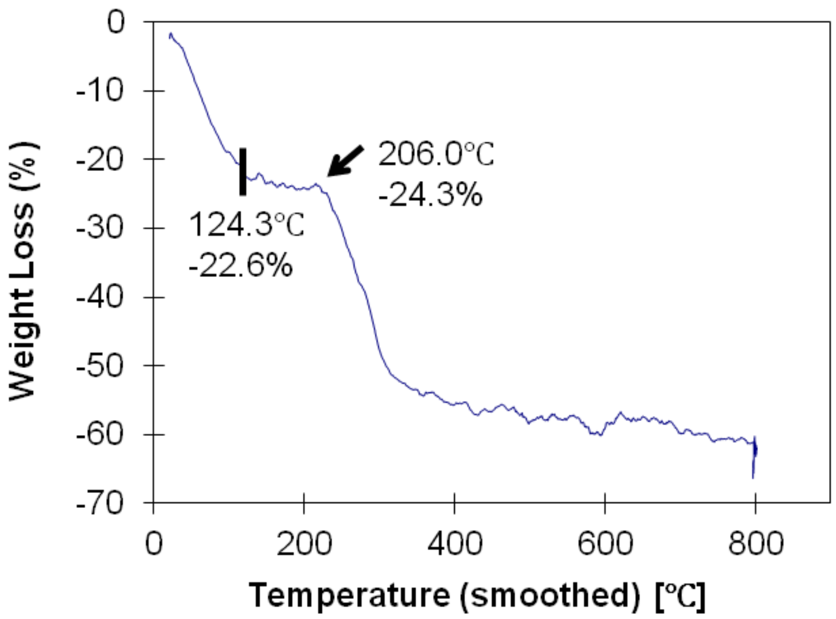

Figure 4.4. Thermogravimetric analysis (TGA ) of dsDNA.

Table 4.1. Comparison of TGA data of dsDNA.

| Samples | [a]dsDNA | [b]dsDNA |
|---|---|---|
| Weight loss at 124 °C (%) | -22.6 | -8.0 |
| Weight loss at 206 °C (%) | -24.3 | -10.6 |
| Ash at 600 °C (%) | 41.2 | 48 |
| Ash at 800 °C (%) | ~38 | ~ |

[a]dsDNA used in this experiment.

[b]dsDNA used in reference paper.[194]

As shown in Table 4.1, approximately 38 % of dsDNA ash remained at 800 °C. However, with sonication assistance during the preparation of dsDNA/SWNT dispersion, the dsDNA ash at 800 °C in the system could differ from the value of 38 % for dsDNA raw material. Therefore, mass balance of dsDNA/SWNT dispersion by tracking the masses of initial samples before centrifugation, sediment and supernatant after centrifugation, showed that the dsDNA ash at 800 °C in the supernatant of concentrated dsDNA/SWNT suspension should be lower than 38 %. In order to determine the percentage of dsDNA ash at the end of TGA, a 0.75 wt % dsDNA-0.1 wt % SWNT (Unidym SWNT) dispersion was prepared by only sonication and evaporated to obtain 7.65 wt % dsDNA-1.02 wt % SWNT suspension. The resulting concentrated suspension was analyzed by TGA under nitrogen with several runs as shown in Figure 4.5 to indicate the final weight percents remaining.

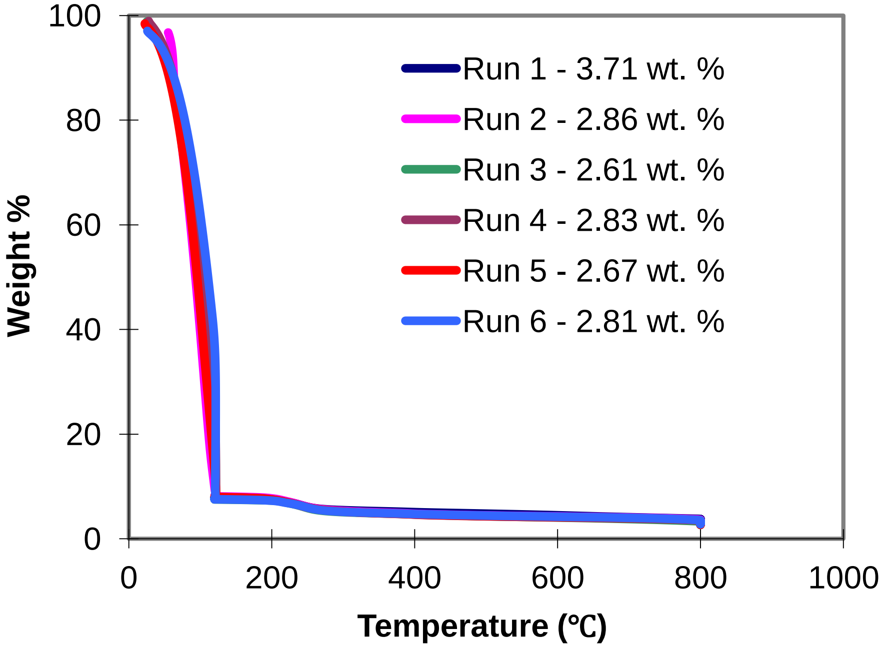

Figure 4.5. TGA profiles of 7.65 wt % dsDNA-1.02 wt % SWNT suspensions.

Therefore, three variables and three equations were used to determine the percentage of dsDNA ash at 800 $^{o}$C. At 150 $^{o}$C, the mass is sum of dsDNA and SWNT, since water is all evaporated. At 800 $^{o}$C, the mass is sum of remaining dsDNA and SWNT. SWNT mass does not change during the whole process. Again, the dsDNA:SWNT weight ratio is 7.65:1.02. Example calculation is shown below;

*dsDNA mass=x (mg), SWNT mass=y (mg), percent of dsDNA remaining=z %*

*For run 2: total sample put in=26.6549 mg; final weight % left=2.86 %;*

*at 150 $^{o}$C, sample weight %=8.01 %.*

*So,* at 150 $^{o}$C $\quad x+y=26.6549\times 8.01\,\%=2.14$

at 800 $^{o}$C $\quad (z\,\%)\times x+y=26.6549\times 2.86\,\%=0.76$

$$x=7.48\times y$$

*After calculation;* $\quad x=1.88;\ y=0.25;\ z\,\%=27.08\,\%$

All the TGA data of 7.65 wt % dsDNA-1.02 wt % SWNT dispersion were calculated with the same method and the results are shown in Table 4.2. The results for run 1 were significantly dfferent and not included. The average dsDNA ash percentage at 800 $^{o}$C calculated from run 2-6 were chosen and took the average as z %=27.0 %. Thus, SWNT concentrations of gel-like dsDNA/SWNT (Unidym SWNT) dispersions were calculated by assuming 27.0 % of dsDNA remaining at the end of TGA burning.

Table 4.2. Percentage of dsDNA ash at 800 $^{o}$C.

| 7.65 wt % dsDNA-1.02 wt % SWNT (Unidym SWNT) dispersion | | | | | | |
|---|---|---|---|---|---|---|
| Run | 1 | 2 | 3 | 4 | 5 | 6 |
| z (%) | 41.10 | 27.08 | 26.40 | 27.22 | 25.13 | 29.20 |

### 4.2. DNA Characterization

The majority of DNA/SWNT dispersion research to date has been performed using single stranded DNA (ssDNA). As for the dispersion of SWNT in ssDNA, dispersion of SWNT in dsDNA requires sonication; this results in high localized temperatures and shear. In this work, an ice bath was used to prevent significant heating of the bulk dispersion. In order to investigate whether sonication and/or subsequent centrifugation affected the dsDNA structure, dispersions of dsDNA before and after these processing steps were analyzed using fluorescence spectroscopy and gel electrophoresis. DNA has a characteristic UV absorbance peak in a band centered around 260 nm. In order to determine the length and double-stranded characteristic of DNA used, three sets of DNA solutions (in DI water) with initial concentration of 0.75 wt % were prepared accordingly: DNA aqueous solution before sonication, after sonication, and after sonication and centrifugation. The absorbance of DNA solutions at 260 nm was almost the same before and after sonication/centrifugation (Figure 4.6). Since the hyperchromicity of ssDNA results in a 40% increase in absorbance relative to dsDNA,[72] the absence of any change in the absorbance spectra supports that the solutions contained primarily dsDNA. The absorbance ratio at 260 nm and 280 nm was determined for the DNA raw material. This is a typical test for purity; the measured ratio $A_{260}/A_{280} = 1.86$ was in the range of 1.8 - 2.0 which is generally considered an indication of pure DNA.[72] The $A_{280}$ corresponds to the maximum UV light absorbance of protein.[208] However, DNA molecules were found to be cut into smaller pieces of less than 750 bp during sonication by agarose gel electrophoresis (Figure 4.7). Typically, one base pair equals to 3.4 Ås. So, the molecular length $L$ of DNA after sonication is around 2550 Å, which is 255 nanometers. The aspect ratio $L/d$ of DNA after sonication is 127.5, considering the diameter $d$ is 2 nm. Further indication that DNA molecules remained double stranded after sonication/centrifugation was given by fluorescence spectroscopy. It has been shown that picogreen reagent preferentially binds dsDNA as opposed to ssDNA.[209] If the DNA processing was creating a large amount of ssDNA, there should be a significant decrease in the picogreen relative fluorescence units (RFU) before and after the processing. However, no substantial change occurred in the picogreen RFU between the DNA samples before and after sonication/centrifugation (Figure 4.8). The Coleman group has shown that dsDNA coverage of SWNT bundles occurred over time and most of the nanotube could be covered in about 21 days after preparation of dsDNA/SWNT with sonication assistance and almost all of the nanotube walls were coated with a thin monolayer of DNA by day 35. During this progressive debundeling and coating process, SWNT binding dsDNA may denature on the nanotube surface, however, this is a relatively slow process.[107] Considering that our total evaporation process and characterization of dsDNA/SWNT dispersion were accomplished in a period of four weeks, it is reasonable to conclude that the majority of the DNA was retained as double-stranded DNA.

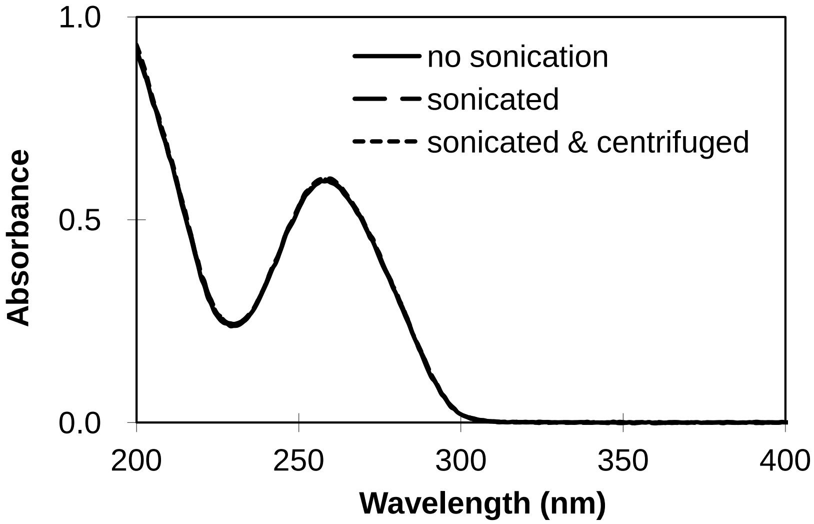

Figure 4.6. UV-Vis Absorbance spectra for DNA only solutions before and after sonication/centrifugation which were prepared from 0.75 wt % initial concentration of DNA in DI water.

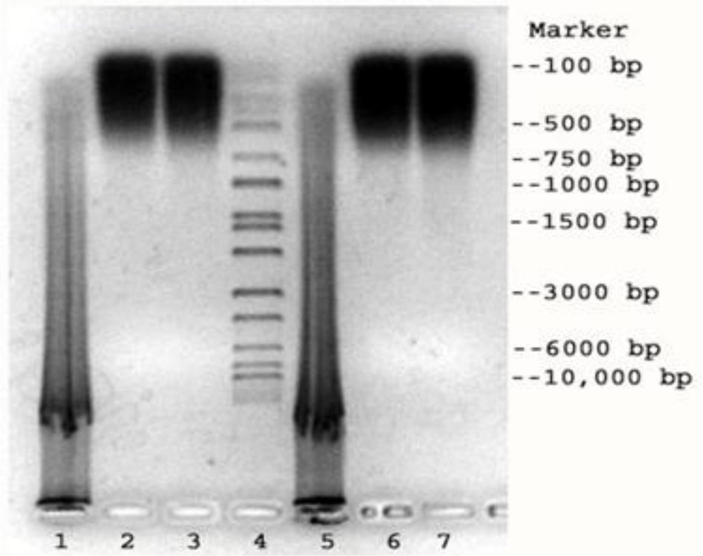

Figure 4.7. Agarose gel electrophoresis of DNA samples in DI water including (1) 7.5 μg salmon sperm genomic DNA (gDNA) before sonication, (2) after sonication, (3) after sonication/centrifugation, (4) 10 μL HiLo DNA marker (Bionexus) and (5) 15 μg salmon sperm gDNA before sonication, (6) after sonication, (7) after sonication/centrifugation.

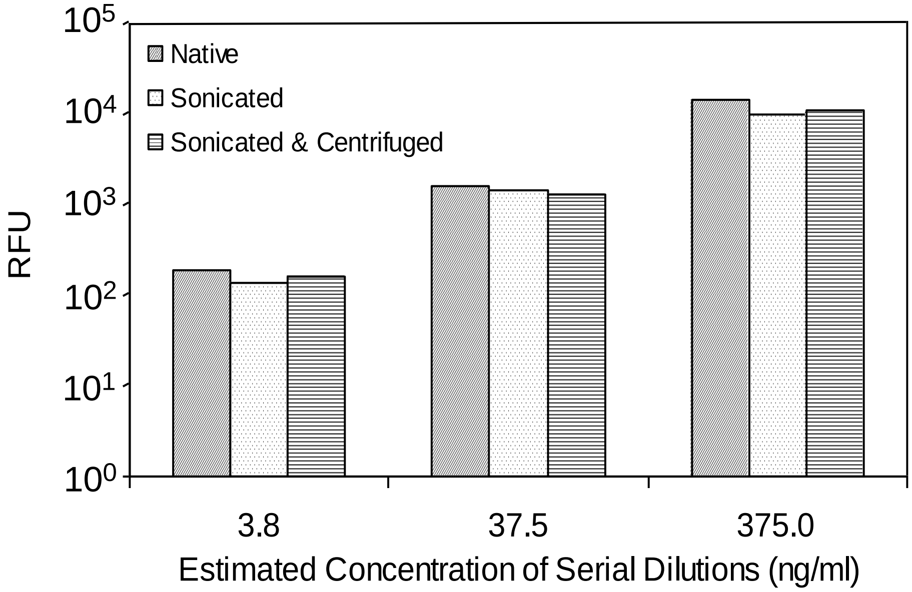

Figure 4.8. Fluorescence quantitation of comparing DNA solutions before and after sonication/centrifugation using picogreen.

### 4.3. Phase Behavior and Rheology of dsDNA/SWNT Dispersions

In this section, the phase behavior of dsDNA/SWNT dispersions produced by two different methods are compared. Evaporation of bulk dispersions, comprised of both bundled and individual SWNT, resulted in nematic phase formation while evaporation of dsDNA/SWNT supernatants resulted in cholesteric phase formation. To the author's knowledge, this is the first lyotropic cholesteric SWNT liquid crystal with interaction of a biopolymer. The origin of the cholesteric structure can be directly attributed to the majority of the dsDNA retaining its helical structure during processing. This structure can be retained or eliminated during processing into aligned films. The potential enhanced biocompatibility of dsDNA/SWNT and the previously never achieved cholesteric microstructure suggest that the range of applications that can be processed from liquid crystalline nanotube dispersions may be even broader than previously thought.

### 4.3.1. Phase Behavior of dsDNA/SWNT Dispersions

Slow evaporation of the dispersions increased the concentration of both dsDNA and SWNT. In addition, marked transitions from isotropic to concentrated anisotropic dispersions were observed. Similar to the findings of Badaire *et al.*[16] for ssDNA/SWNT, the phase behavior of the bulk (non-centrifuged) dispersions was dependent on the dsDNA/SWNT ratio; if insufficient dsDNA was present to stabilize the SWNT, increasing concentration resulted in aggregate formation. In this work, evaporation of a dispersion of 1.0:1.0 dsDNA/SWNT by weight (0.9:1.0 by volume) resulted in the formation of visible aggregates tens to hundreds of microns in diameter due to the presence of an insufficient amount of dsDNA to counteract the inherent 20 - 40 $k_B T/nm$,[45,46] van der Waals attraction between SWNT. In contrast, Badaire *et al.* (2005) observed sufficient stabilization to enable liquid crystalline phase behavior for 1:1 by weight dispersions of ssDNA/SWNT. Since impurities are known to stabilize SWNT dispersions by creating physical impediments to reagglomeration, this discrepancy is largely attributed to the present work using SWNT batches with purity ranging from 92.0 to 99.7 % while Badaire *et al.* used SWNT with 80 % purity.[16] Differences between the type of DNA, the dispersion preparation, and the SWNT size distribution and surface chemistry also likely contributed to differences in phase behavior.

Evaporation of the dispersions containing an excess of dsDNA resulted in the phase behavior typical of dispersions of rods.[47] The dispersions were isotropic at low concentration. With increasing concentration (evaporation) the systems became biphasic, a liquid crystalline phase formed in equilibrium with the isotropic phase. The fraction of birefringent liquid crystal domains increased with concentration until the systems became completely liquid crystalline at a critical volume fraction designated $\phi_{LC}$. Figure 4.9a shows that in the biphasic region, these dispersions exhibited a strand-like spaghetti structures similar to that observed for SWNT in superacids.[19] These strands are nematic liquid crystalline domains where the SWNT are free to translate along the length of the strands. In contrast to the bulk dispersions, the initial birefringent morphology for the dsDNA/SWNT supernatant was narrow moving streams of near-parallel lines indicative of the initial stage of cholesteric liquid crystal formation (Figure 4.9b).

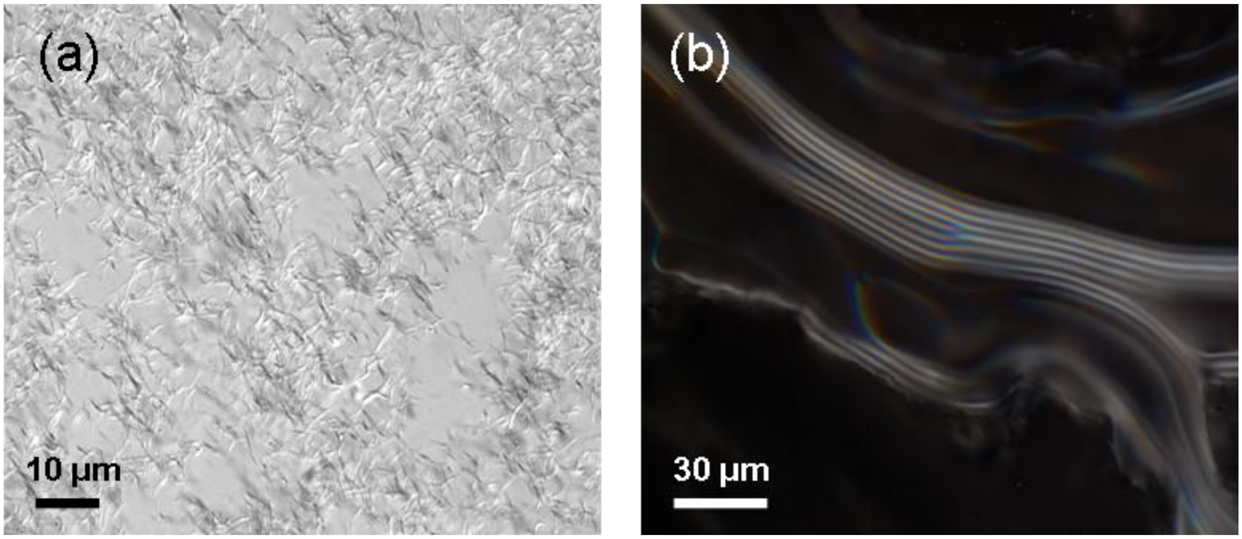

Figure 4.9. dsDNA/SWNT dispersions of (a) 13.6:1.0 by vol. dsDNA:SWNT (15.9:1.0 by weight) without centrifugation at a SWNT concentration of 0.24 vol % and (b) supernatant of 4.4:1.0 dsDNA:SWNT at a SWNT concentration of 0.69 vol % under cross-polarized light on a Nikon Eclipse 80i with Plan Apo VC 60x/1.4 NA oil immersion objective with 60x magnification while image (a) has 2.0 magnification in front of the camera. The scale bars in images are (a) 10 μm and (b) 30 μm.

As shown in Figure 4.10, the differences in morphology between the concentrated bulk dispersions and concentrated supernatants become even more dramatic at higher concentrations. The polydomain nematic structure shown in Figure 4.10a for a concentrated bulk (non-centrifuged) dispersion of 4.3:1.0 dsDNA:SWNT at a concentration of 1.7 vol % SWNT has a similar microstructure to that previously observed for liquid crystals of SWNT/102% $H_2SO_4$,[19,20] MWNTox/$H_20$,[15,190] and ssDNA/SWNT.[16] The SWNT are locally aligned within each domain but are randomly oriented on a larger length scale.

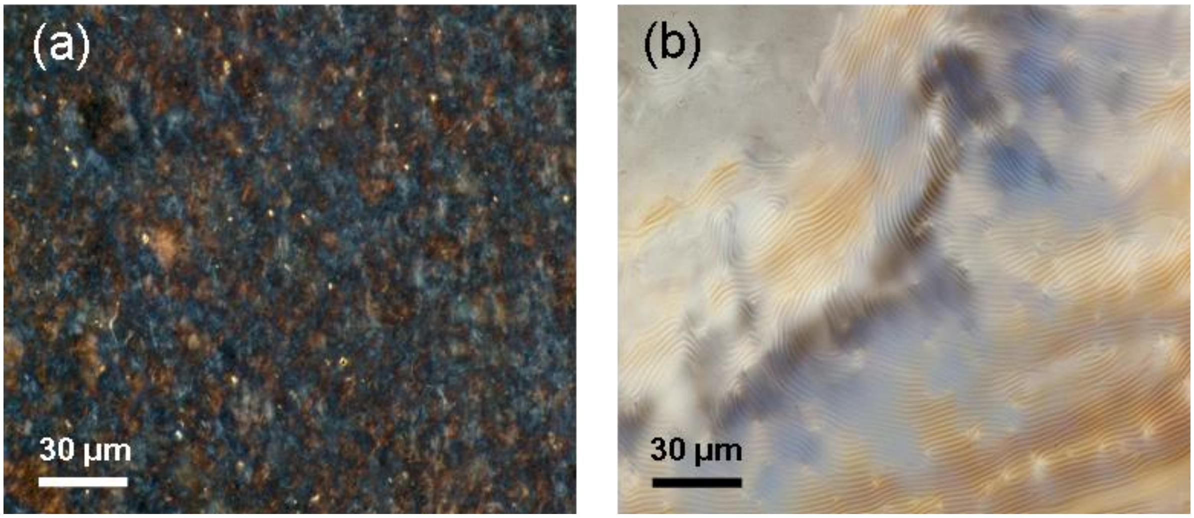

Figure 4.10. Comparison of dsDNA/SWNT dispersions of (a) non-centrifuged 4.3:1.0 by volume dsDNA:SWNT at a SWNT concentration of 1.7 vol % SWNT and (b) supernatant of 4.4:1.0 by volume dsDNA:SWNT at 2.3 vol % SWNT under cross-polarized light on a Nikon Eclipse 80i with Plan Apo VC 60x/1.4 NA oil immersion objective with 60× magnification.

The individual domains of polydomain nematic liquid crystal of bulk dsDNA.SWNT dispersion became bright and dim as the samples were rotated between cross polarizers as shown in Figure 4.11. However, these domains are randomly oriented on larger length scale (~100 μm). For these dispersions, the critical concentration $\phi_{LC}$ for the biphasic to liquid crystal transition depended on the initial dsDNA:SWNT ratio. Cross-polarized optical microscopy was initially used to approximate this transition by determining the lowest concentration at which no isotropic domains were observed. Since this method is somewhat dependent on the magnification and the concentrations tested, rheology was also used for further confirmation of liquid crystalline phase behavior and to substantiate the estimated value of $\phi_{LC}$.

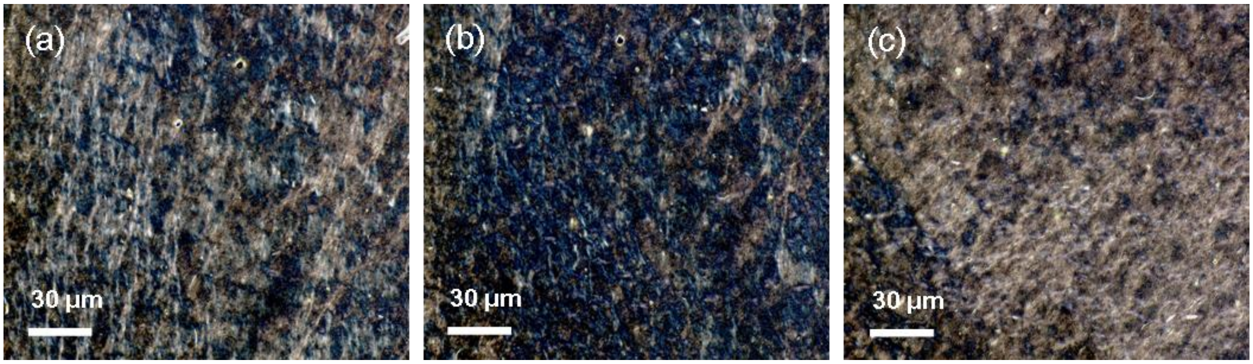

Figure 4.11. Concentrated bulk dispersion of dsDNA:SWNT = 8.5:1.0 (10.0:1.0 by weight) at 0.8 vol % SWNT under cross-polarized light using a Nikon Eclipse 80i with Plan Apo VC 60x/1.4 NA oil immersion objective with 60× magnification. The domains become bright and dark as the sample is rotated at different angles of (a) $0^o$, (b) $30^o$, (c) $90^o$, respectively. The scale bar in the figures is 30 μm.

In a normal polymer solution or colloidal dispersion, the low shear viscosity increases with concentration. However, for liquid crystalline dispersions, viscosity does not change monotonically with increasing concentration. The viscosity increases with concentration as long as the system is predominantly isotropic. However, the increasing fraction of anisotropic domains eventually results in a decreased resistance to flow. Viscosity therefore decreases with concentration until increasing rod concentration no longer results in increased order. Once the order can no longer be increased, the viscosity once again increases with concentration. Therefore, in the biphasic region, the viscosity versus concentration curve goes through a maximum and then reaches a minimum at approximately $\phi_{LC}$. Based on the minima shown in Figure 4.12, bulk dispersions evaporated from a 8.5:1 dsDNA:SWNT have $\phi_{LC}$ ~ 1.2 vol % while those from 4.3:1.0 dsDNA:SWNT have $\phi_{LC}$ ~ 1.9 vol %. This may indicate the presence of more bundles in the 4.3:1.0 dsDNA:SWNT; since a lower average aspect ratio would result in a higher value of $\phi_{LC}$.

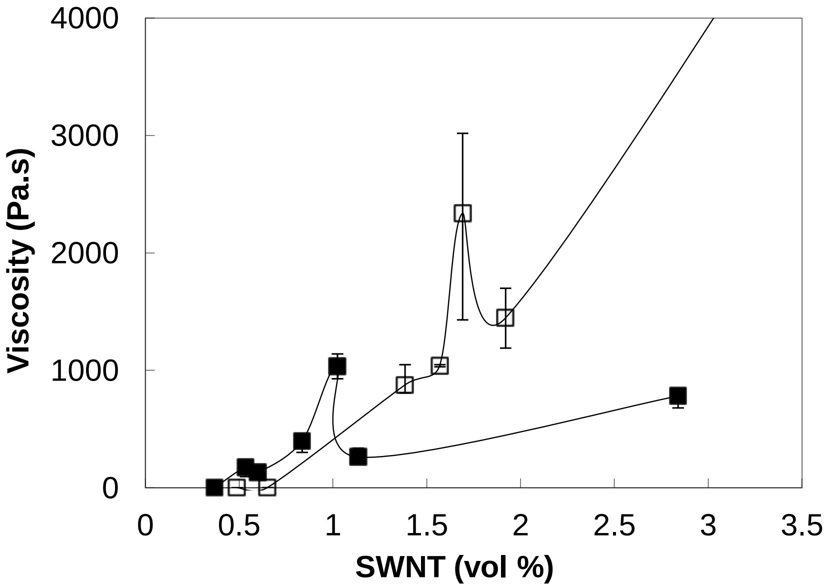

Figure 4.12. Relationship between viscosity and concentration at a shear rate of 0.1 $s^{-1}$ and a temperature of 10 $^{o}C$ for bulk (non-centrifuged) dsDNA/SWNT dispersions obtained from 8.5:1.0 (solid squares) and 4.3:1.0 (open squares) dsDNA:SWNT by volume. Error bars are given for all points, but are smaller than the data markers in many cases. The largest error bars are in the biphasic region at the peak in viscosity; this is consistent with previous research on lyotropic rod-like polymers and SWNT in superacids.

As shown in Figure 4.10b, the liquid crystal formed by concentrating the dsDNA/SWNT supernatants has a dramatically different microstructure than previously obtained lyotropic SWNT liquid crystals. The classical fingerprint texture[120] consisting of dark and light strips under cross-polarized light microscope indicate a cholesteric structure in which the molecules are respectively normal to the plane of polarizer and in the plane of the polarizer.[33,120] Since the helical cholesteric pitch is the distance when the director rotates by 2π, with the range of few-hundred Ås to micrometers, it can be determined easily by measuring the distance between either two bright or dark lines in the micrograph.[137] Figure 4.13 shows the evolution of the cholesteric microstructure and dispersion viscosity with increasing concentration. A cholesteric oily streak texture of thin near-parallel lines started to appear at 0.7 vol % of SWNT (3.6 vol % dsDNA) due to the amount of excess, or free, dsDNA which was not strongly interacting with the SWNT. Large birefringent domains could be observed at 1.5 vol % SWNT where the viscosity was at its maximum value of 2165 $\text{Pa} \cdot \text{s}$. Still further increasing the concentration, resulted in the domains of near-parallel set of swirling lines growing larger and the appearance of many compactly distributed small spherical swirling lines resembling fish-scales. Areas without obvious fingerprint textures resembled oil paint and also exhibited strong birefringence under polarized light. Further increasing concentration resulted in extending birefringent domains; iridescent colors appeared at the concentrations near the viscosity minimum at 2.2 vol % SWNT. Moreover, when the polarizer was extracted all these textures disappeared and the sample was a uniform gray. This indicated uniform dispersion throughout the sample without any noticeable aggregates or clusters. When rotating the specimens relative to the polarizers, different domains of the cholesteric phases changed colors resulting white, beige, orange, purple, light green, and blue regions (Figure 4.14). This was due to Pseudo Bragg reflections which are one of the characteristic optical properties of a cholesteric phase.[120]

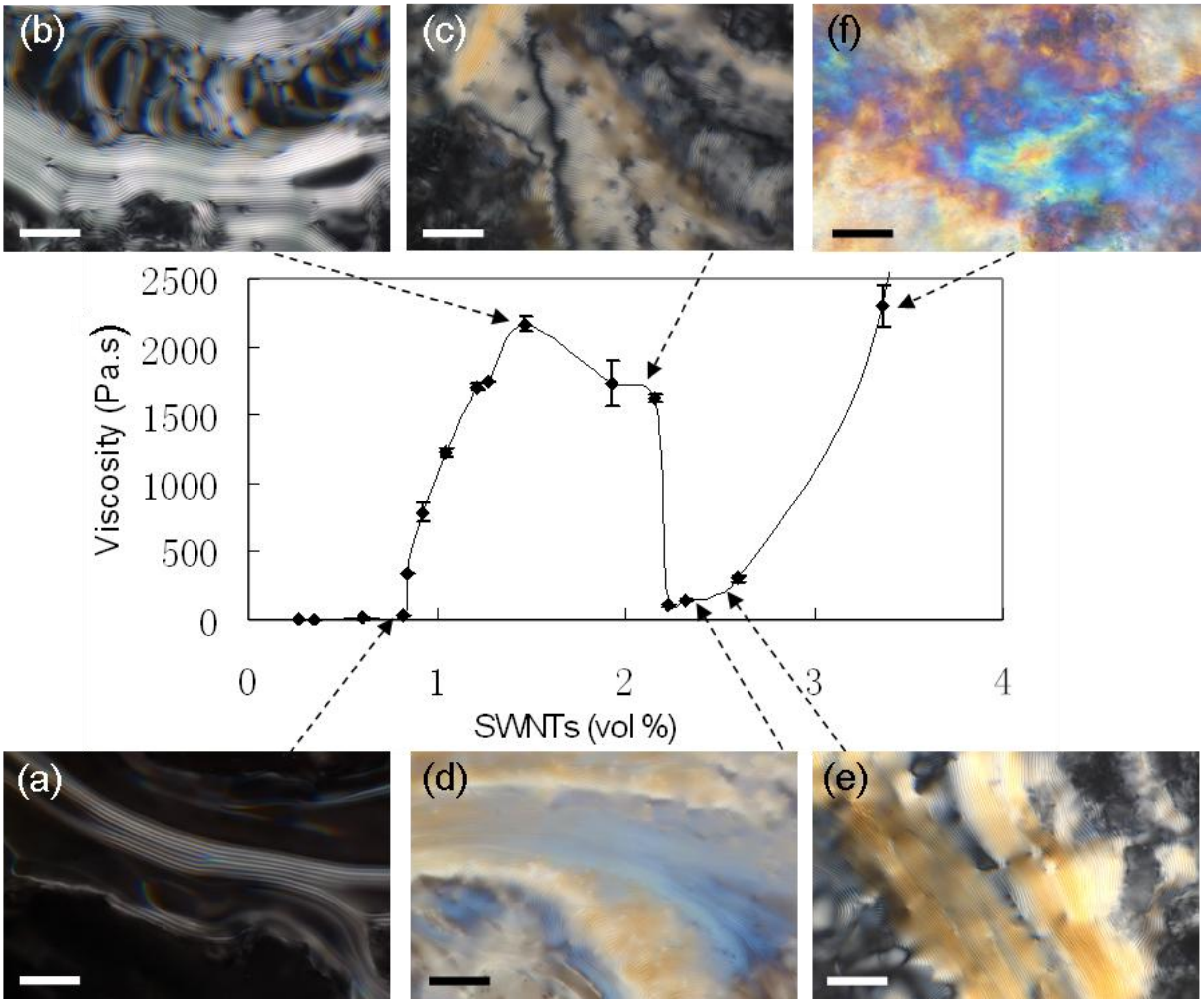

Figure 4.13. Relationship between viscosity and concentration for supernatants of 4.4:1 by volume dsDNA:SWNT at a shear rate of 0.1 $s^{-1}$ and temperature of 10 $^{o}$C. Images were taken under cross-polarized light using a Nikon Eclipse 80i with Plan Apo VC 60x/1.4 NA oil immersion objective with 60× magnification. The SWNT concentrations were (a) 0.69 vol %, (b) 1.5 vol %, (c) 2.0 vol %, (d) 2.3 vol %, (e) 2.5 vol %, and (f) 3.4 vol %. The scale bars are 30 µm.

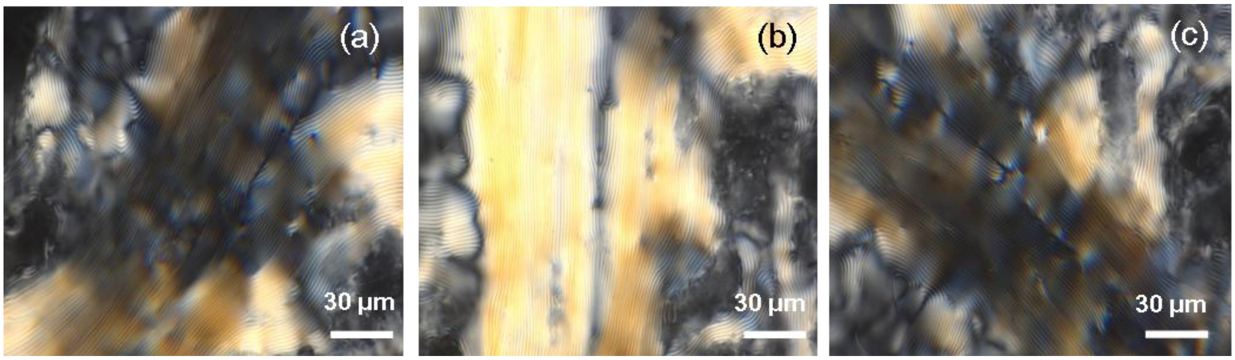

Figure 4.14. Concentrated supernatant of 4.4:1.0 by volume dsDNA:SWNT (5.1:1.0 by weight) at 2.5 vol % SWNT under cross-polarized light on a Nikon Eclipse 80i with Plan Apo VC 60x/1.4 NA oil immersion objective with 60× magnification. The domain colors vary as the sample is rotated at different angles of (a) $0^o$, (b) $40^o$, (c) $100^o$, respectively. The scale bars are 30 μm.

The color variation became more obvious with increasing concentration in response to variations in the helical pitch. The pitch of the dsDNA/SWNT dispersions decreased linearly from 3.45 ± 0.25 μm to 2.65 ± 0.15 μm when the concentration of SWNT increased from 1.2 vol % to 2.0 vol %; this is in the transition range from biphasic to single-phase liquid crystal, and indicates a more ordered alignment of molecules in the cholesteric phase with increasing concentration. With a further increase in concentration to 3.2 vol %, the pitch increased to 3.38 ± 0.53 μm. Moreover, Figure 4.15 shows the relationship between pitch and concentration of cholesteric dsDNA/SWNT dispersion which fits well into the Equation 2.6 given in the section 2.4. Due to the nonmonotonic feature, two different sets of constants $A$ and $k$ were obtained. For dsDNA/SWNT dispersions at lower SWNT concentrations, k = 0.498; A = -1.328 were obtained, while for samples with higher SWNT concentrations, k = -0.494; A = -0.657 were obtained, respectively. It is difficult to measure the cholesteric pitch at lower concentrations due to moving streams of near-parallel lines. At even higher concentrations, the fingerprint texture was absent due to the development of a more solid-like phase; this is supported by a plateau in rheological measurements of storage modulus versus frequency for these dispersions. Kornyshev and Leikin's theory for cholesteric liquid crystals of dsDNA,[141] predicts that cholesteric unwinding would occur at the cholesteric to isotropic and cholesteric to hexagonal transition due to the weakening of biaxial correlation between dsDNA molecules. Van Winkle et al.[33] observed that the cholesteric pitch of aqueous solutions of dsDNA unwinds from 2.2 μm to at least 10 μm before forming the hexagonal phase. Thus, considering the relatively small increase in dsDNA/SWNT pitch, the LC phase was still in cholesteric region at 2.9 vol % of SWNT.

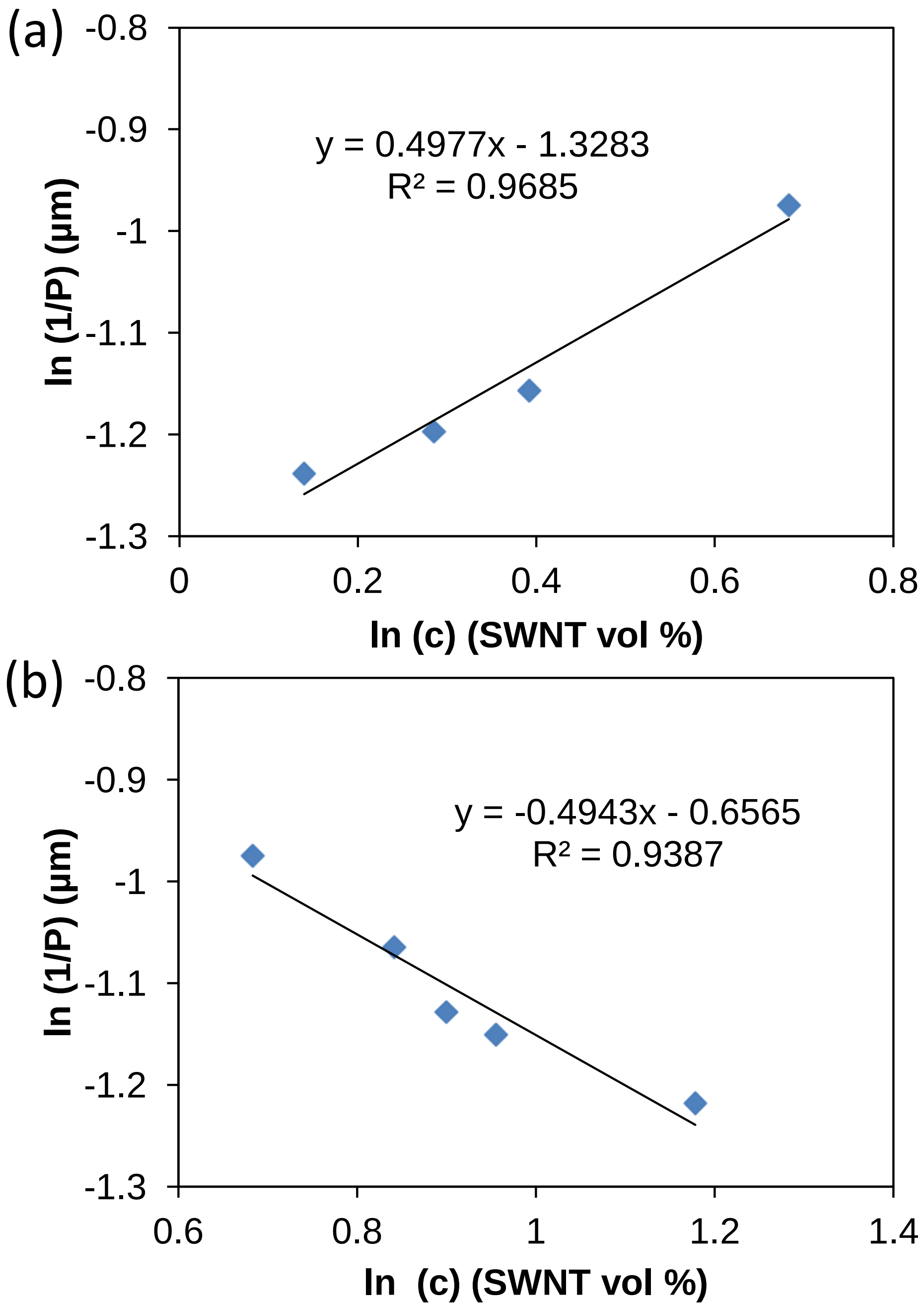

Figure 4.15. Plots of ln(1/*P*) of 4.4:1.0 by volume supernatant dsDNA/SWNT against ln(c) of SWNT concentration at (a) 1.2, 1.3, 1.5, and 2.0 vol %, and (b) 2.0, 2.3, 2.5, 2.6, and 3.2 vol %.

The surprising difference between the microstructures obtained from concentrated bulk dispersions and concentrated supernatants is related to the cholesterogenic nature of dsDNA (Figure 4.16a) and the initial dispersion state of the SWNT. Aqueous dsDNA solutions prepared by the same procedure, but without the addition of SWNT, exhibited cholesteric phase behavior. They became biphasic at 6.2 vol % and fully liquid crystalline at $\phi_{LC}$ ~ 12.6 vol %. These values are markedly higher than those obtained in the presence of SWNT; this indicates that the presence of the higher aspect ratio more rigid SWNT facilitates liquid crystalline phase formation. The pitch of the dsDNA solutions monotonically decreased from 4.35 ± 0.38 to 3.02 ± 0.20 μm while the concentration increased from 8.1 to 19.3 vol %; these values are slightly higher than those for the concentrated dsDNA/SWNT. The structure and pitch of dsDNA cholesterics are dependent on many factors such as molecular length of dsDNA fragments, interaxial spacing of molecules and the solvent condition like osmotic pressure and ionic strength. In addition, steric, van der Waals, and hydration forces may also contribute to macroscopic properties of dsDNA cholesterics.[140,141,210] In the *fd* virus cholesteric system, the authors showed the typical behavior of cholesteric pitch decreasing with increasing concentration in a power law function until saturates at a certain value in solutions with different ionic strength. Slight unwinding of the pitch occurred as the concentration further increased to approach smectic transition. Rapid unwinding of the pitch was also observed as the temperature was increased.[137] As for dsDNA, different results were provided for cholesteric pitch measurement in previous studies. On the one hand, cholesteric unwinding at the cholesteric to isotropic and cholesteric to even higher density phase-hexagonal were reported.[140,141] On the other hand, Van Winkle at al. reported that the pitch was relatively independent of the dsDNA concentration for a wide range

(150-270 mg/ml), but increased with concentration approaching the cholesteric to high-density phase transition.[139]

In the presence of SWNT, there appears to be a competition between the tendency of the dsDNA to form a cholesteric liquid crystal and the tendency of the SWNT to form a nematic liquid crystal. When the initial dispersion is a dsDNA/SWNT supernatant consisting of individual SWNT,[1] the natural tendency of dsDNA to form cholesteric phases dominates; this indicates that the majority of dsDNA retains its helicity over time. The majority of bulk dispersions exhibited the previously described polydomain nematic texture that has been characteristic of all lyotropic carbon nanotube liquid crystals to date. In the case of some bulk dsDNA/SWNT dispersions, such as the 6.4:1.0 dispersion concentrated to 1.3 vol % shown in Figure 4.16b, small fingerprint regions were observed due to the excess amount of free dsDNA. However, these small regions did not form continuous domains and were not visible at higher concentration. We believe that in the bulk dispersions, the presence of SWNT bundles physically impedes the formation of continuous cholesteric domains. In addition, Cathcart *et al.*[107] have suggested that dsDNA denatures in the process of debundling SWNT over a time period of approximately thirty days. Therefore, the presence of SWNT bundles in the bulk dispersion may serve to result in some dsDNA denaturation during the evaporation process and reduce the driving force for cholesteric phase behavior.

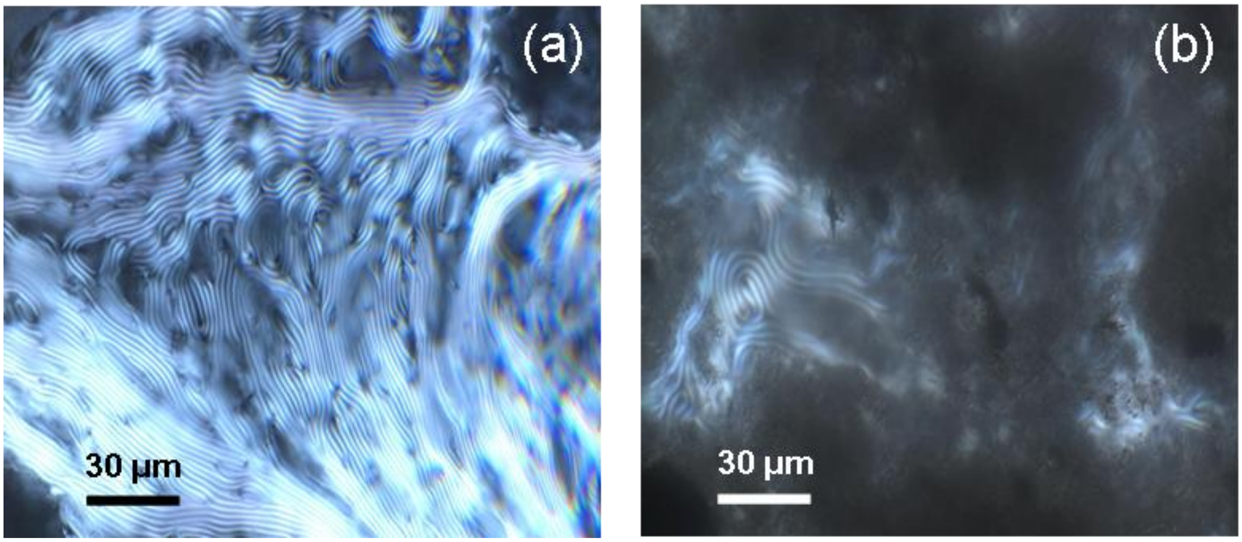

Figure 4.16. Fingerprint texture in (a) 19.3 vol % of dsDNA solution and (b) bulk 6.4:1.0 by volume dsDNA/SWNT dispersion at a SWNT concentration of 1.3 vol % under cross-polarized light on a Nikon Eclipse 80i with Plan Apo VC 60x/1.4 NA oil immersion objective with 60× magnification. The scale bars are 30 μm.

### 4.3.2. Rheology of dsDNA/SWNT Dispersions

**Steady Shear and Dynamic Viscosities.** Before running the test of flow curve for steady shear viscosity, a step rate test was performed to determine the time required to achieve steady-state flow. The duration of transient obtained from this experiment is relatively short when compared to those of characteristic liquid crystalline polymers which are usually as large as 100 shear units, or even more. The shear unit is equal to the product of multiply of shear rate and time $\dot{\gamma} t$. The start up of shear flow of both dsDNA/SWNT supernatant and bulk dispersions and dsDNA only solutions used as references were provided in the Appendix-B. The rheological behavior of dsDNA/SWNT supernatant dispersions at isotropic SWNT concentrations is shown in Figure 4.17. In the dilute regime with SWNT concentration smaller than 912 ppm, the zero-shear viscosity increases slightly as a function of concentration (Figure 4.17a). When the

SWNT concentration enters into semidilute regime around 912 ppm, the zero-shear viscosity increases rapidly as a function of concentration in a relationship of $\eta_0 \propto \phi^3$ (Figure 4.17b). This result agrees with the prediction proposed by the Doi-Edwards theory for semidilute solutions of rods.[47] Above a SWNT concentration of 4956 ppm, the zero-shear viscosity increases more significantly with concentration and deviates from the theory prediction given for semidilute rods. This can be an indication of the isotropic concentrated regime. According to steady shear viscosity obtained for higher concentration dispersions (Figure 4.19), the range of SWNT concentration where the isotropic concentrated regime exists would be starting from 4956 ppm to a concentration value much less than 8540 ppm.

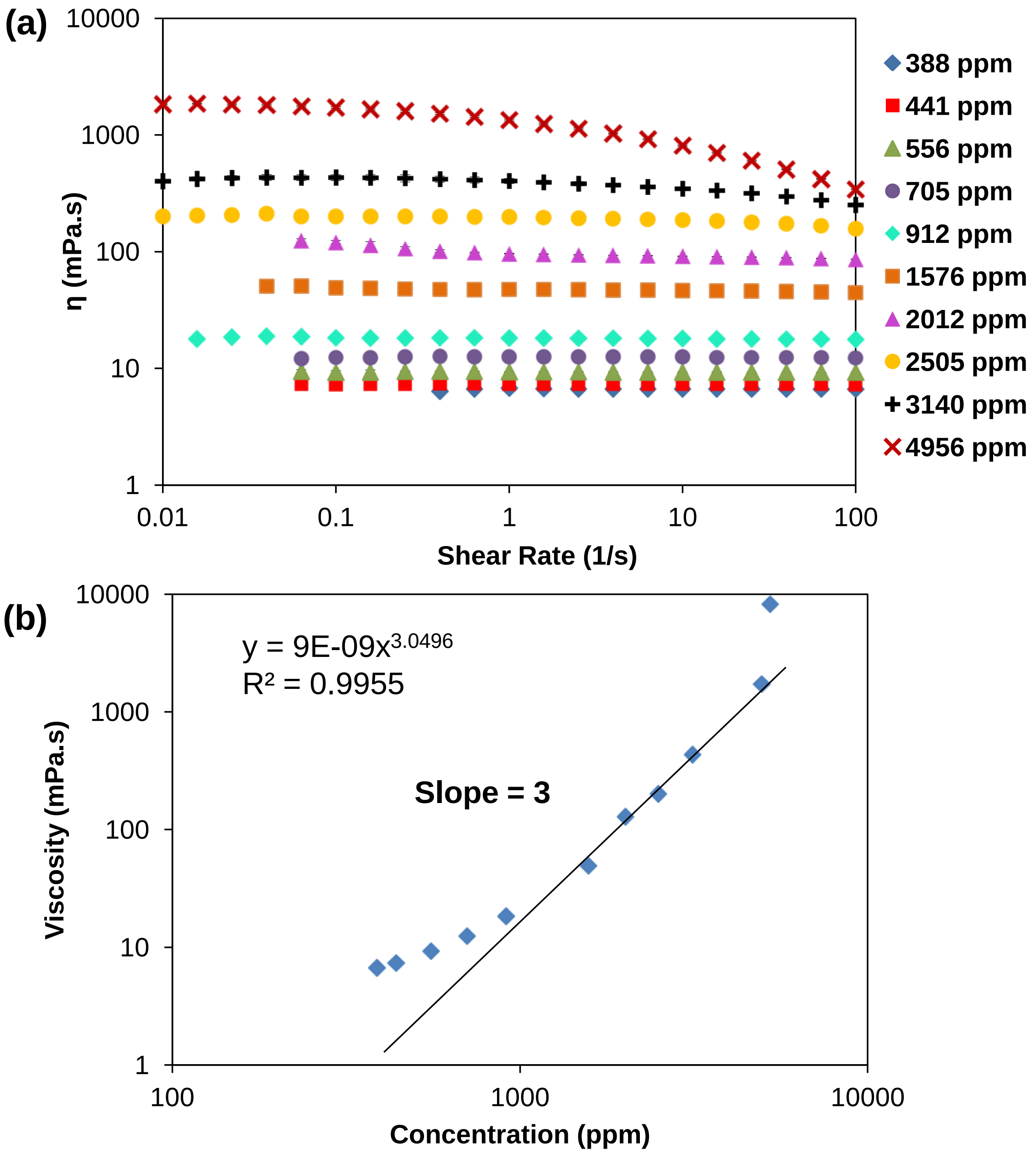

Figure 4.17. (a) Steady shear viscosity of isotropic dsDNA/SWNT (Rice 187.2)supernatant dispersions as a function of shear rate for various SWNT concentrations ranging from dilute ( ≤ 912 ppm) to semidilute (912 – 3140 ppm) to concentrated isotropic (4956 to ≪ 8540 ppm). (b) Zero-shear viscosity as a function of SWNT concentration.

In addition, the viscosities of aqueous dsDNA solutions are shown in Figure 4.18a. These concentrations correspond to those used in the dsDNA/SWNT dispersions. This data therefore provides insight into the effect of the aqueous dsDNA solvent viscosity on the dsDNA/SWNT supernatants. The viscosity of dsDNA only solvents increased slightly with increasing dsDNA concentration from 0.33 to 1.36 vol %. In addition, dsDNA only solvents in this particular concentration range behaved as Newtonian fluids in the measured shear rate range from 0.1 to 100 $s^{-1}$. Figure 4.18b shows the plots for intrinsic viscosity $[\eta] = (\eta - \eta_S)/(\eta_S \phi)$ of supernatant dsDNA/SWNT dispersions at various SWNT concentrations as a function of shear rate; $\eta$ is the viscosity of supernatant dsDNA/SWNT dispersion, $\eta_S$ is the relative dsDNA only solvent viscosity, and $\phi$ is the volume fraction of SWNT. For supernatant of dsDNA/SWNT dispersions at dilute regime from 388 to 912 ppm SWNT, the intrinsic viscosities were close to each other. However, significant decrease in intrinsic viscosity was observed at higher SWNT concentration of 1576 ppm, which again confirmed that this particular concentration was in the semidilute regime. According to Kirkwood-Auer-Batchelor (KAB) relationship for a dilute dispersion of Brownian rods, which is given in the Equation 2.14 in the section 2.8.1, the average aspect ratio $\langle L/d \rangle$ of rods in dilute dispersions can be calculated from their intrinsic viscosity. Generally, the intrinsic viscosity was determined from a master curve created by dilute dispersions at various concentrations to minimize the error. As in Figure 4.18b, although no shear thinning behavior existed in the measured shear rate range, by making an assumption that the viscosity plateau of dsDNA/SWNT dilute dispersions was reflective of KAB rod behavior, a SWNT aspect ratio $\langle L/d \rangle$ of 233 was obtained according to KAB equation. However, there is a marked discrepancy between this calculated average aspect ratio value and that measured by atomic force microscopy (AFM). The $\langle L/d \rangle$ of SWNT (Rice 187.2), which is used in this part of experiment, was determined to be 826 by AFM. The significant difference in $\langle L/d \rangle$ can be caused by the inability to access the shear thinning region at high shear rates, which made it impossible to know if samples were following KAB rod behavior. In addition, just changing a couple of tubes counted by AFM can dramatically change the average aspect ratio measured.[149]

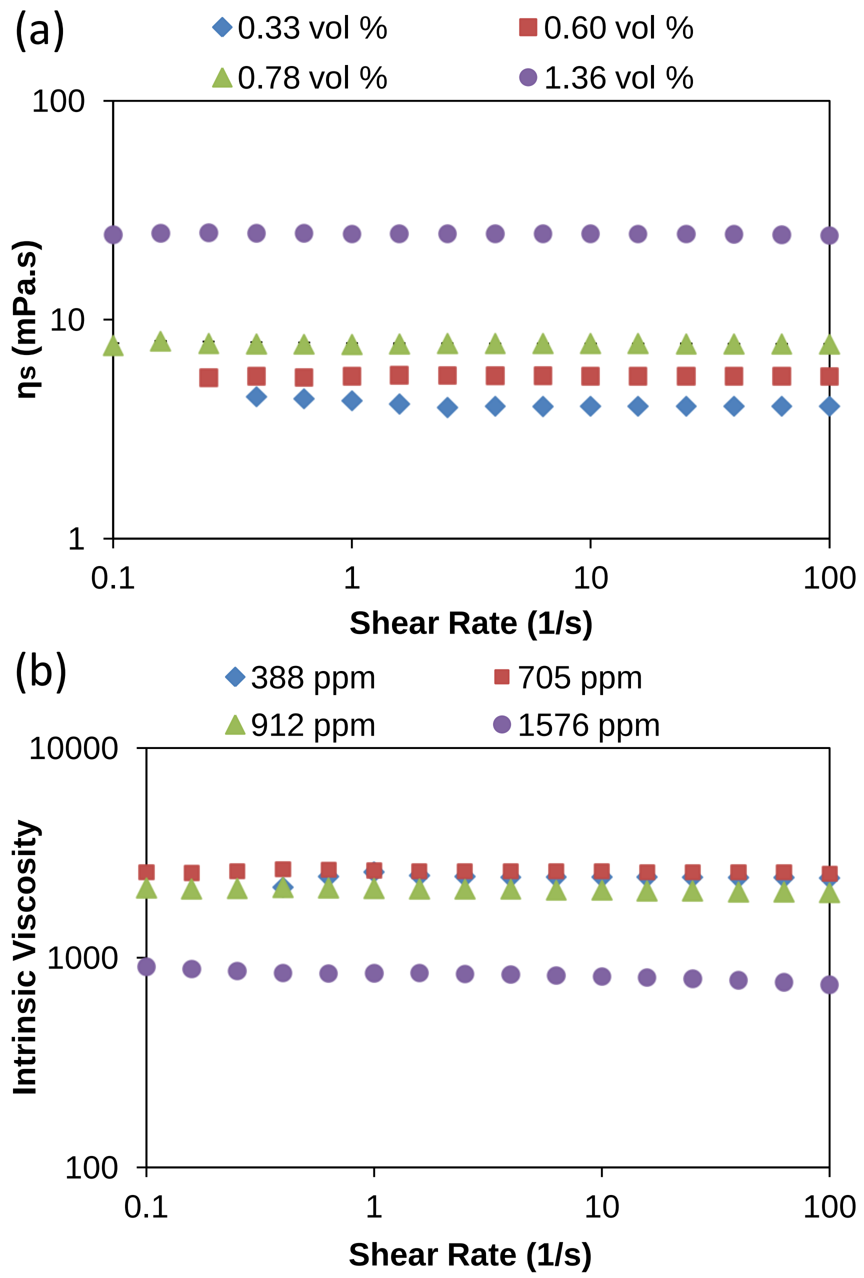

Figure 4.18. (a) dsDNA only solvent viscosity $\eta_s$ versus shear rate at concentrations corresponding to the same dsDNA concentrations in supernatant of dsDNA/SWNT (Rice 187.2) dispersions at 388, 705, 912, and 1576 ppm SWNT. (b) Intrinsic viscosity versus shear rate for supernatant dsDNA/SWNT dispersions in the dilute regime (from 388 to 705 ppm SWNT) and semidilute regime (1576 ppm).

The steady shear viscosities of cholesteric phase forming dsDNA/SWNT dispersions with increasing SWNT concentration are shown in Figure 4.19. Generally, the viscosity kept increasing monotonically with SWNT concentration from 0.26 to 1.47 vol % where the local viscosity maximum occurred in the biphasic regime (Figure 4.19 a, b). With further increase in concentration to 2.22 vol % SWNT, the viscosity started to decrease due to the formation of more ordered alignment of the mesogens into liquid crystals. After the system transitioned into a fully liquid crystalline phase, the viscosity once again increased continuously with SWNT concentration (Figure 4.19c). This nonmonotonic relationship of viscosity as a function of concentration is a typical rheological signature of lyotropic LCPs. As shown in Figure 4.19a, at a low concentration of SWNT at 0.26 vol %, the dispersion behaved as Newtonian fluid. When the concentration increased to 0.35 vol % SWNT, the sample started to show shear thinning behavior at a shear rate of 2.0 $s^{-1}$ after a wide viscosity plateau. At 0.60 vol % SWNT concentration, the steady shear viscosity showed a Newtonian plateau up to 0.03 $s^{-1}$ at low shear rates which was followed by a wide region of shear thinning. Although the first two points are slightly lower in viscosity, within the experimental error, they can be considered as being in the plateau value range. With a further increase in SWNT concentration, the shear thinning regions of each sample extended throughout the overall experimental range. Interestingly, at 0.82 vol % SWNT concentration, the viscosity shear thins at lower shear rates which are followed by an inflection plateau at intermediate shear rates, and shear thins again at high shear rates. This particular concentration is the starting point of viscosity increase in the viscosity versus concentration curve as shown in Figure 4.13.

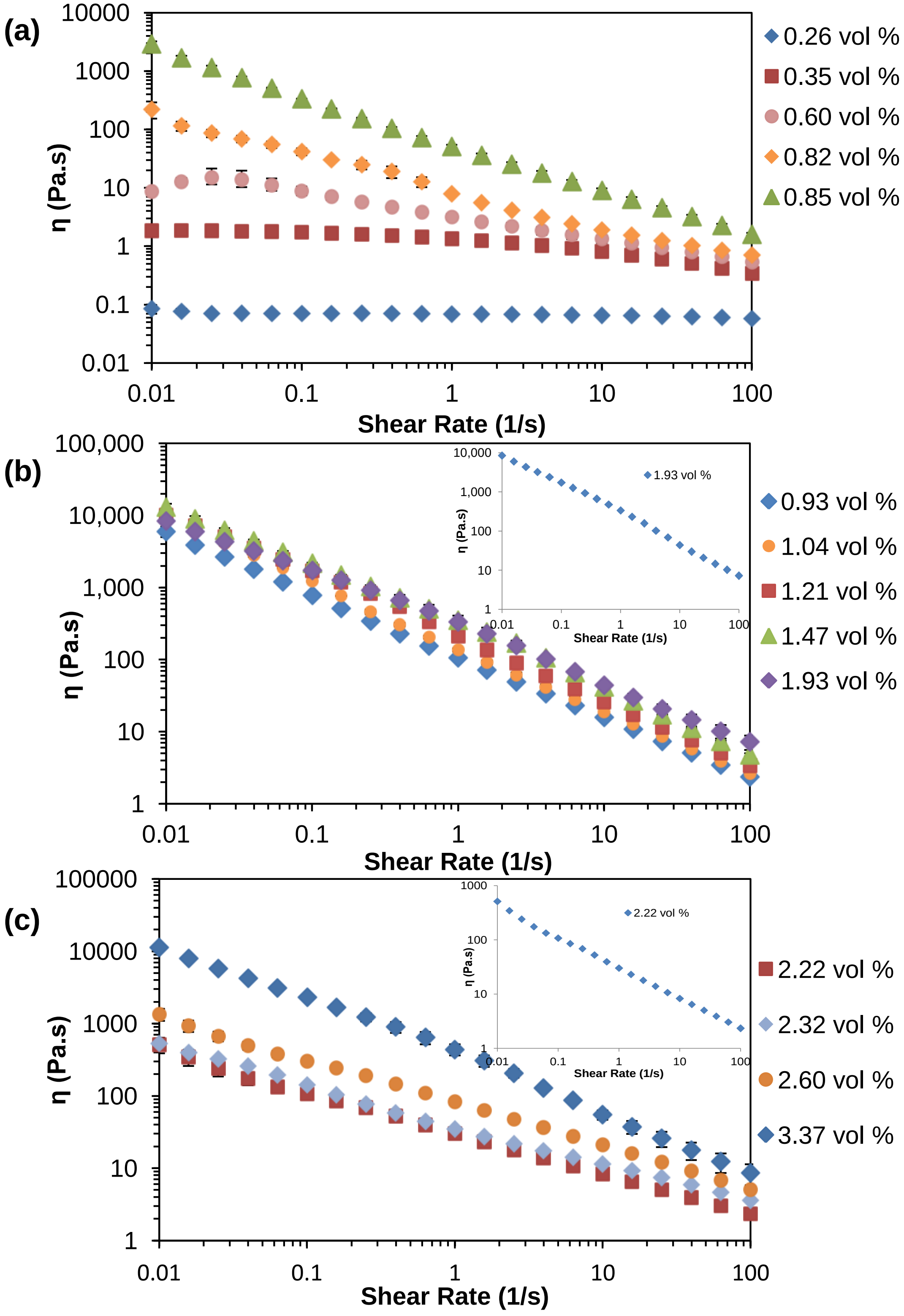

Figure 4.19. The steady shear viscosity of dsDNA/SWNT supernatant dispersions at different SWNT concentrations.

After 0.85 vol % SWNT concentration, samples showed the shear thinning behavior of power law fluids; $\eta = K\dot{\gamma}^{n-1}$; where $\dot{\gamma}$ is the shear rate, *K* is the consistency coefficient related to temperature and *n* is the rate index with n<1 related to shear thinning and n>1 related to shear thickening behavior. However, for several samples with SWNT concentrations higher than 1.47 vol %, which were above the concentration at the local viscosity maximum, the viscosity flow curves showed an inflection point in the shear rate range measured showing slightly different two shear thinning regions. This inconspicuous but reproducible viscosity "kink" (or hesitation) is also observed for many LCPs at a shear rate where the first normal stress difference $N_1$ is in the negative value range.[153,159,162] For dsDNA/SWNT supernatant samples at higher concentrations, negative $N_1$ was obtained within the experimental shear rate range. However, the typical curve of $N_1$ in LCPs which change signs from positive to a negative minimum and become positive again with increasing shear rate is absent in this system. Rheological models for polydomain flow of tumbling rod-like liquid crystals suggest that the kink phenomenon in a shear thinning viscosity is related to a tumbling to oscillating or wagging transition.[157,211] Thus, the steady shear viscosity hesitation observed in this cholesteric phase forming dsDNA/SWNT system may be an indication of the transition from Region 1 to Region II behavior.

The possible three region behavior was also reported for SWNT dispersed in superacids solutions with a very narrow Region II plateau between the two shear thinning regions.[19] Typically, Region I shear thinning is believed to be related to director tumbling in liquid crystalline phase upon shear flow. However, Region I is not seen in all lyotropic nematic polymeric liquid crystals and depends on many factors such as specific materials used, flexibility of rods, defect texture, or the range of shear rates covered.[153] The lack of obvious characteristic Region I behavior in the complex ternary system of dsDNA/SWNT may be caused by several reasons including the orientational defect textures in this system. Both the polydispersity of nanotubes and semiflexibility nature of dsDNA molecules may lead to very complex microstructures in dsDNA/SWNT dispersions which can result in unusual rheological behaviors differing from LCPs. Even 40% PBLG solutions which showed Region I shear thinning also suffered from complex hysteresis consisting of two distinct viscosity braches for steady shear viscosity measurement with different preshearing.[41] This behavior was attributed to the texture elasticity and the change in defect texture upon shear flow indicating that Region I behavior is extremely sensitive to the sample preshear history.

The power law coefficients of steady shear and complex viscosity were given in the Table 4.3. At high enough concentrations of 3.90 and 5.50 vol %, only dynamic measurements are accessable. As for steady shear viscosity test, samples were forced to come out of the measuring plates at a shear rate of 2.5 $s^{-1}$ where the first normal stress $N_1$ had a significant jump from negative $N_1$ values to positive values of over 3000 Pa.

Figure 4.20 shows the complex viscosity as a function of frequency for dsDNA/SWNT supernatant dispersions at various SWNT concentrations. At low concentrations of 0.26 to 0.60 vol % SWNT, the samples were mainly Newtonian with slight shear thinning occurring at high shear rates (Figure 4.20a). After 0.82 vol % of SWNT concentration, samples started to show shear thinning behavior of power law fluids. However, unlike steady shear viscosity, the dynamic viscosity versus frequency curves at high SWNT concentrations did not show viscosity hesitation in the experimental frequency range. Table 4.3 summarizes the change in power law coefficients with increasing SWNT concentration of several dsDNA/SWNT supernatant samples. Marked transitions in power law coefficients occurred at 1.93, 2.22, and 3.37 vol % of SWNT, respectively. Interestingly, the maximum in complex viscosity versus concentration was obtained near 1.93 vol % SWNT which will be discussed in further in Figure 4.22. Although the steady shear viscosity maximum was at 1.47 vol % SWNT at 0.01 and 0.1 $s^{-1}$ shear rate (Figure 4.21a), at a higher shear rate of 1.0 $s^{-1}$, the maximum in steady shear viscosity was obtained near 1.93 vol % SWNT (Figure 4.21b). The fully liquid crystalline phase was determined to occur near 2.22 vol % by both rheology and optical light microscopy as previously shown in Figure 4.13. The marked changes in power law coefficient from 2.60 to 3.37 vol % SWNT, especially for complex viscosity, provided an evidence of a liquid crystalline to gel transition in the system.

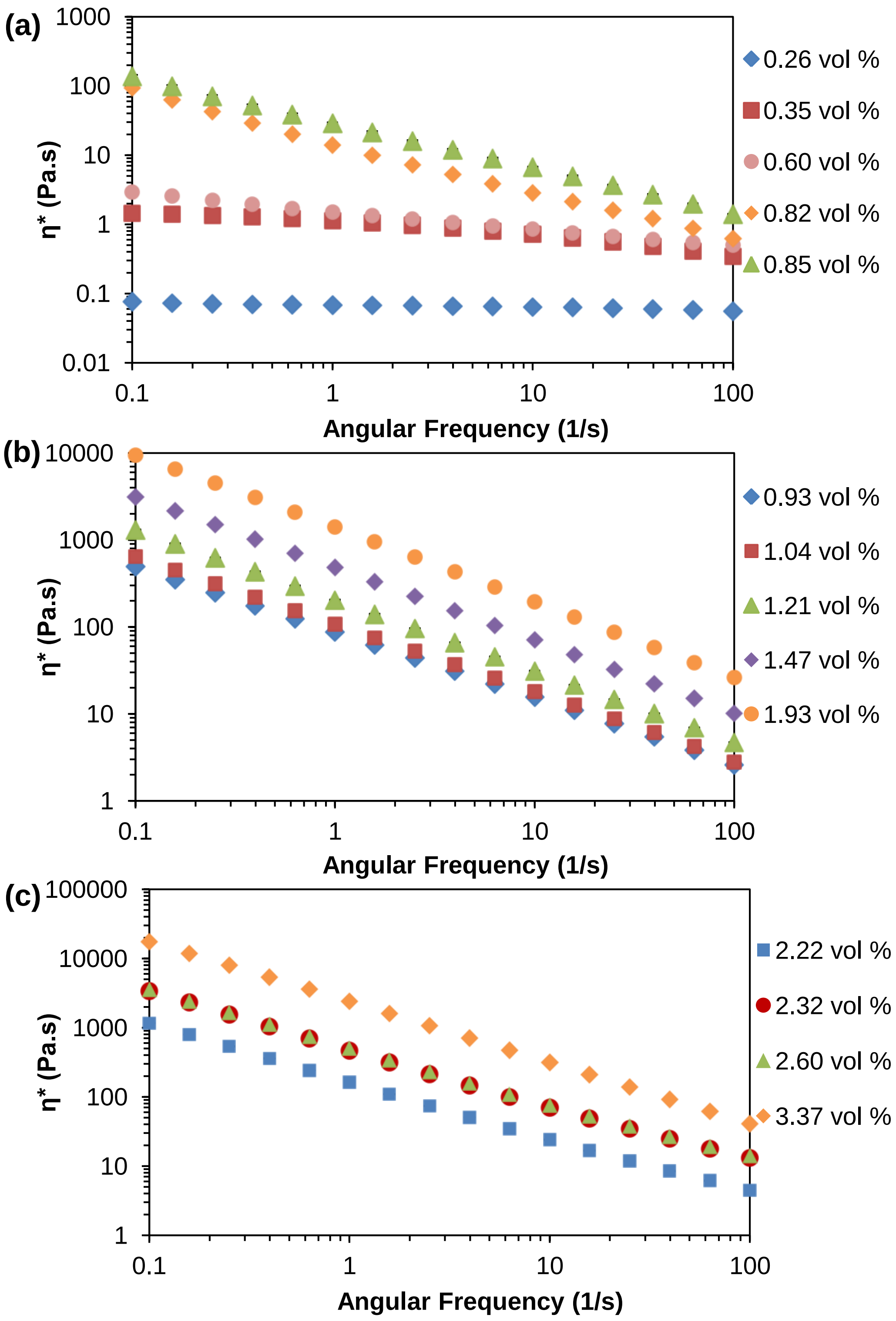

Figure 4.20. The complex viscosity of dsDNA/SWNT supernatant dispersions at different SWNT concentrations.

Table 4.3. Consistency and rate index of steady shear and complex viscosities for dsDNA/SWNT supernatant dispersions behaving as power law fluids at high SWNT concentrations.

| **SWNT Concentration (vol %)** | **Steady Shear Viscosity** | | **Complex Viscosity** | |
|---|---|---|---|---|
| | ***K*** | ***n*** | ***K*** | ***n*** |
| 0.82 | 9.25 | 0.373 | 15.4 | 0.288 |
| 0.85 | 56.5 | 0.201 | 29.4 | 0.349 |
| 0.93 | 112 | 0.150 | 87.4 | 0.245 |
| 1.04 | 148 | 0.110 | 108 | 0.219 |
| 1.21 | 206 | 0.114 | 202 | 0.186 |
| 1.47 | 298 | 0.143 | 476 | 0.170 |
| 1.93 | 281 | 0.223 | 1381 | 0.144 |
| 2.16 | 306 | 0.262 | 1353 | 0.138 |
| 2.22 | 30.8 | 0.434 | 167 | 0.186 |
| 2.32 | 39.9 | 0.457 | 483 | 0.187 |
| 2.60 | 80.9 | 0.410 | 521 | 0.190 |
| 3.37 | 363 | 0.211 | 2371 | 0.121 |
| 3.90 | ~ | ~ | 12674 | 0.111 |
| 5.50 | ~ | ~ | 200229 | 0.069 |

Figure 4.21 shows the viscosity versus concentration curves at different shear rates from 0.01 to 100 $s^{-1}$ for dsDNA/SWNT supernatant dispersions. Similar behavior of abrupt drop in viscosity was obtained at various shear rates of 0.01, 0.1, and 1 $s^{-1}$ at the transition from isotropic to cholesteric state. The value of viscosity maximum was higher at lower shear rates measured. For viscosities at 10 $s^{-1}$ shear rate, the nonmonotonic trend is not so obvious, while at high shear rates of 100 s-1, the viscosity maximum was erased. According to Kiss and Porter, the viscosity maximum of liquid crystalline polymer PBG in m-cresol also decreased and slightly shifted to lower concentration with increasing shear rate.[155]

The complex viscosity η* also showed the same nonmonotonic behavior as steady shear viscosity as a function of concentration at various angular frequencies from 0.1 to 100 1/s as shown in Figure 4.22. The maximum in η* was obtained near 1.93 vol % SWNT which is slightly higher than the concentration, 1.47 vol %, where the steady shear viscosity maximum was obtained. Also, the value of η* maximum decreased with increasing frequency. For complex viscosity, even at high frequencies of 10 and 100 1/s, the curves showed an obvious maximum in the biphasic regime.

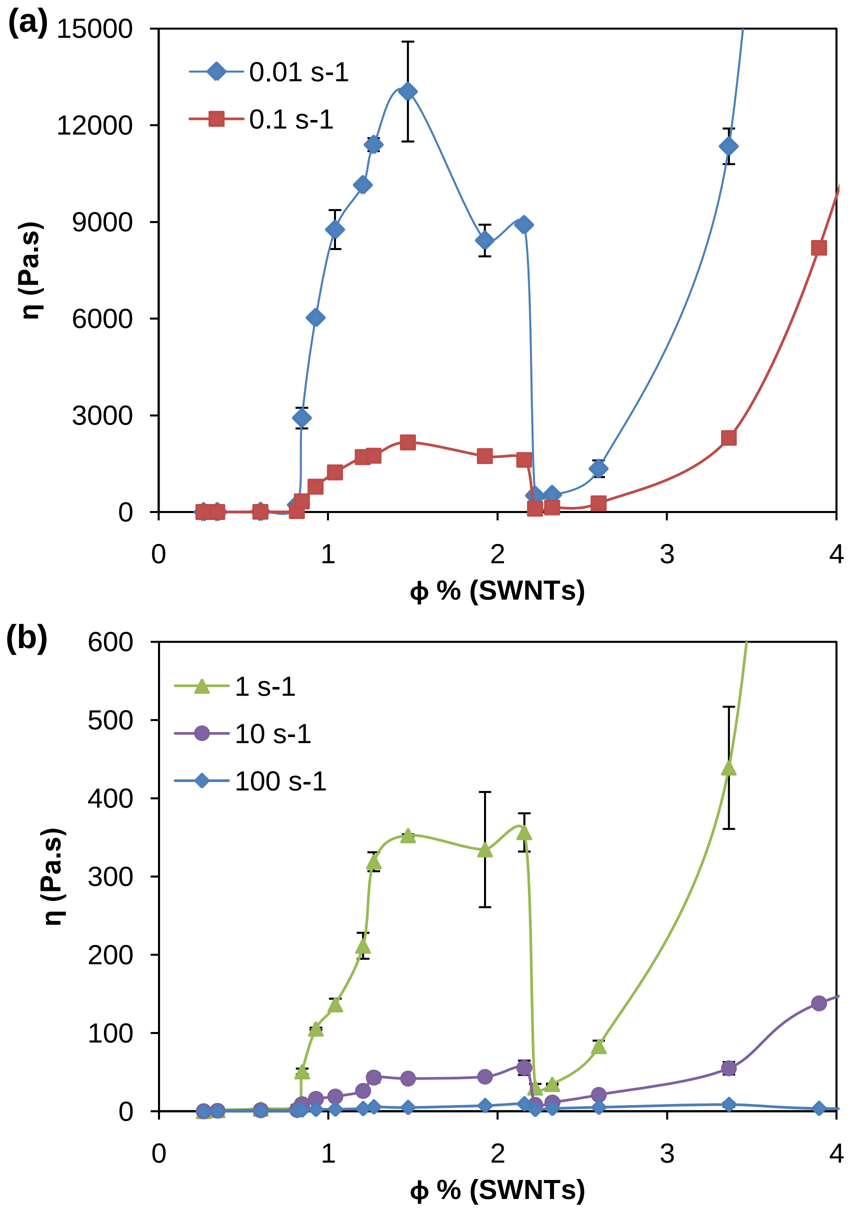

Figure 4.21. The steady shear viscosity versus concentration at various shear rates for dsDNA/SWNT supernatant dispersions.

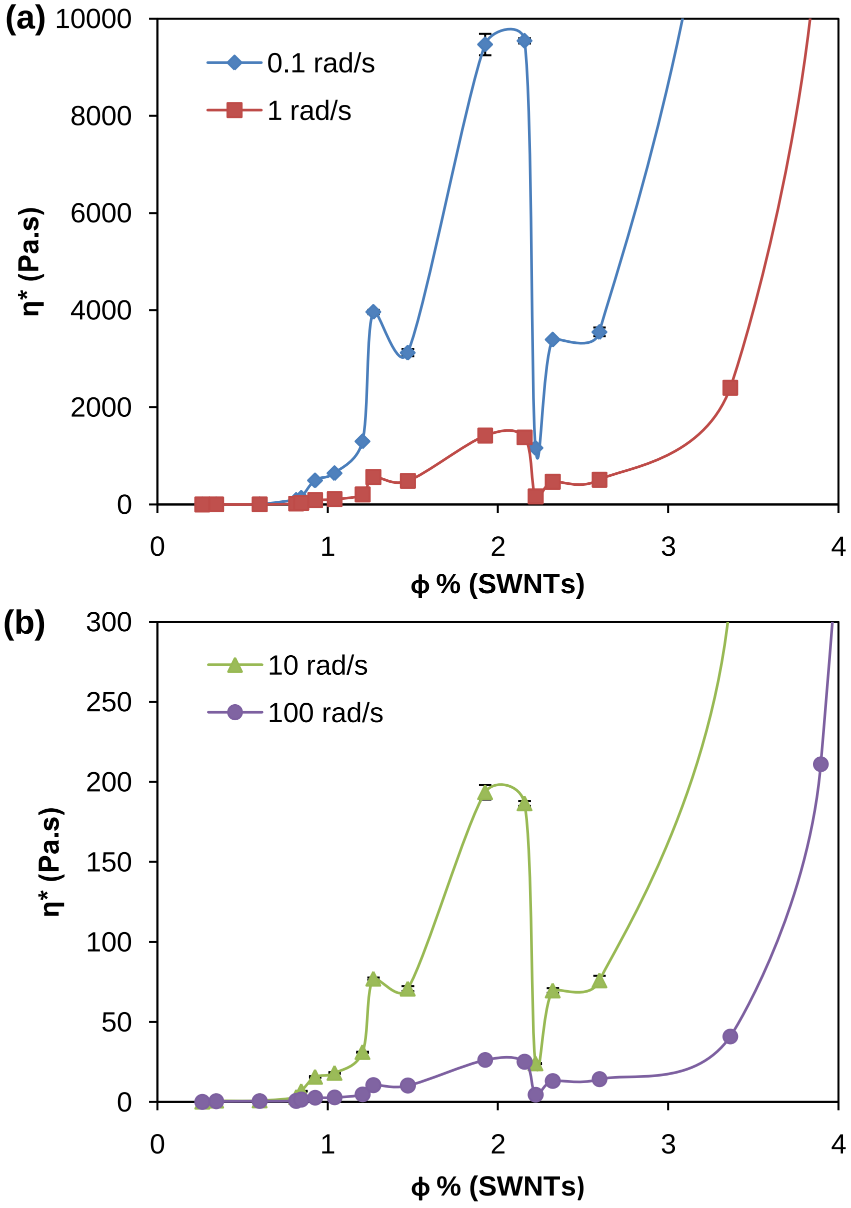

Figure 4.22. The complex viscosity versus concentration curves at various frequencies for dsDNA/SWNT supernatant dispersions.

The viscosity kinks in steady shear viscosities were also observed for various nematic dsDNA/SWNT (noncentrifuged) dispersions with different dsDNA:SWNT volume ratios (Figure 4.23). Generally, the viscosity kinks were more obvious when the SWNT concentrations were near the $\phi_{LC}$ value where the corresponding viscosity is at its local minimum in the viscosity versus concentration curves. According to the nonmonotonic relationship of viscosity versus concentration for bulk dsDNA/SWNT dispersions, the $\phi_{LC}$ values are ~1.13, 3.91, and 1.92 vol % of SWNT for 8.5:1, 6.4:1, and 4.3:1 volume ratio of dsDNA:SWNT, respectively. The relatively large $\phi_{LC}$ of 3.91 vol % SWNT obtained for 6.4:1 dsDNA/SWNT by volume may be a consequence of using SWNT with different aspect ratios than the 8.5:1 and 4.3:1 volume ratio dispersions used the same type of SWNT. Additional data on steady shear viscosity of 6.4:1 by volume of dsDNA:SWNT bulk dispersions and dsDNA only solution as references are provided in the Appendix-B.

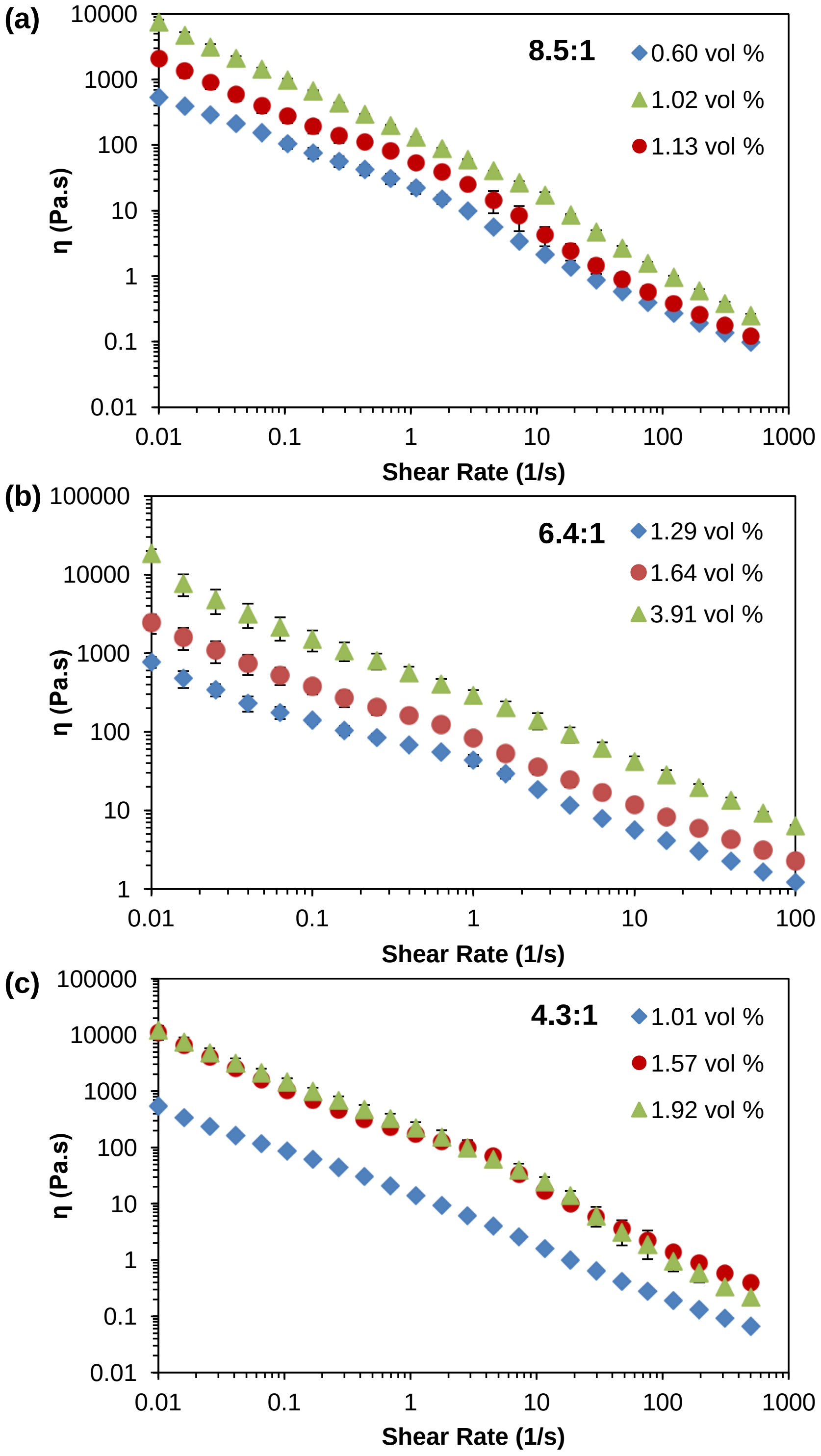

Figure 4.23. The steady shear viscosity of bulk dsDNA/SWNT (noncentrifuged) dispersions with (a) 8.5:1, (b) 6.4:1, and (c) 4.3:1 of dsDNA/SWNT ratio by volume at various SWNT concentrations.

**Time-Concentration Superposition.** Figure 4.24 shows the viscosity master curve for the dsDNA/SWNT supernatant created by shifting with respect to stress and inverse time shift factors to the reference concentration. For each sample, reduced steady shear viscosity, $\eta_r = (\eta\ b_c)/a_c$, was plotted against the reduced shear rate, $\dot{\gamma}_{\mathrm{r}} = \dot{\gamma}\, a_c$, where $\eta$ is the steady shear viscosity and $\dot{\gamma}$ is the shear rate. The stress and inverse time shift factors are defined as $b_c = c_{\mathrm{ref}}/c$ and $a_c = (\eta_0/\eta_{0,\mathrm{ref}})(c_{\mathrm{ref}}/c)$, respectively where c is the SWNT concentration. The subscript *ref* indicates the reference concentration which was chosen to be 1.21 vol % SWNT, while *0* and *r* refer to the zero shear viscosity and reduced variable, respectively. The zero shear viscosities were derived from Carreau-Yasuda model by fitting the existing data of Power Law fluids into the model. Even though the time - concentration superposition is not perfect, the master curve of dsDNA/SWNT supernatant dispersions at 10 $^{\mathrm{o}}$C showed two slight inflection points indicating the possible characteristic three region flow behavior of LCPs.[48,212]

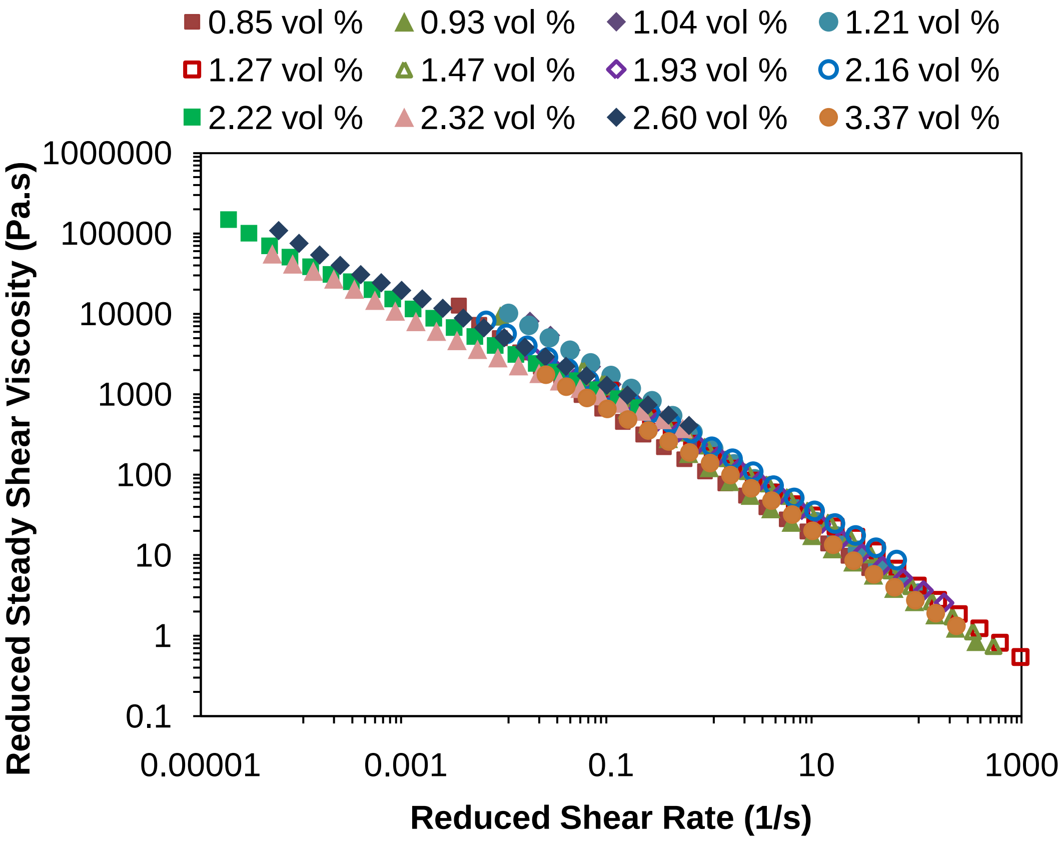

Figure 4.24. Time - concentration superposition of steady shear viscosities of dsDNA/SWNT supernatant dispersions.

The effects of concentration on steady shear viscosities were also analyzed by plotting the viscosity against the shear stress which is shown in Figure 4.25. When the samples were isotropic, the viscosity increased dramatically with a slight increase in concentration from 0.26 to 0.35 vol % SWNT and showed Newtonian behavior with the onset of shear thinning only at high shear rates (Figure 4.25a). At 0.60 vol % SWNT, the shear thinning behavior dominates with little observable plateau indicating an isotropic to anisotropic alignment transition in the system. In fact, the lowest concentration where the near-parallel lines of fingerprint texture were detected by the optical microscope is 0.69 vol % SWNT. With further increase in concentration, the sample transition from significant shear thinning to possible yielding behavior especially at 1.21 vol % SWNT where the yield stress is estimated to be about 215 Pa (Figure 4.25b). The stress at which the viscosity decreases by greater than an order of magnitude is considered as the yield stress. It can be also taken as the maximum stress below which no flow occurs. Many commercially important materials such as emulsions and concentrated suspensions exhibit yield stress and the performance of the materials are largely affected by the value of the yield stress.[213] When the concentration increased to the vicinity of fully liquid crystal phase around 2.22 vol % or above, the viscosity curves showed two distinct shear thinning regions with different slopes separated by a seemingly Newtonian plateau, especially at 2.22 and 2.60 vol % SWNT concentration. The shear thinning Region I at lower shear rates may become more evident if even lower shear rates were accessible in the experiment.

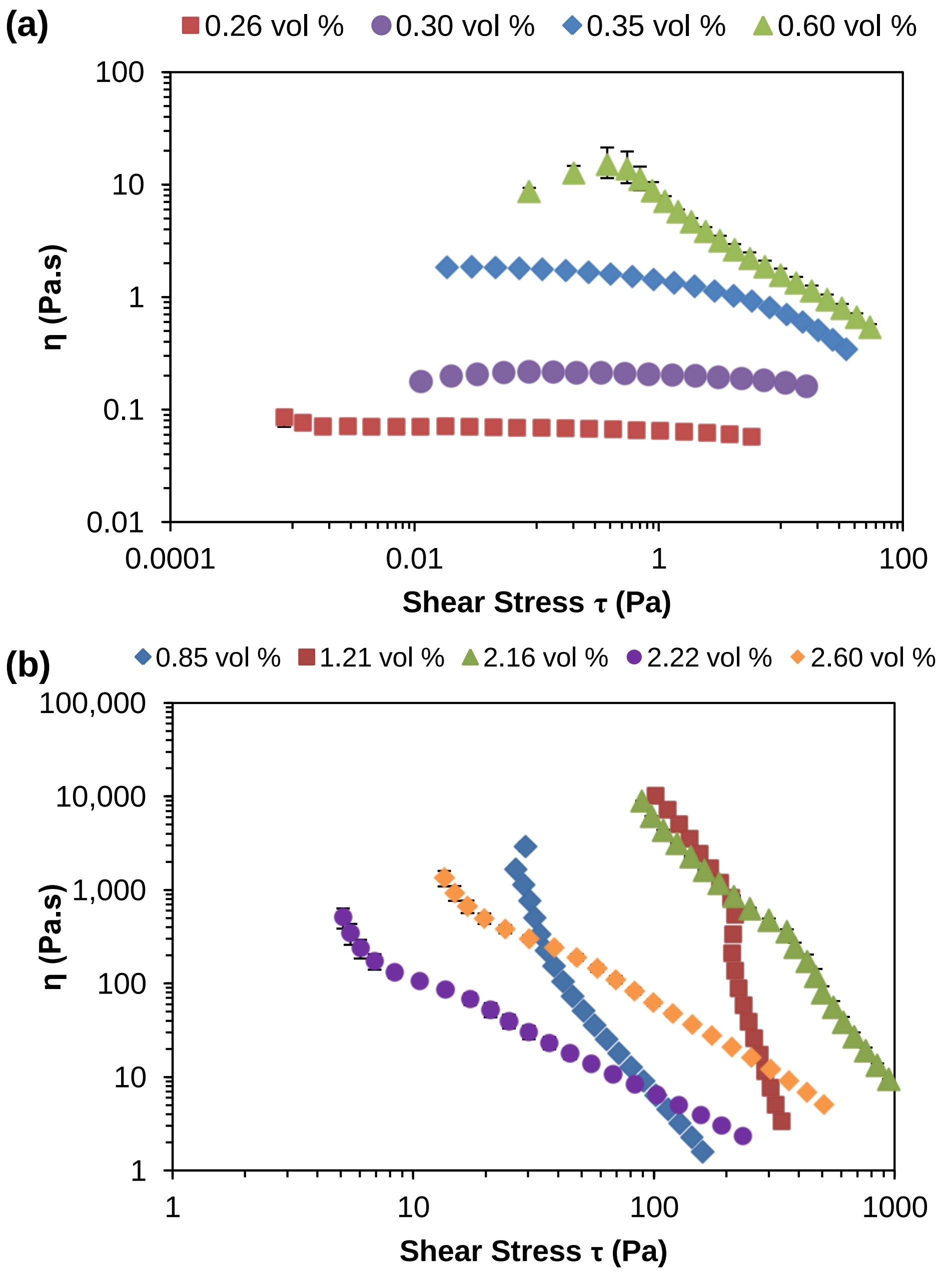

Figure 4.25. The effect of concentration on steady shear viscosities of dsDNA/SWNT supernatant dispersions.

Figure 4.26 shows the steady shear viscosity change as a function of shear stress for various bulk dsDNA/SWNT dispersions with different dsDNA:SWNT volume ratios. When the SWNT concentrations were in the biphasic regime, the viscosity showed similar behavior with increasing shear stress for bulk dispersions of nematic liquid crystals when compared to cholesteric dsDNA/SWNT dispersions. However, at SWNT concentrations of $\phi_{LC}$, where the viscosities were at minimum, such as 1.13 (Figure 4.26a), 3.91(Figure 4.26b), and 1.92 (Figure 4.26c) vol % of SWNT respectively, the viscosity versus shear stress curves showed different behavior than their cholesteric counterparts. More specifically, at SWNT concentrations of $\phi_{LC}$ for nematic bulk dispersions, the viscosity drops more rapidly with more than four orders of magnitude within a narrow range of increasing shear stress much smaller than an order of magnitude. Also, at $\phi_{LC}$ of nematic bulk dispersions, samples showed obvious yielding behavior instead of shear thinning regions with different slopes when compared to cholesteric dispersions at $\phi_{LC}$ of near 2.22 vol % SWNT. Near the critical concentration of $\phi_{LC}$ for cholesteric dispersions, the viscosity shear thins over shear stress range more than an order of magnitude.

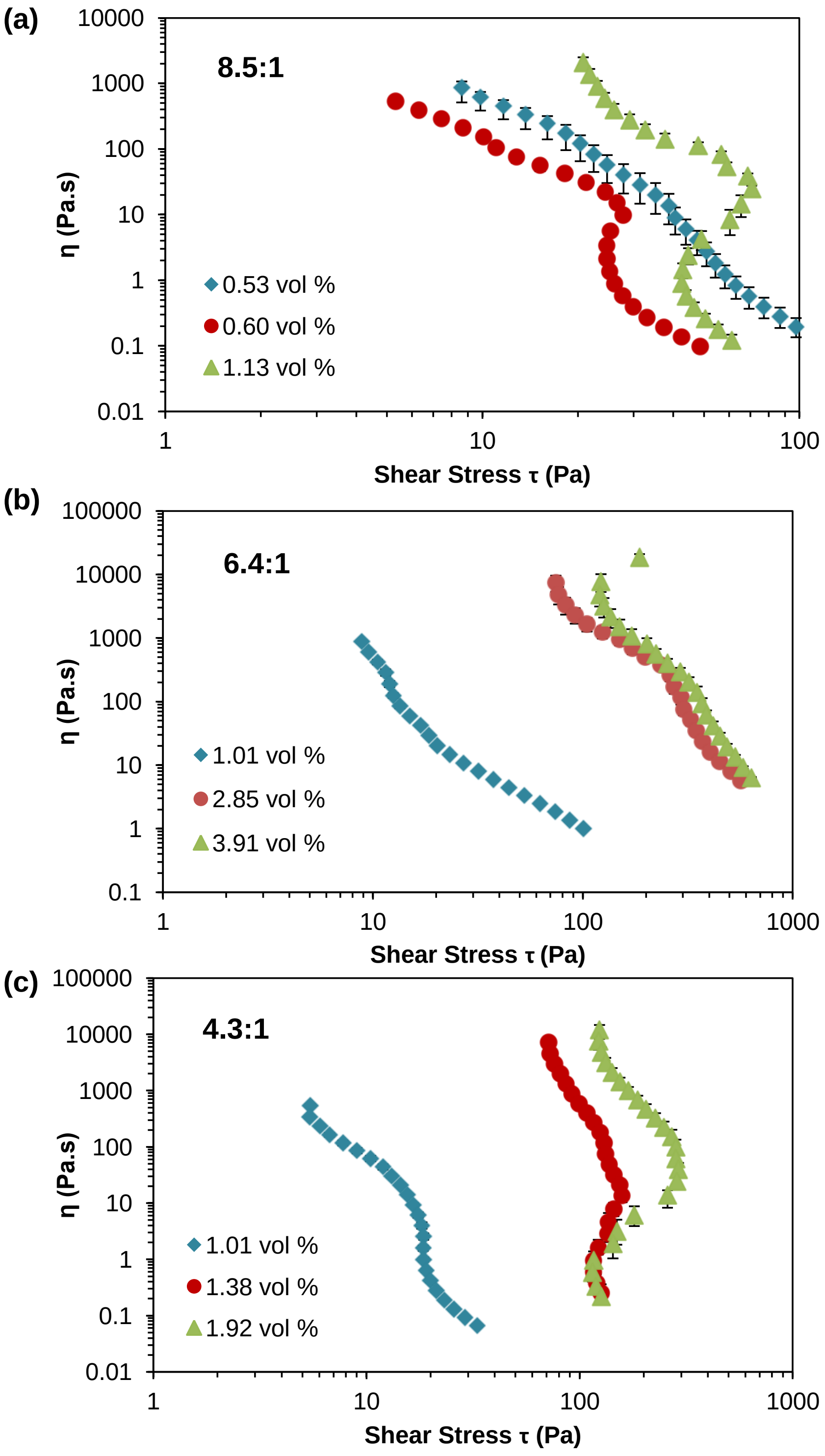

Figure 4.26. The steady shear viscosity versus shear stress plots of bulk dsDNA/SWNT (noncentrifuged) dispersions with (a) 8.5:1, (b) 6.4:1, and (c) 4.3:1 of dsDNA/SWNT ratio by volume at various SWNT concentrations.

**Cox-Merz Rule.** Ordinary polymers follow the empirical Cox-Merz rule that the steady shear viscosity and complex viscosity at the same shear rate or angular frequencies overlap very well for the entire concentration range. However, this rule is not obeyed for lyotropic nematic LCPs except in the isotropic regime. Interestingly, for cholesteric phase forming dsDNA/SWNT supernatant dispersions, Cox-Merz rule is alternately obeyed and disobeyed in the anisotropic regimes with increasing SWNT concentration. When the Cox-Merz rule is not obeyed, the steady state value drops either below or rise above the oscillatory values. The origin of this atypical behavior of alternately obeying and disobeying the Cox-Merz rule is not clear. However, this may be due to the more sensitive nature of dynamic measurement to shear history which caused deviation from steady shear values especially at lower angular frequencies for lower SWNT concentrations in the biphasic region. Liquid crystal samples in biphasic region tend to have complex flow behaviors with large errors between different runs. In addition, when the Cox-Merx rule was not obeyed in some of the samples in biphasic region, the steady shear and complex viscosities only deviated from each other slightly. At higher shear rates and angular frequencies, both viscosities seemed to overlap with each other. More specifically, at low concentration of 0.35 vol % SWNT, the complex viscosity overlaps to the steady shear viscosity at equal values of shear rate and angular frequency in the entire range of 0.1-100 $s^{-1}$ as shown in Figure 4.27a. When the concentration increased to 0.60 vol % SWNT, the complex viscosity started to deviate more obviously from steady shear viscosity at low shear rate/frequency which is shown in Figure 4.27b. This particular concentration is close to that of 0.69 vol % SWNT where the first cholesteric oily streak texture of thin parallel lines were captured by polarized light optical microscopy. The deviation to Cox-Merz rule at lower shear rate/frequency continued to apply for samples when the SWNT concentration increased up to 0.85 vol % which is the onset of apparent viscosity increase in the viscosity versus concentration curve. Unexpectedly, with further increase of the SWNT concentration in the biphasic regime from 0.93 to 1.21 vol %, the complex and steady shear viscosities again overlapped each other within the error range (Figure 4.27a). This concentration range is typically in the left shoulder of the viscosity maximum in the viscosity versus concentration curve where the viscosity increases with concentration. For the next two samples with higher concentrations of 1.27 and 1.47 vol % SWNT, the complex and steady shear viscosities slightly deviated from each other in the measured shear rate/frequency range. The 1.47 vol % SWNT is the concentration where the steady shear viscosity reaches its maximum value of 2165 Pa.s. After this point, when the concentration increased further to transition from biphasic to liquid crystal phase, the deviation from Cox-Merz rule became much obvious through the entire measured shear rate/frequency range (Figure 4.27b). Not obeying the empirical Cox-Merz rule is additional evidence of cholesteric liquid crystalline phase formation in the supernatant of dsDNA/SWNT dispersions.

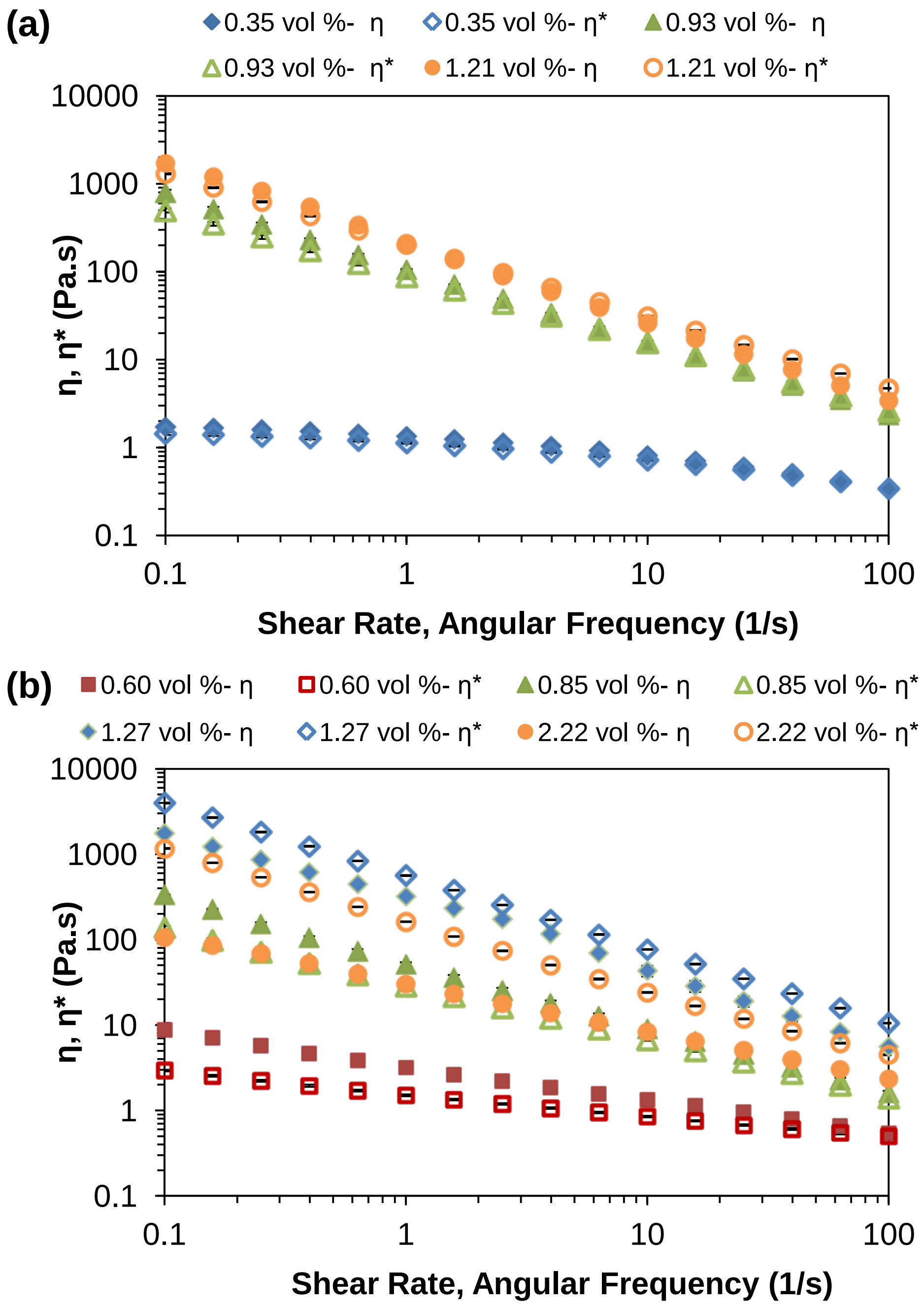

Figure 4.27. Cox-Merz rule alternately (a) obeyed and (b) not obeyed at different SWNT concentrations for dsDNA/SWNT supernatant dispersions. Several concentrations were selected as examples in this figure.

Similarly, for nematic bulk dsDNA/SWNT dispersions of 6.4:1 volume ratio, the empirical Cox-Merz rule was not followed for several anisotropic samples. In Figure 4.28, the Cox-Merz rule was not obeyed for the biphasic sample of 3.31 vol % SWNT. However, at lower SWNT concentration of 1.01 vol %, the steady shear and complex viscosities overlap with each other at the same shear rates and angular frequencies. Additional results for both dsDNA/SWNT supernatant and bulk dispersions and dsDNA only solution on not obeying the empirical Cox-Merz rule are given in the Appendix-B.

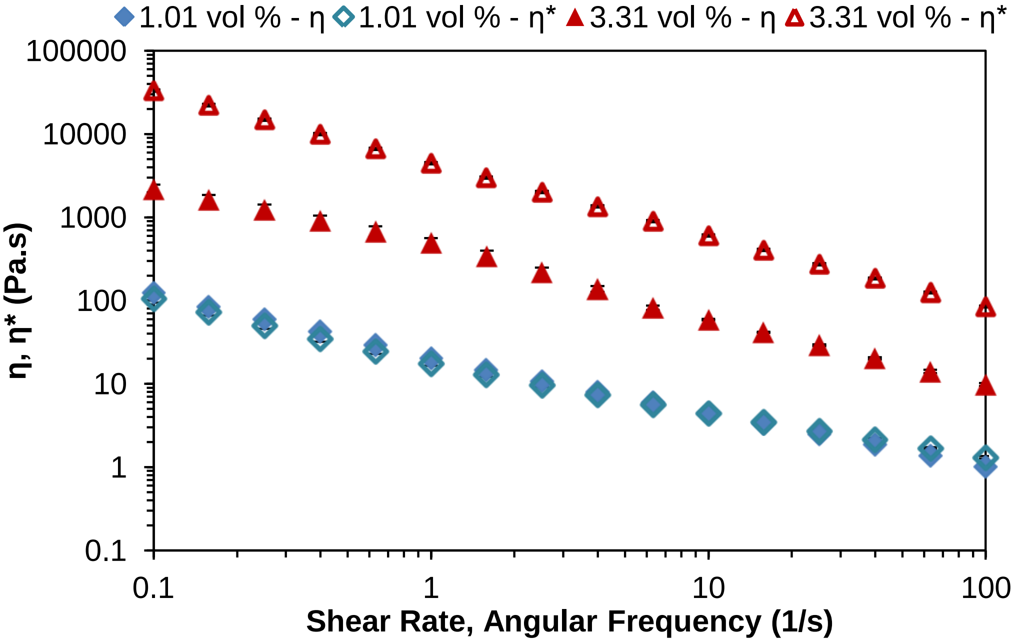

Figure 4.28. Cox-Merz rule not obeyed at higher SWNT concentrations for bulk dsDNA/SWNT (noncentrifuged) dispersions with 6.4:1 dsDNA/SWNT ratio by volume.

**Dynamic Modulus.** The dynamic data in this research were obtained within the linear viscoelastic region (LVE) as determined by amplitude sweep measurements at an angular frequency of 10 1/s. Amplitude sweep data can be found in Appendix-B. Figure 4.29 shows the loss factor tan (δ) which is the ratio of the viscous to elastic modulus, as a function of angular frequency of dsDNA/SWNT supernatant dispersions at different SWNT concentrations. The loss factor tan δ obtained from frequency sweep is a measurement of sample rigidity which indicates its deformation behavior. Thus, a sample has a solid-like behavior when its tan δ value is smaller than one indicating that the elastic behavior dominates over the viscous behavior and vice versa if tan δ value is larger than one. When the SWNT concentration reached to 0.82 vol %, tan δ became smaller than one and exhibited solid-like behavior which indicates that the elastic behavior dominates over the viscous behavior. While for dsDNA/SWNT dispersions with SWNT concentrations lower than 0.82 vol %, the viscous behavior dominated over the elastic behavior and tan δ was larger than one.

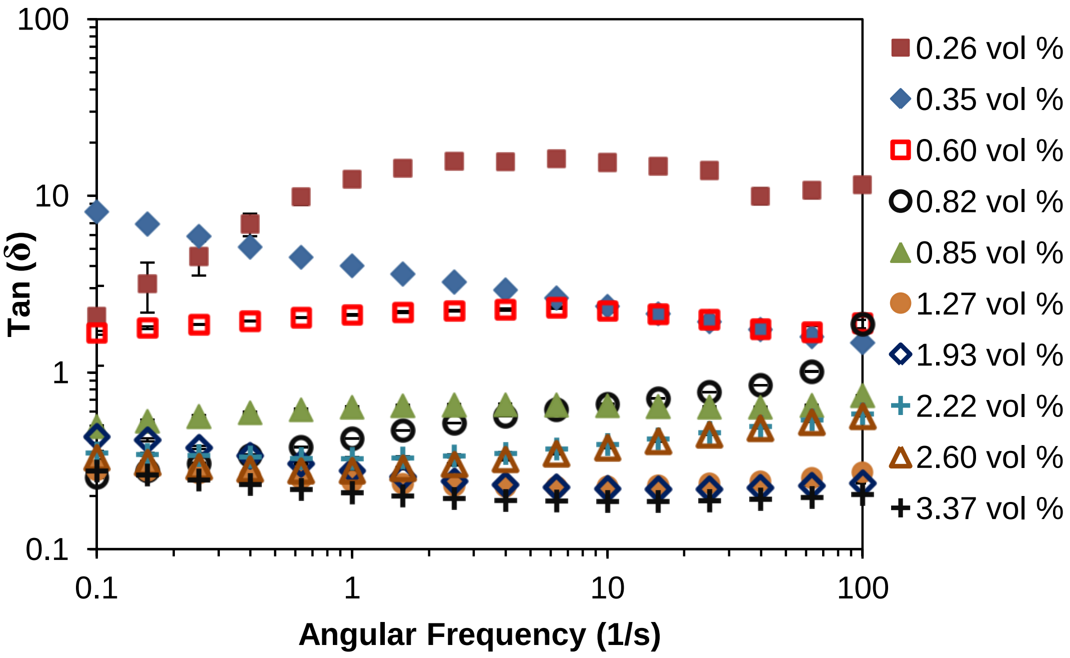

Figure 4.29. The ratio of the viscous to elastic modulus (tan (δ) = G”/G’) versus frequency for dsDNA/SWNT supernatant dispersions at different SWNT concentrations.

The storage modulus versus frequency of dynamic data for dsDNA/SWNT supernatant dispersions at various SWNT concentrations is shown in Figure 4.30. In general, the storage modulus G’ showed the similar nonmonotonic relationship with concentration as the steady shear viscosity. The G’ kept increasing when the SWNT concentration increased from isotropic to biphasic phase, then started to decrease during the transition from biphasic to fully liquid crystal phase. Once the molecular orientation in the system was not significantly affected by increasing concentration, the G’ once again increased as a function of increasing concentration. The dynamic data of samples at less than 0.26 vol % SWNT was not experimentally accessible. In Figure 4.30a, two apparent jumps of more than an order of magnitude increase in G’ at low frequency were detected at low SWNT concentrations; one was the increase from 0.26 to 0.35 vol %, and the other was from 0.60 to 0.82 vol %, respectively. In fact, from 0.60 to 0.82 vol %, the G’ increased by almost two orders of magnitude and the slope of the curve decreased to level up at low frequency. A plateau in G’ at low frequencies indicates a possible formation of a network while the apparent jump in low frequency modulus G’ more than an order of magnitude is indicative of a percolation threshold.[214] Generally, rheological percolation is identified by the formation of a plateau in G’ at low frequencies in dynamic tests resulting from an apparent yield stress.[215] Two apparent jumps observed in this system may indicate an existence of two percolation thresholds. It is hypothesized that one of them is related to excess dsDNA network and another one is related to SWNT percolation. With further increase in concentration, the slope of the curves decreased indicating the formation of a stiffer structure. At high SWNT concentrations, larger than 3.37 vol %, the G’ became independent of frequency indicating the development of more solid-like phase (Figure 4.30b).

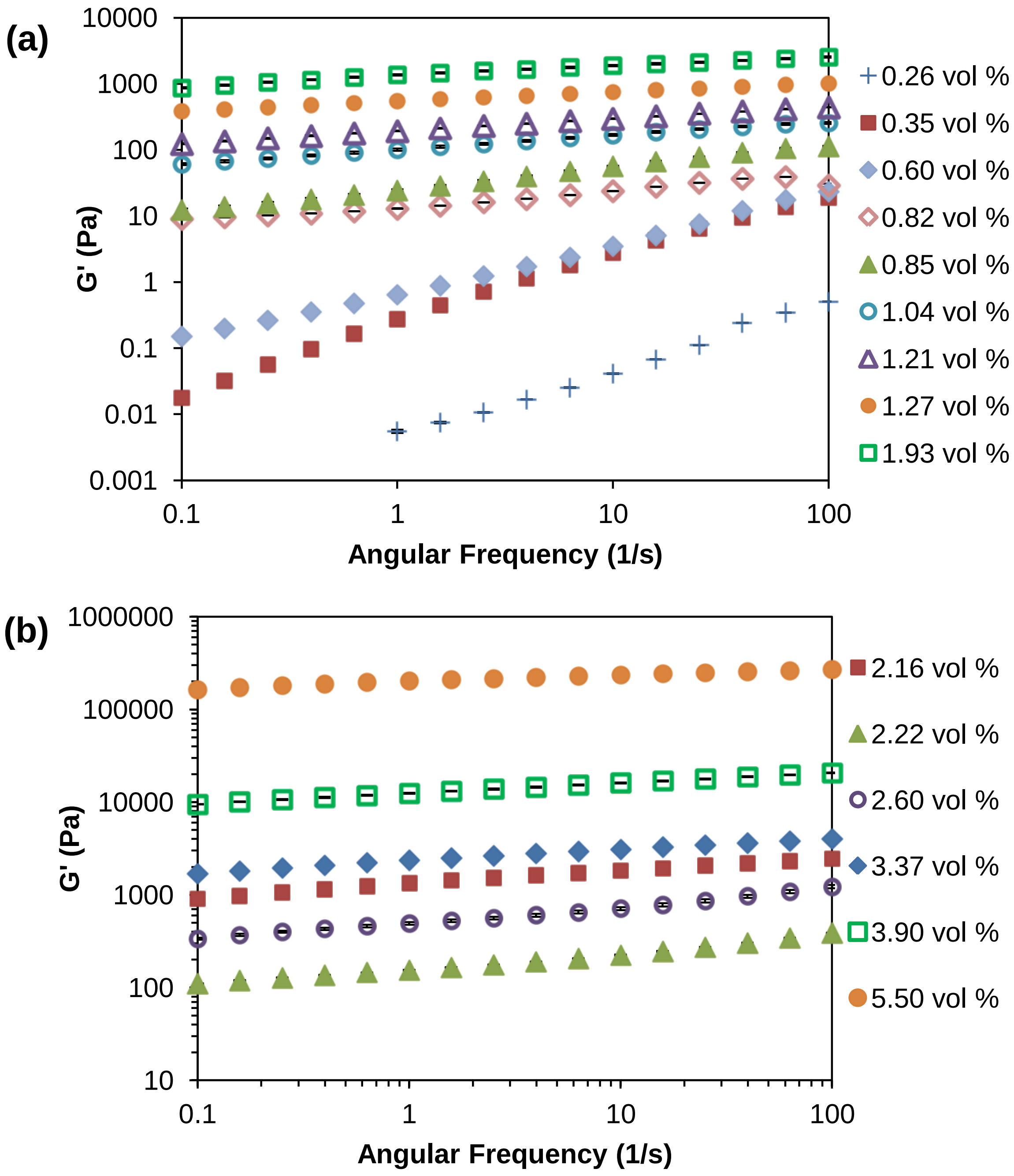

Figure 4.30. Elastic (storage) modulus G’ as a function of frequency for dsDNA/SWNT supernatant dispersions at different SWNT concentrations.

Furthermore, the data in Figure 4.30a were used to estimate the percolation concentration by varying $\phi^*$ to obtain the best linear fit of the double log plot of $G_0'$ versus ($\phi$ - $\phi^*$) where $G_0'$ is the plateau modulus, $\phi$ is the volume fraction of nanotubes, and $\phi^*$ is the percolation volume fraction. As mentioned earlier, the plateau in G' and more than an order of magnitude increase in G' at low frequency were considered to be the indication of percolation threshold. Near the percolation threshold, $G_0' \propto (\phi - \phi^*)^{\nu}$, where ν is the percolation exponent. Two groups of data were considered; one group of data is from 0.82 – 1.27 vol % SWNT samples (Figure 4.31a), and another one is from 0.26 – 1.27 vol % SWNT samples (Figure 4.31b). The $G_0'$ values at higher SWNT concentrations were not included. Because at high SWNT concentrations, samples contained a high fraction of anisotropic phase and G’ began to decrease as a function of ϕ. In Figure 4.31a, the best linear fit of $R^2$= 0.945 was obtained for $\phi^*$=0.62 vol % and the percolation exponent ν = 2.78 ± 0.16 from the slope of the double log plot of $G_0'$ at 0.1 1/s angular frequency versus ($\phi$ - $\phi^*$). The percolation concentration 0.62 vol % may be related to the network formation of rigid SWNT. While for the other group of data in Figure 4.31b, the best linear fit was obtained for $\phi^*$=0.21 vol % with ν = 3.62 ± 0.05 and $R^2$= 0.980. The lower percolation concentration 0.21 vol % may be caused by the dominating network of semiflexible free dsDNA. A percolation threshold of $\phi^*$=0.11 vol % SWNT and ν = 1.6 were obtained experimentally for SWNT superacids system.[151] It was reported that a percolation exponent of 2.1 ± 0.2 obtained by simulation corresponds to percolation bonds that resist stretching but can rotate freely, while percolation bonds which resist both stretching and rotation have a percolation exponent of 3.75 ± 0.11.[214,216] The percolation exponent obtained in this work indicates that the SWNT network in the dsDNA/SWNT system was composed of associating rods.

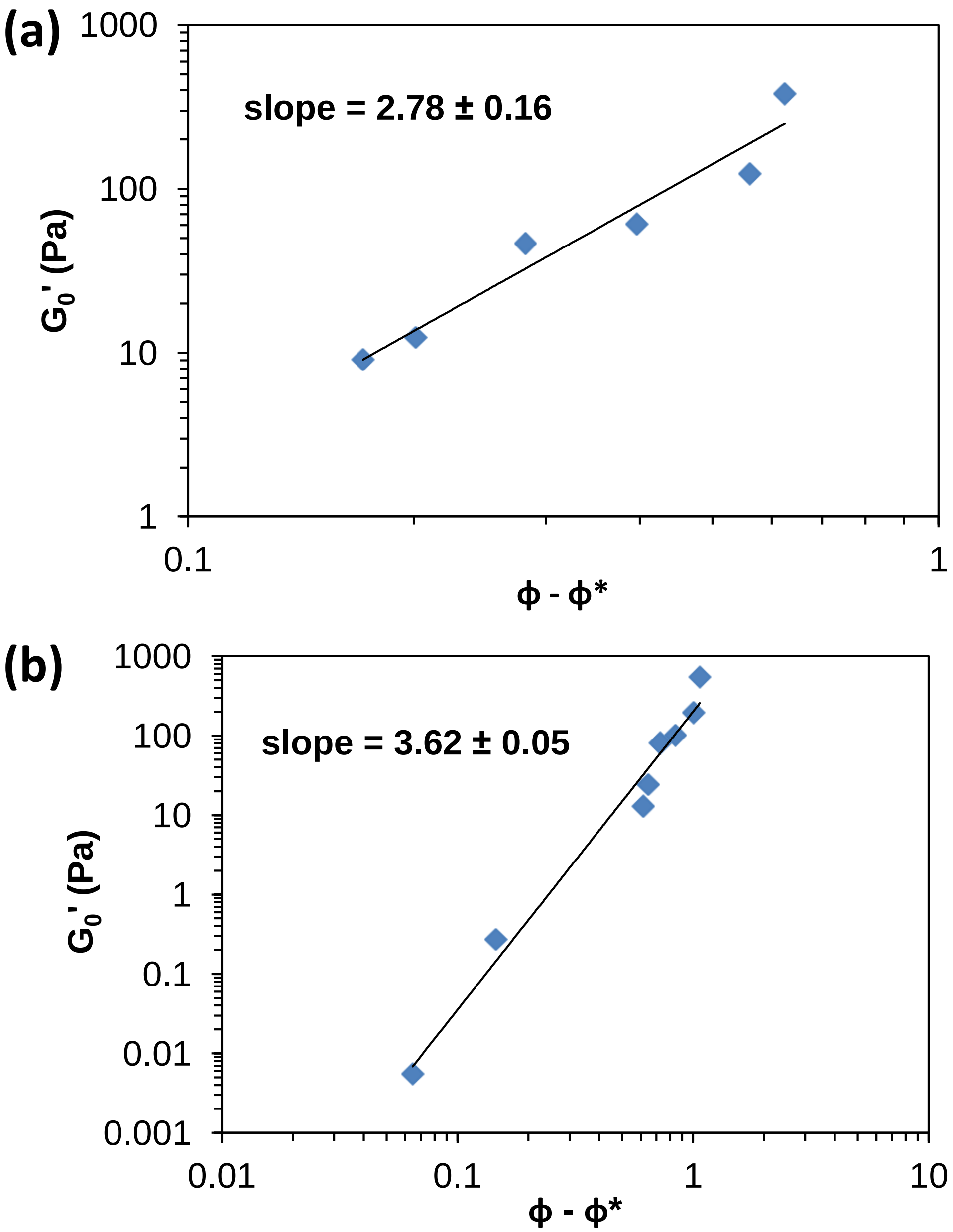

Figure 4.31. (a) The storage plateau modulus $G_0'$, obtained at 0.1 $s^{-1}$ angular frequency, versus the reduced volume fraction ($\phi$ - $\phi^*$) of SWNT. The value of $\phi^*$=0.6175 vol % gave the best linear fit with $R^2$=0.945 and $\nu$ =2.78 ± 0.16. (b) The value of $\phi^*$=0.2101 vol % gave the best linear fit with $R^2$=0.980 and $\nu$ =3.62 ± 0.05 for $G_0'$ at 1 $s^{-1}$ angular frequency versus ($\phi$ - $\phi^*$) of SWNT.

In addition, the Cole-Cole plot of relationship between G’ and G” is shown in Figure 4.32. With increasing SWNT concentration from 0.60 to 0.85 vol %, the increase in storage modulus G’ at a given value of loss modulus G” indicated an evolution of structural change occurring in supernatant dsDNA/SWNT dispersions. In addition to having increased G’ for a given G” value, the slops of G’ against G” curves increased consistently with increasing SWNT concentration, indicating the formation of a more complex structure. The Cole-Cole plots of bulk dispersions are provided in Appendix-B.

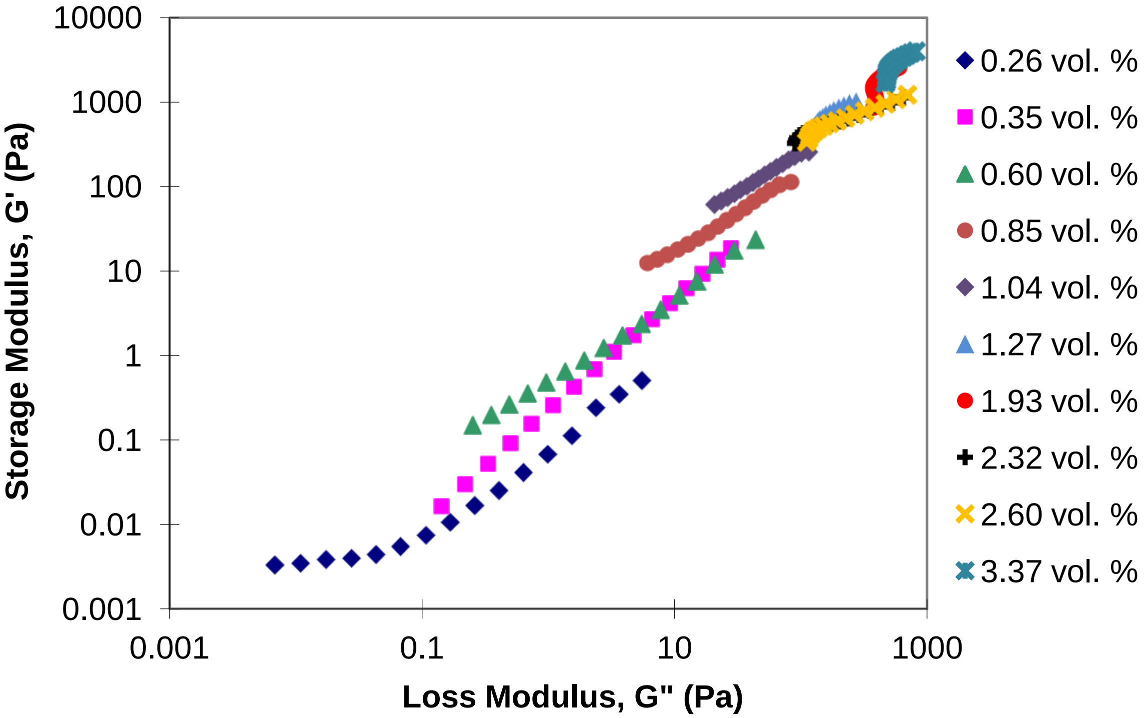

Figure 4.32 Cole-Cole plots show the storage modulus as a function of loss modulus and increasing SWNT concentration for supernatant 4.4:1.0 volume ratio of dsDNA:SWNT dispersions.

The loss modulus G” of dsDNA/SWNT dispersions at various SWNT concentrations as a function of frequency are shown in Figure 4.33. The G” jumped up to more than an order of magnitude at lower angular frequencies from 0.26 to 0.35 vol % of SWNT concentration. At the same time, the slope of the curve kept decreasing as the SWNT concentration increased from 0.26 to 1.93 vol % SWNT and showed a low frequency plateau at 1.93 vol % of SWNT concentration (Figure 4.33a). With further increase in concentration at 2.22 and 2.60 vol %, respectively, the G” curves showed steep increases in slopes at higher angular frequencies, although plateaus were obtained at lower angular frequencies (Figure 4.33b). It was determined from the steady state viscosity versus concentration curve that fully cholesteric liquid crystalline phase was formed at around a SWNT concentration of 2.22 vol %. The fully liquid crystalline phase tend to flow align easier than biphasic phase at high angular frequencies causing the increase of viscous behavior of the liquid crystal dispersion. This may be the reason the steep increase in the G” curve slope at higher angular frequency for liquid crystal samples. When the concentration increased further to become larger than 3.37 vol %, the G” showed a plateau again indicating a solid phase formation.

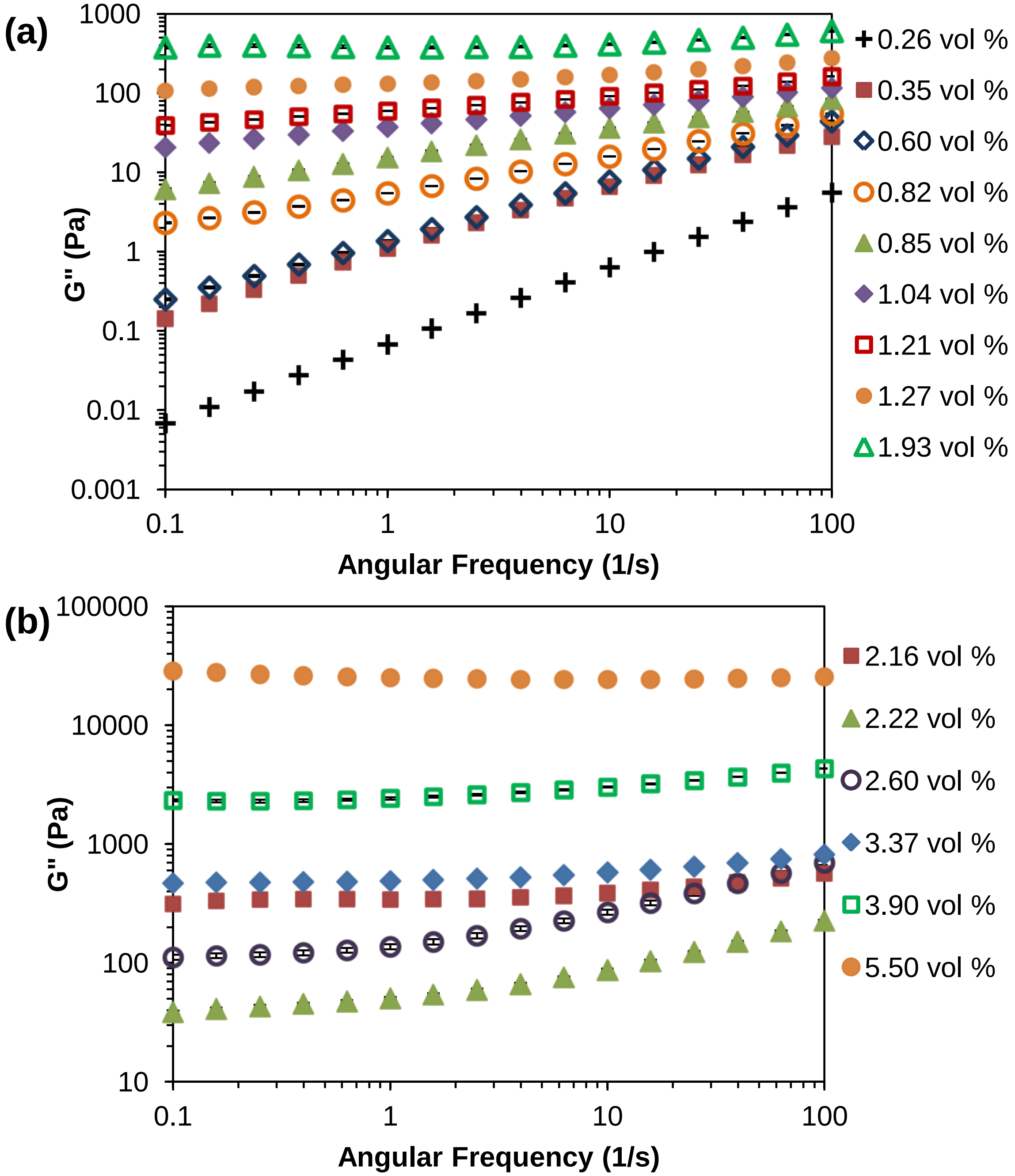

Figure 4.33. Viscous (loss) modulus G” as a function of frequency for dsDNA/SWNT supernatant dispersions at different SWNT concentrations.

Both the G’ and G” at a certain angular frequencies showed a nonmonotonic relationship with increasing SWNT concentration in dsDNA/SWNT supernatant dispersions as shown in Figure 4.34. Initially, the G’ at 0.1 1/s kept increasing rapidly with concentration and reached a maximum near 1.93 vol % SWNT. The maximum in G’ at 0.1 1/s was obtained at similar SWNT concentration as the dynamic viscosity maximum at the same frequency. An equally rapid decrease of G’ occurred as the amount of anisotropic phase increased and showed a local minimum at 2.22 vol % SWNT. After this point, the G’ started to continuously increase again as a function of concentration. The same trends were observed at different frequencies, yet the value of the G’ maximum increased with increasing frequency. The maximum in G’ was also shifted to slightly lower SWNT concentration when increasing frequency from 0.1 to 100 1/s. Similarly, the local maximums and minimums obtained for loss modulus G” at 0.1 to 10 1/s frequencies with increasing concentration were at the very similar SWNT concentrations of storage modulus G’ versus concentration curves (Figure 4.34b). However, there are no apparent changes in the G” maximum values at different frequencies, and no obvious shift in concentration was observed. The curve for G” versus concentration at 100 1/s frequency was not included due to a data point fluctuation.

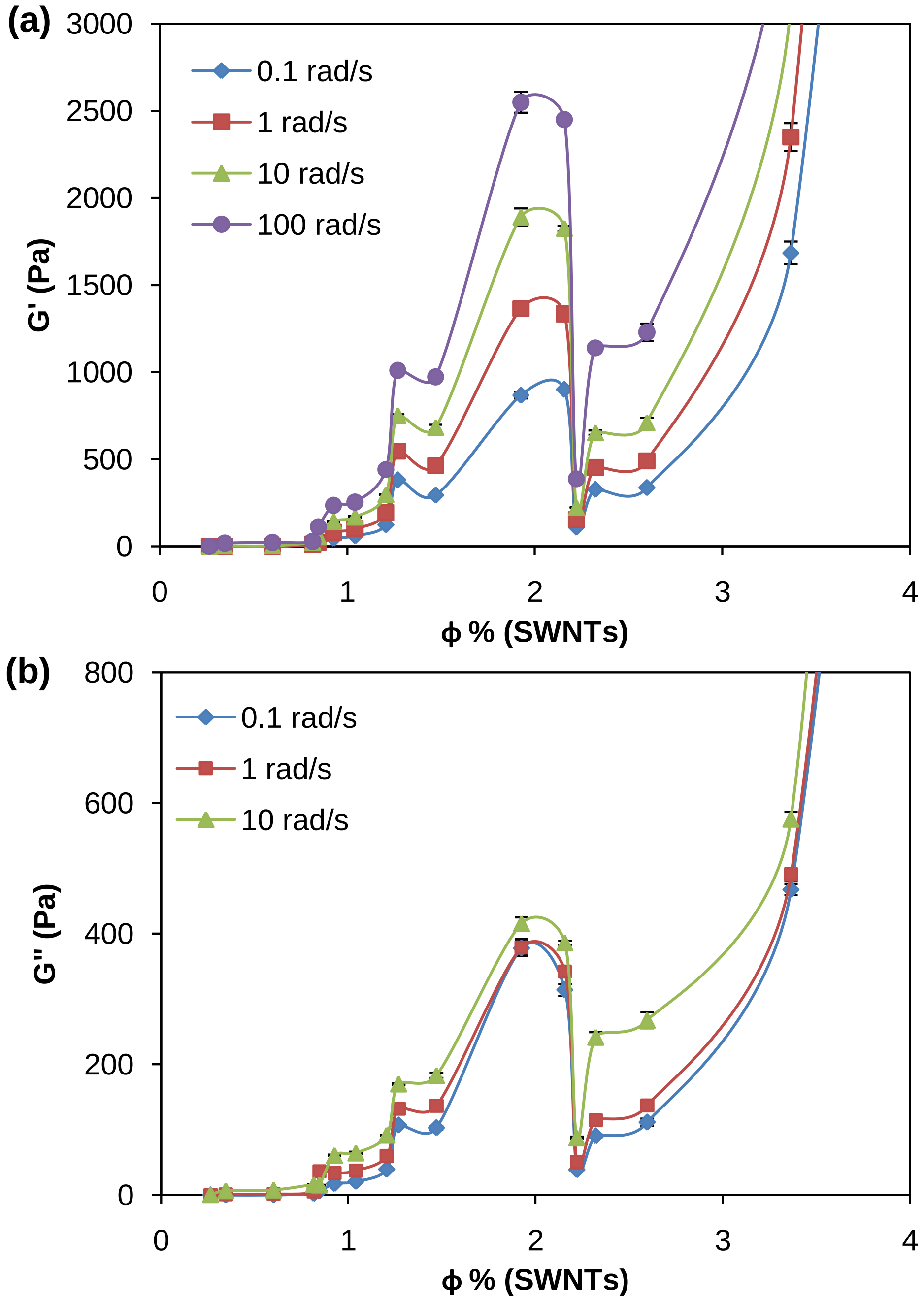

Figure 4.34. The (a) G’ and (b) G” as a function of concentration at different angular frequency for dsDNA/SWNT supernatant dispersions.

**Temperature Study.** Studies of temperature effects on the rheology of supernatant dsDNA/SWNT dispersions at isotropic and higher concentration and concentrated bulk dispersions were investigated by rheology. Temperature was increased in the range of 10 to 35 $^{o}$C for concentrated samples. At an even higher temperature of 40 $^{o}$C for concentrated dispersions, both evaporation and structural change introduced large error in measurements. The time-temperature superposition (TTS) was obtained by shifting collected data with respect to both horizontal and vertical shift factors. For steady shear and complex viscosity, $\eta_r = \eta/a_T$ (or $\eta_r^* = \eta^*/a_T$), was plotted against the reduced shear rate or angular frequency, $\dot{\gamma}_r = \dot{\gamma}\ a_T$ (or $\omega_r = \omega\ a_T$). The inverse time shift factor was defined as $a_T = \eta_0(T)/\eta_0(T_0)$, where $T$ was the measuring temperature and $T_0$ is the reference temperature which was chosen as 25 $^{o}$C. Usually, the stress shift factor is taken as a unity. Figure 4.35 shows the TTS of an isotropic dispersion of supernatant dsDNA/SWNT at 0.33 vol % SWNT concentration. Both the steady shear and complex viscosities decreased with increasing temperature from 10 to 40 $^{o}$C and overlapped to a single master curve in the measured shear rate and angular frequency range, respectively. As for storage modulus, there were deviations at high angular frequencies with increasing temperature. This may have been caused by the fact that at higher temperature, the sample was less viscous and it was difficult to measure storage modulus at higher angular frequencies due to relatively high inertia force of rotating bob.

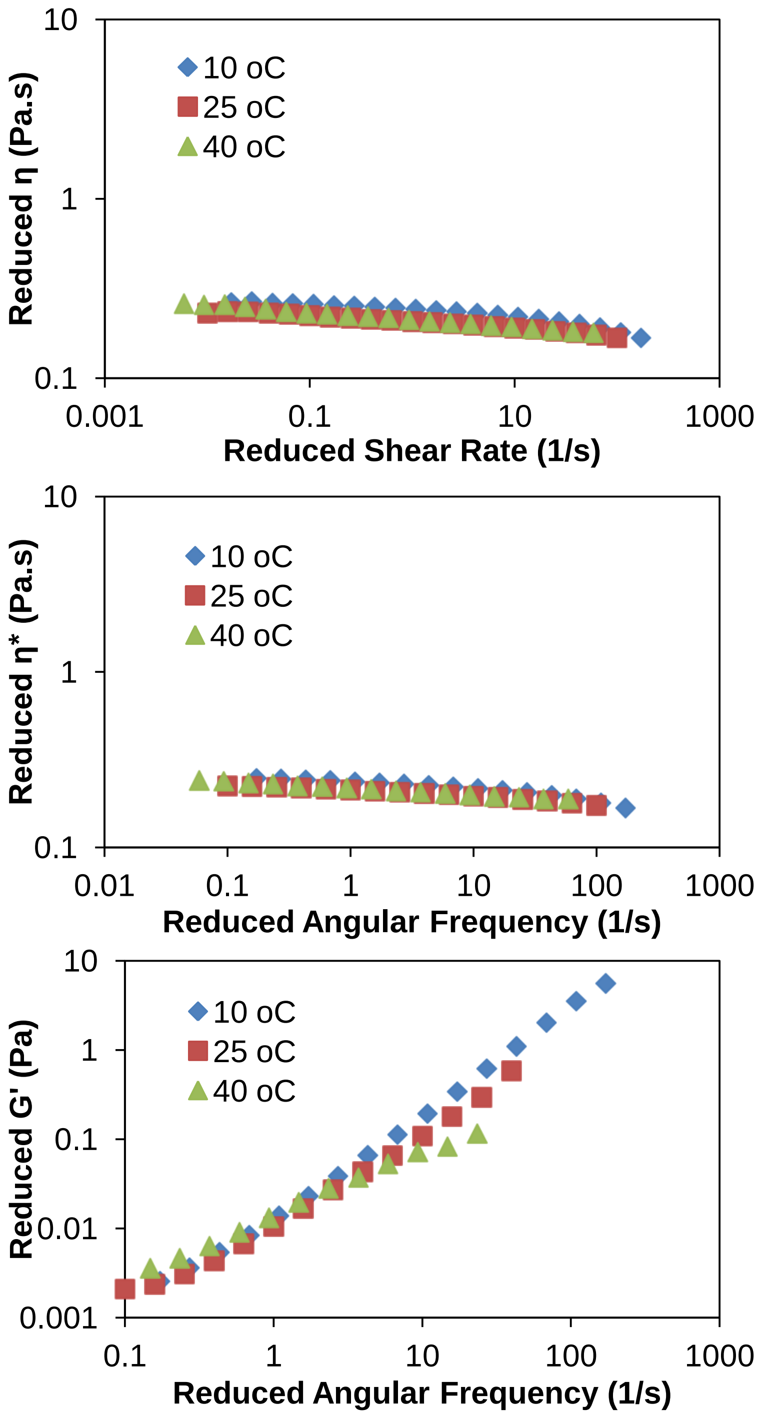

Figure 4.35. Time-temperature superposition of supernatant dsDNA/SWNT (Rice 187.2) dispersions with 4.4:1 dsDNA:SWNT ratio by volume at SWNT concentration of 0.33 vol %; (a) steady shear viscosity versus shear rate, (b) complex viscosity versus angular frequency, and (c) storage modulus versus angular frequency at various temperatures of 10, 25, and 40 $^{o}$C.

Figure 4.36 shows the TTS of concentrated supernatant dsDNA/SWNT dispersions with 3.74 vol % SWNT at different concentration from 10 to 35 $^{o}$C. Similarly, viscosities and storage modulus decreased with increasing temperature. In general, the TTS of concentrated supernatant dispersions gave overlapped master curves. When plotting the reduced steady shear and complex viscosities as a function of reduced shear rate and angular frequencies, viscosity master curves were obtained, though viscosities at 10 $^{o}$C were slightly deviated from master curves. For TTS of the storage modulus, the G' at 10 $^{o}$C had more deviation from the master curve. The shifted values of viscosities and storage modulus at 25 and 35 $^{o}$C overlapped nearly perfectly.

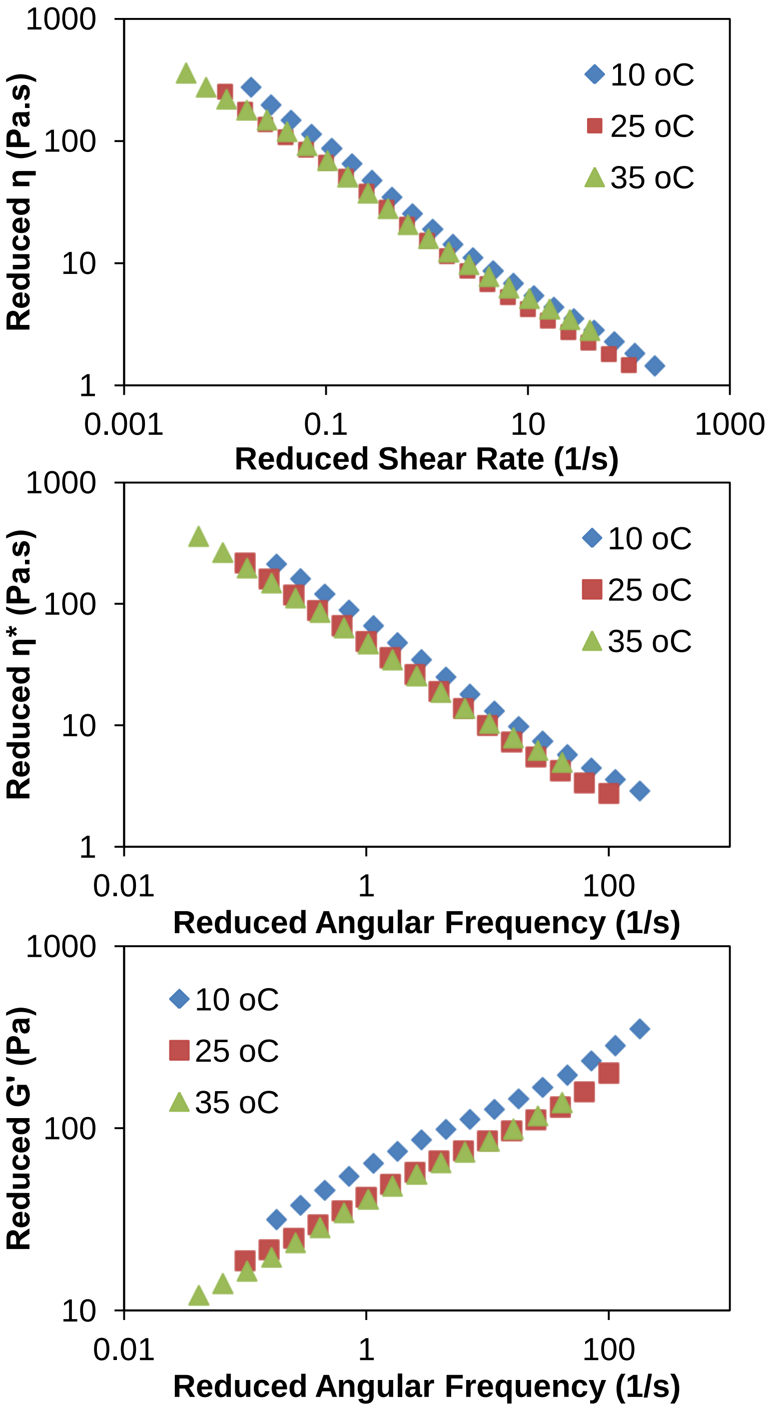

Figure 4.36. Time-temperature superposition of supernatant dsDNA/SWNT (Rice 187.2) dispersions with 4.4:1 dsDNA:SWNT ratio by volume at SWNT concentration of 3.74 vol %; (a) steady shear viscosity versus shear rate, (b) complex viscosity versus angular frequency, and (c) storage modulus versus angular frequency at various temperatures of 10, 25, and 35 $^{o}$C.

Studies of temperature effects on the rheology of 6.4:1 by volume bulk dsDNA/SWNT dispersions at SWNT concentration of 1.67 vol % were also investigated by rheology. When increasing the temperature from 10 to 35 $^{o}$C, a slight decrease in the steady shear viscosity of bulk dsDNA/SWNT dispersion was observed. The TTS of $\eta$ fall onto a master curve showing a rapid shear shear thinning region at lower shear rate and a slower shear thinning region at higher shear rate as shown in Figure 4.37a. More specifically, at a higher temperature of 35 $^{o}$C, it is more obvious that the $\eta$ versus shear rate curve changes from power law shear thinning to detectable two shear thinning regions with different slopes separated by a transition region more like a plateau. This behavior may be due to a structural change or phase transition occurring in the system at higher temperature of 35 $^{o}$C. Further evidence of structural change at 35 $^{o}$C can be seen from the TTS of the dynamic measurement of both complex viscosity and storage modulus as shown in Figure 4.37b,c. Both the $\eta$* and G' at 35 $^{o}$C drifted away from the master curve obtained at 10 and 25 $^{o}$C.

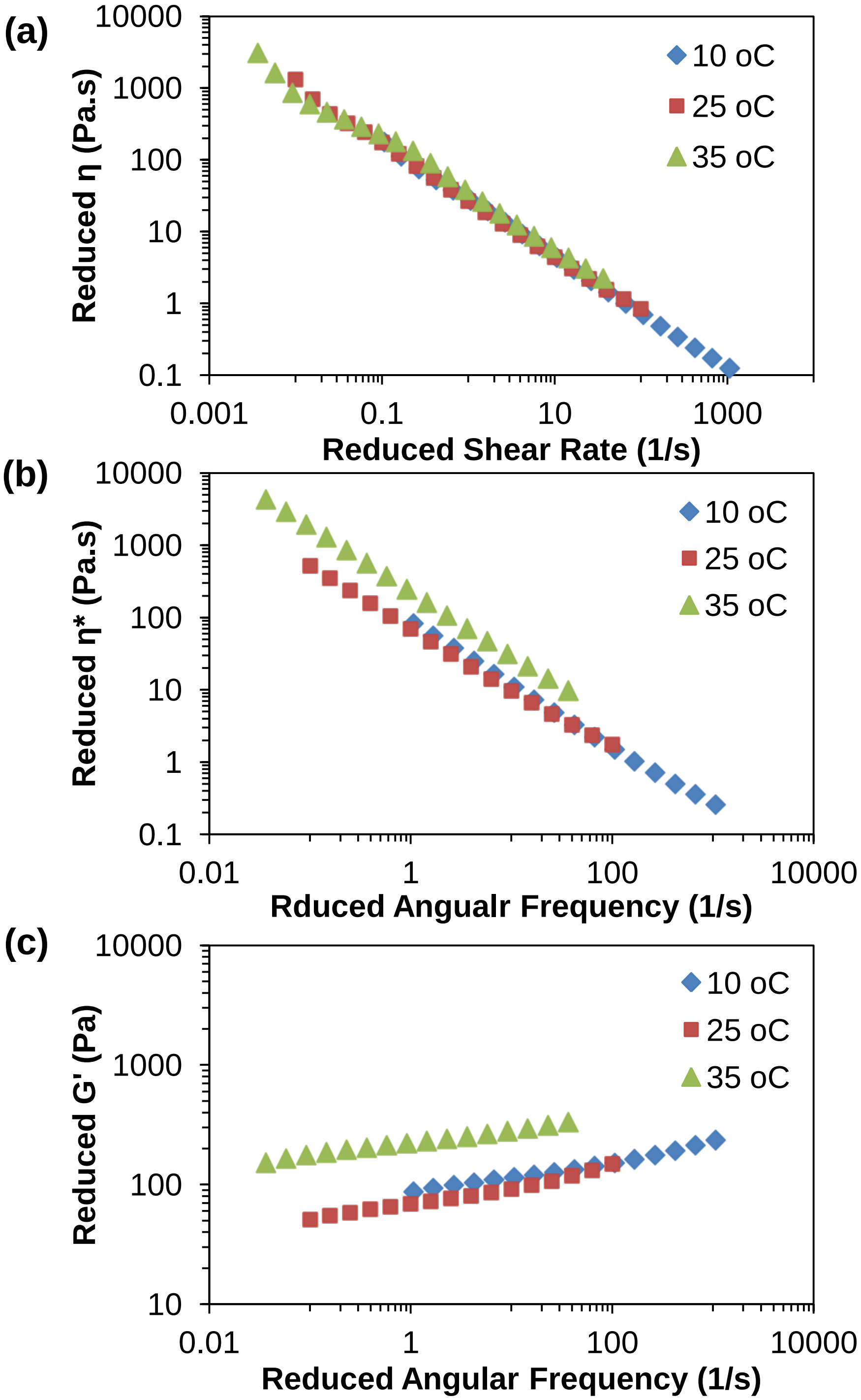

Figure 4.37. Time-temperature superposition of bulk dsDNA/SWNT (Rice 187.2) dispersions with 6.4:1 dsDNA:SWNT ratio by volume at SWNT concentration of 1.67 vol %; (a) steady shear viscosity versus shear rate, (b) complex viscosity versus angular frequency, and (c) storage modulus versus angular frequency at various temperatures of 10, 25, and 35 $^{o}$C.

## 4.4. Conclusions

The phase behavior and rheology of aqueous dsDNA/SWNT dispersions were determined by a combination of polarized optical microscopy. Concentration of bulk (noncentrifuged) dsDNA/SWNT dispersions consisting of both bundled and individual SWNT led to the formation of polydomain nematic phase. While evaporating the supernatant dispersions resulted in cholesteric phase formation. The summary of rheological data obtained from both bulk and supernatant dsDNA/SWNT dispersions and dsDNA only solutions is shown in Table 4.4. Rheology can detect both the biphasic – liquid crystal transition at the critical concentration $\phi_N$ and the liquid crystal – gel transition at even higher concentration. In addition, the nematic and cholesteric phases of dsDNA/SWNT dispersions showed different rheological behavior, especially with different shear thinning behavior in viscosity versus shear stress plots. Reproducible viscosity kinks in both nematic and cholesteric phases may be an indication of director movement transition in the polydomain texture. The empirical Cox-Merz rule was not obeyed in the dsDNA/SWNT system indicating the formation of liquid crystals. Moreover, the percolation threshold can be calculated from the storage modulus in oscillatory test. Temperature effects on rheological characteristics of both nematic and cholesteric dsDNA/SWNT dispersions were investigated and corresponding time – temperature superposition was obtained.

Table 4.4. Comparison of key rheological parameters of three different systems.

| Samples | $\sim\phi_P$ (vol %) | $\eta_{\max}$ (Pa.s) | $\phi_1(\eta_{\max})$ (vol %) | $\eta_{\min}$ (Pa.s) | $\phi_2(\eta_{\min})$ (vol %) | $G'_{\max}$ (Pa) | $\phi_3(G'_{\max})$ (vol %) | $\gamma_C(\phi_3)$ (%) | $\tan\delta(\phi_3)$ | $G'_{\min}$ (Pa) | $\phi_4(G'_{\min})$ (vol %) | $\gamma_C(\phi_4)$ (%) | $\tan\delta(\phi_4)$ |
|---|---|---|---|---|---|---|---|---|---|---|---|---|---|
| Non-centrifuged dsDNA:SWNT=6.4:1 | 1.01 | 2175 | 3.31 | 1500 | 3.91 | 3270 | 3.31 | 3.95 | 0.20 | 2070 | 3.91 | 6.31 | 0.23 |
| Supernatant dsDNA:SWNT=4.4:1 | 0.82 | 2165 | 1.47 | 106.4 | 2.22 | 901.5 | 2.16 | 10 | 0.35 | 110 | 2.22 | 3.98 | 0.35 |
| dsDNA only | 7.1 | 66.55 | 4.53 | 27.35 | 6.17 | | | | | | | | |

1) Max. and Min. are the values at 0.1 $s^{-1}$ shear rate or angular frequency on the nonmonotonic phase transition plots versus volume fraction $\phi$. Maximum value is in the biphasic region, and minimum value usually corresponds to the single LC phase formation.

2) $\phi_P$ is the volume fraction where percolation occurs; $\eta$ is bulk viscosity; $G'$ is storage modulus; $\gamma_C$ is critical strain; $\tan\delta$ is damping factor.

∗ No max. and min. values were obtained from G’ versus volume fractions plots for dsDNA only in this preliminary experiments.

## Chapter 5

## Macroscopic Assembly of Films and Fibers

The remarkable properties of single-walled carbon nanotube (SWNT) can be realized when they are translated into macroscopic objects such as SWNT films and fibers. However, the strong van der Waals interaction and random entanglement of synthesized SWNT remains a key scientific challenge that limits their real world applications. It has previously been shown that processing nematic liquid crystalline dispersions is a promising route for producing aligned solid materials such as films and fibers.[10,20,217] Considerably less is known about processing lyotropic cholesteric dispersions.[48] In this chapter, various SWNT dispersions were assembled into films and fibers by fluid phase processing. In addition, the optical, electrical, and mechanical properties of films and fibers were determined.

### 5.1. dsDNA/SWNT Films

Research on cellulose nanowhisker liquid crystals has shown that retention of helicity during processing can enable films with controllable optical properties that can be used for such circular polarizers, reflective displays and security papers.[22,23] Spreading cholesteric dsDNA/SWNT dispersions (2.0 vol % of SWNT) onto copper tape by roller coating, allowing the coating to dry, and removing the substrate resulted in approximately 20 μm thick films which were translucent under ambient light (Figure 5.1a). Under cross polarized light they appeared either bright or dark depending on the orientation of the polarizer. SEM of these films (Figure 5.2) revealed a aligned densely packed structure comprised of dsDNA/SWNT bundles ranging from 8 to 22 nm in diameter. The alignment and packing in this microstructure is far superior to previously reported aligned dsDNA/SWNT films produced from dilute dispersions using layer-by-layer assembly and drying under a directed air stream.[1] These results may indicate the shear applied during processing induced in a cholesteric to nematic transition such as that previously proposed for rod-like polymer solutions.

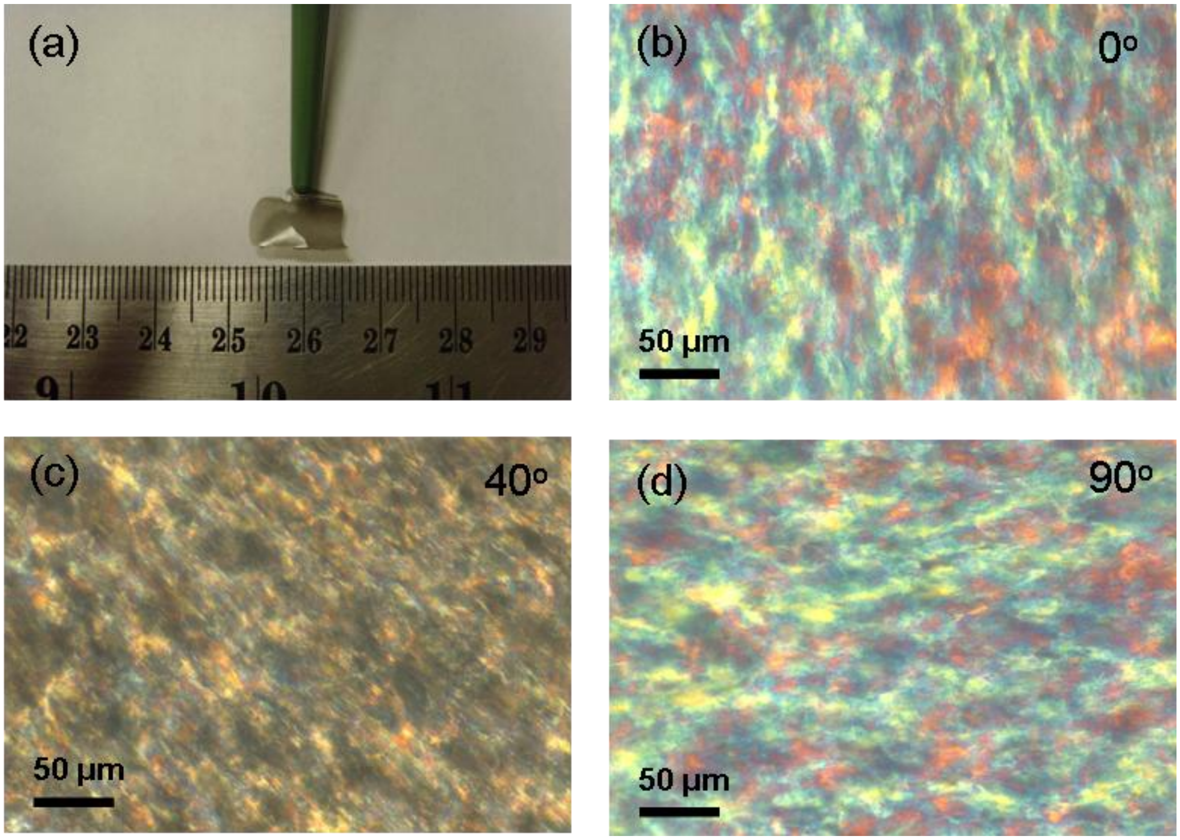

Figure 5.1. (a) Translucent film obtained from a 4.4:1.0 by volume supernatant of dsDNA/SWNT dispersion (~2.0 vol % of SWNT) by shearing at approximately 500 $s^{-1}$ shear rate. (b-d) Cross-polarized optical microcopy images of films prepared without applied shear. The colors vary as the sample is rotated in (d) 0 °, (e) 40 °, and (f) 90 °. Nikon Eclipse 80i with LU Plan Fluor 20x/0.45 objective with 20× magnification and 1.5 magnification in front of the camera was used. The scale bars in the figures are 50 µm.

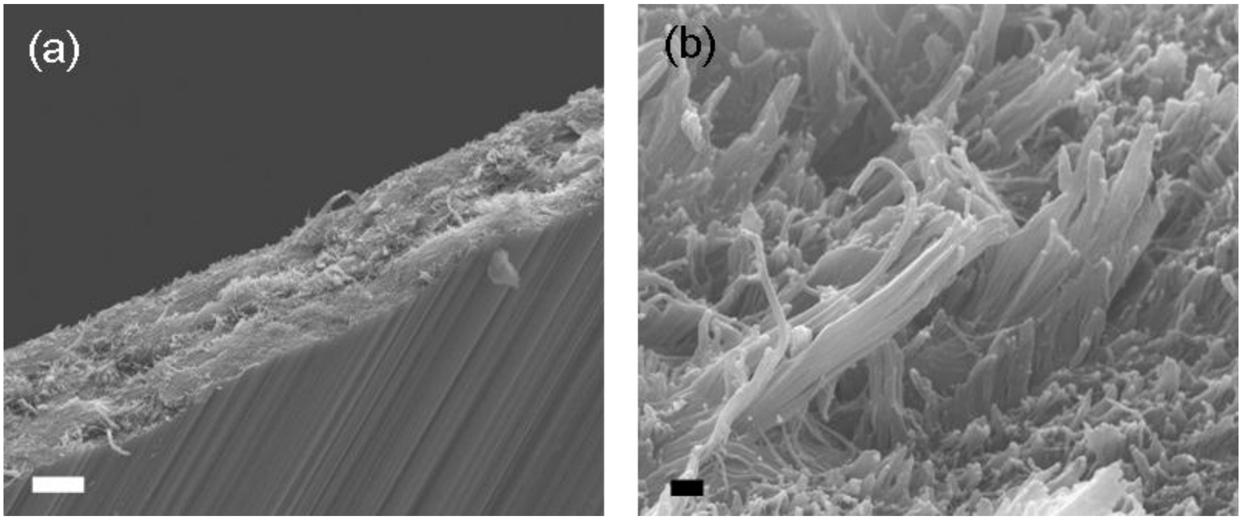

Figure 5.2. SEM images of translucent films obtained from a 4.4:1.0 by volume supernatant of dsDNA/SWNT dispersion (~2.0 vol % of SWNT) by shearing at approximately 500 $s^{-1}$ shear rate. The scale bar in (a) is 10μm and in (b) is 200 nm.

Producing the films by simply dropping the cholesteric dispersions onto the tape and not applying any shear also resulted in materials that were translucent under ambient light. However, under cross polarized light these films showed bright birefringent bands indicative of the retention of cholesteric structure (Figure 5.1 b-d). These films are similar in appearance to those obtained by Lee et al.[218] for films produced from a helical liquid crystalline phase of Au-antistreptavidin M13 virus. Since the effects of shear on cholesteric liquid crystals are not as well understood as the effects of shear on nematic liquid crystal, rheo-optical characterization was used to provide insights into the shear induced unwinding of cholesteric phases into nematic phases. Preliminary investigations of shear effects on the cholesteric pitch of dsDNA/SWNT (Rice 187.2) dispersion at 2.32 vol % SWNT using a Linkam shear cell at a 30 μm gap at a room temperature were performed. When shearing the sample at a small shear rate of 0.25 $s^{-1}$ for a few second ~10s, the cholesteric pitch showed a slight increase from 1.59 ± 0.18 to 1.84 ± 0.24 μm after cessation of shear.

## 5.2. dsDNA/SWNT Fiber Spinning

At the preliminary stage of the fiber spinning research, cholesteric dsDNA/SWNT supernatant dispersions with higher concentrations of SWNT were quenched into various alcohol and acetone coagulants. Fibers were only obtained in some coagulants such as ethanol (95 %), 2-propanol (99.8 +%), and tert-butanol. The surface of these fibers showed various textures including spherical (with diameter 70-150 nm) and rod-like (60-80 nm in width and several hundred nm in length) particles, wavy or smooth structures (Figure 5.3). These different structures could be caused by many factors such as the different coagulants used, residence time, orifice diameter of the syringe needle, and extruding speed which are important in effecting the boundary conditions of fiber coagulating process. Many studies have been conducted to use alcohols (especially ethanol, 2-propanol, and tert-butanol), sometimes adding multivalent cations into the alcohols/water mixtures, to induce DNA condensation which is caused by the charge neutralization of DNA phosphate charge. The dehydrating action of alcohols reduces the water activity through the reduction of dielectric constant of the solvent medium.[219-222] Considering that high purity alcohols were used in this work, DNA molecules on the surface were further aggregated into a fibrous network and transitioned into a more compact DNA structure as shown in Figure 5.3b, c.[219] The formation of relatively smooth and wavy surfaces, it might have been due to the shorter residence time in coagulants in which the spine of hydration stabilizing the DNA was not affected seriously. Moreover, when the residence time in a coagulant was comparatively short, the fiber surface showed continuous fibril structure (Figure 5.3e).

Preliminary EDS elemental analysis showed that the carbon content in fibers decreased along the radius radiation from 72.98-36.84 C wt % in center to 17.88-36.78 C wt % on the surface. In contrast, the phosphorous content increased from 2.91-7.81 P wt % to 6.36-16.58 P wt %. Since the samples were sputter coated with gold for better imaging under SEM, the gold content of 20.98-63.92 Au wt % was also detected on the surface. This could cause error in the elemental percentages. The relative degree of SWNT alignment in dsDNA/SWNT fiber was quantified by the difference in G band at different angles in Raman spectroscopy using 785 nm wavelength laser. The G band corresponds to $sp^2$ tangential mode of the nanotube and was located near 1595 $cm^{-1}$ wavenumber in this fiber sample. The ratio of G peak intensities, with the laser aligned parallel to the fiber’s long axis and perpendicular to the long axis, was in the range of 1.9 to 5, which indicated relatively low alignment of nanotube as shown in Figure 5.4. It is possible that, the complex surface morphology and the DNA coating on the fiber surface prevented signaling the alignment of nanotube in the inner side of fiber sample.

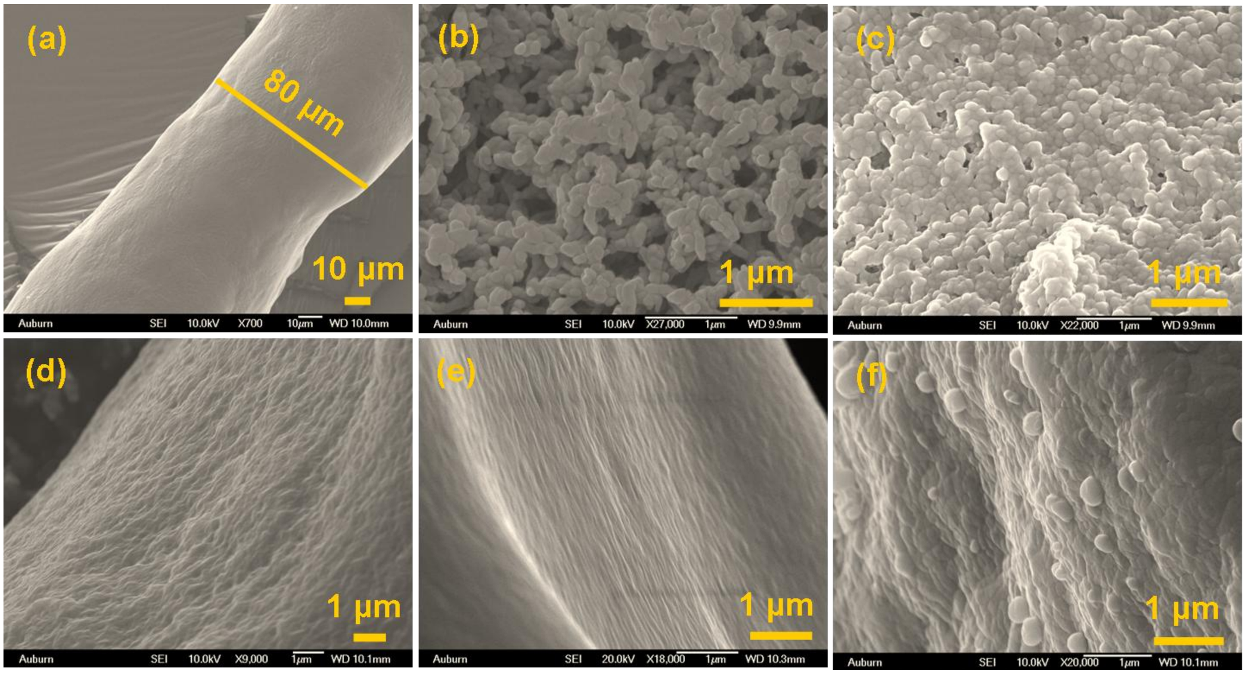

Figure 5.3. Scanning electron microscope images of fibers extruded from cholesteric LC dispersion of dsDNA/SWNT (1.98 vol % of SWNT) in (a), (b), (d), (e) 2-propanol, (c) ethanol, and (f) tert-butanol. The fiber diameter is ~81 μm in (a). The scale bar of the first image is 10 μm and the rest of them are 1 μm.

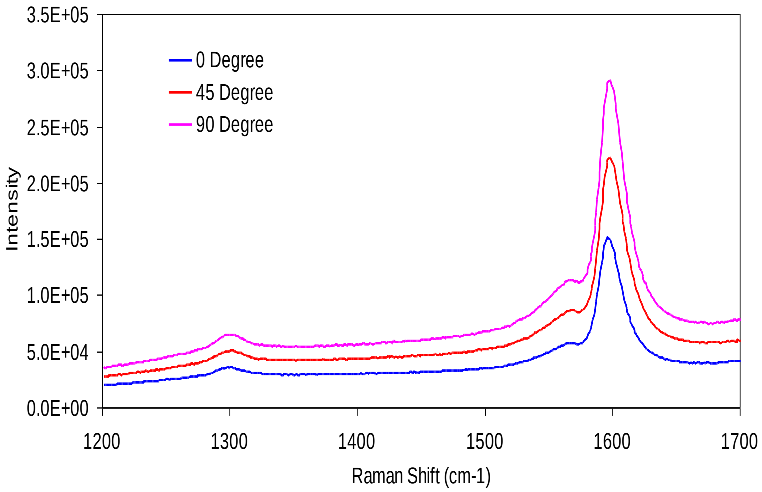

Figure 5.4. Raman Spectra at 785 nm excitation of fiber spun from cholesteric dispersion of dsDNA/SWNT (1.98 vol % SWNT) in ethanol.

In addition, a bulk (noncentrifuged) dispersion with 6.4:1 volume ratio of dsDNA:SWNT at ~ 3.4 vol % SWNT was also assembled into fibers via two separate paths; dry spinning and wet spinning. A 22 G syringe needle (0.41 mm inner diameter) was used and slower injection rate of 0.2 ml/min was chosen for fiber spinning from the bulk dsDNA/SWNT dispersion. The wet spun fibers of dsDNA/SWNT dispersion were coagulated into 1-butanol bath. For dry spinning, a Teflon plate was used to collect the SWNT dispersion extruded from a syringe. Mechanical and electrical properties of the dry spun fibers were determined after they were dried at ambient condition overnight and further vacuum dried at room temperature for 4 hr. The fiber spinning from various SWNT dispersions is still in the preliminary stage toward the development of an improved fiber spinning scheme. Optimization of initial SWNT dispersions and their fiber spinning process is ongoing.

As shown in Figure 5.5, although having an uniform shape in general, the surface structures of fibers produced from bulk (noncentrifuged) dsDNA/SWNT dispersions by either wet spinning in 1-butanol or dry spinning, were still not as smooth as those of PVA coagulated lysozyme/SWNT fibers which are discussed in the next section. Especially for fibers coagulated in 1-butanol, more irregular structures were observed. This is may be due to DNA condensation in the alcohol environment (Figure 5.5b). Interestingly, the surface morphology of dry spun fibers differed depending on whether their surfaces were in contact with air or the Teflon plate (Figure 5.5c, d). The fiber surface in contact with the Teflon plate when drying showed much smoother structures. It is difficult to see the nanotube alignment on the surface due to the DNA coating. However, large amount of small SWNT bundles pulled out from the dsDNA interacted SWNT fiber can be observed at the cross section of fibers (Figure 5.6a). The SWNT bundle size was determined to be around ~15 nm in diameter from Figure 5.6b at higher magnification. In

Figure 5.6c, the cross section of fiber also showed that, dsDNA/SWNT fibers produced by coagulation in 1-butanol had a loose structure overall with many voids and holes inside.

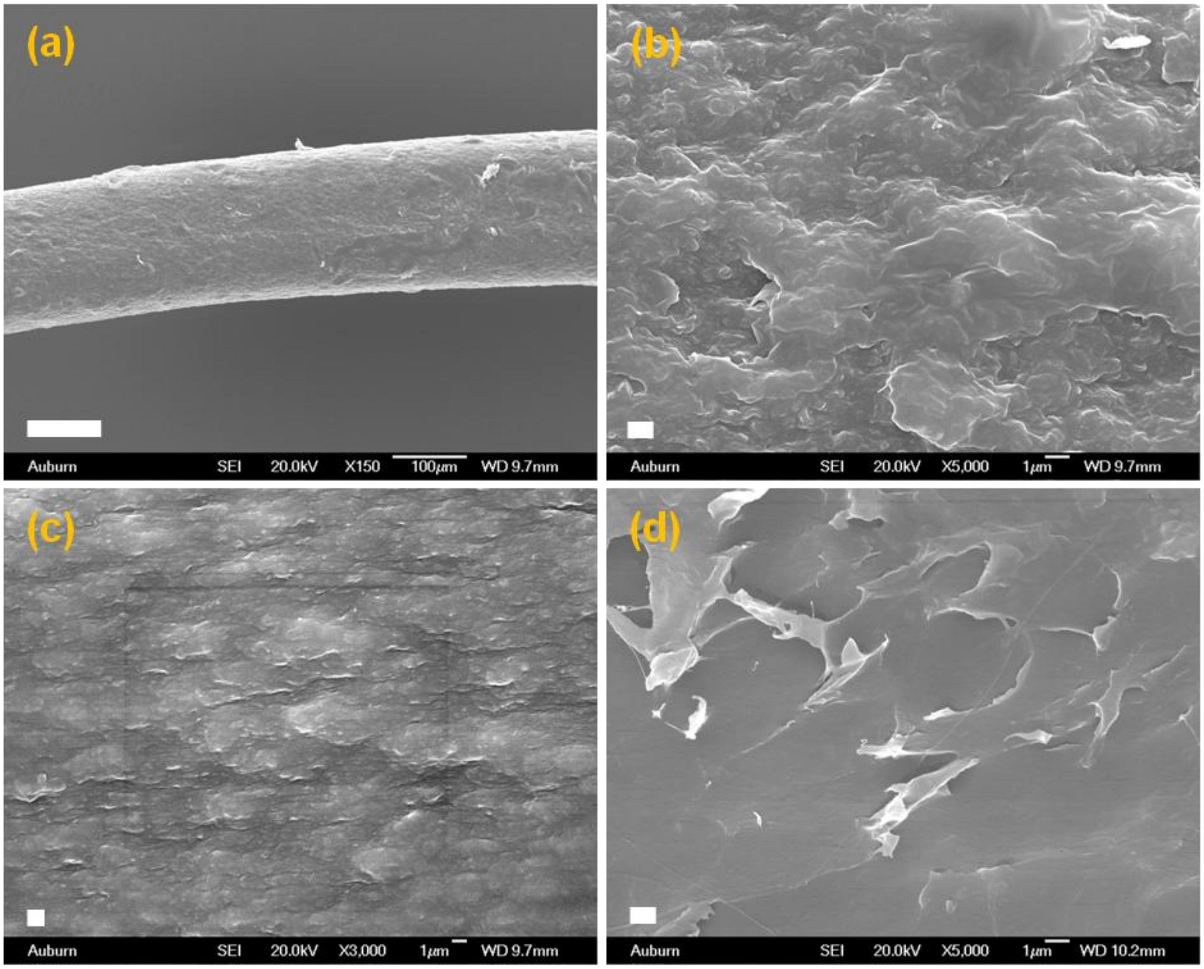

Figure 5.5. Scanning electron micrographs of fibers spun from bulk (noncentrifuged) 6.4:1 by volume dsDNA/SWNT dispersion with ~3.4 vol % SWNT by (a) coagulating in 1-butanol and (b) its subsequent surface structure. For dry spinning fibers, surfaces of fibers (c) in contact with air and (d) Teflon have different structures. The scale bars are (a) 100 μm and (b, c, d) 1 μm.

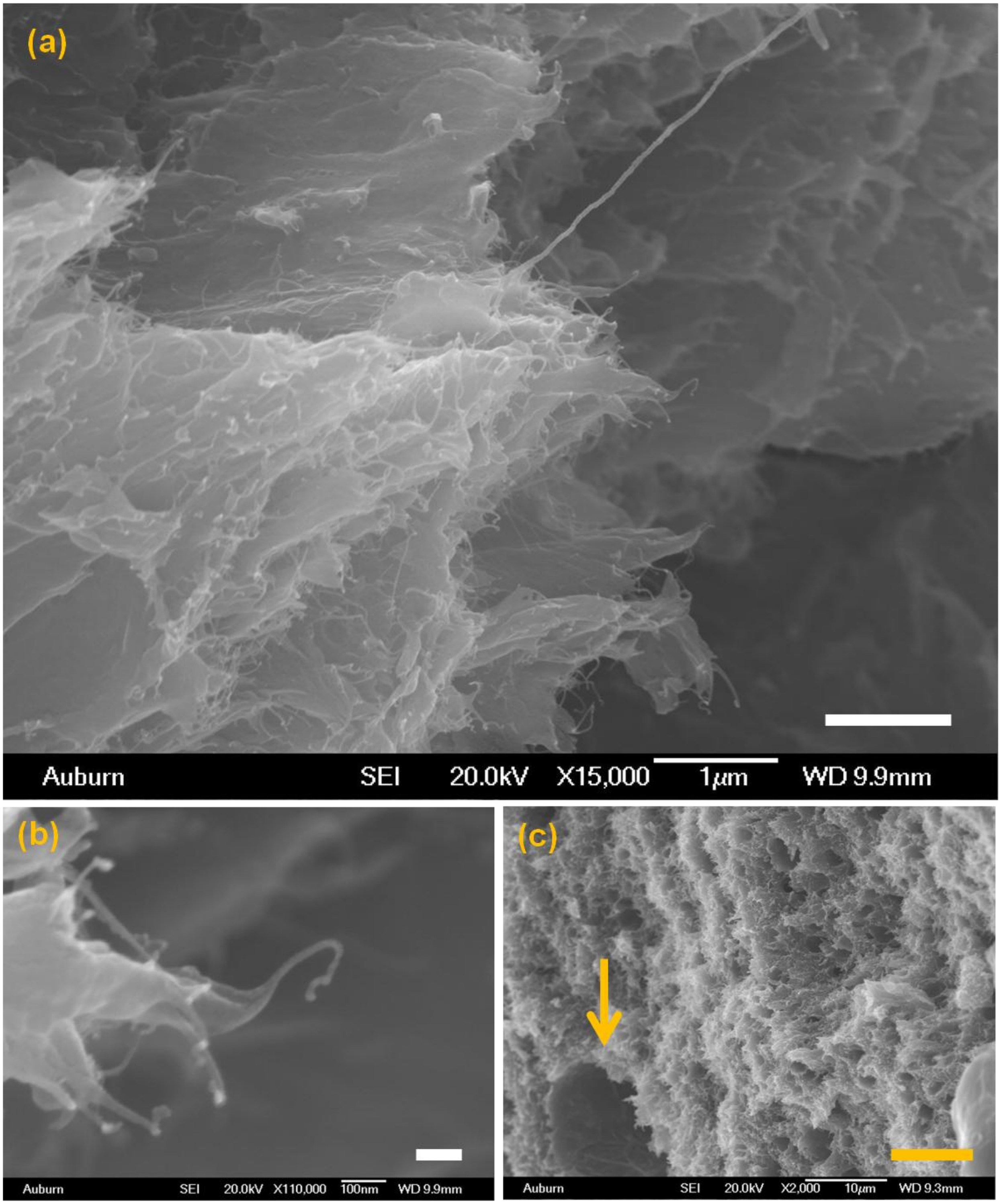

Figure 5.6. Scanning electron micrographs of cross-section structures of fibers produced from bulk 6.4:1 by volume dsDNA/SWNT dispersion with ~3.4 vol % SWNT by (a, b) dry spinning, and (c) coagulation in 1-butanol. The scale bars are (a) 1 μm, (b) 100 nm, and (c) 10 μm.

## 5.3. Lysozyme/SWNT Fiber Spinning

Wet solution spinning of lysozyme/SWNT dispersions into the co-flow stream of a polymer solution was performed in collaboration with Dr. Philippe Poulin's group at Centre de Recherché Paul Pascal - Centre National de la Recherché Scientifique (CRPP-CNRS) in Bordeaux, France. The focus of this work was to improve the dispersion and fiber spinning of single-walled carbon nanotubes in aqueous lysozyme (LSZ). Lysozyme is an enzyme protein with antibacterial activity and its ability to disperse SWNT as individuals has been previously shown by Nepal et al.[1] The addition of cationic surfactant (1-tetradecyl) trimethyl-ammonium bromide (TTAB) into the LSZ/SWNT dispersion plays an important role of stabilizing SWNT through electrostatic repulsion which counteracts with the van der Waals attraction of SWNT.[14,21] TTAB has a cationic detergent with a positively charged ammonium bromide head group and a 14 carbon tail. Although it would be difficult to deconvolute molecular interactions in the complex system of LSZ/TTAB/SWNT aqueous dispersions, the main interactions are considered to be hydrophobic in nature and exist between the sidewall of SWNT, hydrophobic core of LSZ, and hydrophobic alkyl-tail of TTAB.[78,223-225] Both purified and non-purified SWNT were used to prepare LSZ/TTAB/SWNT dispersions for macroscopic assembly into fibers in a 5 wt % polymer PVA coagulation bath. The injection rate of LSZ/TTAB/SWNT dispersion was 50 ml/hr.

The PVA coagulated fibers, shown in Figure 5.7, had conical geometries and smooth surfaces due to PVA coating on the outer side of fibers. Fibers composed of more than one strand, were made through collapsing wet PVA coagulated individual SWNT ribbons on top of one another during hang-drying to produce a single, larger fiber. Looking closely at Figure 5.7a, small ridges near the conical edge of the fiber can be seen. These ridges are due to the collapsing of individual fibers onto one another creating discontinuities in the structure. This phenomenon can be seen much more clearly in Figure 5.7b where the ridges occur not only at the edges but throughout the fiber. The increased discontinuity in the 22 strand fiber is simply due to the increased number of strands that were collapsed. According to SEM, the diameter of a single strand is about 10-15 μm.

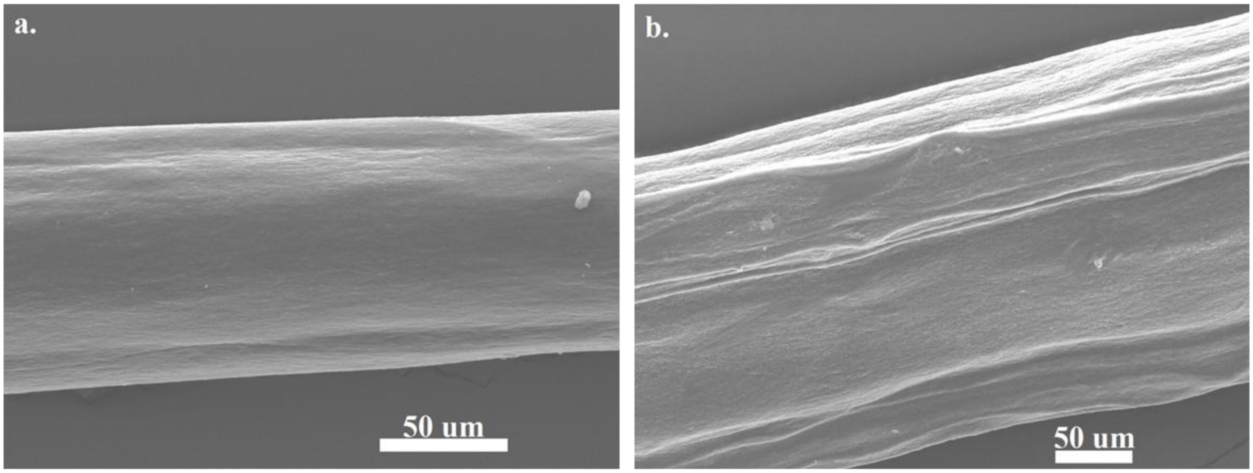

Figure 5.7. Scanning electron micrographs of (a) 7 strands and (b) 22 strands PVA coagulated LSZ/TTAB/SWNT fibers showing smooth structure and evidence of collapsing of multiple fibers.

## 5.4. Fiber Properties

Mechanical and electrical properties were measured on dry SWNT fibers. Table 5.1 shows the electrical resistivity and conductivity of PVA coagulated LSZ/SWNT/TTAB fibers using purified and non purified SWNT and dsDNA/SWNT fibers produced from dry and wet spinning methods. Comparison of the electrical properties shows that dsDNA/SWNT fibers showed much higher resistivity than PVA coagulated LSZ/TTAB/SWNT fibers. Since the initial bulk dispersion of dsDNA/SWNT has high weight ratio of 7.5:1 (6.4:1 by volume) dsDNA:SWNT, the existence of large content of non conducting dsDNA polymer caused high electrical resistivity in the resulting dried fibers. Especially for dsDNA/SWNT fibers coagulated in 1-butanol the resistivity was very high at 145 ± 13.17 Ω·cm. This could be caused by DNA condensation in alcohol resulting in a more electrical resistant structure. As a comparison, the electrical conductivity of PVA coagulated fibers from isotropic dispersion of 0.4 wt% ssDNA-0.4 wt% SWNT was reported to be 0.042 S/cm, which is 23.8 Ω·cm in resistivity.[198] Although the electrical resistivity of LSZ/TTAB/SWNT fibers is relatively lower than that of ssDNA/SWNT fibers, it is still very large when compared to reported values of PVA coagulated SDS/SWNT fibers[14] and fibers consisting solely of SNWTs.[10] When the insulating polymer PVA was used to coagulate the wet spun fibers, it naturally inhibited the flow of electrical current thereby reducing the conductivity of the resulting fibers.

The mechanical properties tested were Young's modulus, tensile strength, and strain at break. Table 5.2 shows the mechanical test data of various SWNT fibers. In general, the mechanical test data shows that PVA coagulated LSZ/TTAB/SWNT fibers were more mechanically robust than dsDNA/SWNT fibers. The reasoning for improved mechanical properties is the incorporation of PVA within the fiber during the coagulation process. The addition of the PVA not only increases the tensile properties of the fiber but also increases the stiffness by providing a strong bridging effect between SWNT bundles.[11,14] Again, the mechanical properties of fibers obtained in this work is still inferior to those of previously reported fibers, including PVA coagulated ssDNA/SWNT fibers which had Young's modulus of 14.1 GPa, and tensile strength of 110 MPa. In order to improve the performance of SWNT fibers, both the initial SWNT dispersion used and the process of fiber spinning need to be optimized in future work.

Table 5.1. Electrical resistivity and conductivity of various SWNT fibers from both wet spun and dry spun assembly methods.

| Sample | Electrical Properties | |
|---|---|---|
| | Electrical Resistivity, ρ (Ω·cm) | Electrical Conductivity, c (S $m^{-1}$) |
| PVA coagulated LSZ/TTAB/SWNT(purified SWNT) fiber | 11.70 ± 2.09 | 8.74 ± 1.40 |
| PVA coagulated LSZ/TTAB/SWNT (non purified SWNT) fiber | 21.56 ± 4.61 | 4.89 ± 1.45 |
| 1-butanol coagulated dsDNA/SWNT fibers | 145 ± 13.17 | 0.69 ± 0.07 |
| Dry spun dsDNA/SWNT fibers | 52.37 ± 4.46 | 1.92 ± 0.17 |

Table 5.2. Mechanical properties of various SWNT fibers from both wet spun and dry spun assembly methods.

| Sample | Mechanical Properties | | |
|---|---|---|---|
| | Young's Modulus (GPa) | Tensile Strength (MPa) | Strain at Failure (%) |
| PVA coagulated LSZ/TTAB/SWNT (purified SWNT) fiber | 3.48 ±0.89 | 49.12 ±10.95 | 6.30 ±7.48 |
| PVA coagulated LSZ/TTAB/SWNT (non purified SWNT) fiber | 5.23 ±1.00 | 67.08 ±16.13 | 18.84 ±13.11 |
| 1-butanol coagulated dsDNA/SWNT fibers | 0.77 ±0.32 | 16.15 ±4.92 | 8.30 ±5.01 |
| Dry spun dsDNA/SWNT fibers | 1.28 ±0.25 | 24.42 ±5.53 | 8.33 ±3.81 |

### 5.5. Conclusions

In general, PVA coagulated LSZ/TTAB/SWNT fibers showed better mechanical and electrical properties than dsDNA/SWNT fibers produced by both wet and dry spinning methods. The PVA polymer provided a strong bridging effect between SWNT bundles and improved the mechanical properties of fibers with a compromise in lowering the electrical properties. The electrical resistivities of dsDNA/SWNT fibers were extremely high especially for wet spinning fibers in 1-butanol. In order to improve the electrical properties of dsDNA/SWNT, one possible approach is to decrease the dsDNA amount in the initial dispersion, but it needs to be sufficient enough to stabilize SWNT and prevent aggregation of nanotubes. Moreover, optimization of both intial SWNT dispersions and fiber spinning schemes is highly required.

# Chapter 6

## Phase Behavior of Lyotropic CNC Suspensions

This section reported the results of a separate collaborative research with Dr. Christopher L. Kitchens at Clemson University. Sulfonated cellulose nanocrystal (CNC) suspensions were prepared at Clemson University. The phase behavior of CNC suspensions were analyzed by rheology and optical microscopy by this work. The rheology of lyotropic CNC suspensions in the wide concentration range from isotropic to fully liquid crystalline regime was investigated to help understand the phase behavior of cholesteric phase forming systems. In this work, the temperature and concentration effects on the phase behavior of lyotropic CNC suspensions were studied by rheology, polarized light microscopy, and rheo-optical measurements using the Linkam shear cell.

### 6.1. Preparation of CNC Suspensions

The CNC used were isolated from cotton cellulose via acid hydrolysis using 64 % sulfuric acid at 45 $^{o}$C for 50 min. The final products were washed with deionized water for several days until the pH remained constant. Aqueous CNC suspensions at different concentrations were prepared by dividing the same batch into several samples and slowly evaporating the water under a nitrogen stream. CNC density of 1.64 g/ml and water density of 0.9970 g/ml were used to convert the unit of CNC weight percent into volume percent. The size distribution of samples determined by AFM showed the average length of 107 nm with a standard deviation (s) of 55 nm, the average width of 20.5 nm (s=6.1 nm), and the average height of 8.9 nm (s=2.8 nm) which has rectangular cross sections. Although washed with deionized water many times, the CNC suspensions are still acidic due to the introduction of $–SO_3H$ group on the nanocrystals surface during the acid hydrolysis process. For example, the pH value of a suspension of 1.59 vol % is 2.9 and become more acidic with increasing concentration. The acidic nature of CNC suspensions used in this work will affect its phase behavior. A detailed description of material preparation is given in Ureña-Benavides et al. 2011.[91]

### 6.2. Polarized Optical Microscopy of CNC Suspensions

The microstructure of liquid crystalline CNC suspensions was studied by polarized light microscopy. As shown in Figure 6.1, at 5.00 vol % only a small amount of liquid crystalline droplets were randomly dispersed in a continuous isotropic phase. The droplets of the anisotropic phase turned bright and dark when rotating the sample under polarized light microscopy while the continuous isotropic phase remained unchanged. With increasing concentration, the volume of liquid crystal phase increased as can be seen in 6.30 vol % sample. At 9.03 vol % the biphasic system consisted of almost uniformly dispersed isotropic and anisotropic phases at a larger region showing a strong birefringent texture. With further increase in concentration to 9.91 vol %, the sample exhibited colorful discontinuous stripes which are a characteristic texture of precholesteric ordering. The presence of an isotropic phase was still detected at the edge of microscopic samples up to 10.4 vol % of CNC, although most of the regions appeared to the birefringent and changed colors when rotated between cross-polarizers. When the concentration was increased to 12.1 vol %, the suspension was entirely birefringent including the edge. Moreover, several domains of uniform stripes resembling fingerprint textures were observed throughout the microscopic sampling indicating a cholesteric liquid crystal formation. As a comparison, the fingerprint texture observed in cholesteric dsDNA/SWNT dispersion was much more obvious. Based on these cross polarized optical microscopy results, the critical concentration of liquid crystal formation lies in the range of 10.4 vol % $< \phi_{LC} <$12.1 vol % which is much higher compared to ~2.22 vol % SWNT for cholesteric dsDNA/SWNT. According to Onsager theory, rods with low aspect ratio form liquid crystal phase at higher concentration. It is reasonable that CNC formed liquid crystal at higher concentration because the aspect ratio of CNC was much smaller compared to that of dsDNA interacted SWNT. When the concentration reached 14.5 vol %, the texture was more random although different domains change colors when rotated under cross-polarizers. However, the system behaved as a gel and no evidence of the cholesteric stripe texture was observed. The change in microstructure was further evidenced by the frequency independence of the storage modulus measured at 10 $^{o}$C.

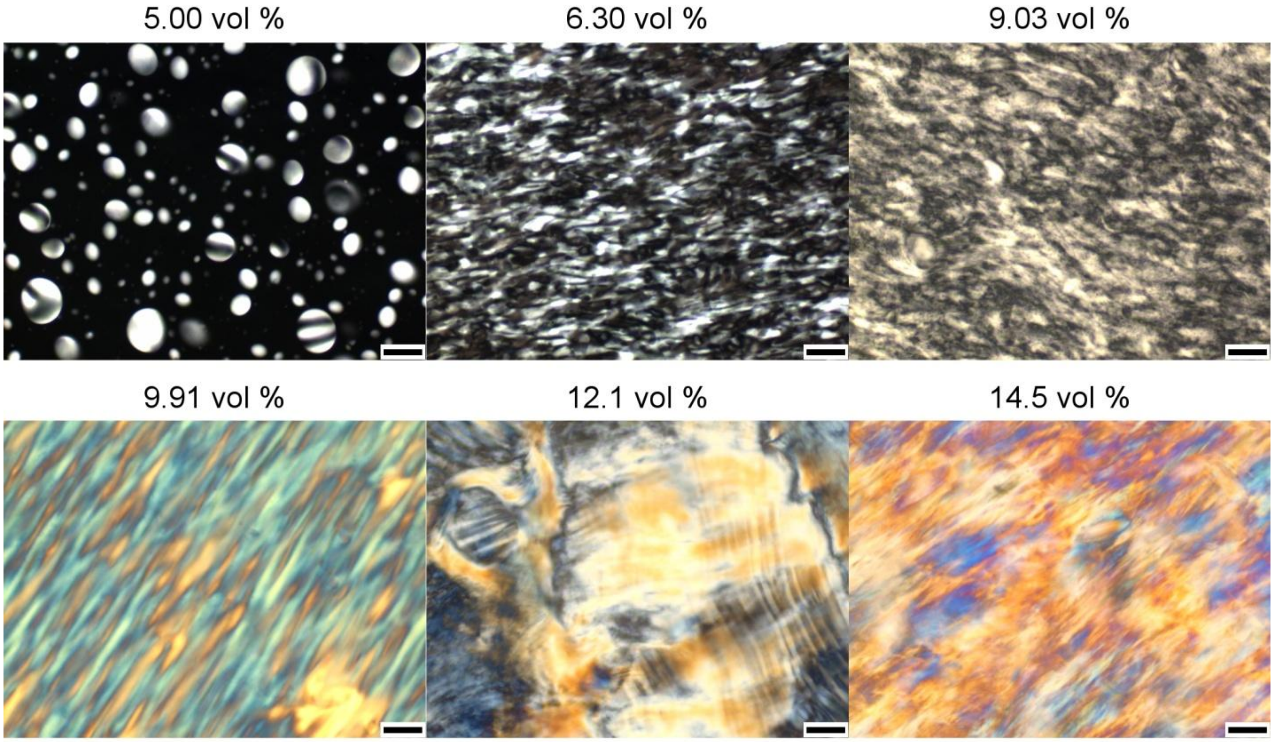

Figure 6.1. Polarized light microscopy of CNC suspensions at various volume percent concentrations at a room temperature. Scale bars are 50 μm.

The microstructural evolution of CNC liquid crystals with temperature was investigated using polarized light microscopy coupled with a Linkam optical rheology system. Figure 6.2 shows temperature effects on the phase behavior of a representative CNC liquid crystal sample of 12.1 vol %. The microscopic images were taken after 12.1 vol % CNC was heated and held for an hour at 35 and 40 $^{o}$C, respectively. The microstructure of CNC at 35 $^{o}$C remained similar to the one at ambient temperature during the experimental period. However, after heating at 40 $^{o}$C, the liquid crystal phase behavior appeared to be changing based on the vanishing of the sample colors under polarized optical microscopy. The change from colorful to bright and dark samples provides evidence that the single phase CNC liquid crystal transitioned into the biphasic regime after heating at 40 $^{o}$C. The steady shear rheology of 12.1 vol % CNC at 40 $^{o}$C also supports this idea; the viscosity increased noticeably at 40 $^{o}$C, while at 10, 25, and 35 $^{o}$C, the viscosity remained unchanged. More details on concentration and temperature effects on CNC rheology are discussed in the following section.

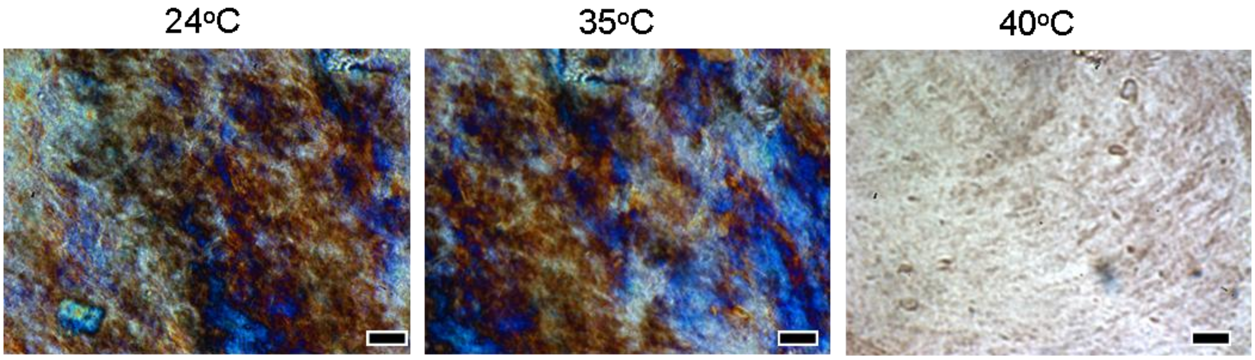

Figure 6.2. Cross polarized microscopy images at 24, 35 and 40 °C of a sample containing 12.1 vol % CNC. The scale bar represents 50 μm.

### 6.3. Rheology of CNC Suspensions

The phase behavior of lyotropic CNC suspensions as a function of concentration and temperature were studied by rheology. In steady shear measurements, the transient behavior of various CNC suspensions were measured before steady shear viscosity to determine the time period required for becoming steady state. Figure 6.3 shows the start up of flow of viscosity versus time for CNC suspensions at different concentrations in biphasic, liquid crystal, and gel regime. Similar to both bulk and supernatant of dsDNA/SWNT dispersions, the anisotropic CNC suspensions also showed short transient behavior. All oscillatory shear data of CNC suspensions were measured in the linear viscoelastic (LVE) region.

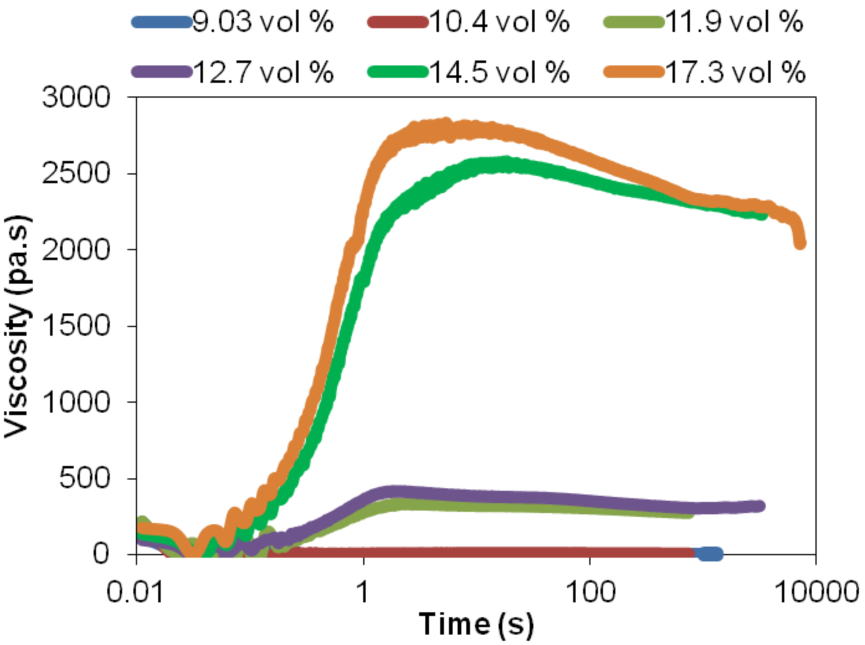

Figure 6.3. Transient behavior of CNC suspensions at various concentrations of biphasic, liquid crystal and gel regime.

**Effects of Temperature on Viscosity.** As mentioned earlier, many of the nanocylinder liquid crystal dispersions including SWNT in superacids[19] and low aspect ratio CdSe-cylcohexane[178] showed temperature insensitivity in phase behavior. The rheological behavior of CNC suspensions as a function of temperature was investigated at three different CNC concentrations which were representative of the isotropic, biphasic and liquid crystal phases. As shown in Figure 6.4a, at the isotropic concentration of 3.07 vol %, the steady shear viscosity decreased with increasing temperature; this is a common behavior for predominantly isotropic dispersions. Furthermore, the wide Newtonian plateau in viscosity was observed at all temperatures measured at this concentration. The inception of the shear thinning region at 30 $s^{-1}$ shear rate was apparent at both 10 and 25 $^{o}$C.

For the biphasic sample of 6.99 vol % CNC, clear evidence of three region flow behavior, a typical rheological signature for lyotropic LCPs systems, was observed as shown in Figure 6.4b. However, for cholesteric dsDNA/SWNT dispersions, only slight deflection points separating two shear thinning regions with different slopes were observed. At the lower shear rate region, all viscosities at three different temperatures showed Region I shear thinning and followed by apparent Region II plateaus starting from about 0.5 $s^{-1}$ shear rate with the most obvious plateau at 10 $^{o}$C. The intermediate Region II resembling low shear rate "Newtonian plateau" is generally associated with director wagging[48] or vorticity alignment.[226] At even higher shear rates, samples showed Region III shear alignment. Overall, the viscosities at 6.99 vol % CNC concentration were still affected by temperature which decreased as a function of increasing temperature.

With a further increase in concentration to a fully liquid crystalline sample of 12.1 vol % CNC, the viscosity was temperature independent between 10 and 35 $^{o}$C with shear thinning behavior throughout the measured shear rate range (Figure 6.4c). This indicates that, even for low aspect ratio CNC nanorods, the viscosity is insensitive to temperature when it becomes a liquid crystal. However, at 40$^{o}$C, a marked increase in viscosity was observed especially at lower shear rates. This was initially thought to be due to the evaporation of solvent during the measurements. Another possible reason for the viscosity increase was that, with the temperature increase from 35 to 40 $^{o}$C, the microstructure of liquid crystal CNC may transition into biphasic phase leading to an increase in viscosity. Hot stage optical microscopy revealed a pronounced increase in isotropic domains when heating from 35 to 40 $^{o}$C, and the color texture vanished with time showing only bright and dark domains. This suggests that there was a change in phase behavior between 35 and 40 $^{o}$C. Similar behavior has been observed for rod like polymers since in those systems increasing temperature resulted in a changed solvent quality.

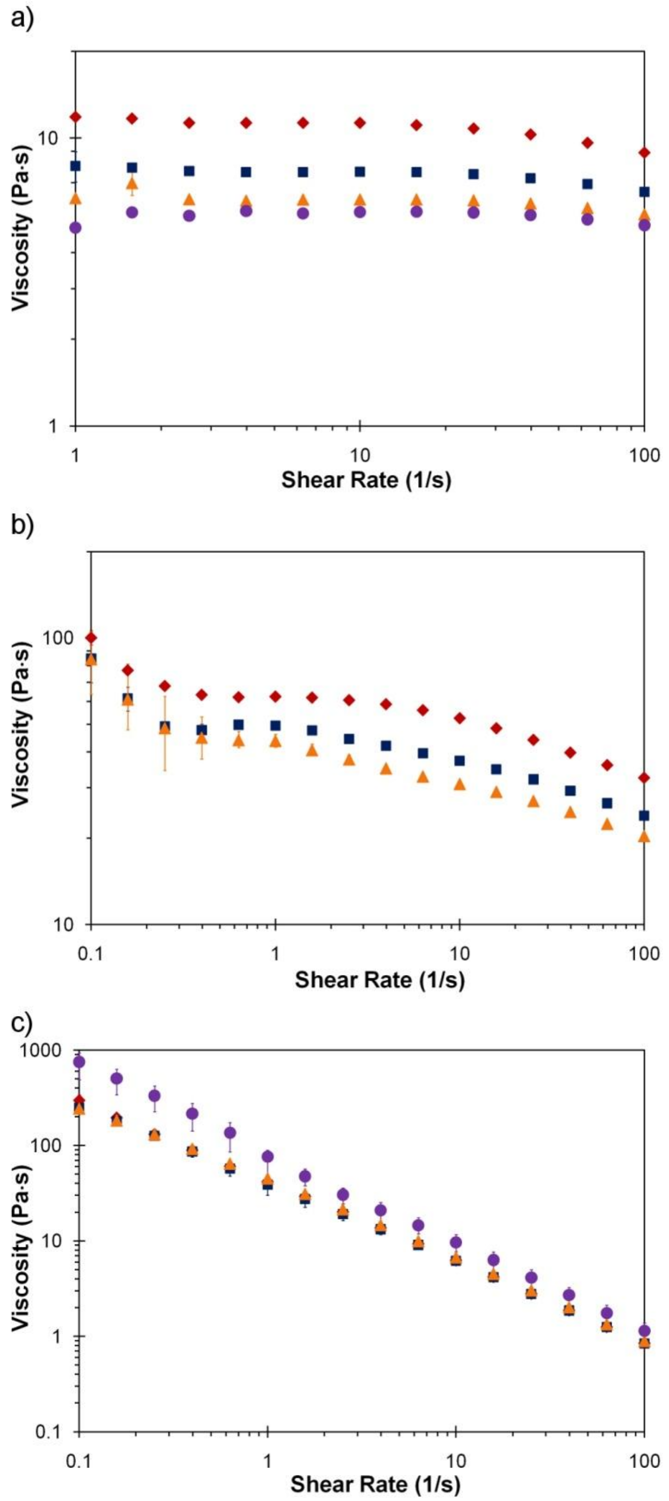

Figure 6.4. Steady shear viscosity versus shear rate at 10 (red diamonds), 25 (blue squares), 35 (orange triangles) and 40 °C (purple circles) of CNC suspensions with concentrations of (a) 3.07 vol %, (b) 6.99 vol %, and (c) 12.1 vol %.

**Viscosity and Modulus versus Concentration.** In a normal polymer solution or colloidal dispersion, the low shear viscosity increases with concentration. However, for liquid crystalline dispersions, one of the hallmarks is that the low shear viscosity versus concentration curve goes through a maximum in the biphasic regime. Similar behavior has also been reported for the elastic and viscous modulii.[48] Figure 6.5a shows the complex and steady shear viscosity change as a function of increasing CNC concentration at 0.1 and 1.0 $s^{-1}$ shear rate or angular frequency. Although no maximum was obtained for steady shear viscosity through the entire concentration range measure, a change in slope occurred in the biphasic regime at 7.69 vol % CNC concentration. This contrast to the viscosity maximum observed for both nematic and cholesteric dsDNA/SWNT dispersions and the typical rheological behavior of LCPs. On the other hand, slight maximum peaks were obtained for complex viscosity $\eta^*$ and storage modulus G' at 12.1 vol % CNC concentration, which is fully liquid crystal according to optical microscopy (Figure 6.5ab). No maxima were observed in the biphasic regime. With further increase in concentration, the samples evolved to gel state where viscosities and storage and loss modulii became independent of concentration. The origin of the discrepancy between this system with LCPs is not clear. However, it is interesting to note that another micron length CNC system also showed unexpected behavior where only a tiny maximum was obtained for steady shear viscosity versus concentration curve at the critical concentration $\phi_I$ where the sample became biphasic.[227] Considering the acidic nature of the CNC suspensions, it is hypothesized that the change in the ionic strength with increasing CNC concentration caused changes in attractive interactions of molecules and resulted in this anomalous behavior. The impact of ionic strength on the phase behavior and attractive interactions needs to be explored in the future research.

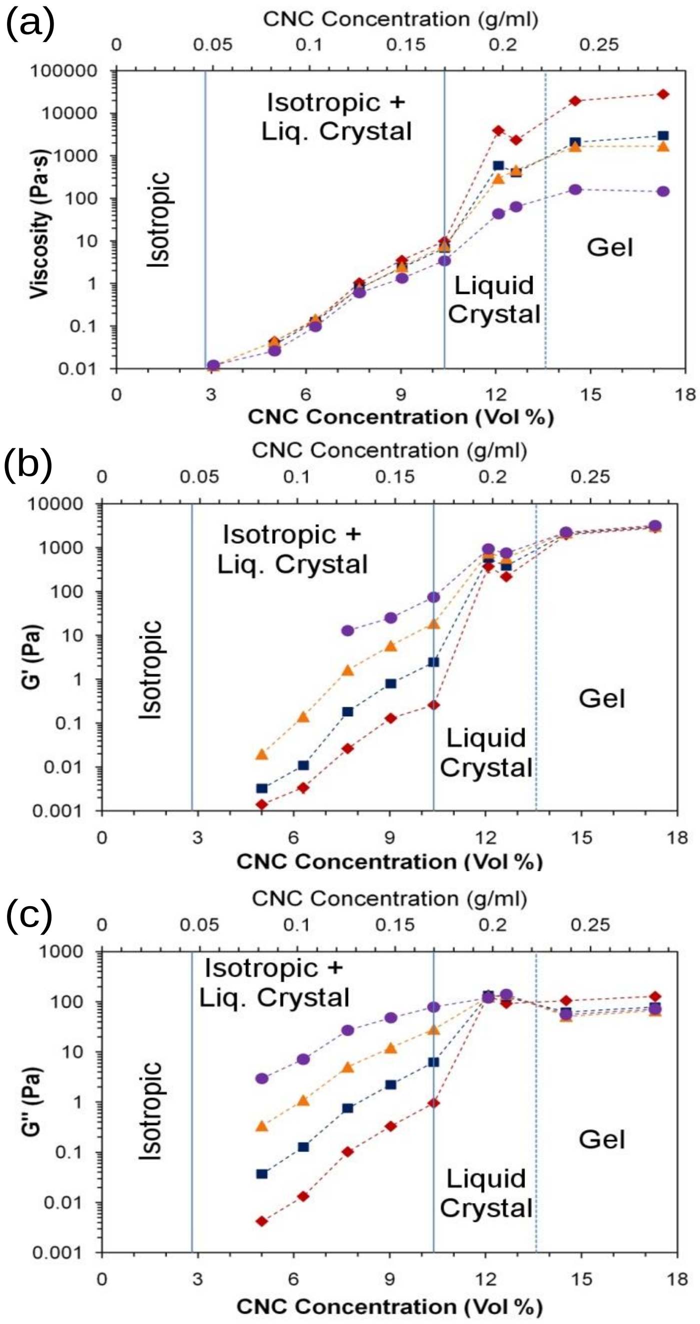

Figure 6.5. Rheological properties versus concentration; (a) complex viscosity at 0.1 $s^{-1}$ (red diamonds), 1.0 $s^{-1}$ (blue squares), and steady shear viscosity at 0.1 $s^{-1}$ (orange triangles), 1.0 $s^{-1}$ (purple circles); (b) storage and (c) loss modulus at 0.1 $s^{-1}$ (red diamonds), 1.0 $s^{-1}$ (blue squares), 10 $s^{-1}$ (orange triangles) and 100 $s^{-1}$ (purple circles). The solid vertical lines indicate a phase transition; the discontinuous vertical line indicates an approximate liquid crystal to gel transition.

## 6.4. Conclusions

Aqueous dispersions of sulfonated CNC produced from cotton show lyotropic phase behavior. Based on cross-polarized optical microscopy, a liquid crystalline phase was obtained in the concentration range of 10.4 vol % < $\phi_{LC}$ < 12.1 vol % and exhibited the fingerprint texture characteristic of a cholesteric liquid crystal. At even higher concentration, the system transitioned to a birefringent gel. The temperature effect on the change in phase behavior between 35 to 40 $^{o}$C was also detected. Although the typical nonmonotonic relationship of viscosity and modulus in LCPs was not observed for CNC suspensions, the three-region rheological behavior of LCPs was obtained for biphasic and liquid crystalline samples of CNC suspensions. The discrepancy of phase behavior between CNC nanorod suspensions and LCPs may have been caused by polydispersity and introduction of electrostatic interactions in the CNC system. This hypothesis provides a foundation for future research.

## Chapter 7

## Conclusions

Integrating carbon nanotubes (CNTs) with natural biopolymers, especially dsDNA, have broadened the potential applications of remarkable nanomaterials to biofunctional materials as well as other engineering applications. The characteristics of nature's toolbox could be exploited to help understand and process nanomaterials to achieve a breakthrough in nanotechnology. Carbon nanotubes are considered to be one of the most promising materials in nanoscale science and technology with great potential applications. However, translating the remarkable mechanical, thermal and electrical properties of individual nanotubes into macroscopic objects of neat films and fibers is scientifically challenged by the isotropic random entanglement of pristine SWNT. Understanding the phase behavior of biopolymers-stabilized CNTs is important for the development of nanotube based biomaterials as well as other types of nanomaterials. Since many biopolymers, especially DNA, are proven to be good dispersing agents for CNTs, uniform dispersion of nanotubes in small bundles or even in individuals at the first stage can be successfully obtained by binding biomolecules to CNTs either by covalent or non-covalent functionalization.

In this study, both cholesteric and nematic liquid crystal phases of pristine SWNT stabilized in aqueous dsDNA solvent were observed. When dsDNA/SWNT liquid crystals were produced from a bulk dispersion, the presence of SWNT bundles appeared to inhibit cholesteric phase formation and the nematic texture typical of other lyotropic SWNT liquid crystals resulted. When the liquid crystal was produced from a supernatant comprised only of individual SWNT, the helicity of the dsDNA was able to drive the assembly of a cholesteric liquid crystal. To the author's knowledge, this is both the first report of biopolymer stabilized lyotropic cholesteric SWNT liquid crystalline phase and one of a very few systems capable of forming either cholesteric or nematic phases. The ultimate microstructure of films produced from the cholesteric dispersions was found to be shear dependent. These results will enable new fundamental investigations comparing nematic and cholesteric liquid crystalline phase behavior and shear response. In addition, they potentially provide a foundation for previously unachievable applications that utilize both the intrinsic properties of SWNT and the controlled optical properties of cholesteric films. Furthermore, preliminary investigation of the macroscopic assembly of fibers from dsDNA/SWNT and LSZ/TTAB/SWNT has shown sufficient promise to warrant additional research.

Significant insights were gained into the rheology and phase behavior of aqueous dsDNA/SWNT. In the semidilute regime, the supernatant of dsDNA/SWNT dispersion followed the predicted rheological behavior given by Doi-Edwards theory. In the fully liquid crystal regime, the nematic and cholesteric dsDNA/SWNT dispersions showed different rheological behavior in steady shear viscosities at SWNT concentrations near critical concentration of $\phi_{LC}$. In addition, slow evaporation led to phase transitions from isotropic to liquid crystalline phase which were accompanied by the characteristic nonmonotonic relationship of rheology as a function of increasing SWNT concentration. As expected, the empirical Cox-Merz rule was not obeyed for the dsDNA/SWNT liquid crystals. However, not all of the rheological signatures anticipated based on lyotropic liquid crystal polymers (LCPs) were observed. Although plots of steady shear viscosity versus shear rate for several liquid crystal samples showed two distinct shear thinning regions, they lacked the obvious three region behavior characteristic of many

LCPs. In addition to dsDNA/SWNT system, the phase behavior and microstructure of another cholesterogenic system, cellulose nanocrystal (CNC) suspensions, were investigated as a function of concentration and temperature. For sulfonated CNC suspensions, only slight maxima were obtained in liquid crystal region for complex viscosity and storage modulus as a function of increasing concentration. However, steady shear viscosity and loss modulus did not show maximum values throughout the entire concentration range investigated. Interestingly, typical three-region rheological behavior of LCPs was observed for CNC suspensions in biphasic and liquid crystalline phases. In addition, temperature study of CNC suspensions showed a possible phase transition in liquid crystal phases at higher temperature of 40 $^{o}$C.

These results of this research highlight that while nanorod dispersions have many parallels with rodlike polymer solutions, the complicance of polydispersity and various molecular interactions such as van der Waals forces and electrostatic interactions can result in unusual phase behaviors. Understanding the rheology and phase behavior of the dispersions is critical to controlling the properties of bulk materials such as films and fibers comprised of nanoscale building blocks.

## References

1 Nepal, D., Balasubramanian, S., Simonian, A. L. & Davis, V. A. Strong antimicrobial coatings: Single-walled carbon nanotubes armored with biopolymers. *Nano Letters* **8**, 1896 (2008).

2 Kang, S., Pinault, M., Pfefferle, L. D. & Elimelech, M. Single-walled carbon nanotubes exhibit strong antimicrobial activity. *Langmuir* **23**, 8670 (2007).

3 Pangule, R. C. *et al.* Antistaphylococcal nanocomposite films based on enzyme-nanotube conjugates. *ACS Nano*, 874 (2010).

4 Shin, S. R. *et al.* DNA-wrapped single-walled carbon nanotube hybrid fibers for supercapacitors and artificial muscles. *Advanced Materials* **20**, 466 (2008).

5 Collins, P. G., Bradley, K., Ishigami, M. & Zettl, A. Extreme oxygen sensitivity of electronic properties of carbon nanotubes. *Science* **287**, 1801 (2000).

6 Li, J. *et al.* Carbon nanotube nanoelectrode array for ultrasensitive DNA detection. *Nano Letters* **3**, 597 (2003).

7 Tans, S. J. *et al.* Individual single-wall carbon nanotubes as quantum wires. *Nature* **386**, 474 (1997).

8 Cao, J., Wang, Q., Wang, D. & Dai, H. Suspended carbon nanotube quantum wires with two gates. *Small* **1**, 138 (2005).

9 Dillon, A. C. *et al.* Storage of hydrogen in single-walled carbon nanotubes. *Nature* **386**, 377 (1997).

10 Ericson, L. M. *et al.* Macroscopic, neat, single-walled carbon nanotube fibers. *Science* **305**, 1447 (2004).

11 Poulin, P., Vigolo, B. & Launois, P. Films and fibers of oriented single wall nanotubes. *Carbon* **40**, 1741 (2002).

12 Dalton, A. B. *et al.* Super-tough carbon-nanotube fibres. *Nature* **423**, 703 (2003).

13 Zhang, M., Atkinson, K. R. & Baughman, R. H. Multifunctional carbon nanotube yarns by downsizing an ancient technology. *Science* **306**, 1358 (2004).

14 Vigolo, B. *et al.* Macroscopic fibers and ribbons of oriented carbon nanotubes. *Science* **290**, 1331 (2000).

15 Song, W. H., Kinloch, I. A. & Windle, A. H. Nematic liquid crystallinity of multiwall carbon nanotubes. *Science* **302**, 1363 (2003).

16 Badaire, S. *et al.* Liquid crystals of DNA-stabilized carbon nanotubes. *Advanced Materials* **17**, 1673 (2005).

17 Moulton, S. E., Maugey, M., Poulin, P. & Wallace, G. G. Liquid crystal behavior of single-walled carbon nanotubes dispersed in biological hyaluronic acid solutions. *Journal of the American Chemical Society* **129**, 9452 (2007).

18 Islam, M. F. *et al.* Nematic nanotube gels. *Physical Review Letters* **92**, 88303 (2004).

19 Davis, V. A. *et al.* Phase behavior and rheology of swnts in superacids. *Macromolecules* **37**, 154 (2004).

20 Davis, V. A. *et al.* True solutions of single-walled carbon nanotubes for assembly into macroscopic materials. *Nature Nanotechnology* **4**, 830 (2009).

21 Zakri, C. & Poulin, P. Phase behavior of nanotube suspensions: From attraction induced percolation to liquid crystalline phases. *Journal of Materials Chemistry* **16**, 4095 (2006).

22 Orts, W. J., Godbout, L., Marchessault, R. H. & Revol, J. F. Enhanced ordering of liquid crystalline suspensions of cellulose microfibrils: A small angle neutron scattering study. *Macromolecules* **31**, 5717 (1998).

23 Pan, J. H., Hamad, W. & Straus, S. K. Parameters affecting the chiral nematic phase of nanocrystalline cellulose films. *Macromolecules* **43**, 3851 (2010).

24 Davis, V. A. Liquid crystalline assembly of nanocylinders. *Journal of Materials Research* (2011).

25 Nepal, D. & Geckeler, K. E. Proteins and carbon nanotubes: Close encounter in water. *Small* **3**, 1259 (2007).

26 Nepal, D., Sohn, J. I., Aicher, W. K., Lee, S. & Geckeler, K. E. Supramolecular conjugates of carbon nanotubes and DNA by a solid-state reaction. *Biomacromolecules* **6**, 2919 (2005).

27 Hobbie, E. K. *et al.* Self-assembly of ordered nanowires in biological suspensions of single-wall carbon nanotubes. *ACS Nano* **3**, 189 (2009).

28 Onsager, L. The effects of shape on the interaction of colloidal particles. *Annals of the New York Academy of Sciences* **51**, 627 (1949).

29 Adams, M., Dogic, Z., Keller, S. L. & Fraden, S. Entropically driven microphase transitions in mixtures of colloidal rods and spheres. *Nature* **393**, 349 (1998).

30 Dogic, Z., Frenkel, D. & Fraden, S. Enhanced stability of layered phases in parallel hard spherocylinders due to addition of hard spheres. *Physical Review E* **62**, 3925 (2000).

31 Strzelecka, T. E., Davidson, M. W. & Rill, R. L. Multiple liquid-crystal phases of DNA at high-concentrations. *Nature* **331**, 457 (1988).

32 Nakata, M. *et al.* End-to-end stacking and liquid crystal condensation of 6-to 20-base pair DNA duplexes. *Science* **318**, 1276 (2007).

33 Vanwinkle, D. H., Davidson, M. W. & Rill, R. L. Terraces in the cholesteric phase of DNA liquid-crystals. *Journal of Chemical Physics* **97**, 5641 (1992).

34 Zakharova, S. S., Jesse, W., Backendorf, C. & van der Maarel, J. R. C. Liquid crystal formation in supercoiled DNA solutions. *Biophysical Journal* **83**, 1119 (2002).

35 Sipski, M. L. & Wagner, T. E. Probing DNA quaternary ordering with circular-dichroism spectroscopy - studies of equine sperm chromosomal fibers. *Biopolymers* **16**, 573 (1977).

36 Livolant, F. Cholesteric organization of DNA invivo and invitro. *European Journal of Cell Biology* **33**, 300 (1984).

37 Rill, R. L., Livolant, F., Aldrich, H. C. & Davidson, M. W. Electron-microscopy of liquid-crystalline DNA - direct evidence for cholesteric-like organization of DNA in dinoflagellate chromosomes. *Chromosoma* **98**, 280 (1989).

38 Baek, S. G., Magda, J. J., Larson, R. G. & Hudson, S. D. Rheological differences among liquid-crystalline polymers. Ii. Disappearance of negative n in densely packed lyotropes and thermotropes. *Journal of Rheology* **38**, 1473 (1994).

39 Huang, C. M., Magda, J. J. & Larson, R. G. The effect of temperature and concentration on n and tumbling in a liquid crystal polymer. *Journal of Rheology* **43**, 31 (1999).

40 Hongladarom, K., Secakusuma, V. & Burghardt, W. R. Relation between molecular orientation and rheology in lyotropic hydroxypropylcellulose solutions. *Journal of Rheology* **38**, 1505 (1994).

41 Walker, L. M., Wagner, N. J., Larson, R. G., Mirau, P. A. & Moldenaers, P. The rheology of highly concentrated pblg solutions. *Journal of Rheology* **39**, 925 (1995).

42 Larson, R. G. & Mead, D. W. Time and shear-rate scaling laws for liquid crystal polymers. *Journal of Rheology* **33**, 1251 (1989).

43 Baek, S. G., Magda, J. J. & Larson, R. G. Rheological differences among liquid-crystalline polymers. I. The first and second normal stress differences of pbg solutions. *Journal of Rheology* **37**, 1201 (1993).

44 Hongladarom, K. & Burghardt, W. R. Molecular alignment of polymer liquid crystals in shear flows. 2. Transient flow behavior in poly (benzyl glutamate) solutions. *Macromolecules* **26**, 785 (1993).

45 O'Connell, M. J. *et al.* Band gap fluorescence from individual single-walled carbon nanotubes. *Science* **297**, 593 (2002).

46 Girifalco, L. A., Hodak, M. & Lee, R. S. Carbon nanotubes, buckyballs, ropes, and a universal graphitic potential. *Physical Review B* **62**, 13104 (2000).

47 Doi, M. & Edwards, S. F. The theory of polymer dynamics. 1986. (Oxford University Press, Clarendon).

48 Larson, R. G. The structure and rheology of complex fluids. 1999. (Oxford University Press, New York).

49 Marrucci, G. Rheology of nematic polymers. *In Liquid Crystallinity in Polymers: Principles and Fundamental Properties, A. Ciferri, ed.* 1991*(*VCH, New York).

50 Kroto, H. W., Heath, J. R., O'Brien, S. C., Curl, R. F. & Smalley, R. E. C 60: Buckminsterfullerene. *Nature* **318**, 162 (1985).

51 Iijima, S. Helical microtubules of graphitic carbon. *Nature* **354**, 56 (1991).

52 Iijima, S. & Ichihashi, T. Single-shell carbon nanotubes of 1-nm diameter (vol 363, pg 603, 1993). *Nature* **364**, 737 (1993).

53 Bethune, D. S. *et al.* Cobalt-catalyzed growth of carbon nanotubes with single-atomic-layerwalls. *Nature* **363**, 605 (1993).

54 Thess, A. *et al.* Crystalline ropes of metallic carbon nanotubes. *Science* **273**, 483 (1996).

55 Journet, C. *et al.* Large-scale production of single-walled carbon nanotubes by the electric-arc technique. *Nature* **388**, 756 (1997).

56 Liu, J. *et al.* Fullerene pipes. *Science* **280**, 1253 (1998).

57 Scott, C. D. *et al.* Iron catalyst chemistry in modeling a high-pressure carbon monoxide nanotube reactor. *Journal of Nanoscience and Nanotechnology* **3**, 63 (2003).

58 Tsang, S. C. *et al.* Immobilization of small proteins in carbon nanotubes: High-resolution transmission electron microscopy study and catalytic activity (september, pg 1803, 1995). *Journal of the Chemical Society-Chemical Communications*, 2579 (1995).

59 Tsang, S. C. *et al.* Immobilization of platinated and iodinated oligonucleotides on carbon nanotubes. *Angewandte Chemie-International Edition in English* **36**, 2198 (1997).

60 Fujita, M., Saito, R., Dresselhaus, G. & Dresselhaus, M. S. Formation of general fullerenes by their projection on a honeycomb lattice. *Physical Review B* **45**, 13834 (1992).

61 Moniruzzaman, M. & Winey, K. I. Polymer nanocomposites containing carbon nanotubes. *Macromolecules* **39**, 5194 (2006).

62 Dresselhaus, M. S., Dresselhaus, G. & Saito, R. Carbon fibers based on c60 and their symmetry. *Physical Review B* **45**, 6234 (1992).

63 Wildoer, J. W. G., Venema, L. C., Rinzler, A. G., Smalley, R. E. & Dekker, C. Electronic structure of atomically resolved carbon nanotubes. *Nature* **391**, 59 (1998).

64 Dresselhaus, M. S., Dresselhaus, G. & Saito, R. Physics of carbon nanotubes. *Carbon* **33**, 883 (1995).

65 Baughman, R. H., Zakhidov, A. A. & de Heer, W. A. Carbon nanotubes - the route toward applications. *Science* **297**, 787 (2002).

66 Che, J. W., Cagin, T. & Goddard, W. A. Thermal conductivity of carbon nanotubes. *Nanotechnology* **11**, 65 (2000).

67 Hone, J. *et al.* Electrical and thermal transport properties of magnetically aligned single walt carbon nanotube films. *Applied Physics Letters* **77**, 666 (2000).

68 Anthony, T. R. *et al.* Thermal diffusivity of isotopically enriched $^{12}$c diamond. *Physical Review B* **42**, 1104 (1990).

69 Berber, S., Kwon, Y. K. & Tomanek, D. Unusually high thermal conductivity of carbon nanotubes. *Physical Review Letters* **84**, 4613 (2000).

70 Krishnan, A., Dujardin, E., Ebbesen, T. W., Yianilos, P. N. & Treacy, M. M. J. Young's modulus of single-walled nanotubes. *Physical Review B* **58**, 14013 (1998).

71 Gao, G. H., Cagin, T. & Goddard, W. A. Energetics, structure, mechanical and vibrational properties of single-walled carbon nanotubes. *Nanotechnology* **9**, 184 (1998).

72 Sinden, R. R. DNA structure and function. 1994. (Academic Press).

73 Vanoss, C. J., Smeenk, R. J. T. & Aarden, L. A. Inhibition of association vs dissociation of high-avidity DNA anti-DNA complexes - possible involvement of secondary hydrogen-bonds. *Immunological Investigations* **14**, 245 (1985).

74 Marmur, J. & Doty, P. Determination of base composition of deoxyribonucleic acid from its thermal denaturation temperature. *Journal of Molecular Biology* **5**, 109 (1962).

75 Jones, R. A. L. Soft condensed matter. 2002. (Oxford University Press, USA).

76 Nepal, D. & Geckeler, K. E. Ph-sensitive dispersion and debundling of single-walled carbon nanotubes: Lysozyme as a tool. *Small* **2**, 406 (2006).

77 da Silva, M. A., Farhat, I. A., Areas, E. P. G. & Mitchell, J. R. Solvent-induced lysozyme gels: Effects of system composition and temperature on structural and dynamic characteristics. *Biopolymers* **83**, 443 (2006).

78 Matsuura, K. *et al.* Selectivity of water-soluble proteins in single-walled carbon nanotube dispersions. *Chemical Physics Letters* **429**, 497 (2006).

79 White, J. S. & White, D. C. Sourcebook of enzymes. 1997. (CRC).

80 da Silva, M. A. & Areas, E. P. G. Solvent-induced lysozyme gels: Rheology, fractal analysis, and sol-gel kinetics. *Journal of Colloid and Interface Science* **289**, 394 (2005).

81 Szymanska, A., Hornowski, T., Kozak, M. & Slosarek, G. The saxs and rheological studies of hewl amyloid formation. *Acta Physica Polonica A* **114**, 447 (2008).

82 Eichhorn, S. J. Cellulose nanowhiskers: Promising materials for advanced applications. *Soft Matter* **7**, 303.

83 Dong, X. M., Kimura, T., Revol, J. F. & Gray, D. G. Effects of ionic strength on the isotropic-chiral nematic phase transition of suspensions of cellulose crystallites. *Langmuir* **12**, 2076 (1996).

84 Elazzouzi-Hafraoui, S. *et al.* The shape and size distribution of crystalline nanoparticles prepared by acid hydrolysis of native cellulose. *Biomacromolecules* **9**, 57 (2007).

85 Samir, M. A. S. A., Alloin, F. & Dufresne, A. Review of recent research into cellulosic whiskers, their properties and their application in nanocomposite field. *Biomacromolecules* **6**, 612 (2005).

86 Revol, J. F. *et al.* Chiral nematic suspensions of cellulose crystallites; phase separation and magnetic field orientation. *Liquid Crystals* **16**, 127 (1994).

87 Sakurada, I., Nukushina, Y. & Ito, T. Experimental determination of the elastic modulus of crystalline regions in oriented polymers. *Journal of Polymer Science* **57**, 651 (1962).

88 Tashiro, K. & Kobayashi, M. Theoretical evaluation of three-dimensional elastic constants of native and regenerated celluloses: Role of hydrogen bonds. *Polymer* **32**, 1516 (1991).

89 Uematsu, Y. & Uematsu, I. Mesomorphic Order in Polymers and Polymerization in Liquid Crystalline Media. ed. A. Blumstein ACS Symposium Series 74, 136 (1978).

90 Guo, J. X. & Gray, D. G. In: Gilbert rd (ed) cellulosic polymers, blends and composites. 1994. (Hanser Publishers, New York).

91 E. E. Ureña-Benavides, G. A., V. A. Davis, C. L. Kitchens. Rheology and phase behavior of concentrated cellulose nanocrystal aqueous suspensions. *Macromolecules* **44**, 8990 (2011).

92 Wong, S. S., Joselevich, E., Woolley, A. T., Cheung, C. L. & Lieber, C. M. Covalently functionalized nanotubes as nanometre-sized probes in chemistry and biology. *Nature* **394**, 52 (1998).

93 Weiss, P. S. A conversation with prof. Angela belcher: Leader in biotemplated nanomaterials. *ACS Nano* **2**, 1508 (2008).

94 Shim, M., Kam, N. W. S., Chen, R. J., Li, Y. M. & Dai, H. J. Functionalization of carbon nanotubes for biocompatibility and biomolecular recognition. *Nano Letters* **2**, 285 (2002).

95 Bottini, M. *et al.* Adsorption of streptavidin onto single-walled carbon nanotubes: Application in fluorescent supramolecular nanoassemblies. *Journal of Nanoscience and Nanotechnology* **6**, 3693 (2006).

96 Sanchez-Pomales, G., Santiago-Rodriguez, L. & Cabrera, C. R. DNA-functionalized carbon nanotubes for biosensing applications. *Journal of Nanoscience and Nanotechnology* **9**, 2175 (2009).

97 Albertorio, F., Hughes, M. E., Golovchenko, J. A. & Branton, D. Base dependent DNA-carbon nanotube interactions: Activation enthalpies and assembly-disassembly control. *Nanotechnology* **20** (2009).

98 Anand, S. V. & Mahapatra, D. R. Quasi-static and dynamic strain sensing using carbon nanotube/epoxy nanocomposite thin films. *Smart Materials & Structures* **18** (2009).

99 Liu, Z. *et al.* Drug delivery with carbon nanotubes for in vivo cancer treatment. *Cancer Research* **68**, 6652 (2008).

100 Pantarotto, D. *et al.* Functionalized carbon nanotubes for plasmid DNA gene delivery. *Angewandte Chemie* **116**, 5354 (2004).

101 Bianco, A., Kostarelos, K. & Prato, M. Applications of carbon nanotubes in drug delivery. *Current Opinion in Chemical Biology* **9**, 674 (2005).

102 Shvedova, A. A. *et al.* Unusual inflammatory and fibrogenic pulmonary responses to single-walled carbon nanotubes in mice. *American Journal of Physiology-Lung Cellular and Molecular Physiology* **289**, L698 (2005).

103 Chou, C. C. *et al.* Single-walled carbon nanotubes can induce pulmonary injury in mouse model. *Nano Letters* **8**, 437 (2008).

104 Warheit, D. B. *et al.* Comparative pulmonary toxicity assessment of single-wall carbon nanotubes in rats. *Toxicological Sciences* **77**, 117 (2004).

105 Johnson, D. R., Methner, M. M., Kennedy, A. J. & Steevens, J. A. Potential for occupational exposure to engineered carbon-based nanomaterials in environmental laboratory studies. *Environmental Health Perspectives* **118**, 49.

106 Ao, G., Nepal, D., Aono, M. & Davis, V. A. Cholesteric and nematic liquid crystalline phase behavior of double-stranded DNA stabilized single-walled carbon nanotube dispersions. *ACS Nano* **5**, 1450 (2011).

107 Cathcart, H. *et al.* Ordered DNA wrapping switches on luminescence in single-walled nanotube dispersions. *Journal of the American Chemical Society* **130**, 12734 (2008).

108 Hughes, M. E., Brandin, E. & Golovchenko, J. A. Optical absorption of DNA-carbon nanotube structures. *Nano Letters* **7**, 1191 (2007).

109 Tu, X. M., Manohar, S., Jagota, A. & Zheng, M. DNA sequence motifs for structure-specific recognition and separation of carbon nanotubes. *Nature* **460**, 250 (2009).

110 Pividori, M. & Alegret, S. DNA adsorption on carbonaceous materials. *Immobilisation of DNA on Chips I*, 1 (2005).

111 Chen, R. J. & Zhang, Y. Controlled precipitation of solubilized carbon nanotubes by delamination of DNA. *The Journal of Physical Chemistry B* **110**, 54 (2006).

112 Meng, S., Maragakis, P., Papaloukas, C. & Kaxiras, E. DNA nucleoside interaction and identification with carbon nanotubes. *Nano Letters* **7**, 45 (2007).

113 Zheng, M. *et al.* DNA-assisted dispersion and separation of carbon nanotubes. *Nature Materials* **2**, 338 (2003).

114 Arnold, M. S., Green, A. A., Hulvat, J. F., Stupp, S. I. & Hersam, M. C. Sorting carbon nanotubes by electronic structure using density differentiation. *Nature Nanotechnology* **1**, 60 (2006).

115 Feazell, R. P., Nakayama-Ratchford, N., Dai, H. & Lippard, S. J. Soluble single-walled carbon nanotubes as longboat delivery systems for platinum (iv) anticancer drug design. *Journal of the American Chemical Society* **129**, 8438 (2007).

116 Gao, H., Kong, Y., Cui, D. & Ozkan, C. S. Spontaneous insertion of DNA oligonucleotides into carbon nanotubes. *Nano Letters* **3**, 471 (2003).

117 Zhao, X. & Johnson, J. K. Simulation of adsorption of DNA on carbon nanotubes. *Journal of the American Chemical Society* **129**, 10438 (2007).

118 Okada, T., Kaneko, T., Hatakeyama, R. & Tohji, K. Electrically triggered insertion of single-stranded DNA into single-walled carbon nanotubes. *Chemical Physics Letters* **417**, 288 (2006).

119 Lu, G., Maragakis, P. & Kaxiras, E. Carbon nanotube interaction with DNA. *Nano Letters* **5**, 897 (2005).

120 Donald, A. M., Windle, A. H. & Hanna, S. Liquid crystalline polymers. 2006. (Cambridge University Press).

121 Rizvi, T. Z. Liquid crystalline biopolymers: A new arena for liquid crystal research. *Journal of Molecular Liquids* **106**, 43 (2003).

122 Xin, X. *et al.* Incorporation of carbon nanotubes into a lyotropic liquid crystal by phase separation in the presence of a hydrophilic polymer. *Langmuir* **26**, 3562.

123 Rai, P. K. *et al.* Isotropic-nematic phase transition of single-walled carbon nanotubes in strong acids. *Journal of the American Chemical Society* **128**, 591 (2006).

124 Papkov, S. Liquid crystalline order in solutions of rigid-chain polymers. *Liquid Crystal Polymers I*, 75 (1984).

125 Frenkel, D. Structure of hard-core models for liquid crystals. *The Journal of Physical Chemistry* **92**, 3280 (1988).

126 Green, M. J., Parra-Vasquez, A. N. G., Behabtu, N. & Pasquali, M. Modeling the phase behavior of polydisperse rigid rods with attractive interactions with applications to single-walled carbon nanotubes in superacids. *Journal of Chemical Physics* **131** (2009).

127 Khokhlov, A. R. & Semenov, A. N. On the theory of liquid-crystalline ordering of polymer chains with limited flexibility. *Journal of Statistical Physics* **38**, 161 (1985).

128 Flory, P. J. & Ronca, G. Theory of systems of rodiike particles: Ii. Thermotropic systems with orientation-dependent interactions. *Molecular Crystals and Liquid Crystals* **54**, 311 (1979).

129 Flory, P. J. Phase equilibria in solutions of rod-like particles. *Proceedings of the Royal Society of London. Series A. Mathematical and Physical Sciences* **234**, 73 (1956).

130 Flory, P. J. Statistical thermodynamics of mixtures of rodlike particles. 6. Rods connected by flexible joints. *Macromolecules* **11**, 1141 (1978).

131 Flory, P. J. & Abe, A. Statistical thermodynamics of mixtures of rodlike particles. 1. Theory for polydisperse systems. *Macromolecules* **11**, 1119 (1978).

132 Barry, E., Hensel, Z., Dogic, Z., Shribak, M. & Oldenbourg, R. Entropy-driven formation of a chiral liquid-crystalline phase of helical filaments. *Physical Review Letters* **96** (2006).

133 Lu, L. H. & Chen, W. Large-scale aligned carbon nanotubes from their purified, highly concentrated suspension. *ACS Nano* **4**, 1042.

134 Hobbie, E. K. *et al.* Self-assembly of ordered nanowires in biological suspensions of single-wall carbon nanotubes. *ACS Nano* **3**, 189 (2008).

135 Russell, D. W. The enzymes, regulation, and genetics of bile acid synthesis. *Annual Review of Biochemistry* **72**, 137 (2003).

136 Tasis, D., Tagmatarchis, N., Bianco, A. & Prato, M. Chemistry of carbon nanotubes. *Chemical Reviews* **106**, 1105 (2006).

137 Dogic, Z. & Fraden, S. Cholesteric phase in virus suspensions. *Langmuir* **16**, 7820 (2000).

138 Livolant, F. Cholesteric organization of DNA invivo and invitro. *European Journal of Cell Biology* **33**, 300 (1984).

139 Vanwinkle, D. H., Davidson, M. W., Chen, W. X. & Rill, R. L. Cholesteric helical pitch of near persistence length DNA. *Macromolecules* **23**, 4140 (1990).

140 Stanley, C. B., Hong, H. & Strey, H. H. DNA cholesteric pitch as a function of density and ionic strength. *Biophysical Journal* **89**, 2552 (2005).

141 Kornyshev, A. A., Leikin, S. & Malinin, S. V. Chiral electrostatic interaction and cholesteric liquid crystals of DNA. *European Physical Journal E* **7**, 83 (2002).

142 Wierenga, A. M. & Philipse, A. P. Low-shear viscosity of isotropic dispersions of (brownian) rods and fibres; a review of theory and experiments. *Colloids and Surfaces A: Physicochemical and Engineering Aspects* **137**, 355 (1998).

143 Marshall, B. D., Davis, V. A., Lee, D. C. & Korgel, B. A. Rotational and translational diffusivities of germanium nanowires. *Rheologica Acta* **48**, 589 (2009).

144 Mead, D. W. & Larson, R. G. Rheooptical study of isotropic solutions of stiff polymers. *Macromolecules* **23**, 2524 (1990).

145 Marceau, S., Dubois, P., Fulchiron, R. & Cassagnau, P. Viscoelasticity of brownian carbon nanotubes in pdms semidilute regime. *Macromolecules* **42**, 1433 (2009).

146 Mori, Y., Ookubo, N., Hayakawa, R. & Wada, Y. Low frequency and high frequency relaxations in dynamic electric birefringence of poly ( benzyl l glutamate) in m cresol. *Journal of Polymer Science: Polymer Physics Edition* **20**, 2111 (1982).

147 Kirkwood, J. G. & Plock, R. J. Non newtonian viscoelastic properties of rod like macromolecules in solution. *The Journal of Chemical Physics* **24**, 665 (1956).

148 Batchelor, G. K. The stress system in a suspension of force-free particles. *Journal of Fluid Mechanics* **41**, 545 (1970).

149 Parra-Vasquez, A. N. G. *et al.* Simple length determination of single-walled carbon nanotubes by viscosity measurements in dilute suspensions. *Macromolecules* **40**, 4043 (2007).

150 Duggal, R. & Pasquali, M. Dynamics of individual single-walled carbon nanotubes in water by real-time visualization. *Physical Review Letters* **96**, 246104 (2006).

151 Davis, V. A. Phase behavior and rheology of single-walled carbon nanotubes (swnts) in superacids with application to fiber spinning. *Dissertation of Doctor of Philosophy, Rice University* (2006).

152 Ciferri, A. Liquid crystallinity in polymers: Principles and fundamental properties. 1991 (Wiley-VCH).

153 Walker, L. & Wagner, N. Rheology of region-i flow in a lyotropic liquid-crystal polymer - the effects of defect texture. *Journal of Rheology* **38**, 1525 (1994).

154 Mackley, M. R., Pinaud, F. & Siekmann, G. Observation of disclinations and optical anisotropy in a mesomorphic copolyester. *Polymer* **22**, 437 (1981).

155 Kiss, G. & Porter, R. S. 193 (John Wiley & Sons).

156 Marrucci, G. & Maffettone, P. L. A description of the liquid-crystalline phase of rodlike polymers at high shear rates. *Macromolecules* **22**, 4076 (1989).

157 Larson, R. G. Arrested tumbling in shearing flows of liquid-crystal polymers. *Macromolecules* **23**, 3983 (1990).

158 Larson, R. G. Constitutive equations for polymer melts and solutions. *Butterworths*, 364 (1988).

159 Grizzuti, N., Cavella, S. & Cicarelli, P. Transient and steady-state rheology of a liquid crystalline hydroxypropylcellulose solution. *Journal of Rheology* **34**, 1293 (1990).

160 Semenov, A. N. Rheological properties of a liquid crystal solution of rod-like molecules. *Soviet Physics JETP* **66**, 321 (1983)

161 Maffettone, P. L. & Marrucci, G. The nematic dumbbell model. *Journal of Rheology* **36**, 1547 (1992).

162 Moldenaers, P. & Mewis, J. Transient behavior of liquid crystalline solutions of poly (benzylglutamate). *Journal of Rheology* **30**, 567 (1986).

163 Sakamoto, K., MacKnight, W. J. & Porter, R. S. Dynamic and steady-shear melt rheology of and ethylene-methacrylic acid copolymer and its salts. *Journal of Polymer Science Part A-2: Polymer Physics* **8**, 277 (1970).

164 Earnest Jr, T. R. & MacKnight, W. J. Effect of hydrogen bonding and ionic aggregation on the melt rheology of an ethylene-methacrylic acid copolymer and its sodium salt. *Journal of Polymer Science: Polymer Physics Edition* **16**, 143 (1978).

165 Cox, W. P. & Merz, E. H. Correlation of dynamic and steady flow viscosities. *Journal of Polymer Science* **28**, 619 (1958).

166 Marrucci, G. Dynamics of entanglements: A nonlinear model consistent with the cox-merz rule. *Journal of Non-Newtonian Fluid Mechanics* **62**, 279 (1996).

167 Ianniruberto, G. & Marrucci, G. On compatibility of the cox-merz rule with the model of doi and edwards. *Journal of Non-Newtonian Fluid Mechanics* **65**, 241 (1996).

168 Mead, D. W., Larson, R. G. & Doi, M. A molecular theory for fast flows of entangled polymers. *Macromolecules* **31**, 7895 (1998).

169 Mead, D. W. Analytic derivation of the cox-merz rule using the mld "toy" model for polydisperse linear polymers. *Rheologica Acta* **50**, 837 (2011).

170 Larson, R. G. & Doi, M. Mesoscopic domain theory for textured liquid crystalline polymers. *Journal of Rheology* **35**, 539 (1991).

171 Marrucci, G. Rheology of liquid crystalline polymers. *Pure Applied Chemistry* **57**, 1545 (1985).

172 Larson, R. G. & Mead, D. W. Development of orientation and texture during shearing of liquid-crystalline polymers. *Liquid Crystals(UK)* **12**, 751 (1992).

173 Harrison, P. & Navard, P. Investigation of the band texture occurring in hydroxypropylcellulose solutions using rheo-optical, rheological and small angle light scattering techniques. *Rheologica Acta* **38**, 569 (1999).

174 Dealy, J. & Plazek, D. Time-temperature superposition-A users guide. *Rheology Bulletin* **78**, 16 2009.

175 Williams, M. L., Landel, R. F. & Ferry, J. D. The temperature dependence of relaxation mechanisms in amorphous polymers and other glass-forming liquids. *Journal of the American Chemical Society* **77**, 3701 (1955).

176 Ferry, J. D. Viscoelastic properties of polymers.1980. (John Wiley & Sons Inc).

177 Van Gurp, M. & Palmen, J. Time-temperature superposition for polymeric blends. *Rheology Bulletin* **67**, 5 (1998).

178 Li, L. S., Marjanska, M., Park, G. H. J., Pines, A. & Alivisatos, A. P. Isotropic-liquid crystalline phase diagram of a cdse nanorod solution. *The Journal of Chemical Physics* **120**, 1149 (2004).

179 Odijk, T. Theory of lyotropic polymer liquid crystals. *Macromolecules* **19**, 2313 (1986).

180 Fakhri, N., Tsyboulski, D. A., Cognet, L., Weisman, R. B. & Pasquali, M. Diameter-dependent bending dynamics of single-walled carbon nanotubes in liquids. *Proceedings of the National Academy of Sciences* **106**, 14219 (2009).

181 Gittes, F., Mickey, B., Nettleton, J. & Howard, J. Flexural rigidity of microtubules and actin filaments measured from thermal fluctuations in shape. *Journal of Cell Biology* **120**, 923 (1993).

182 Smith, D. E., Perkins, T. T. & Chu, S. Dynamical scaling of DNA diffusion coefficients. *Macromolecules* **29**, 1372 (1996).

183 Kudin, K. N., Scuseria, G. E. & Yakobson, B. I. C_ {2} f, bn, and c nanoshell elasticity from ab initio computations. *Physical Review B* **64**, 235406 (2001).

184 Yakobson, B. I. & Couchman, L. S. Persistence length and nanomechanics of random bundles of nanotubes. *Journal of Nanoparticle Research* **8**, 105 (2006).

185 Gittes, F. & MacKintosh, F. C. Dynamic shear modulus of a semiflexible polymer network. *Physical Review E* **58**, 1241 (1998).

186 Shankar, V., Pasquali, M. & Morse, D. C. Theory of linear viscoelasticity of semiflexible rods in dilute solution. *Journal of Rheology* **46**, 1111 (2002).

187 Hirsch, A. Functionalization of single-walled carbon nanotubes. *Angewandte Chemie-International Edition* **41**, 1853 (2002).

188 Krause, B., Petzold, G., Pegel, S. & Potschke, P. Correlation of carbon nanotube dispersability in aqueous surfactant solutions and polymers. *Carbon* **47**, 602 (2009).

189 Zhang, S. J., Li, Q. W., Kinloch, I. A. & Windle, A. H. Ordering in a droplet of an aqueous suspension of single-wall carbon nanotubes on a solid substrate. *Langmuir* **26**, 2107.

190 Song, W. H. & Windle, A. H. Isotropic-nematic phase transition of dispersions of multiwall carbon nanotubes. *Macromolecules* **38**, 6181 (2005).

191 Schmidt, R. H., Kinloch, I. A., Burgess, A. N. & Windle, A. H. The effect of aggregation on the electrical conductivity of spin-coated polymer/carbon nanotube composite films. *Langmuir* **23**, 5707 (2007).

192 Zamora-Ledezma, C. *et al.* Anisotropic thin films of single-wall carbon nanotubes from aligned lyotropic nematic suspensions. *Nano Letters* **8**, 4103 (2008).

193 Deegan, R. D. *et al.* Capillary flow as the cause of ring stains from dried liquid drops. *Nature* **389**, 827 (1997).

194 Cataldo, F. DNA degradation with ozone. *International Journal of Biological Macromolecules* **38**, 248 (2006).

195 Gupta, V. B. & Kothari, V. K. *Manufactured Fibre Echnology*. 1997 (Springer).

196 Treacy, M. M. J., Ebbesen, T. W. & Gibson, J. M. Exceptionally high young's modulus observed for individual carbon nanotubes. *Nature* **381**, 678 (1996).

197 Pasquali, M. *et al.* Neat carbon nanotube articles processed from super acid solutions and methods for production thereof. 2009. (WO Patent WO/2009/058,855).

198 Barisci, J. N. *et al.* Properties of carbon nanotube fibers spun from DNA-stabilized dispersions. *Advanced Functional Materials* **14**, 133 (2004).

199 Endres, R. G., Cox, D. L. & Singh, R. R. P. Colloquium: The quest for high-conductance DNA. *Reviews of Modern Physics* **76**, 195 (2004).

200 Xu, Y. Q., Peng, H. Q., Hauge, R. H. & Smalley, R. E. Controlled multistep purification of single-walled carbon nanotubes. *Nano Letters* **5**, 163 (2005).

201 Lucas, A. *et al.* Kinetics of nanotube and microfiber scission under sonication. *The Journal of Physical Chemistry C* **113**, 20599 (2009).

202 Cheng, Q., Debnath, S., Gregan, E. & Byrne, H. J. Ultrasound-assisted swnts dispersion: Effects of sonication parameters and solvent properties. *The Journal of Physical Chemistry C* **114**, 8821.

203 Hilding, J., Grulke, E. A., Zhang, Z. G. & Lockwood, F. J. Dispersion of carbon nanotubes in liquids. *Journal of Dispersion Science Technology **24***, 2003, 1.

204 Sato, J. & Breedveld, V. Evaporation blocker for cone-plate rheometry of volatile samples. *Applied Rheology* **15**, 390 (2005).

205 Gupta, R. K. Polymer and composite rheology. 2000. (CRC).

206 Macosko, C. W. & Larson, R. G. Rheology: Principles, measurements, and applications. 1994. (VCH New York).

207 Kumar, A. & Gupta, R. K. Fundamentals of polymer engineering. 2003 (CRC).

208 Sancar, A. Structure and function of DNA photolyase. *Biochemistry* **33**, 2 (1994).

209 Singer, V. L., Jones, L. J., Yue, S. T. & Haugland, R. P. Characterization of picogreen reagent and development of a fluorescence-based solution assay for double-stranded DNA quantitation. *Analytical Biochemistry* **249**, 228 (1997).

210 Kornyshev, A. A. & Leikin, S. Electrostatic interaction between long, rigid helical macromolecules at all interaxial angles. *Physical Review E* **62**, 2576 (2000).

211 Marrucci, G. & Maffettone, P. L. Nematic phase of rodlike polymers. Ii. Polydomain predictions in the tumbling regime. *Journal of Rheology* **34**, 1231 (1990).

212 Onogi, S. & Asada, T. Rheology and rheo-optics of polymer liquid crystals. *Rheology* **1**, 127 (1980).

213 Yoshimura, A. S., Prud'Homme, R. K., Princen, H. M. & Kiss, A. D. A comparison of techniques for measuring yield stresses. *Journal of Rheology* **31**, 699 (1987).

214 Hough, L. A., Islam, M. F., Janmey, P. A. & Yodh, A. G. Viscoelasticity of single wall carbon nanotube suspensions. *Physical Review Letters* **93**, 168102 (2004).

215 Huang, Y. Y., Ahir, S. V. & Terentjev, E. M. Dispersion rheology of carbon nanotubes in a polymer matrix. *Physical Review B* **73**, 125422 (2006).

216 Sahimi, M. & Arbabi, S. Mechanics of disordered solids. Ii. Percolation on elastic networks with bond-bending forces. *Physical Review B* **47**, 703 (1993).

217 Vollrath, F. & Knight, D. P. Liquid crystalline spinning of spider silk. *Nature* **410**, 541 (2001).

218 Lee, S. W., Wood, B. M. & Belcher, A. M. Chiral smectic c structures of virus-based films. *Langmuir* **19**, 1592 (2003).

219 Roy, K. B., Antony, T., Sakena, A. & Bohidar, H. B. Ethanol-induced condensation of calf thymus DNA studied by laser light scattering. *Journal of Physical Chemistry B* **103**, 5117 (1999).

220 Matzeu, M., Onori, G. & Santucci, A. Condensation of DNA by monohydric alcohols. *Colloids and Surfaces B-Biointerfaces* **13**, 157 (1999).

221 Knight, J. D. & Adami, R. C. Stabilization of DNA utilizing divalent cations and alcohol. *International Journal of Pharmaceutics* **264**, 15 (2003).

222 Bloomfield, V. A. DNA condensation. *Current Opinion in Structural Biology* **6**, 334 (1996).

223 Hayashi, K., Kugimiya, M., Imoto, T., Funatsu, M. & Bigelow, C. C. Inhibitory interaction of cationic detergents with the active center of lysozyme. Ii. Ph dependence of the interaction. *Biochemistry* **7**, 1467 (1968).

224 Bordbar, A. K., Hosseinzadeh, R. & Norozi, M. H. Interaction of a homologous series of n-alkyl trimethyl ammonium bromides with eggwhite lysozyme. *Journal of Thermal Analysis and Calorimetry* **87**, 453 (2007).

225 Sun, Z. *et al.* Quantitative evaluation of surfactant-stabilized single-walled carbon nanotubes: Dispersion quality and its correlation with zeta potential. *The Journal of Physical Chemistry C* **112**, 10692 (2008).

226 Montesi, A., Pena, A. A. & Pasquali, M. Vorticity alignment and negative normal stresses in sheared attractive emulsions. *Physical Review Letters* **92**, 58303 (2004).

227 Bercea, M. & Navard, P. Shear dynamics of aqueous suspensions of cellulose whiskers. *Macromolecules* **33**, 6011 (2000).

## Appendix 1

The conversion of SWNT concentration from a unit of milligram per liter (1 mg/L=1 ppm) measured by UV-Vis spectrophotometer into volume fraction $\phi$ (vol %) is given as follows:

$$\phi = \frac{m_{SWNTs} \times 10^{-6}}{\rho_{SWNTs}} \times {}^{100}\!/_{100} \tag{1}$$

where,

$m_{SWNTs}$ = Mass of SWNT in dsDNA/SWNT dispersion (mg/L)

$\rho_{SWNTs}$ = Density of SWNT (1.45 g/cm$^3$)

The conversion of SWNT concentration from mass fraction $\omega$ (wt %) measured by Thermogravimetric analysis into volume fraction $\phi$ (vol %) is given as follows:

$$\phi = \frac{m_{SWNTs}/\rho_{SWNTs}}{m_{SWNTs}/\rho_{SWNTs} + m_{DNA}/\rho_{DNA} + m_{H_2O}/\rho_{H_2O}} \times {}^{100}\!/_{100} \tag{2}$$

where,

$m_{SWNTs}$ = Mass of SWNT in dsDNA/SWNT dispersion (g)

$m_{DNA}$ = Mass of dsDNA in dsDNA/SWNT dispersion (g)

$m_{H_2O}$ = Mass of water in dsDNA/SWNT dispersion (g)

$\rho_{SWNTs}$ = Density of SWNT (1.45 g/cm$^3$)

$\rho_{DNA}$ = Density of dsDNA (1.7 g/cm$^3$)

$\rho_{H_2O}$ = Density of water (1.0 g/cm$^3$)

Table 1. The conversion of SWNT concentration into volume fraction for evaporated samples starting from 0.75 wt % dsDNA-0.1 wt % SWNT dispersion without centrifugation.

| Samples: non-centrifuged dsDNA/SWNT dispersion with dsDNA:SWNT = 7.5:1 | $\rho_{SWNTs}$ (g/cm$^3$) | $\rho_{DNA}$ (g/cm$^3$) | $\rho_{H_2O}$ (g/cm$^3$) | $\omega$ (wt %) | $\phi$ (vol %) |
|---|---|---|---|---|---|
| 1 | 1.45 | 1.7 | 1.0 | 0.70 | 0.49 |
| 2 | 1.45 | 1.7 | 1.0 | 1.10 | 0.77 |
| 3 | 1.45 | 1.7 | 1.0 | 1.25 | 0.88 |
| 4 | 1.45 | 1.7 | 1.0 | 1.44 | 1.01 |
| 5 | 1.45 | 1.7 | 1.0 | 1.82 | 1.29 |
| 6 | 1.45 | 1.7 | 1.0 | 2.30 | 1.64 |
| 7 | 1.45 | 1.7 | 1.0 | 3.01 | 2.18 |
| 8 | 1.45 | 1.7 | 1.0 | 3.88 | 2.85 |
| 9 | 1.45 | 1.7 | 1.0 | 4.47 | 3.31 |
| 10 | 1.45 | 1.7 | 1.0 | 5.21 | 3.91 |
| 11 | 1.45 | 1.7 | 1.0 | 6.07 | 4.62 |

Table 2. The conversion of SWNT concentration into volume fraction for evaporated samples of supernatant of 0.75 wt % dsDNA-0.1 wt % SWNT (original dispersion) after centrifugation.

| Samples: supernatant of dsDNA/SWNT dispersion with dsDNA:SWNT = 5.1:1 | $\rho_{SWNTs}$ (g/cm$^3$) | $\rho_{DNA}$ (g/cm$^3$) | $\rho_{H_2O}$ (g/cm$^3$) | $\omega$ (wt %) | $\phi$ (vol %) |
|---|---|---|---|---|---|
| 1 | 1.45 | 1.7 | 1.0 | 0.38 | 0.26 |
| 2 | 1.45 | 1.7 | 1.0 | 0.49 | 0.35 |
| 3 | 1.45 | 1.7 | 1.0 | 0.85 | 0.60 |
| 4 | 1.45 | 1.7 | 1.0 | 1.15 | 0.82 |
| 5 | 1.45 | 1.7 | 1.0 | 1.19 | 0.85 |
| 6 | 1.45 | 1.7 | 1.0 | 1.30 | 0.93 |
| 7 | 1.45 | 1.7 | 1.0 | 1.46 | 1.04 |
| 8 | 1.45 | 1.7 | 1.0 | 1.68 | 1.21 |
| 9 | 1.45 | 1.7 | 1.0 | 1.76 | 1.27 |
| 10 | 1.45 | 1.7 | 1.0 | 2.03 | 1.47 |
| 11 | 1.45 | 1.7 | 1.0 | 2.62 | 1.93 |
| 12 | 1.45 | 1.7 | 1.0 | 2.91 | 2.16 |
| 13 | 1.45 | 1.7 | 1.0 | 2.99 | 2.22 |
| 14 | 1.45 | 1.7 | 1.0 | 3.12 | 2.32 |
| 15 | 1.45 | 1.7 | 1.0 | 3.45 | 2.60 |
| 16 | 1.45 | 1.7 | 1.0 | 4.37 | 3.37 |
| 17 | 1.45 | 1.7 | 1.0 | 4.97 | 3.90 |
| 18 | 1.45 | 1.7 | 1.0 | 6.69 | 5.50 |

Table 3. The conversion of dsDNA concentration into volume fraction for evaporated samples of dsDNA only solution with starting concentration of 0.75 wt % after sonication and centrifugation.

| Samples: dsDNA solution | $\rho_{DNA}$ (g/cm$^3$) | $\rho_{H_2O}$ (g/cm$^3$) | $\omega$ (wt %) | $\phi$ (vol %) |
|---|---|---|---|---|
| 1 | 1.7 | 1.0 | 0.80 | 0.47 |
| 2 | 1.7 | 1.0 | 5.34 | 3.21 |
| 3 | 1.7 | 1.0 | 6.44 | 3.90 |
| 4 | 1.7 | 1.0 | 7.46 | 4.53 |
| 5 | 1.7 | 1.0 | 8.12 | 4.94 |
| 6 | 1.7 | 1.0 | 8.78 | 5.36 |
| 7 | 1.7 | 1.0 | 10.06 | 6.17 |
| 8 | 1.7 | 1.0 | 11.49 | 7.09 |
| 9 | 1.7 | 1.0 | 12.63 | 7.84 |
| 10 | 1.7 | 1.0 | 13.08 | 8.13 |
| 11 | 1.7 | 1.0 | 15.53 | 9.76 |
| 12 | 1.7 | 1.0 | 19.63 | 12.56 |
| 13 | 1.7 | 1.0 | 24.75 | 16.21 |
| 14 | 1.7 | 1.0 | 28.88 | 19.28 |

## Appendix 2

### *Step Rate Test*

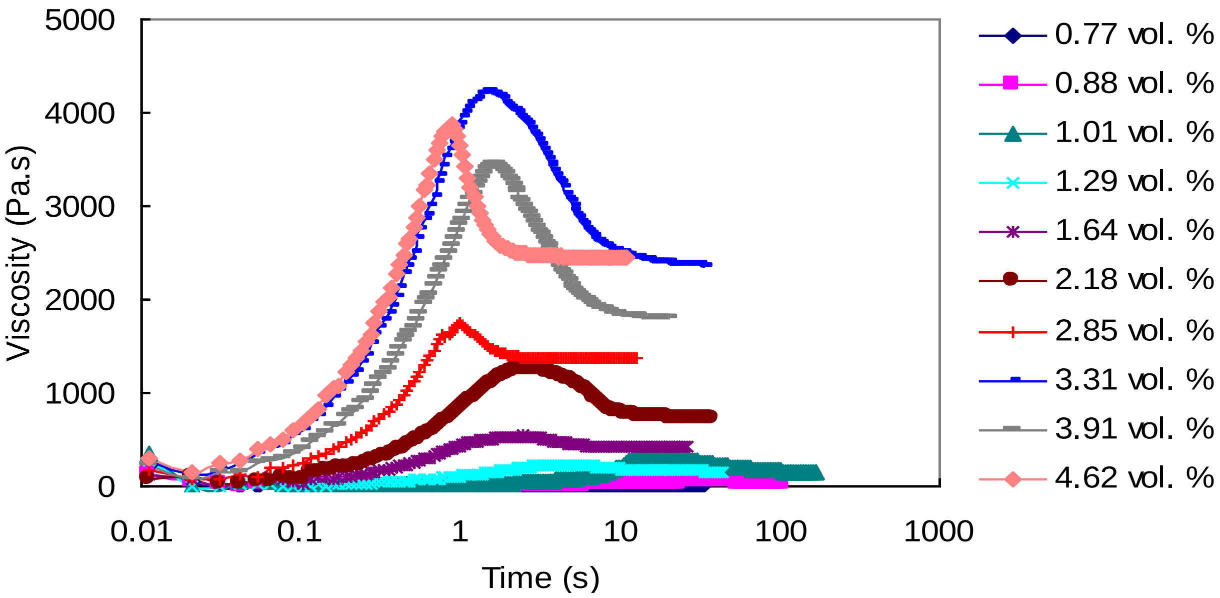

Figure 1. The start up of a shear flow indicated by viscosity versus time at 0.1 $s^{-1}$ shear rate for bulk 6.4:1.0 volume ratio of dsDNA:SWNT dispersions.

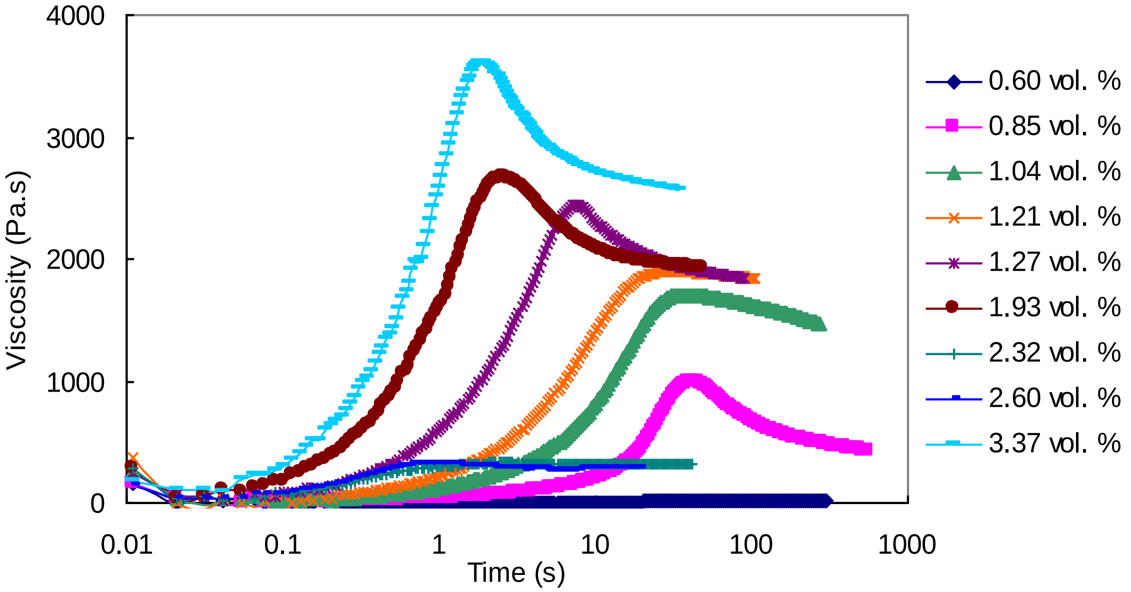

Figure 2. The start up of a shear flow indicated by viscosity versus time at 0.1 $s^{-1}$ shear rate for supernatant 4.4:1.0 volume ratio of dsDNA:SWNT dispersions.

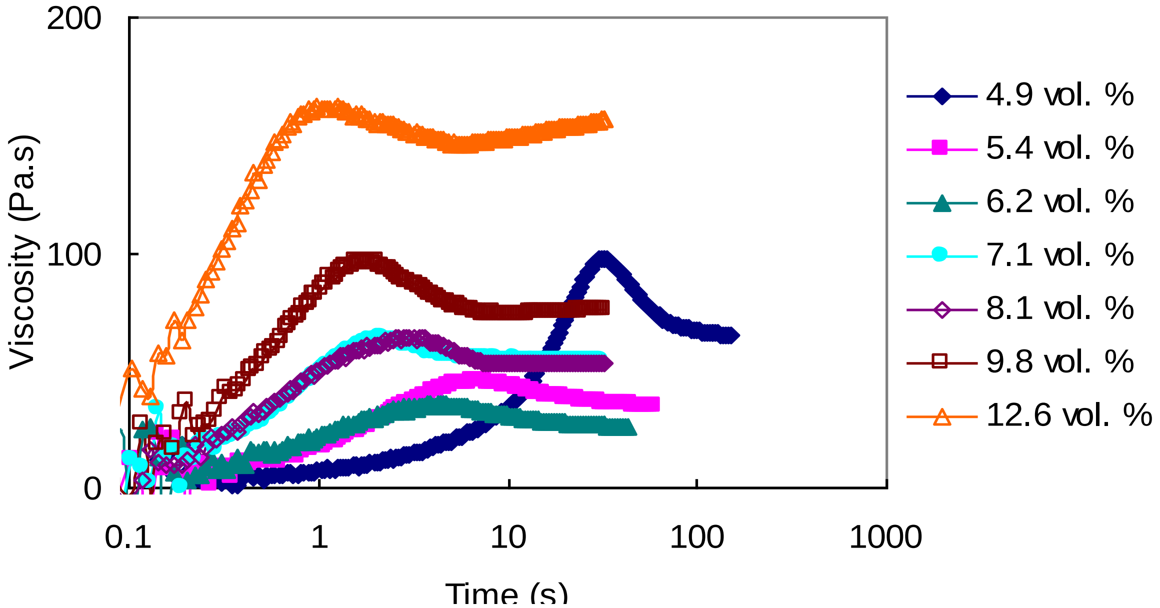

Figure 3. The start up of a shear flow indicated by viscosity versus time at 0.1 $s^{-1}$ shear rate for dsDNA only solutions after sonication and centrifugation.

***Steady-Shear Viscosity***

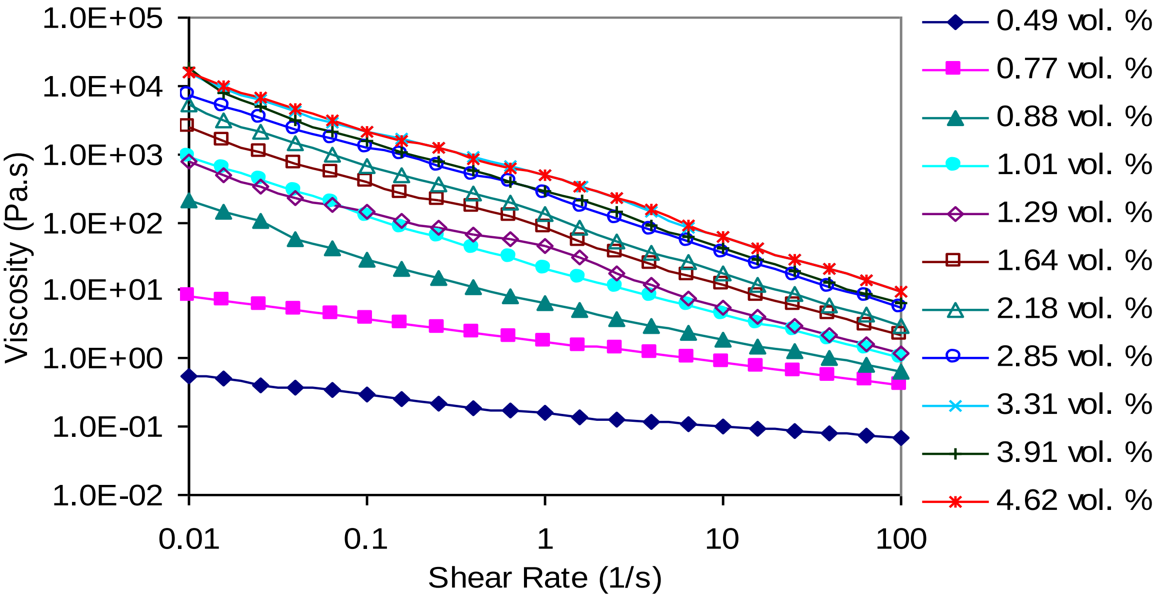

Figure 4. The steady-state shear viscosity with increasing SWNT concentration for bulk 6.4:1.0 volume ratio of dsDNA:SWNT dispersions.

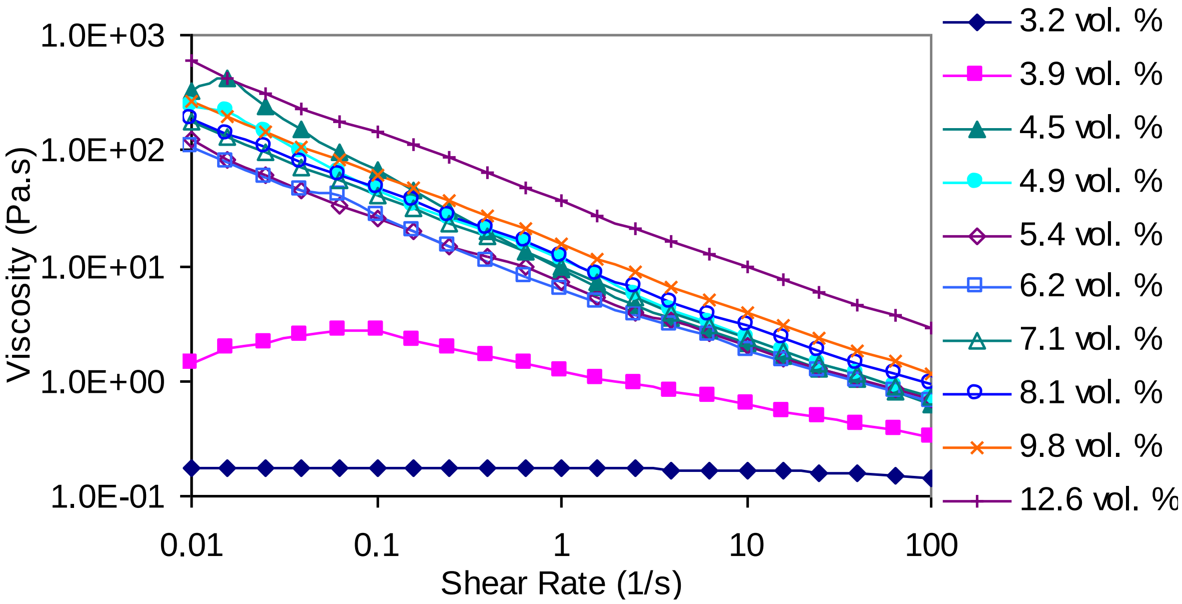

Figure 5. The steady-state shear viscosity with increasing dsDNA concentration for dsDNA only solutions after sonication and centrifugation.

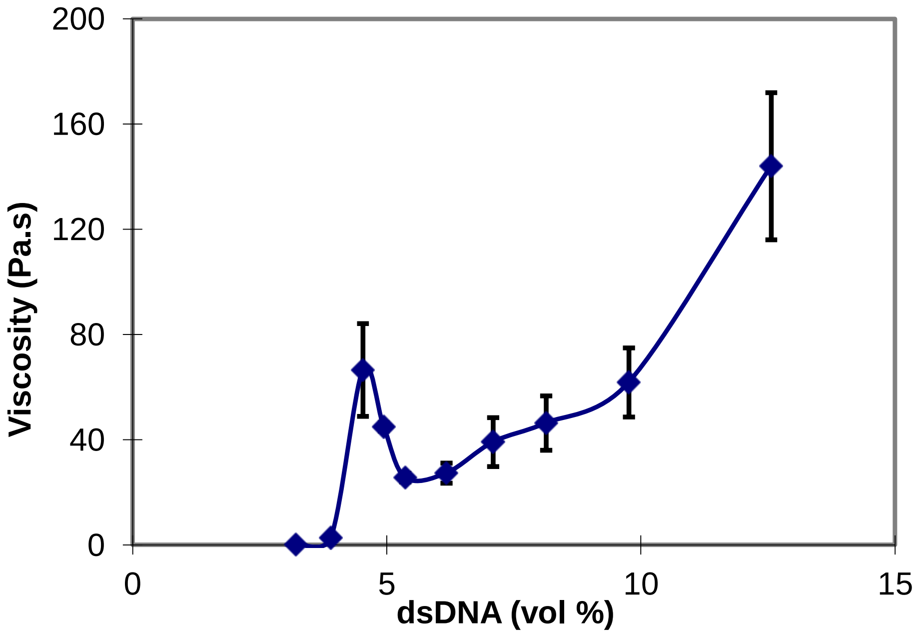

Figure 6. Relationship between viscosity and concentration for dsDNA only solutions at a shear rate of 0.1 $s^{-1}$ and temperature of 10 $^{o}$C.

***Cox-Merz Rule Not Obeyed***

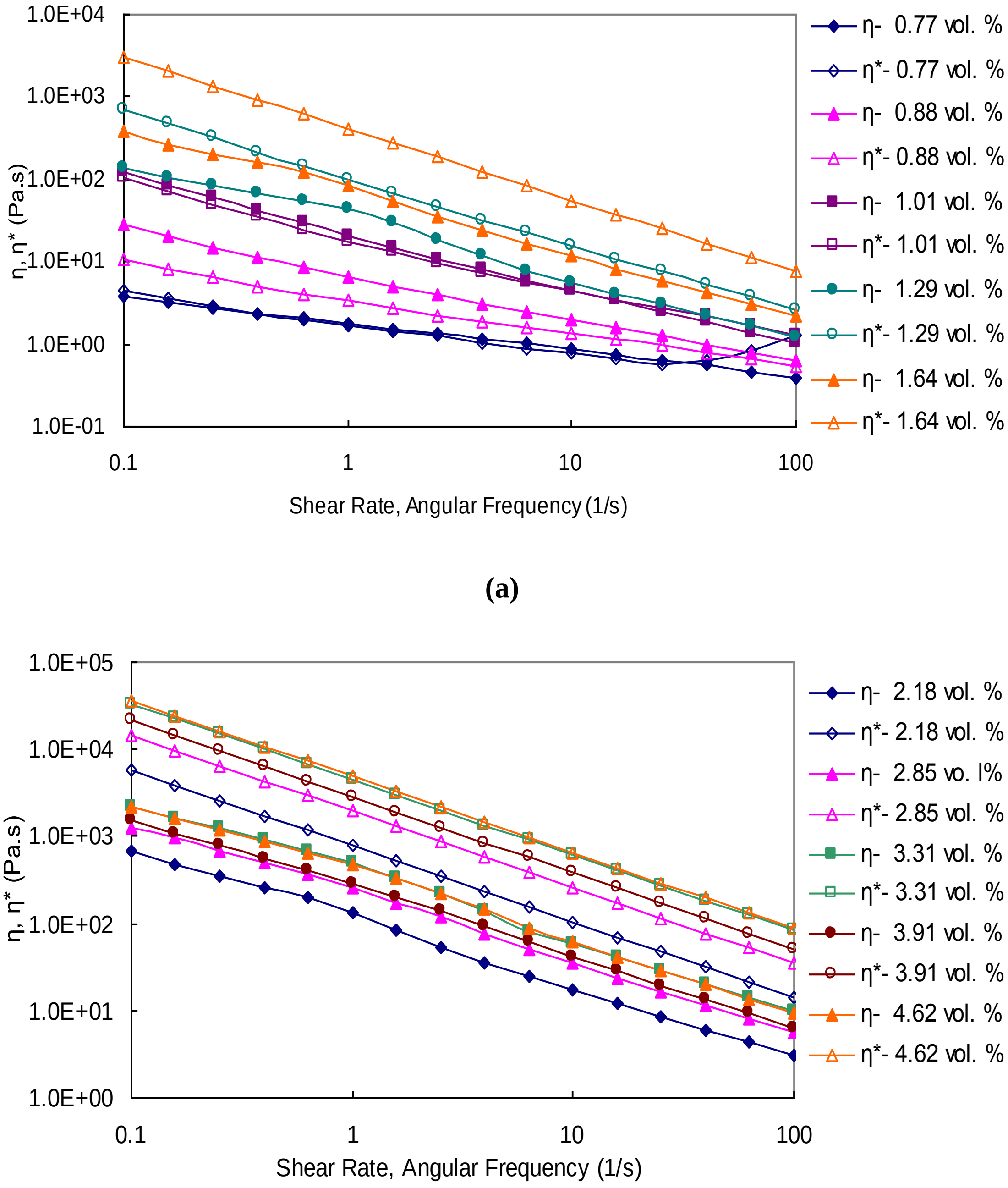

**(a)**

**(b)**

Figure 7. The steady shear viscosity and complex viscosity as a function of shear rate and angular frequency with increasing SWNT concentration for bulk 6.4:1.0 volume ratio of dsDNA:SWNT dispersions.

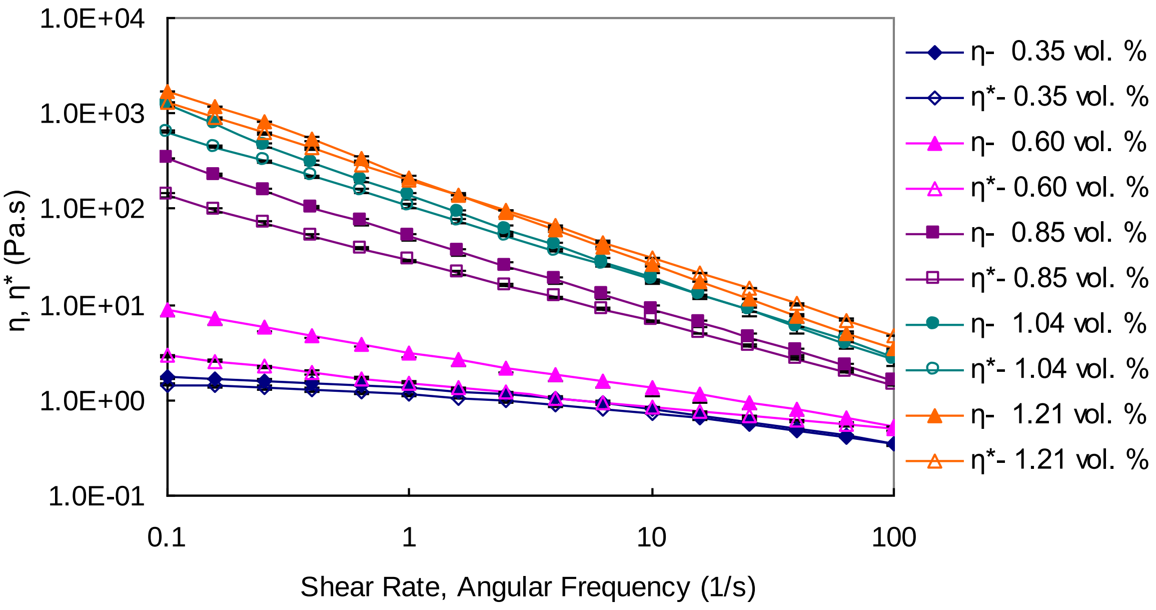

(a)

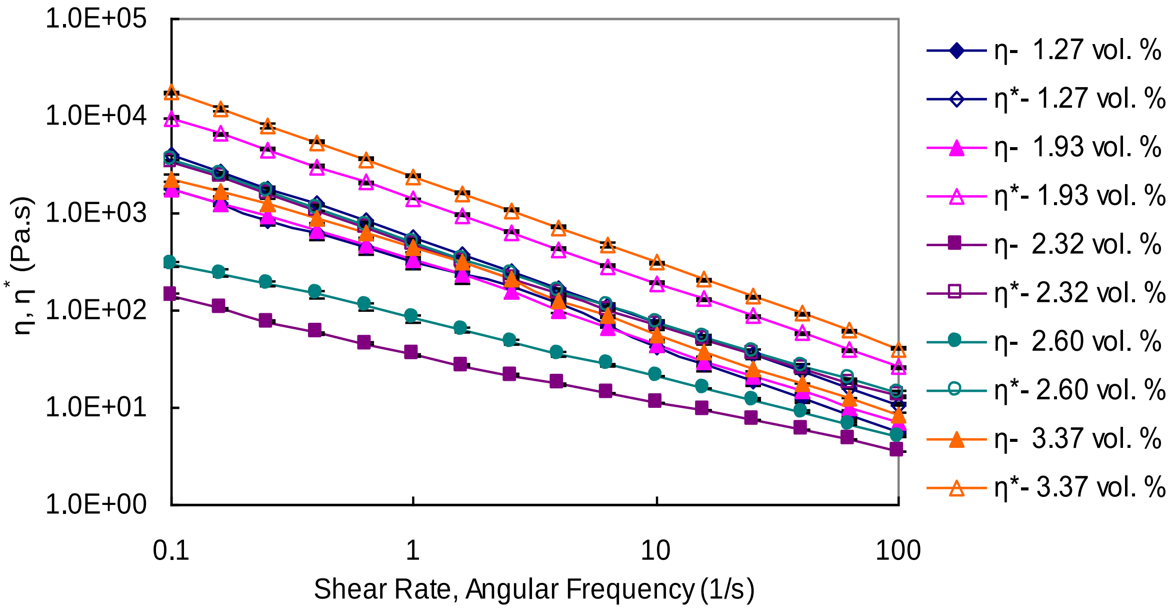

(b)

Figure 8. The steady shear viscosity and complex viscosity as a function of shear rate and angular frequency with increasing SWNT concentration for supernatant 4.4:1.0 volume ratio of dsDNA:SWNT dispersions.

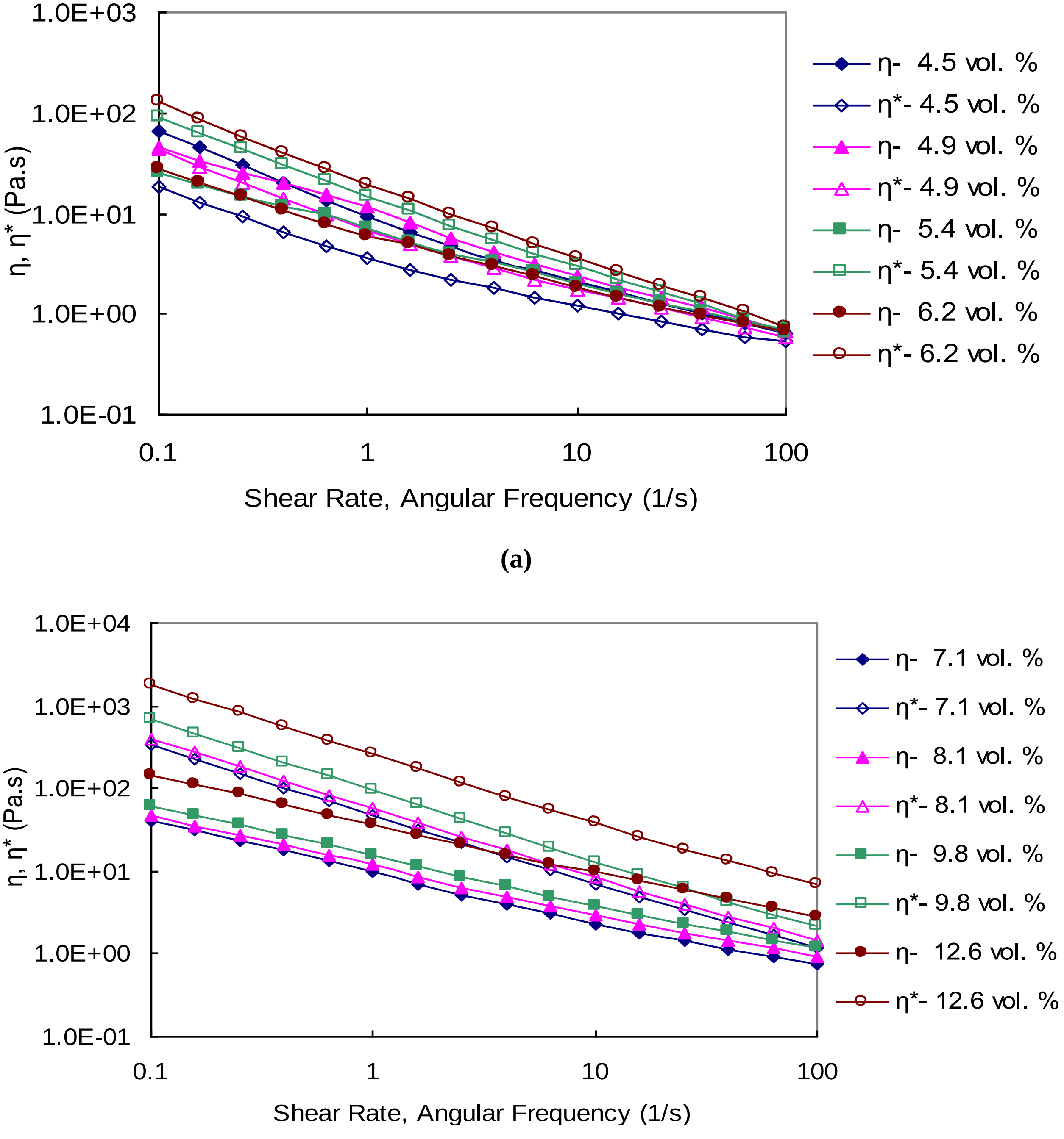

**(a)**

**(b)**

Figure 9. The steady shear viscosity and complex viscosity as a function of shear rate and angular frequency with increasing DNA concentration for dsDNA only solutions after sonication and centrifugation.

***Amplitude Sweep Test***

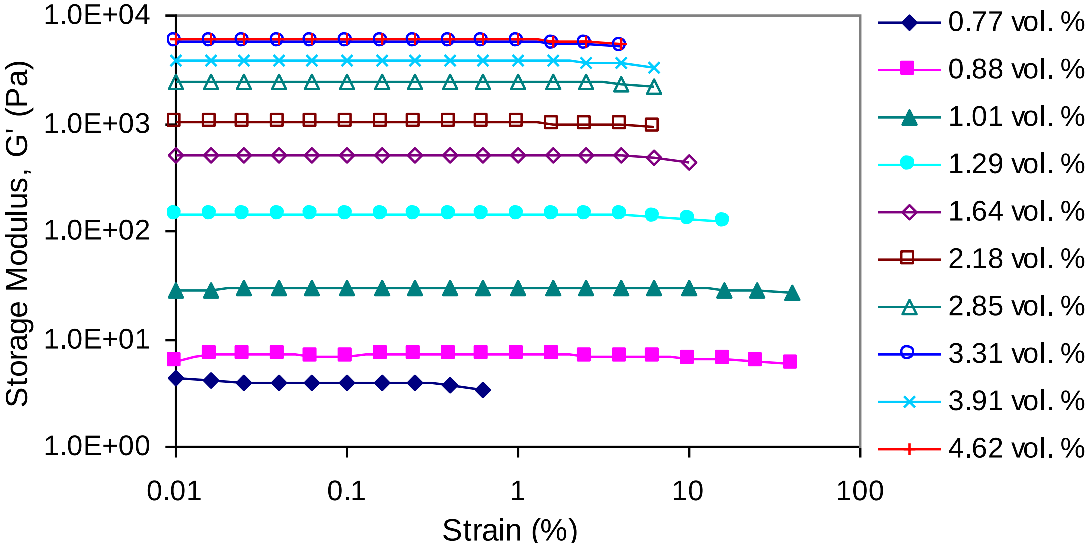

Figure 10. The linear viscoelastic (LVE) region of bulk 6.4:1.0 volume ratio of dsDNA:SWNT dispersions at different SWNT concentrations indicated by the linear function of storage modulus with strain at a fixed angular frequency of 10 $s^{-1}$.

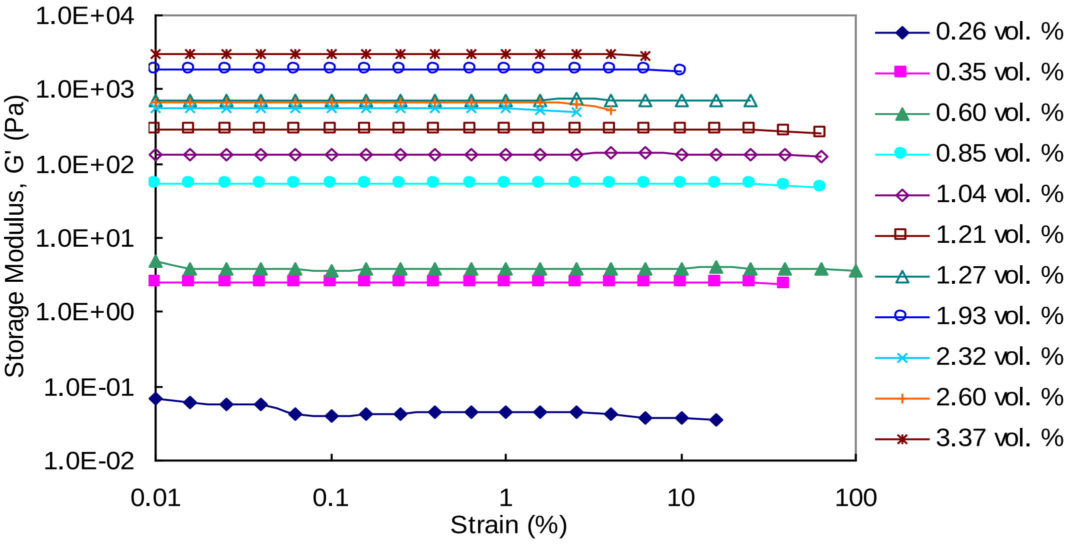

Figure 11. The linear viscoelastic (LVE) region of supernatant 4.4:1.0 volume ratio of dsDNA:SWNT dispersions at different SWNT concentrations indicated by the linear function of storage modulus with strain at a fixed angular frequency of 10 $s^{-1}$.

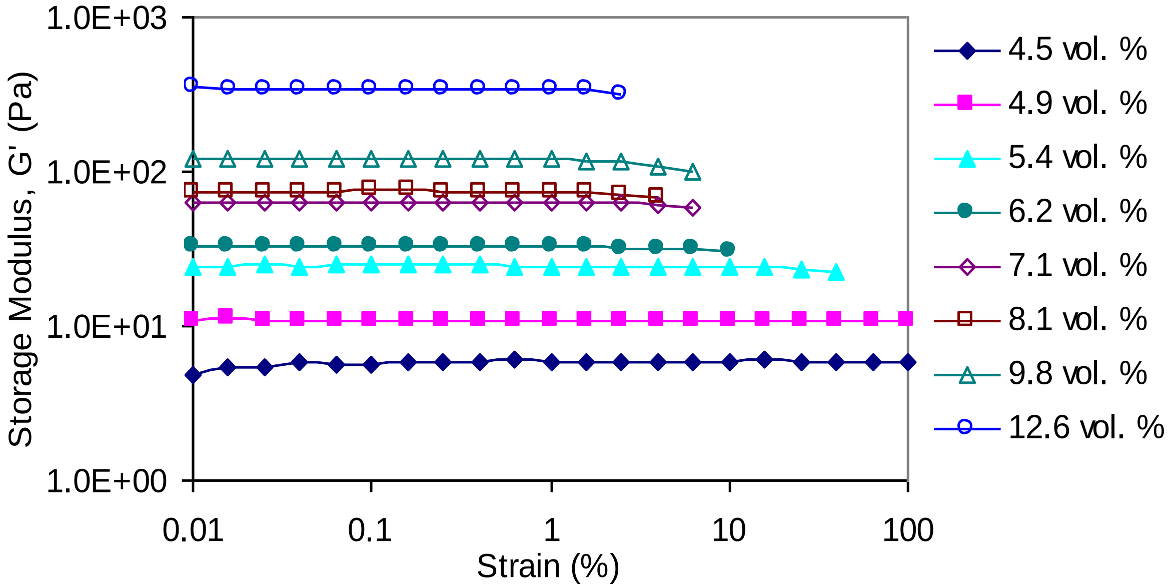

Figure 12. The linear viscoelastic (LVE) region of dsDNA only solutions after sonication and centrifugation at different DNA concentrations indicated by the linear function of storage modulus with strain at a fixed angular frequency of 10 $s^{-1}$.

***Frequency Sweep Test***

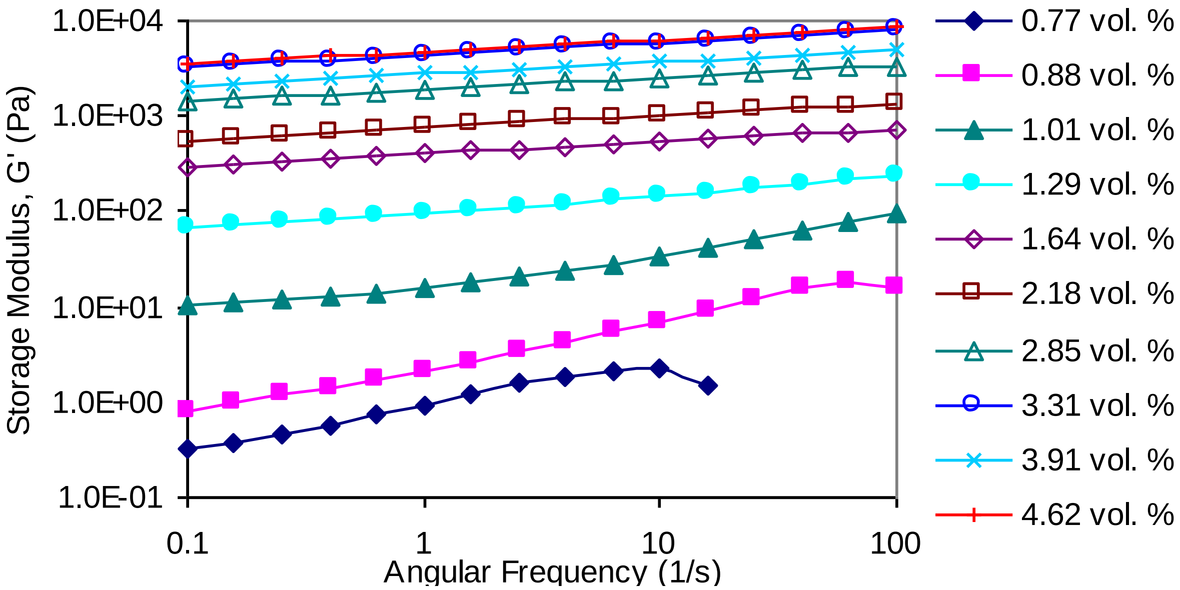

Figure 13. The storage modulus response as a function of angular frequency and increasing SWNT concentration for bulk 6.4:1.0 volume ratio of dsDNA:SWNT dispersions.

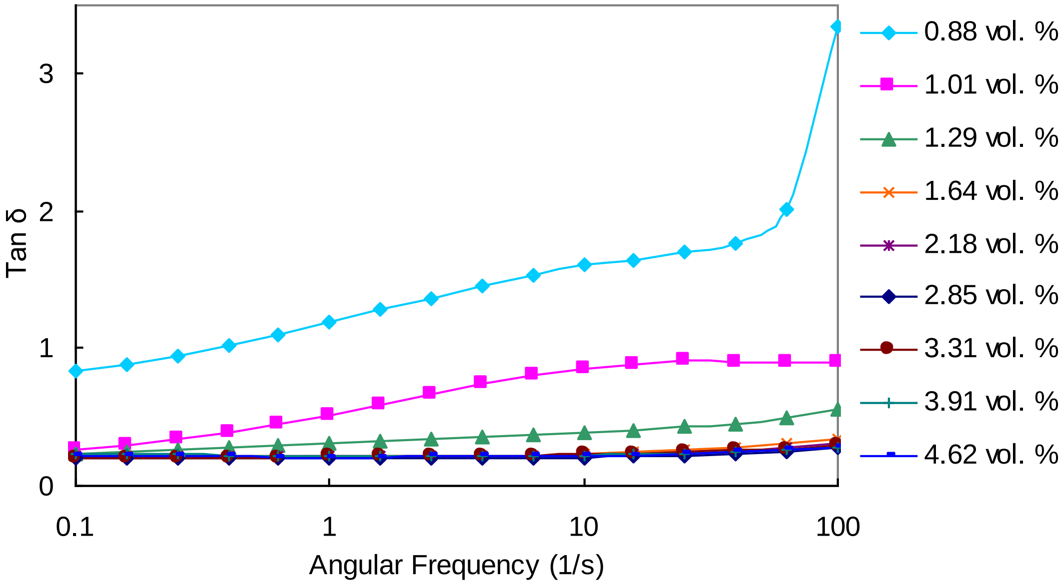

Figure 14. The loss factor tan δ as a function of angular frequency and increasing SWNT concentration for bulk 6.4:1.0 volume ratio of dsDNA:SWNT dispersions.

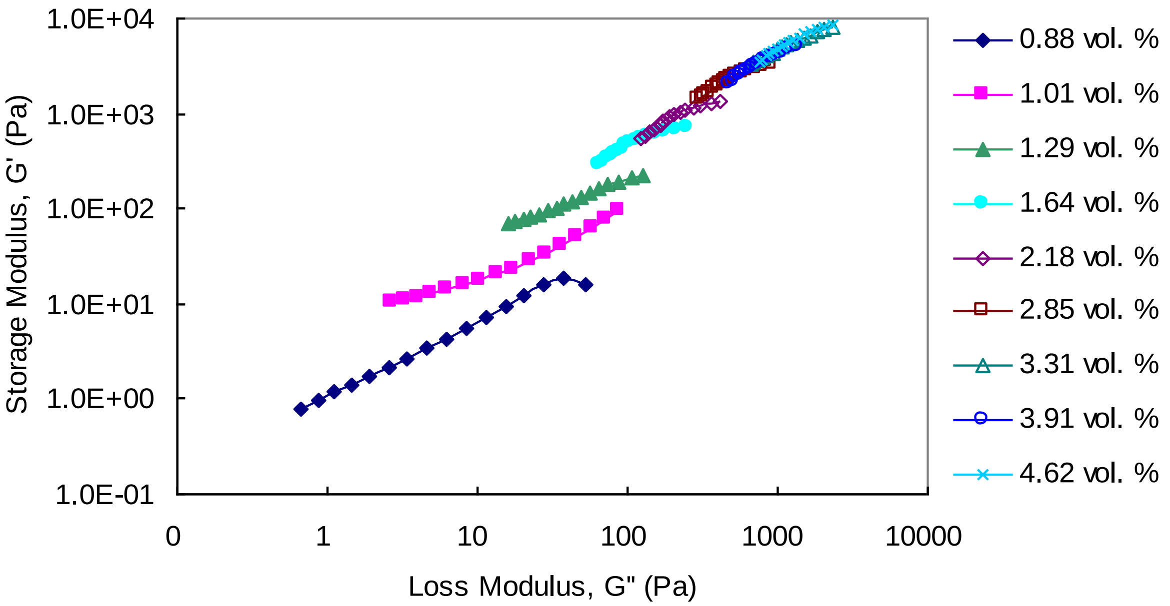

Figure 15. Cole-Cole plots show the storage modulus as a function of loss modulus and increasing SWNT concentration for bulk 6.4:1.0 volume ratio of dsDNA:SWNT dispersions.

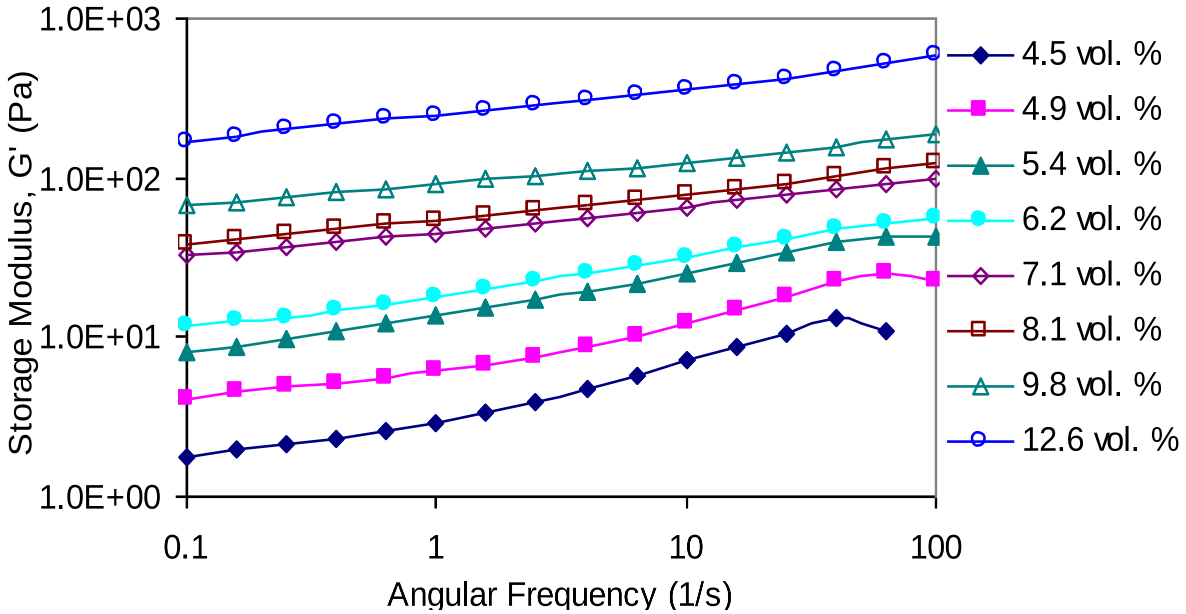

Figure 16. The storage modulus response as a function of angular frequency and increasing DNA concentration for dsDNA only solutions after sonication and centrifugation.

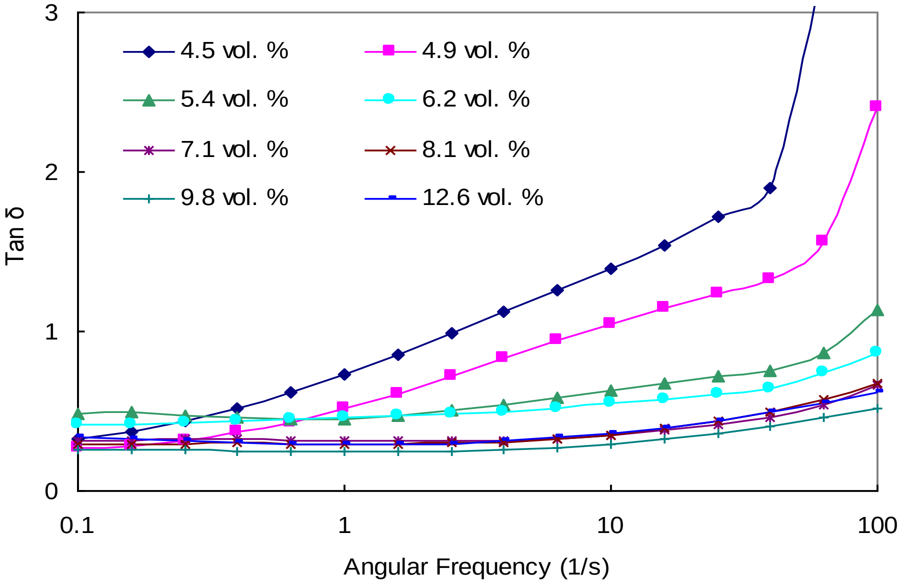

Figure 17. The loss factor tan δ as a function of angular frequency and increasing DNA concentration for dsDNA only solutions after sonication and centrifugation.

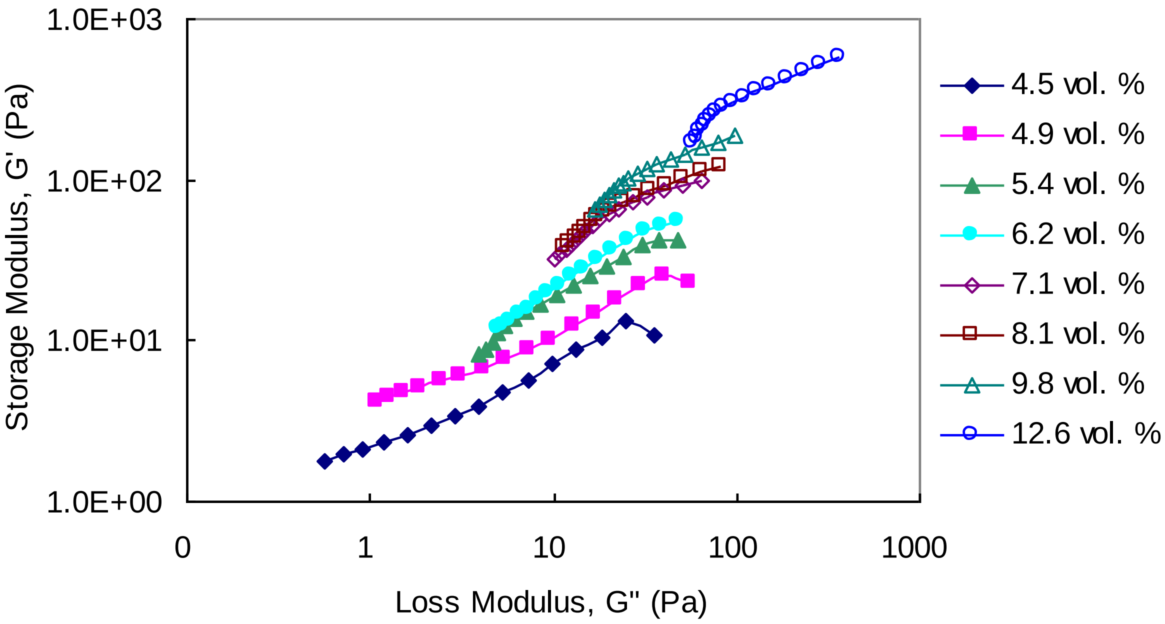

Figure 18. Cole-Cole plots show the storage modulus as a function of loss modulus and increasing DNA concentration for dsDNA only solutions after sonication and centrifugation.